

Sheffield Hallam University

Inclusion behaviour in the liquid core during continuous casting.

JIANG, Guang S.

Available from the Sheffield Hallam University Research Archive (SHURA) at:

<http://shura.shu.ac.uk/19876/>

A Sheffield Hallam University thesis

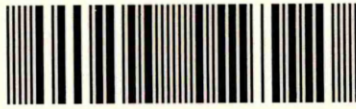
This thesis is protected by copyright which belongs to the author.

The content must not be changed in any way or sold commercially in any format or medium without the formal permission of the author.

When referring to this work, full bibliographic details including the author, title, awarding institution and date of the thesis must be given.

Please visit <http://shura.shu.ac.uk/19876/> and <http://shura.shu.ac.uk/information.html> for further details about copyright and re-use permissions.

101 394 246 9



Sheffield Hallam University

REFERENCE ONLY

30/3/95 - 18-10

ProQuest Number: 10697182

All rights reserved

INFORMATION TO ALL USERS

The quality of this reproduction is dependent upon the quality of the copy submitted.

In the unlikely event that the author did not send a complete manuscript and there are missing pages, these will be noted. Also, if material had to be removed, a note will indicate the deletion.



ProQuest 10697182

Published by ProQuest LLC (2017). Copyright of the Dissertation is held by the Author.

All rights reserved.

This work is protected against unauthorized copying under Title 17, United States Code
Microform Edition © ProQuest LLC.

ProQuest LLC.
789 East Eisenhower Parkway
P.O. Box 1346
Ann Arbor, MI 48106 – 1346

**INCLUSION BEHAVIOUR IN THE LIQUID CORE
DURING CONTINUOUS CASTING**

GUANG SHENG JIANG

**A thesis submitted in partial fulfilment of the
requirements of the Council for National Academic Awards
for the degree of Doctor of Philosophy**

March 1992

**Sheffield City Polytechnic in collaboration with the
United Engineering Steel Ltd, Stocksbridge Engineering Steels**

ACKNOWLEDGEMENTS

I am greatly indebted to the following for their help and friendship I have received during the course of completion of the thesis:-

SERC for the financial support;

Professor A. W. D. Hills for his continuous guidance, encouragement, receptivity and contagious enthusiasm for the subject, and who, as a supervisor, has a great share of the author's acknowledgements concerning this work as a whole;

Mr. N. Dzmeiko for his continuous help and assistance throughout all the experimental work;

Dr. I. G. Davies, who has very kindly welcomed author's requests for assistance and advices;

Mr. D. Latimer for his guidance and friendship throughout my three-year stay at Sheffield City Polytechnic, and to all of his staff in the Process Section for their assistance;

Mr. P. Fisher and the staff at the Photographic Unit for the photography;

Mr. T. Reynolds, Mr. R. Hill and colleagues at Davy Distington Ltd for their support and assistance at the final stage of the work.

Technicians, secretaries, Librarians, Lecturers, and other staff members at Sheffield City Polytechnic for their prompt and efficient services;

The research assistants, my fellow students, in the department for their help at various stages of the work.

For the evidence of their help, it is all there in the thesis.

And finally to my wife Xiumei for her patience, understanding and untiring support through it all.

INCLUSION BEHAVIOUR IN THE LIQUID CORE DURING CONTINUOUS CASTING

by Guang Sheng Jiang

ABSTRACT

Water models using perspex have been built to study the fluid flow and recirculation patterns developed in the sump of a steel continuous casting machine and the influences these have on the behaviour of inclusions. An experimental method has been devised to simulate the behaviour of inclusions in the sump and to study the apportionment of the input flux of inclusions between the molten mould powder layer and the strand. The method entails the uses of finely dispersed coloured paraffin oil in the inlet stream together with a floating colourless paraffin layer on the top of the water in the model mould to simulate the molten powder layer on top of the molten steel.

A theoretical model has been formulated which relates the inclusion separation in the sump to the fluid flow there. The inclusion removal ratio in the sump for a given continuous casting machine can be predicted using this theoretical model. The model, using the properties of liquid steel and practicable casting speeds, demonstrates that the removal of inclusions of small size ($< 40 \mu\text{m}$) from the mould sump is less than 5% efficient.

Inclusion agglomeration plays an important role in inclusion removal. It has been shown that deep submersion of the SEN enhances the agglomeration of inclusion particle. Under certain conditions, for example, the average particle diameter in the meniscus region has been found to be as much as three times its value at the SEN nozzle.

The use of fine alumina flakes or small air bubbles, together with a plane light source, has been found to be very successful in studying the fluid flow patterns developed in three-dimensional models. Employing this method, the fluid flow patterns developed on different planes within the model mould have been viewed and recorded photographically. The photographs so obtained have helped to explain the results obtained for the removal of inclusions. The fluid flow patterns developed when small outside diameter nozzles with deep SEN submerged depths are used have been found to be of benefit to the removal of inclusions.

Increasing the SEN submerged depth promotes inclusion agglomeration and hence increases the inclusion removal ratio. Reducing the nozzle outside diameter and the casting speed increases the inclusion removal ratio in the sump. But the influences of these latter changes are not very strong, so that inclusion removal consideration need not influence the design strategies used for the casting speed and nozzle outside diameter. The SEN port angle has a little effect on the inclusion removal when using deep SEN submerged depth.

Although argon stream introduced into the tundish nozzle stream can protect the nozzle blockage, it is not beneficial to the inclusion removal in the sump.

CONTENTS

	page
ACKNOWLEDGEMENTS	0.3
ABSTRACT	0.4
LIST OF SYMBOLS	0.9
LIST OF TABLES	0.15
LIST OF FIGURES	0.18
LIST OF PLATES	0.24
1 INTRODUCTION	
1.1 Foreword	1:1
1.2 The objective of the investigation	1:1
	to 1:2
2 LITERATURE SURVEY	
2.1 General overview	2:1
2.1.1 Development of continuous casting	2:1
2.1.2 Quality requirements for the continuously cast products	2:2
2.2 Fluid flow patterns	2:2
2.2.1 Empirical approach	2:3
2.2.1.1 Experimental methods	2:3
2.2.1.2 Water modelling	2:5
2.2.1.3 Radioactive tracer studies	2:16
2.2.2 Theoretical approach	2:16
2.2.2.1 Mathematical model	2:17
2.2.2.2 Methods of solving mathematical models	2:20
2.2.3 Factors affecting the fluid flow patterns within the mould	2:22
2.2.3.1 Effect of mould and SEN geometries	2:22
2.2.3.2 Effect of the casting speed and the cooling rate	2:22
2.2.3.3 Effect of the submerged depth of SEN	2:23
2.2.3.4 Effect of the mould powders	2:23
2.2.3.5 Effect of gas bubbling through the SEN	2:23
2.2.3.6 Effect of EMS in the mould or below the mould	2:23
2.3 Inclusion separation	2:27
2.3.1 The mechanisms of inclusion separation	2:27
2.3.1.1 Floatation	2:27
2.3.1.2 Eddy diffusion	2:28
2.3.2 Empirical approach	2:30
2.3.3 Theoretical approach	2:36
2.3.4 Factors affecting inclusion separation	2:41
	to 2:41
3 EXPERIMENTAL TECHNIQUES	
3.1 Development and control of water model system	3:1
3.1.1 Introduction	3:1
3.1.2 Choice of scale	3:1

3.1.3	Model design calculations	3:5
3.1.4	Mould	3:7
3.1.5	Tundish and tundish nozzles	3:8
3.1.6	Ladle	3:12
3.1.7	Water flow modes	3:12
3.1.8	Control of water levels	3:19
3.1.9	Water flow rate measurement	3:19
3.2	Experimental techniques for fluid flow pattern visualization	3:21
3.2.1	Choice of tracers	3:21
3.2.2	Preparation and addition of the tracers	3:23
3.2.3	Illumination of fluid flow domain	3:24
3.2.4	Recording of the fluid flow patterns	3:27
3.3	Experimental technique for simulating inclusion separation	3:27
3.3.1	Introduction	3:27
3.3.2	Method of simulation	3:27
3.3.3	Preparation of the coloured paraffin	3:27
3.3.4	Coloured paraffin injection system	3:28
3.3.4.1	Injection assembly	3:28
3.3.4.2	Injection nozzles	3:30
3.4	Analytical techniques	3:30
3.4.1	Analytical equipment	3:30
3.4.2	Sampling technique	3:30
3.4.3	Sample preparation	3:31
3.4.4	Calibration curve	3:31
3.4.5	Absorbance analyses	3:36
3.5	Experimental technique for measuring inclusion particle sizes	3:36
		to 3:40
4	THEORETICAL DEVELOPMENT	
4.1	Inclusion mass transfer coefficient at the meniscus surface incorporating the effect of Stokes rise	4:1
4.1.1	Introduction	4:1
4.1.2	Transport equations and boundary conditions	4:3
4.1.3	Solution of transport equations	4:4
4.1.4	Average inclusion diffusion flux	4:5
4.1.5	Effective mass transfer coefficient for inclusion removal	4:7
4.2	Zonal sump flow model used to analyse inclusion removal	4:13
4.2.1	Description of the flow field	4:13
4.2.2	Description of the mass fluxes in the sump	4:16
4.2.3	Description of the inclusion fluxes	4:18
4.2.4	Inclusion removal model	4:23
4.2.5	Γ equation	4:31
		to 4:34
5	EXPERIMENTAL RESULTS	
5.1	Fluid flow studies	5:1
5.1.1	Introduction	5:1
5.1.2	Effect of SEN geometry	5:1
5.1.3	Effect of SEN submerged depth	5:2

5.1.4	Effect of casting speed	5:4
5.1.5	Entry nozzle stream penetration	5:4
5.2	Inclusion separation studies	5:4
5.2.1	Introduction	5:4
5.2.2	Effect of SEN submerged depth	5:5
5.2.3	Effect of SEN geometry	5:6
5.2.4	Effect of gas bubbling	5:6
5.2.5	Effect of casting speed	5:8
5.2.6	Effect of the size of injection nozzle	5:8
5.3	Inclusion particle size measurement	5:8
		to 5:121
6	DISCUSSION	
6.1	Accuracy and errors of the experimental method	6:1
6.1.1	Flowrate measurement	6:3
6.1.2	Calculation of casting speed from the flowrate measurement	6:4
6.1.3	Colorimetric measurement	6:5
6.1.4	Coloured and colourless paraffin volume measurement	6:5
6.1.5	Errors in inclusion removal ratio determination	6:6
6.2	Fluid flow patterns developed	6:6
6.2.1	Effect of SEN geometry	6:7
6.2.2	Effect of SEN submerged depth	6:12
6.2.3	Effect of casting speed	6:14
6.3	Interpretation of experimental results	6:14
6.3.1	Determination of the values of a , β , ζ and v	6:16
6.3.2	Analysis of the results for Γ	6:25
6.3.3	Analysis of the results for D and R	6:26
6.3.4	Sensitivity to changes in the P_{mixing} parameter values	6:34
6.3.5	Sensitivity to changes in the value of β	6:35
6.3.6	Sensitivity to changes in the value of the inclusion mass transfer coefficient	6:38
6.3.7	Effects of the operation practice on the inclusion removal	6:42
6.3.7.1	Effect of SEN geometry	6:42
6.3.7.2	Effect of SEN submerged depth	6:43
6.3.7.3	Effect of SEN port angle	6:47
6.3.7.4	Effect of gas bubbling	6:48
6.3.7.5	Effect of casting speed	6:51
6.4	Estimation of the values of the diffusion mass transfer coefficients from the experimentally measured inclusion removal ratios	6:51
6.5	Role of inclusion agglomeration in the sump flow patterns	6:55
6.6	Predication of inclusion agglomeration rates due to turbulent shear and gravity field flow	6:57
6.7	Prediction of $\eta_{\text{inclusion}}$ for steel casting system (prototype)	6:70
		to 6:79

7	CONCLUSIONS	7:1 to 7:2
8	FURTHER WORK	8:1 to 8:1
9	REFERENCES	9:1 to 9:9

APPENDIX 1	Estimation of the values of the mixing parameters based on jet entrainment theory	A1:1
A1.1	Velocity profile in a round submerged jet	A1:1
A1.2	Velocity variation along the axis of a round submerged jet	A1:4
A1.3	Momentum conservation	A1:7
A1.4	Jet entrainment	A1:9
A1.5	Jet entrainment flux	A1:11
A1.6	Values of Γ_{JR} and Γ_{JM}	A1:12 to A1:14
APPENDIX 2	Programme List	A2:1 to A2:7

LIST OF SYMBOLS

a	fractional jet projected area (see Equation (4.35)); constant
A_B	mould cross section area at meniscus
A_J	jet projected area onto a horizontal plane
b	width of the billet mould, mm; constant (see Equation (A1.12))
C_a	concentration of inclusion of diameter a
C_μ	empirical constant (see Equation (4.24))
C_{St}	material property related constant (see Equation (6.54)), $m^{-1}.s^{-1}$
d_d	SEN port diameter, mm
d_p	diameter of particle, mm
d_z	inside diameter of the nozzle, mm
D	diameter of the orifice, mm
D_E	eddy diffusivity, $m^2.s^{-1}$
D_p	diameter of particle, mm
D_p	diameter of particle, m
D_T	turbulent diffusivity, $m^2.s^{-1}$
D_z	outside diameter of the nozzle, mm
e	enhancement factor (see equation 4.59)
f_d	mass fraction of inclusion of diameter D_p
f_J	volume fraction of inclusions in the jet stream
f_R	volume fraction of inclusion in the recirculation region
F	total cross section area of jet
Fr	Froude Number

g	gravitational acceleration, $m.s^{-2}$
h	fluid hydraulic head above the orifice, m
h_f	fluid hydraulic head scale factor
j_a	flux of inclusions of a diameter a
J	denote the jet entrainment zone
k	turbulence kinetic energy
$K_1, K_2, K_3, \sigma_k, \sigma_\epsilon$	empirical constants
l	Prandtl mixing length, mm
L	characteristic length; width of the bloom mould, mm; SEN length, mm
L_f	length scale factor
L_m	length in the model, m
L_p	length in the prototype, m
m	mass flow through cross section of jet, $Kg.s^{-1}$
m_o	momentum flow of the fluid at jet pole, $Kg.m.s^{-2}$
m_x	momentum flow through a jet at a distance x from jet pole, $Kg.m.s^{-2}$
\dot{m}_d''	mass flux of inclusions, $Kg.m^{-2}.s^{-1}$
$\overline{\dot{m}_d''}$	average mass flux of inclusions, $Kg.m^{-2}.s^{-1}$
M	denote the mixing zone
\dot{M}_c	casting mass flow rate, $Kg.s^{-1}$
\dot{M}_{JM}	interchange mass flux between the jet entrainment zone and the mixing zone, $Kg.m^{-2}.s^{-1}$
\dot{M}_{JR}	interchange mass flux between the jet entrainment zone and the recirculation zone, $Kg.m^{-2}.s^{-1}$
n_1, n_2	numbers of particle of radius r_1 and r_2 in unit volume

\dot{N}	collision rate
\dot{N}_{grad}	collision rate due to velocity gradient
\dot{N}_{St}	collision rate due to stokes rise
Q_f	volume flow rate scale factor
r	distance from the jet axis, mm
r_c	distance between the jet axis and the point at which the velocity is equal to the half of the axial velocity, mm
r_o	nozzle radius of a jet, mm
R	denote the recirculation zone; ratio of inclusion diameters
Re	Reynolds Number
t	time, s
t_f	time scale factor
u	velocity, m.s ⁻¹
u_m	axial velocity (velocity on the jet axis), m.s ⁻¹
u_o	axial velocity at jet pole, m.s ⁻¹
U_r	Stokes' rising velocity of particle, m.s ⁻¹
U_{Δ}	velocity gradient, s ⁻¹
v_c	casting speed, m.min ⁻¹
V	velocity, m.s ⁻¹
V_f	velocity scale factor
\dot{V}_J	initial volume flow from jet, m ³ .s ⁻¹
\dot{V}_x	volume flow through a given section of jet at a distance x, m ³ .s ⁻¹
$\dot{V}_{entrain}$	jet entrainment volume flow, m ³
$V_{injected}$	volume of coloured paraffin injected, ml
$V_{in\ slag}$	volume of coloured paraffin absorbed into the slag

layer, ml

V_y	normal component to the surface of eddy velocity, $m.s^{-1}$
V_J	volumetric flowrate of fluid of the jet stream, $m^3.s^{-1}$
V_R	volumetric flowrate of fluid within the recirculation region, $m^3.s^{-1}$
V_{St}	inclusion relative rising velocity, $m.s^{-1}$
V_λ	eddy velocity of size λ_0 , $m.s^{-1}$
We	Weber Number
W_i	weight of particles injected, Kg
W_t	weight of particles remained in tundish, Kg
x	distance between a given section and jet pole, mm
y	distance from the surface, mm
Y	distance between two particles normal to the flow direction
α^*	dimensionless effective inclusion mass transfer coefficient
α_d	effective mass transfer coefficient for the removal of inclusions of diameter D_p , $m.s^{-1}$
β	ratio of liquid flux as defined in Equation (4.57)
ψ	integration variable; limit of relative error
ϵ	rate of dissipation of turbulence kinetic energy; limit of absolute error
$\dot{\epsilon}_0$	stirring power per unit volume
λ_0	size of the eddies, mm
μ	molecular viscosity, $N.s.m^{-2}$
μ_{eff}	effective viscosity, $N.s.m^{-2}$
μ_s	viscosity of liquid steel, $N.s.m^{-2}$
μ_t	turbulent viscosity, $N.s.m^{-2}$

ν	kinematic viscosity, $m^2.s^{-1}$
ρ	density, $Kg.m^{-3}$
ρ_e	resistivity of the fluid
ρ_p	density of particle, $Kg.m^{-3}$
ρ_S	density of liquid steel, $Kg.m^{-3}$
γ	as defined in Equation (6.27), mm^{-2}
θ	SEN port angle
σ	surface tension, $dyne.cm^{-1}$
τ	time, s
τ_e	total exposure time of fluid packet at the meniscus, s
τ_e^*	dimensionless exposure time of fluid packet at the meniscus
ξ	dimensionless distance from the jet axis (see Equation (A1.7));
Δ	absolute error
Δf_R	increment of the volume fraction of inclusions in the recirculation zone
ΔR	change of electrical resistance of the fluid
Δu	velocity difference between two particles (collision height), $m.s^{-1}$
δ	relative error
v	dimensionless Stokes rise velocity (see Equation (4.34))
ζ	obscuration factor of the upper surface of the meniscus
Γ	dimensionless liquid flux
Γ_{xx}	dimensionless liquid interchange flux between zones
Ψ	particle collision volume per unit time, $m^3.s^{-1}$
Φ	variable as defined in Equation (4.47)
$\Gamma_{entrain}$	dimensionless jet entrainment mass flux

Γ_{en} dimensionless jet entrainment mass flux
 $\eta_{inclusion}$ inclusion separation ratio in percentile terms
 $|\partial u/\partial y|$ absolute value of the velocity gradient along a
direction perpendicular to the direction of flow

subscript

d denote that for inclusion of diameter d
 m model;
mixing zone
 p prototype (steel casting system)
 R recirculation zone
 JM denote that between jet entrainment and mixing zones
 JR denote that between jet entrainment and recirculation zones

LIST OF TABLES

Table No.	Titles	Page
TABLE 3.1	Physical properties of water at 20°C and steel at 1600°C	3:4
TABLE 3.2	Billet tundish nozzle dimensions	3:4
TABLE 3.3	Bloom tundish nozzle dimensions	3:17
TABLE 3.4	Effect of heating process on the colour changes of the samples	3:33
TABLE 3.5	Calibration Data	3:35
TABLE 5.1	Effect of SEN submerged depth on nozzle stream penetration	5:9
TABLE 5.2	Effect of SEN submerged depth on inclusion removal (Nozzle 1)	5:10
TABLE 5.3	Effect of SEN submerged depth on inclusion removal (Nozzle 2)	5:11
TABLE 5.4	Effect of SEN submerged depth on inclusion removal (Nozzle 3)	5:12
TABLE 5.5	Effect of SEN submerged depth on inclusion removal (Nozzle 4)	5:13
TABLE 5.6	Effect of SEN submerged depth on inclusion removal (Nozzle 5)	5:14
TABLE 5.7	Effect of SEN submerged depth on inclusion removal (Nozzle 6)	5:15
TABLE 5.8	Effect of SEN submerged depth on inclusion removal (Nozzle 7)	5:16
TABLE 5.9	Effect of SEN submerged depth on inclusion removal (Nozzle 8)	5:17

TABLE 5.10	Effect of SEN submerged depth on inclusion removal (Nozzle 9)	5:18
TABLE 5.11	Effect of SEN submerged depth on inclusion removal (Nozzle 10)	5:19
TABLE 5.12	Effect of SEN submerged depth on inclusion removal (Nozzle 11)	5:20
TABLE 5.13	Effect of gas bubbling on inclusion removal (Nozzle 1)	5:21
TABLE 5.14	Effect of gas bubbling on inclusion removal (Nozzle 4)	5:23
TABLE 5.15	Effect of gas bubbling on inclusion removal (Nozzle 5)	5:24
TABLE 5.16	Effect of gas bubbling on inclusion removal (Nozzle 10)	5:25
TABLE 5.17	Effect of casting speed on inclusion removal	5:26
TABLE 5.18	Effect of SEN submerged depth on inclusion removal for large injection nozzle	5:47
TABLE 5.19	Effect of SEN submerged depth on inclusion removal for small injection nozzle	5:48
TABLE 5.20	Diameters of the particles generated from the large injection nozzle	5:49
TABLE 5.21	Diameters of the particles generated from the small injection nozzle	5:50
TABLE 6.1	Values of ζ for the bloom mould model	6:23
TABLE 6.2	Values of ζ for the billet mould model	6:23
TABLE 6.3	Example of screen output	6:30
TABLE 6.4	The values of R	6:31

TABLE 6.5	The values of α^* estimated from the experimentally measured inclusion removal ratios	6:53
TABLE 6.6	The value of D_T estimated from the experimentally measured inclusion removal ratio	6:56
TABLE 6.7	Predictions on the inclusion removal ratios $\eta_{inclusion}$ for bloom steel casting system (prototype)	6:74
TABLE 6.8	Predictions on the inclusion removal ratios $\eta_{inclusion}$ for billet steel casting system (prototype)	6:76

LIST OF FIGURES

Figure No.	Captions	Page
Figure 2.1	Schematic representation of the fluid flow field	2:8
Figure 2.2	Sketches over the fluid flow pattern developed in a CC-mould using different submerged entry nozzles	2:10
Figure 2.3	Water model experiment on fluid flow pattern influenced by the exit angle of nozzle	2:12
Figure 2.4	Profile of submerged entry nozzles	2:13
Figure 2.5	Fluid flow patterns of resin particles in water pool	2:14
Figure 2.6	Relation between extracted large inclusion ($>50 \mu\text{m}$) content in accumulated zone of slabs and penetration depth of casting stream in sump	2:15
Figure 2.7	Mould fluid flow pattern with a straight-discharge SEN (no gas bubbling)	2:24
Figure 2.8	Mould fluid flow pattern with a straight-discharge SEN (with gas bubbling)	2:25
Figure 2.9	Mould fluid flow pattern with a 4-ported SEN (with gas bubbling)	2:26
Figure 2.10	Percent separation of glass microspheres as a function of dimensionless time	2:32
Figure 2.11	Principle of particle detection by the E.S.Z. method	2:34
Figure 2.12	Schematic of the E.S.Z. system	2:35
Figure 2.13	Photograph of E.S.Z. probe developed	2:35
Figure 2.14	Comparison of weight-based separation ratios using the weighing method and the E.S.Z. method	2:37

Figure 2.15	Comparison of weight-based separation ratios using the weighing method and the E.S.Z. method	2:38
Figure 3.1	Experimental set up for recirculation mode	3:2
Figure 3.2	Sketches of the billet mould assembly	3:9
Figure 3.3	Sketches of the bloom mould assembly	3:10
Figure 3.4	Sketches of the tundish assembly	3:11
Figure 3.5	Design of submerged entry nozzle	3:13
Figure 3.6	Design of submerged entry nozzle with horizontal outlets	3:14
Figure 3.7	Design of submerged entry nozzle with upward outlets	3:15
Figure 3.8	Design of submerged entry nozzle with downward outlets	3:16
Figure 3.9	Sketches of the water flow modes employed	3:18
Figure 3.10	Experimental set-up for the rotameter calibration	3:20
Figure 3.11	Rotameter calibration curve	3:22
Figure 3.12	Injection nozzle set-up	3:25
Figure 3.13	Sketches of the slide slit used in the projector	3:25
Figure 3.14	Sketches of the plane light source arrangement	3:26
Figure 3.15	Sketches of the coloured paraffin injection System	3:29
Figure 3.16	Sketches of the sample suction system	3:32
Figure 3.17	Calibration curve	3:34
Figure 3.18	Sketch of the tube for viewing the particle generation	3:38
Figure 3.19	Experimental arrangement for close-up viewing	3:39
Figure 3.20	Experimental arrangement for general viewing	3:40

Figure 4.1	Stokes velocity and mass transfer coefficients as a function of inclusion size	4:11
Figure 4.2	Schematic diagram of mixing regions in the sump of a continuous casting machine showing the interchange fluxes (Bloom)	4:14
Figure 4.3	Schematic diagram of mixing regions in the sump of a continuous casting machine showing the interchange fluxes (Billet)	4:15
Figure 4.4	Schematic representation of mixing zones in sump of a continuous casting machine	4:17
Figure 4.5	Schematic diagram of inclusion interchange fluxes between zones	4:19
Figure 4.6	Schematic diagram of inclusion interchange fluxes in conductance net-work form	4:24
Figure 5.1	The position of the view planes	5:27
Figure 5.2	Effect of SEN submerged depth on length of jet penetration zone	5:28
Figure 5.3	Effect of SEN submerged depth on the proportion of inclusion removed to the 'slag' layer (Nozzle 1)	5:29
Figure 5.4	Effect of SEN submerged depth on the proportion of inclusion removed to the 'slag' layer (Nozzle 2)	5:30
Figure 5.5	Effect of SEN submerged depth on the proportion of inclusion removed to the 'slag' layer (Nozzle 3)	5:31
Figure 5.6	Effect of SEN submerged depth on the proportion of inclusion removed to the 'slag' layer (Nozzle 4)	5:32
Figure 5.7	Effect of SEN submerged depth on the proportion of inclusion removed to the 'slag' layer (Nozzle 5)	5:33

Figure 5.8	Effect of SEN submerged depth on the proportion of inclusion removed to the 'slag' layer (Nozzle 6)	5:34
Figure 5.9	Effect of SEN submerged depth on the proportion of inclusion removed to the 'slag' layer (Nozzle 7)	5:35
Figure 5.10	Effect of SEN submerged depth on the proportion of inclusion removed to the 'slag' layer (Nozzle 8)	5:36
Figure 5.11	Effect of SEN submerged depth on the proportion of inclusion removed to the 'slag' layer (Nozzle 9)	5:37
Figure 5.12	Effect of SEN submerged depth on the proportion of inclusion removed to the 'slag' layer (Nozzle 10)	5:38
Figure 5.13	Effect of SEN submerged depth on the proportion of inclusion removed to the 'slag' layer (Nozzle 11)	5:39
Figure 5.14	Effect of SEN geometry on the proportion of inclusion removed to the 'slag' layer (billet)	5:40
Figure 5.15	Effect of SEN port angle on the inclusion removal efficiency for different submerged depth	5:41
Figure 5.16	Effect of gas bubbling on the proportion of inclusion removed in the billet caster	5:42
Figure 5.17	Effect of gas bubbling on the proportion of inclusion removed in the bloom caster (Nozzle 4)	5:43
Figure 5.18	Effect of gas bubbling on the proportion of inclusion removed in the bloom caster (Nozzle 5)	5:44
Figure 5.19	Effect of gas bubbling on the proportion of inclusion removed in the bloom caster (Nozzle 10)	5:45
Figure 5.20	Effect of casting speed on the proportion of inclusion removed to the 'slag' layer	5:46

Figure 5.21	Effect of injection nozzle size on the inclusion removal ratio in the bloom mould model	5:119
Figure 6.1	Sketch of the fluid flow pattern developed in the billet mould sump	6:8
Figure 6.2	Sketch of the fluid flow pattern developed in the bloom mould sump	6:9
Figure 6.3	Jet projected area in the bloom mould	6:17
Figure 6.4	Jet projected area in the billet mould	6:19
Figure 6.5	Determination of D_p and R for an SEN submerged depth of 220 mm	6:28
Figure 6.6	The values of R and SEN submerged depth	6:32
Figure 6.7	The particle diameter and SEN submerged depth	6:33
Figure 6.8	Inclusion removal efficiency in the bloom mould model (effect of Γ)	6:36
Figure 6.9	Inclusion removal efficiency in the bloom mould model (effect of β)	6:39
Figure 6.10	Inclusion removal efficiency in the bloom mould model (effect of α^*)	6:41
Figure 6.11	Relationship between stirring force and the number of inclusions for each stirring direction	6:45
Figure 6.12	Schematic view of M-EMS stirring directions	6:46
Figure 6.13	Schematic view of the flow pattern developed in the mould with gas bubbling	6:50
Figure 6.14	Generic slice of the unitary collision volume	6:58
Figure 6.15	Diagram of particles rising under Stokes Law	6:61
Figure 6.16	Diagram of particles moving with fluid in a velocity gradient field	6:62

Figure 6.17	Collision volume involved in the gradient collision	6:64
Figure 6.18	Illustration of the approach of a larger particle to a smaller one	6:68
Figure 6.19	Collision efficiency E as a function of σ	6:69
Figure 6.20	Grazing particle trajectories for values of $\sigma = 0.2, 0.7, 5.0$	6:69
Figure 6.21	Inclusion removal efficiency in the bloom caster (effect of V_c)	6:75
Figure 6.22	Inclusion removal efficiency in the billet caster (effect of V_c)	6:77
Figure 6.23	Inclusion removal efficiency in the bloom caster (effect of ζ)	6:78
Figure 6.24	Inclusion removal efficiency in the billet caster (effect of ζ)	6:79
Figure A1.1	Diagram of a submerged free jet	A1:2
Figure A1.2	Dimensionless velocity profile in the main region of axially symmetric submerged jet	A1:3

LIST OF PLATES

Plate No.	Captions	Page
Plate 5.1	Fluid flow patterns developed on plane 1 when different SEN were used	5:51
Plate 5.2	Fluid flow patterns developed on plane 2 when different SEN were used	5:53
Plate 5.3	Fluid flow patterns developed on plane 3 when different SEN were used	5:55
Plate 5.4	Fluid flow patterns developed on plane 1 when different SEN were used	5:57
Plate 5.5	Fluid flow patterns developed on plane 2 when different SEN were used	5:59
Plate 5.6	Fluid flow patterns developed on plane 3 when different SEN were used	5:61
Plate 5.7	Fluid flow patterns developed on central plane when different bifurcated SEN were used	5:63
Plate 5.8	Fluid flow patterns developed on central plane when different bifurcated SEN were used	5:65
Plate 5.9	Fluid flow patterns developed on central plane when different bifurcated SEN were used	5:67
Plate 5.10	Fluid flow patterns developed on central plane when different bifurcated SEN were used	5:69
Plate 5.11	Fluid flow patterns developed on central plane when different bifurcated SEN were used	5:71
Plate 5.12	Fluid flow patterns developed on plane 1 using Nozzle 1 at different submerged depths	5:73

Plate 5.13	Fluid flow patterns developed on plane 2 using Nozzle 1 at different submerged depths	5:75
Plate 5.14	Fluid flow patterns developed on plane 3 using Nozzle 1 at different submerged depths	5:77
Plate 5.15	Fluid flow patterns developed on plane 1 using Nozzle 1 at different submerged depths	5:79
Plate 5.16	Fluid flow patterns developed on plane 2 using Nozzle 1 at different submerged depths	5:81
Plate 5.17	Fluid flow patterns developed on plane 3 using Nozzle 1 at different submerged depths	5:83
Plate 5.18	Fluid flow patterns developed on plane 1 using Nozzle 2 at different submerged depths	5:85
Plate 5.19	Fluid flow patterns developed on plane 2 using Nozzle 2 at different submerged depths	5:87
Plate 5.20	Fluid flow patterns developed on plane 3 using Nozzle 2 at different submerged depths	5:89
Plate 5.21	Fluid flow patterns developed on plane 1 using Nozzle 2 at different submerged depths	5:91
Plate 5.22	Fluid flow patterns developed on plane 2 using Nozzle 2 at different submerged depths	5:93
Plate 5.23	Fluid flow patterns developed on plane 3 using Nozzle 2 at different submerged depths	5:95
Plate 5.24	Fluid flow patterns developed on plane 1 using Nozzle 3 at different submerged depths	5:97
Plate 5.25	Fluid flow patterns developed on plane 2 using Nozzle 3 at different submerged depths	5:99
Plate 5.26	Fluid flow patterns developed on plane 3 using Nozzle 3 at different submerged depths	5:101

Plate 5.27	Fluid flow patterns developed on plane 1 using Nozzle 3 at different submerged depths	5:103
Plate 5.28	Fluid flow patterns developed on plane 2 using Nozzle 3 at different submerged depths	5:105
Plate 5.29	Fluid flow patterns developed on plane 3 using Nozzle 3 at different submerged depths	5:107
Plate 5.30	Fluid flow patterns developed on central plane using Nozzle 4 at different submerged depths	5:109
Plate 5.31	Fluid flow patterns developed on central plane using Nozzle 5 at different submerged depths	5:111
Plate 5.32	Fluid flow patterns developed on central plane using Nozzle 9 at different submerged depths	5:113
Plate 5.33	Fluid flow patterns developed on central plane using Nozzle 11 at different submerged depths	5:115
Plate 5.34	Fluid flow patterns developed on plane 1 using Nozzle 3 at different casting speeds	5:117
Plate 5.35	Close-up view of the tip area when particles being generated	5.120
Plate 5.36	General view of the tip area when particles being generated	5.121
Plate 6.1	Fluid flow pattern observed in the bloom mould model	6.10
Plate 6.2	View of the meniscus when small SEN submerged depth was being used	6:13

1. INTRODUCTION.

1.1. Foreword.

Continuous casting is, today, a process used extensively throughout the metallurgical industry and, because the number of plants installed with continuous casting machines is increasing steadily, problems associated with the operation and design of the machines are receiving greater attention.

Although many mathematical models have dealt fairly successfully with predicting solidification profiles and fluid flow patterns of liquid steel during continuous casting, the behaviour of inclusions and the quantitative description of their removal in the sump has been neglected.

Water models have also been extensively employed in recent years to obtain flow descriptions by means of visualization techniques but, although they can also be utilized to study the behaviour of inclusions in the sump of continuous casting machines, no such work has been previously reported in the literature.

1.2. The objective of the investigation.

The basic objective of the present work is to improve understanding of the factors affecting the internal quality of continuously cast billets, blooms and slabs — particularly on the mechanisms of inclusion removal in the molten sump — by studying the fluid flow and recirculation patterns in the sump and the behaviour of inclusions in those flows. Since the behaviour of these inclusions has a crucial bearing on the cleanness of the steel produced the

principal aim of the present research is to examine this behaviour. Of particular interest will be the feature of the flow patterns that can be controlled and are shown to influence the proportion of inclusions that can be incorporated into the molten flux layer maintained on the liquid metal meniscus.

These consist of:-

- a) Studying the fluid flow and recirculation in the sump of a continuous casting machine in a room temperature three dimensional model.
- b) Developing a method for studying the apportionment of input inclusions between the molten mould powder layer and the solidification zone by using finely dispersed dye-marked organic liquid phase in the inlet stream and a floating organic layer to simulate the molten powder layer on top of the molten steel meniscus;
- c) Studying the effect of fluid flow in the sump on inclusion removal in the room temperature model using the method developed;
- d) Varying the operating and design parameters such as nozzle size, position and geometry and casting speed to elucidate their effect on inclusion removal mechanisms;

2. LITERATURE SURVEY.

2.1. General overview.

In order to understand the influences of fluid flow in the sump on inclusion removal during continuous casting, it is important to appreciate the key developments of previous workers.

The purpose of the present literature survey is not to be a thorough review of the literature, but rather to enable the experimental results and conclusions to be considered in their right perspective, and to serve as a basis on which the new ideas and theories will be developed.

2.1.1. Development of continuous casting.

In the past three decades, continuous casting has emerged as a widely used technology in modern steel plants^[1-4]. This is because the continuous casting process has offered numerous technical and economical advantages. They are, mainly:-

- a) 10% and more higher yield compared to traditional ingot methods.
- b) More uniform and higher quality of the final product.
- c) Reduced energy consumption together with the potential for even less energy consumption through hot charging of continuously cast products to the rolling mill furnace.
- d) Reduced operating costs.
- e) Less capital and depreciation costs.
- f) Good environmental conditions.

- g) Improved working and safety conditions for the operators.
- h) Process suited for integral automation.
- i) High productivity.
- j) Less space and time required to convert liquid steel into solidified product.

Because of the improved yield and the operating cost benefits, the continuous casting process will dominate the production schedule of most steelmaking plants in the near future, especially in view of the technological developments under way. Indeed, the continuous casting ratio is likely to increase to more than 90% by the end of this century.

2.1.2. Quality requirements for the continuously cast products.

Continuous casting of steel has become a widely used process and an important development in the manufacture of steel. The ratio of continuously cast steel on the total steel production had been increased dramatically in the last two decades^[1]. Concurrent with this increase in production levels are the stringent quality requirements. These quality aspects — mainly surface finish and internal cleanness — have become crucial with progressively increasing machine throughputs and larger product dimensions. Therefore, steel cleanness and strict composition control are now becoming the primary concern of steelmakers. After investigation, several authors^[4-13] have found that metal flow in the mould is an important parameter bearing upon the quality of continuously cast products.

2.2. Fluid flow patterns.

It is well known that the fluid flow of liquid steel plays an important role in the whole process of continuous casting. In fact, the beginning of the continuous casting process is primarily concerned with liquid metal flow in the tundish and the mould. Thus the concepts of fluid flow and hydrodynamics have been used to solve major problems and to improve the efficiency of the process. Research work leading to better understanding of liquid metal flow has been carried out extensively, mainly in two ways, an empirical approach and a theoretical approach.

2.2.1. Empirical approach.

The fluid flow problems involved in the continuous casting process are often too complicated to be treated using fundamental equations without the introduction of approximations and boundary conditions in the calculations. Fortunately, there are several experimental methods available nowadays which could be employed to study the flow patterns developed.

2.2.1.1. Experimental methods.

The experimental methods used to study fluid flow patterns in the continuous casting process may be classified into two groups, namely water modelling studies on different scale physical model systems and radioactive tracer studies on full scale operating plant.

The stimulus-response method and the elapse-time photographic technique are the most commonly used methods for studying fluid flow within the continuous casing system via the water models. The

stimulus-response method can be explained as: "Do something to a system and then see how the system responds". By using this method, the residence-time distribution can be obtained^[24-25], and hence desired information about the fluid flow in the continuous casting system will be revealed.

When taking pictures of the fluid flow pattern in water models, the following techniques are available for fluid flow visualization:

- a) Particle-addition into the water systems.
- b) Dye-injection into the streams.
- c) Use of a slit light sources to illuminate the fluid flow domain two-dimensionally.

Plastic particles, glass beads, vanadium pentoxide, the tea leaves, computer card punchings, sawdust and even gas bubbles are some of the additions made so that flow can be seen and photographically recorded. Dye injected into the model can be used to demonstrate the configuration of the inlet stream and its penetration depth. The use of the slit light source allows visualization of the fluid flow pattern on a definite plane without the interference caused by other parts of the fluid flow domain.

For the quantitative description of the fluid flow pattern, the following methods^[28-31] can be used to measure the flow velocity at certain points in the domain:

- a) Impact tube and static pressure tap with manometer.
- b) Form drag strain gauge system with strain amplifier and recorder.

- c) Laser doppler anemometer.
- d) Thermistor probe.
- e) Hot film anemometry.
- f) Stroboscopic photography.

2.2.1.2. Water modelling.

The literature describing water model studies is very extensive. [3-28]

The fluid flow of liquid steel in the actual continuous casting system is very difficult to measure or observe. Even in the open pouring situation, the observation can only be made on the open pouring streams. In this sense, a water model is very useful and highly instructive. But the results obtained on the physical model are meaningful and useful only if physical similarity between physical model and actual system is achieved.

To obtain similarity between two flowing systems, the following four conditions must be satisfied. [31-33]

a) Geometric Similarity:

the ratio of any length in one system to the corresponding length in the other system is constant. This ratio is termed as the scale factor.

b) Kinematic Similarity:

the streamlines in one system are geometrically similar to the streamlines in the other system.

c) Dynamic Similarity:

the magnitude of forces at corresponding location in each system are in a fixed ratio.

d) Thermal Similarity:

the dimensionless numbers involving heat transfer or convective flow are equal in both systems.

Thermal similarity is not important in modelling the upper region in the mould of the continuous casting system since thermal gradients are small and convective forces are negligible. This is fortunate, as it is difficult to achieve both thermal and fluid flow similitude in the same model. [32]

Kinematic similarity is observed in the model that attains dynamic and geometric similarity. The principal forces to be considered in obtaining dynamic similarity in the continuous casting mould are inertial, gravitational, viscous and surface tension forces. The various ratios of these forces form certain dimensionless numbers. Dynamic similarity exists if these numbers have the same value in both the model and the actual system.

Three important dimensionless numbers in fluid flow are:-

$$\text{Froude No } Fr = \frac{V^2}{gL} = \frac{\textit{inertial force}}{\textit{gravity force}}$$

$$\text{Reynolds No } Re = \frac{VL}{\nu} = \frac{\textit{inertial force}}{\textit{viscous force}}$$

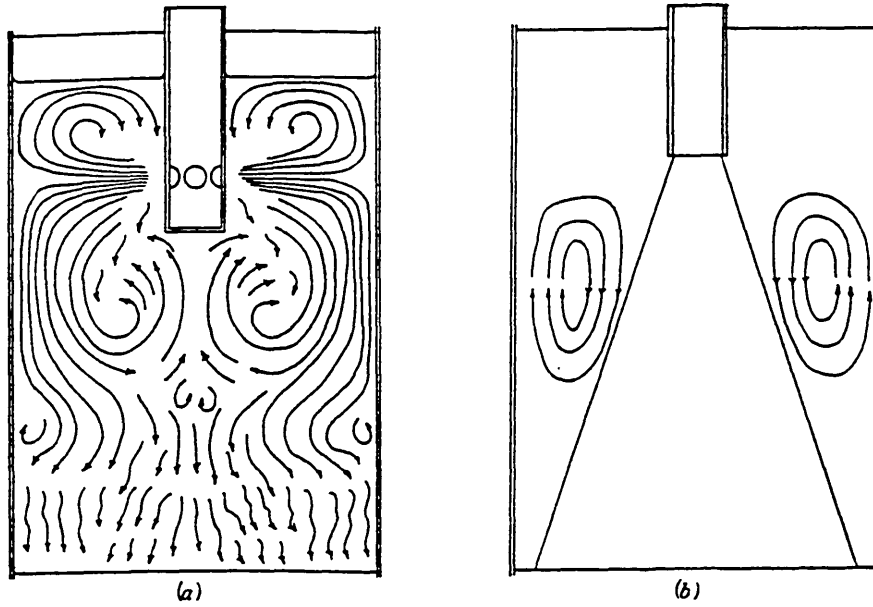
$$\text{Weber No } We = \frac{\rho V^2 L}{\sigma} = \frac{\text{inertial force}}{\text{surface tension force}}$$

where: V : stream velocity;
 g : gravitational constant;
 L : characteristic length;
 ν : kinematic viscosity;
 σ : surface tension;
 ρ : density.

Because of difference of the physical properties of water at room temperature and molten steel, table 3.1, it is impossible to satisfy simultaneously all the three dimensionless numbers mentioned above in the same model of a given particular scale.^[34] It requires a full scale water model to satisfy Reynolds and Froude numbers concurrently. But a model of 0.6 scale is needed to satisfy the Froude and Weber numbers concurrently. It had been demonstrated by Heaslip et al.^[34] that the Froude number alone could be satisfied at any scale in a mould water model as long as all metering orifices and fluid hydraulic heads in the modelling system are varied in accordance with a single scaling factor. To decide what scale of model should be used, the extent to which similitude is necessary in modelling the actual system must be considered.

A full scale model has been used by Szekely and Yadoya^[28] to examine velocity profiles in round continuous casting moulds using submerged vertical outlet and horizontal outlet nozzles. The flow fields obtained are shown in figure 2.1. It was also found that, for the vertical outlet nozzles, the flow patterns did not depend markedly on

Figure 2.1



Schematic representation of the fluid flow field. [28]

(a) — radial flow nozzle;

(b) — straight nozzle.

the flow rates through the system, except that, at higher flow rates, the jet penetrated more deeply into the column. The jet penetration depth was found to be about 4 to 6 mould diameters. For the horizontal outlet nozzles, the jet penetration depth varied between half and one mould diameters.

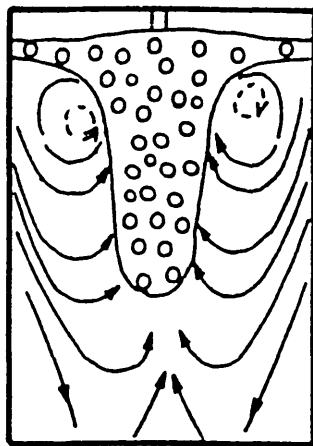
Using a full scale model, Wei and Carlsson^[14] studied the flow patterns developed in a bloom mould when different submerged entry nozzles (SEN) are used. The results are given in figure 2.2. They found that vertical outlet nozzles gave a high degree of by-passing and horizontal outlets nozzles gave some plug flow inside the mould.

Later on a full scale water model of continuous casting system was built by Hibbins et al.^[3] to investigate mould fluid flow conditions with different submerged nozzles. The results were of great assistance in operating the bloom caster at the author's steelworks.

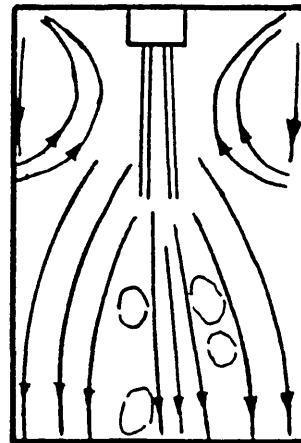
Of the recent work, the paper by Tai et al.^[4] is perhaps the most noteworthy as these investigators have shown that rotating fluid flow can be developed in bloom continuous casting mould when a four-ports nozzle is installed unsymmetrically relative to the rectangular mould. Industrial experiments have shown that the rotating metal flow developed in the mould by turning the nozzle axis 15 degrees is beneficial in improving the internal cleanness of low carbon steel and reducing the erosion rate of nozzle refractories.

The 0.6-scale models, in which Froude-Weber criteria are satisfied, have proven popular in the study of fluid flow in continuous casting moulds. As early as in 1960's, several Russian investigators^[5,35-37] examined the mould flows when different submerged entry nozzles were

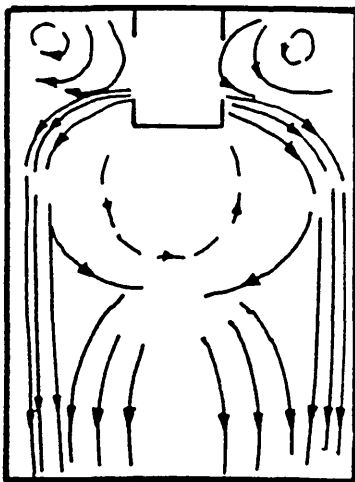
Figure 2.2



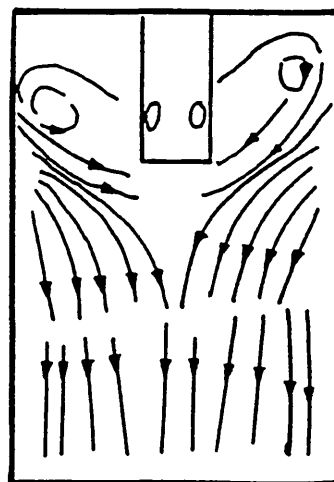
Open stream



Vertical outlet



Two holed outlet



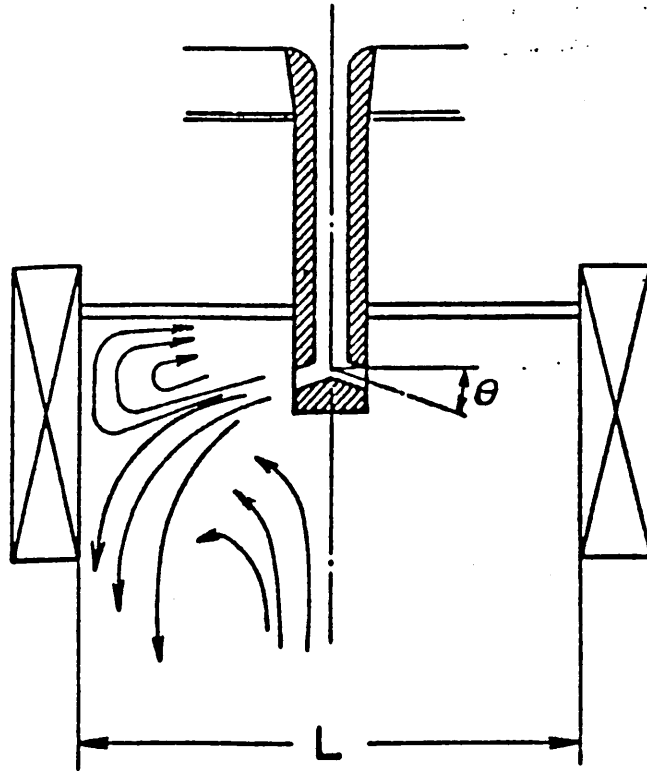
Four holed outlet

Sketches over the fluid flow pattern developed in a CC-mould using different submerged entry nozzles. [14]

employed. Astrov et al.^[5] used a three-fifth scale water model to study the effects of the port sloping angle of the submerged multi-ports nozzles on the fluid flow in the mould. After careful study using a 2/3-scale model, Robertson and Sheridan^[16] suggested a suitable multi-stream arrangement for continuously casting 36 x 5.5in slabs to eliminate the longitudinal split formed in the centre of the broad face. Mould flow patterns produced by bifurcated nozzles have been studied by Mills and Barnhardt^[11]. As result of their investigations, the need for skin scarfing (i.e., to improve surface quality) was eliminated from a production plant. McPherson^[17] has similarly reported the water modelling results about a continuous slab caster with the aid of an 0.6-scale model.

Other scale models, in which only the Froude criterion is satisfied, are appropriate for studying the flow patterns and their relation to phenomena such as vortex formation and fluid residence time and its distribution. A 1/2.5-scale model was used by Nemoto and Kawawa^[15] to observe the stream patterns in the mould. Figure 2.3 shows one of their results. They found that, when the exit angle θ is too small, the meniscus is exposed to oxidation by the air and when the angle is too big, the steel temperature in the meniscus is lower than required. Their investigation suggested the optimum value of θ for different dimensions of the mould. After the investigations using a 1/4-scale model, Habu et al.^[38] have suggested that the use of a diverging bottle shaped submerged entry nozzle, shown in figure 2.4, reduces the jet penetration depth, and, therefore, the number of large inclusions accumulated in the strand, as shown in figure 2.5 and figure 2.6.

Figure 2.3



Water model experiment on fluid flow pattern influenced by the exit angle of nozzle^[15]

Simulation factor:

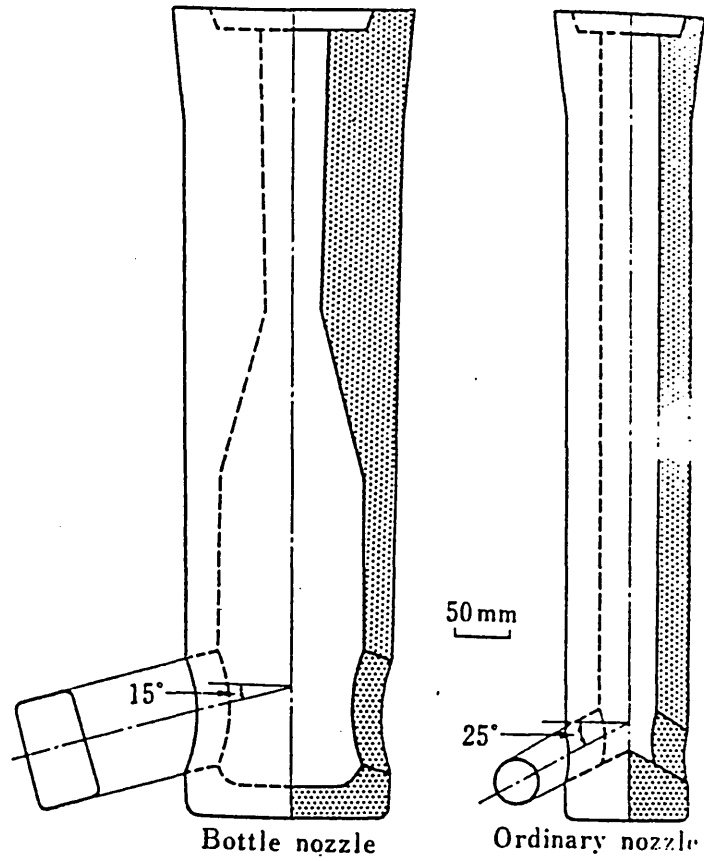
$$Fr = \frac{V^2}{L g}$$

V: stream speed;

L: length;

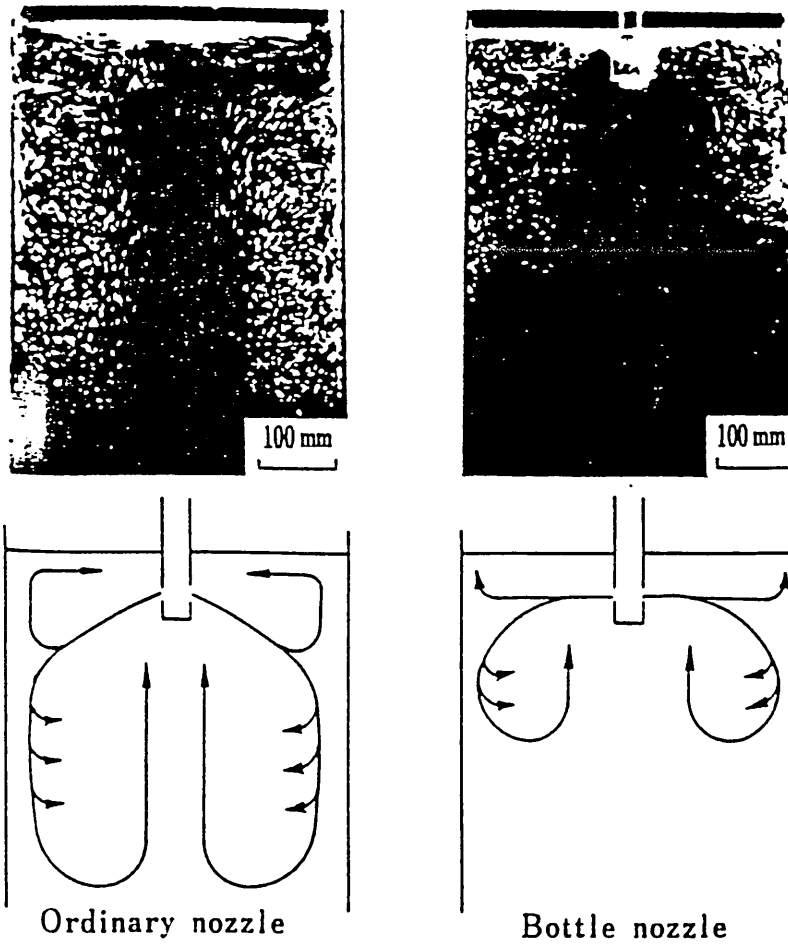
g: gravitational acceleration.

Figure 2.4

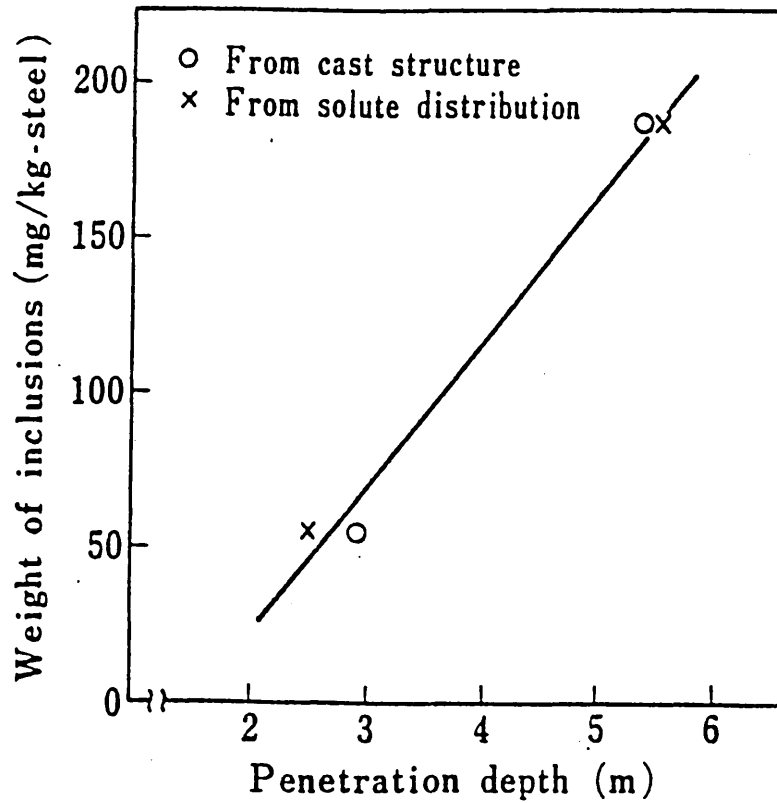


Profile of submerged entry nozzles [38]

Figure 2.5



Fluid flow patterns of resin particles in water pool. [38]

Figure 2.6

Relation between extracted large inclusion ($>50 \mu\text{m}$) content
in accumulated zone of slabs and penetration depth
of casting stream in sump. [38]

2.2.1.3. Radioactive tracer studies.

In contrast to the large number of reported investigations concerned with water modelling studies, the literature available on the radioactive tracer studies in operating continuous casting mould is rather scanty. [39-41] The work done by Krainer et al. [39] and Arnoult et al. [40] respectively in the past gave the picture of the flow patterns in the sump. As a result of their investigations, it was generally agreed that for the straight nozzles the liquid pool may be divided into three regions — the upper region where there exists turbulent recirculation driven by the incoming metal stream, an intermediate zone where the liquid flow is driven by natural convection, and finally a lower part where fluid motion is negligible because of the confined nature of the spaces available for flow. It was also found that the stream penetrates to a length of about 4 to 6 mould widths. The radioactive tracer method is very useful at obtaining information on the depth and shape of the sump. But this method could not be used to investigate the fluid flow phenomena more quantitatively, it has not been used quite often nowadays.

2.2.2. Theoretical approach.

At the present time, the problems relating to fluid flow behaviour in continuous casting process cannot be solved theoretically. This is not only because the continuous casting process itself is very complicated, but also because the fundamental equations which describe fluid flow are often too complex to be solved even using large computers. For instance, the Navier-Stokes equation and the continuity equation together fully describe fluid flow behaviour, [43]

but they are extremely complex and their solution, even with the aid of large computers, requires simplifications and assumptions to be made about a number of aspects, e.g. choice of a turbulence approximation, treatment of boundaries and numerical methods of solution. The simplifications and assumptions chosen, together with the fundamental equations, make up a mathematical model. It is obvious that such mathematical models need to be validated against experimental measurements.

2.2.2.1. Mathematical model.

Mathematical models are primarily confined to heat transfer and solidification phenomena where the fluid flow is usually treated rather simply. Such models were presented by a number of authors, among them are Savage and Pritchard,^[44] Adenis et al.,^[45] Hills,^[46] Donaldson and Hess,^[47] Mizikar,^[48] Fahidy^[49] and Szekely and Stanek.^[50] Later, as the development of the turbulence theory^[51-55] and the improvement of numerical methods for solving multidimensional turbulent flow problems have progressed,^[56] mathematical models of fluid flow in steelmaking processes have been developed by several investigators.^[57-61] Recently, several mathematical models^[62-66] have been developed to analyse fluid flow in continuous casting tundishes. Up to now, however, little work^[57,67] has been published on mathematical models of fluid flow in continuous casting moulds. The following section, therefore, reviews work dealing with the mathematical models of fluid flow in continuous casting tundishes.

The mathematical model developed by Debroy and Sychterz^[63] is a two-

dimensional one, which describes isothermal, incompressible, steady state and turbulent fluid flow in tundishes. The fundamental equations used for flow predictions are the equation of continuity and the Navier-Stokes equation in two dimensions. For the computation of the turbulent viscosity, μ_t , the prandtl's mixing length hypothesis is used, which can be written as^[68]:-

$$\mu_t = \rho l^2 \left| \frac{\partial u}{\partial y} \right|$$

where: ρ : density of the medium;

μ_t : turbulent viscosity;

l : prandtl mixing length;

$|\partial u/\partial y|$: absolute value of the velocity gradient along a direction perpendicular to the direction of flow.

The mixing length is defined as:-

$$l = 0.4y.$$

where: y : distance to the nearest wall.

The effective viscosity is expressed as:-

$$\mu_{eff} = \mu_t + \mu.$$

where: μ_{eff} : effective viscosity;

μ : molecular viscosity of the medium.

Tanaka et al.^[62] introduced a three-dimensional mathematical model

of tundish systems. The equation of continuity and the Navier-Stokes equation in three dimensions were used as the fundamental equations. They employed the k - ϵ model of Jones and Launder^[69] to calculate the turbulent viscosity. According to Jones and Launder, the turbulent viscosity is determined as:-

$$\mu_t = K_1 \rho k^2 / \epsilon$$

The governing equations for k and ϵ are respectively:-

$$\frac{\partial}{\partial x_i} (\rho u_i k - \frac{\mu_{eff}}{\sigma_k} \frac{\partial k}{\partial x_i}) = G - \rho \epsilon$$

and

$$\frac{\partial}{\partial x_i} (\rho u_i \epsilon - \frac{\mu_{eff}}{\sigma_\epsilon} \frac{\partial \epsilon}{\partial x_i}) = (K_2 G - K_3 \rho \epsilon) \epsilon / k$$

$$\text{where: } G = \mu_t \frac{\partial u_j}{\partial x_i} \left(\frac{\partial u_j}{\partial x_i} + \frac{\partial u_i}{\partial x_j} \right)$$

k : turbulence kinetic energy;

ϵ : rate of dissipation of turbulence kinetic energy;

μ_{eff} : effective viscosity;

μ_t : turbulent viscosity;

$K_1, K_2, K_3, \sigma_k, \sigma_\epsilon$: empirical constants.

They solved the above equations together with boundary conditions.

The results were found to be in a good agreement with the

experimental results they obtained from the physical models.

Similar mathematical models were developed by He and Sahai,^[64]
Szekely and El-Kaddah^[65] and Ilegbusi and Szekely.^[66]

Szekely et al.^[65-66] used mathematical models to study fluid flow in the tundishes when flow control devices, such as dams and wires, were employed. The PHOENICS computational package was used for the solution of the equations. And the removal of inclusions in different tundish designs was also assessed.

2.2.2.2. Methods of solving mathematical models

The solution procedures of the mathematical models of fluid flow in continuous casting system are mainly through the solution of the finite difference equations which are derived from the governing differential equations. Thus the methods involve the derivation of finite difference formulations from the differential equations and boundary conditions as well as methods for solving the resulting set of simultaneous non-linear algebraic equations.

The following methods have been used to derive finite difference formulations from the differential equations and the boundary conditions:-^[70]

- a) from Taylor-series expansions;
- b) through the integration over a finite volume.

There are many kinds of schemes which may be used in deriving finite difference equations. They are, mainly:-

- a) central difference scheme;

b) upwind difference scheme.

For the solution of a set of simultaneous non-linear algebraic equations, successive-substitution techniques must be employed. When using this method, initial guesses for the values of the variables are substituted into successive-substitution formulae which have been derived from the algebraic equations, and new values are calculated, then these values are used as new guesses to the solution and so on. Such procedures are commonly referred as iterative. Iterative methods of solving simultaneous algebraic equations may be divided into two main groups:- [70]

- a) "block" methods;
- b) "point" methods.

In the "block" methods, use is made of matrix inversion techniques as part of the iteration cycle; but in the "point" methods, use is only made of the procedure of successive-substitution.

Within the "point" methods, the following three methods are available:- [70]

- a) Jacobi method:
 - each cycle of the iteration only involves values of the variables from the previous cycle;
- b) Gauss-Seidel method:
 - new values are used as soon as they become available;
- c) Successive-relaxation method:
 - provisional values are first calculated using the Gauss-Seidel method, and then the final values are computed

using a relaxation parameter.

For the solving of multidimensional equation, there are also several other methods available. Among them are the alternating direction implicit (ADI) methods^[71-73], explicit splitting methods^[74-75] and Generalized ADI methods^[76-78].

Nowadays, some of these solution methods have been embodied in computational packages, such as PHOENICS, FLUENT, etc.

2.2.3. Factors affecting the fluid flow patterns within the mould.

Fluid flow patterns in moulds are affected by a number of factors. The main ones are the mould and SEN geometries, the casting speed and the cooling rate, submerged depth of SEN, mould powders, gas bubbling through the SEN, and EMS in the mould or below the mould.

2.2.3.1. Effect of mould and SEN geometries.

It is obvious that the type and dimensions of the mould will affect the flow patterns developed within it. So each investigation was conducted on a definite mould.^[3,4,10,14,28] The shape and dimensions of SEN also have the effect on the flow patterns established in the mould.

2.2.3.2. Effect of the casting speed and the cooling rate.

As it could be expected that reducing the casting speed will result in a shallower liquid pool, corresponding to an increased cooling rate, and a higher casting speed will result in a deeper liquid pool, corresponding to a slower cooling rate. As the domain within which

the flow pattern is established changes, and so does the flow pattern itself.

2.2.3.3. Effect of the submerged depth of SEN.

The submerged depth of the SEN has a strong influence on the motion of the liquid steel on the top of the mould, especially on the turbulent motion. The less is the submerged depth, the more turbulent is the motion of the liquid steel close to the liquid surface. A deeper submerged depth of the SEN is preferable, in order to reduce the turbulent motion of the liquid steel on the top of mould, in order to achieve improved surface quality of cast products.

2.2.3.4. Effect of the mould powders.

Mould powders have little effect on the flow patterns in the mould. Their main roles are to prevent the liquid steel from reoxidation, to absorb the inclusions which separate from the steel during casting, to act as a thermal insulator and to lubricate the mould.

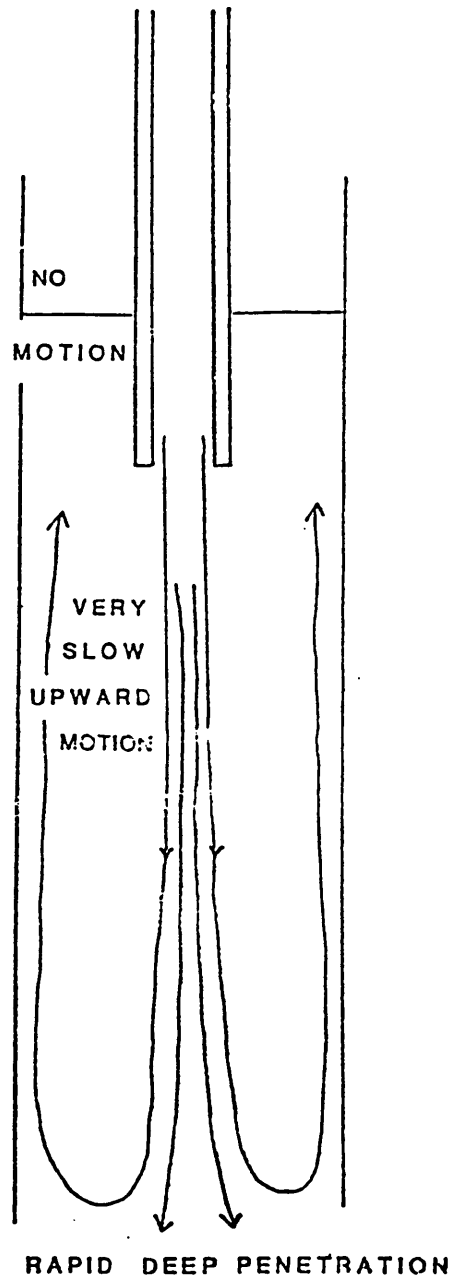
2.2.3.5. Effect of gas bubbling through the SEN.

Gas bubbling through the SEN markedly reduces the stream penetration into the liquid pool.^[3] Figure 2.7 shows the mould fluid flow pattern without gas bubbling, and figure 2.8 and figure 2.9 show the mould fluid flow patterns with gas bubbling.

2.2.3.6. Effect of EMS in the mould or below the mould.

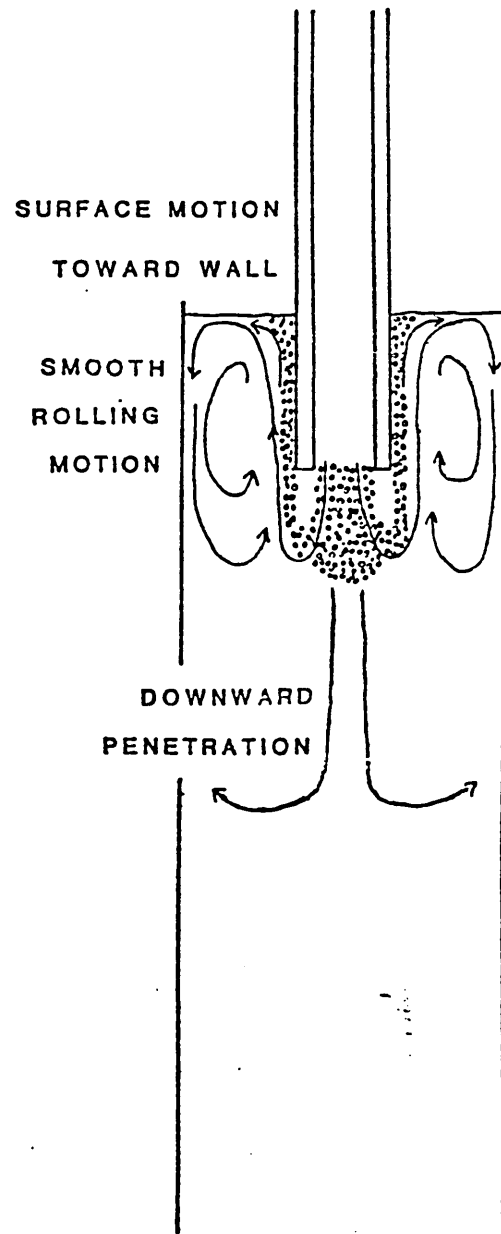
The application of electromagnetic stirring (EMS) in the mould or below the mould causes the rotational flow in the liquid pool. If the

Figure 2.7



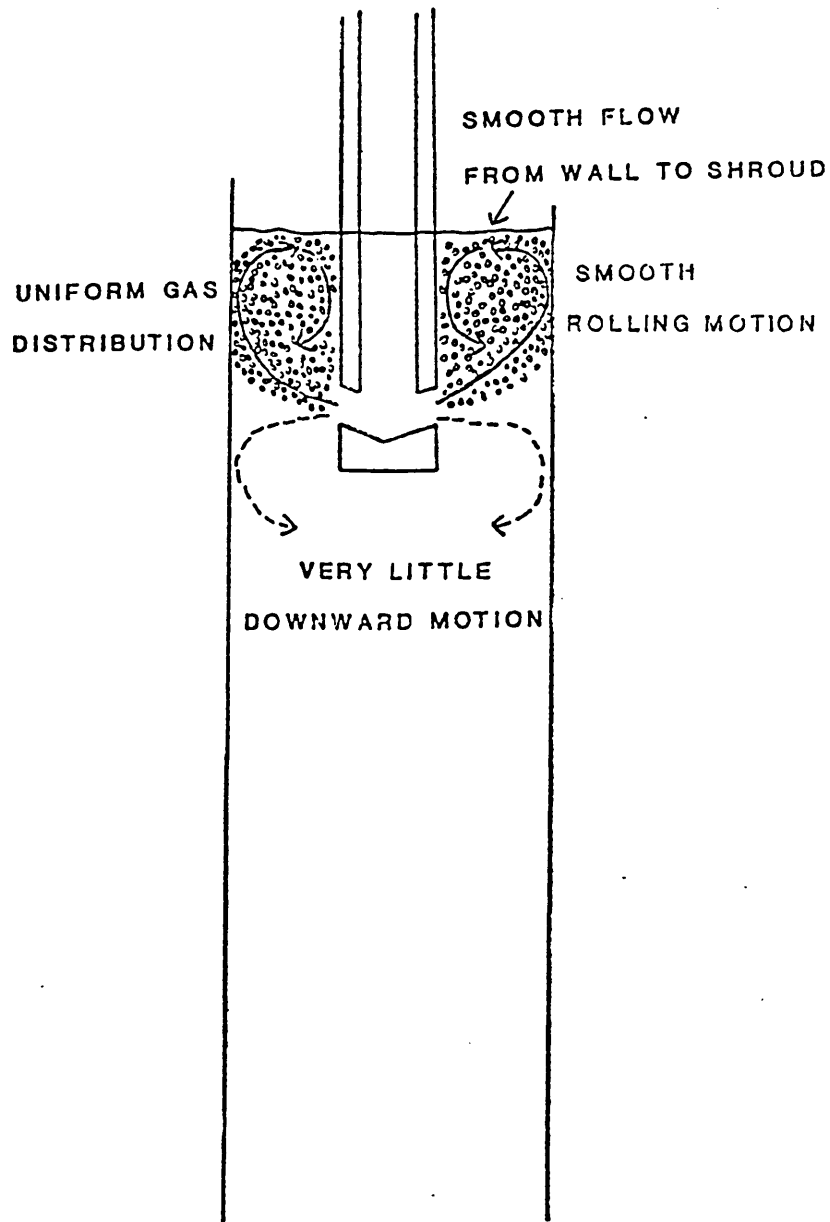
Mould fluid flow pattern with a
straight-discharge SEN. [3]
(no gas bubbling)

Figure 2.8



Mould fluid flow pattern with a
straight-discharge SEN. [3]
(with gas bubbling)

Figure 2.9



Mould fluid flow pattern with a
4-ported SEN. [3]
(with gas bubbling)

rotation extent is justified, this rotational flow induced is of benefit to the internal quality aspects of cast products. [79]

2.3. Inclusion separation.

The liquid sump in the continuous casting mould provides the last chance for inclusion separation. The extent of the removal of inclusions in the sump is closely related to the quality of the cast products. It is essential that the nature of inclusion removal in the sump is properly understood so that every effort can be made to promote inclusion separation there.

2.3.1. The mechanisms of inclusion separation.

The mechanisms of inclusion separation from the liquid steel is not yet fully understood. Two possible mechanisms, floatation and eddy diffusion, are discussed in the following sections.

2.3.1.1. Floatation.

The inclusion particles, either liquid or solid, existing in liquid steel tend to rise due to the buoyancy. Miyashita et al. [80] have studied the rising velocities of inclusions in a quiescent steel bath and found that they follow Stokes' law, which may be written as:-

$$U_r = \frac{D_p^2 (\rho - \rho_p) g}{18 \mu}$$

where: U_r : rising velocity of particle;

D_p : diameter of particle;

ρ : density of the medium;

ρ_p : density of particle;

g : gravitational acceleration;

μ : molecular viscosity.

Thus, for 20-micron and 100-micron particles, having a density some 0.4 times that of liquid steel, the rising velocities would be of the order of 0.16 mm.s^{-1} and 4.00 mm.s^{-1} , respectively. These velocities are much smaller than the withdraw speed in the mould, so inclusions cannot be removed from the liquid steel in the sump through floatation. In fact, Miyashita et al.^[80], as well as various other authors^[81-83], have demonstrated that Stokes' law cannot be applied directly to a stirred or agitated steel bath to work out inclusion removal rates. Removal rates of inclusion particles in such baths are much higher than would be predicted by Stokes' law. Some other kinds of mechanism must be involved.

2.3.1.2. Eddy diffusion.

When liquid steel is stirred or agitated by gas purging, electromagnetic stirring, or impact of an incoming jet stream, the flow of the liquid steel will be turbulent. Eddies, turbulent changes of velocity, will therefore exist in the melt and inclusions will be removed by eddy diffusion. It has been found that^[84-86] the eddies formed will be in a size ranging from the linear dimensions of the reactor down to a size λ_0 so small that viscosity becomes important, i.e.

$$\frac{\lambda_0 V_\lambda}{\nu} \approx 1$$

where: $V_\lambda \propto \left[\frac{\dot{\epsilon}_0 \nu}{\rho} \right]^{0.25}$

λ_0 : size of the eddies;

V_λ : eddy velocity of size λ_0 ;

ν : kinematic viscosity of steel;

$\dot{\epsilon}_0$: stirring power per unit volume;

ρ : density of steel.

For eddy diffusion close to a surface to which inclusions are going to be removed, Fick's first law of diffusion may be applied which could be written in the form:-

$$j_a = -D_E \frac{dC_a}{dy}$$

where: j_a : flux of inclusions of a diameter a ;

C_a : concentration of inclusion of diameter a ;

y : distance from the surface;

D_E : eddy diffusivity.

Now the eddy diffusivity D_E may be obtained using the prandtl mixing length model^[87]

$$D_E = V_y \cdot l$$

where: $l = 0.4y$

l : Prandtl mixing length;

y : distance from the surface;

V_y : normal component to the surface of eddy velocity.

Engh and Lindskog^[96] employed this theory to study the inclusion removal to refractory walls. The effective removal velocity of the inclusion at the walls was obtained. However, they have not discussed the removal of inclusions to the top slag — the only possible way for the inclusion removal from the strand in the sump.

2.3.2. Empirical approach.

Unlike empirical investigations of fluid flow patterns in continuous casting moulds, experimental studies of inclusion separation in moulds are relatively rare. It appears that neither experimental methods nor empirical data about the inclusion separation ratio in moulds have been published in the previous metallurgical literature, although several publications^[88-91] about inclusion separation in tundishes exist.

Kemeny et al.^[88] proposed a model for inclusion removal in a tundish based on a study of residence times in a full-scale water model. They assumed that inclusions of specific diameter would be removed from the system once they had reached the surface according to the Stokes' Law.

Sahai and Ahuja^[89] measured actual inclusion separation ratios in a tundish, using a one-third scale model. Their method of analysis relied on weighing particles filtered from water samples taken from

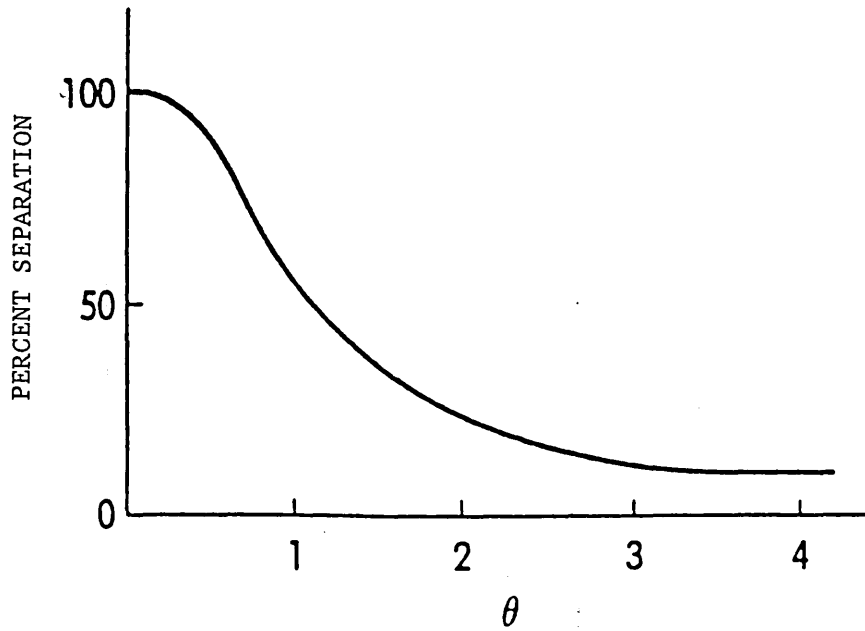
the tundish at a specific times after particles had been injected into the entry stream. Hollow glass microspheres (44-75 micron diameter and 0.6 g.cm^{-3} apparent density) were used to simulate wetting inclusions in molten steel and polyethylene powder (106-150 micron diameter and 0.91 g.cm^{-3} density) to simulate the non-wetting inclusions. A measured amount of the particles, dispersed in small quantity of water, was injected into the entry stream and water was allowed to run through the tundish for the specified period of time, after which the inlet and exit streams were stopped. The water contained in the tundish was collected and filtered. The walls of the model tundish were washed to collect any adhering particles. All the particles were carefully dried and weighed to calculate the inclusion separation ratio which was defined as:-

$$\eta_{inclusion} = \frac{W_t}{W_i} \times 100$$

where: $\eta_{inclusion}$: inclusion separation ratio in percentile terms;
 W_t : weight of particles remained in tundish;
 W_i : weight of particles injected.

The extent of inclusion separation for a given flow condition, depended upon the time allowed. Figure 2.10 shows one of their examples for the inclusion separation ratio of the injected particles as a function of time. As can be seen from this figure, the inclusion separation ratio reached a steady-state value in about three times the nominal residence time. Sahai and Ahuja^[89] therefore used these steady-state values in analysing their results.

Figure 2.10



Percent separation of glass microspheres
as a function of dimensionless time. [89]

Nakajima et al.^[90] developed a technique for the detection and on-line analysis of inclusions in model tundishes. The technique is based on the electric sensing zone (E.S.Z.) principle: when a small particles pass through an electrically insulated orifice the electrical resistance of a fluid electrolyte flowing through the orifice increases in accordance with a particle's volume. Voltage pulses generated in the presence of an electrical current can be measured, and the number and size of particles counted. This principle is shown schematically in figure 2.11.

The change in electrical resistance of the fluid, when a small particle passes through the cylindrical orifice, is given by^[90]:-

$$\Delta R = \frac{4\rho_e d^3}{\pi D^4} [1 - 0.8(d/D)^3]^{-1}$$

where: ΔR : change of electrical resistance of the fluid;

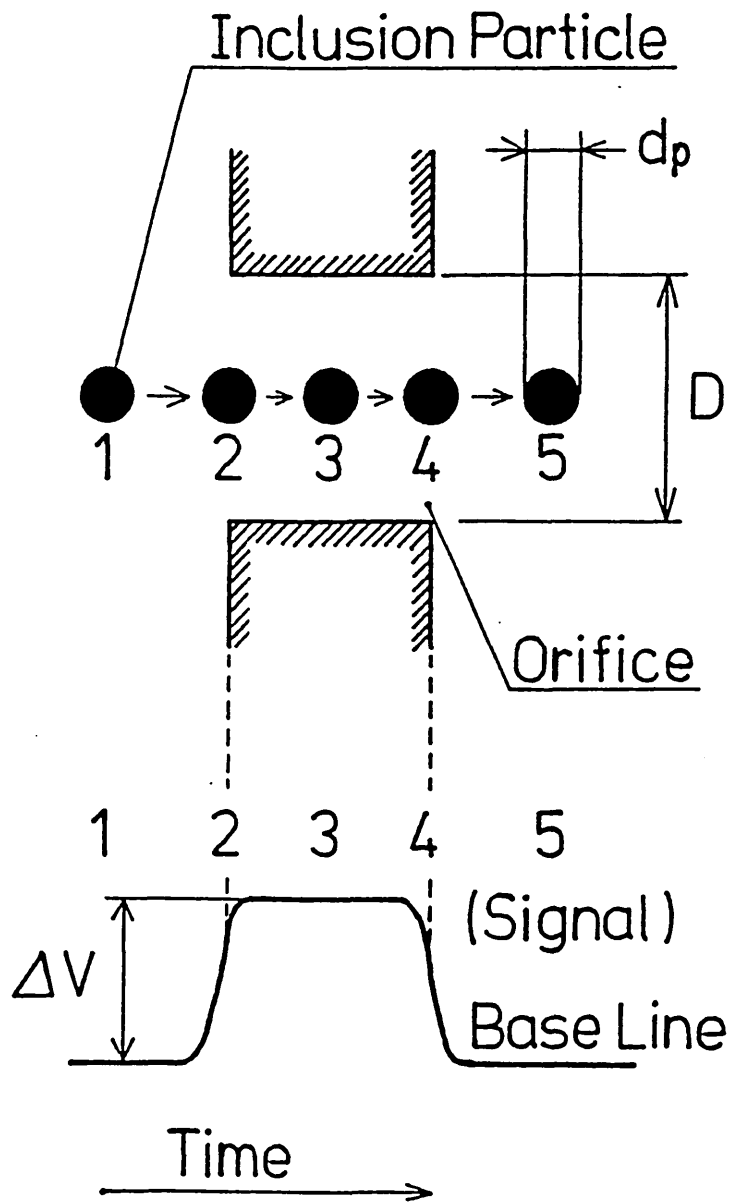
ρ_e : resistivity of the fluid;

d_p : diameter of the particle;

D : diameter of the orifice.

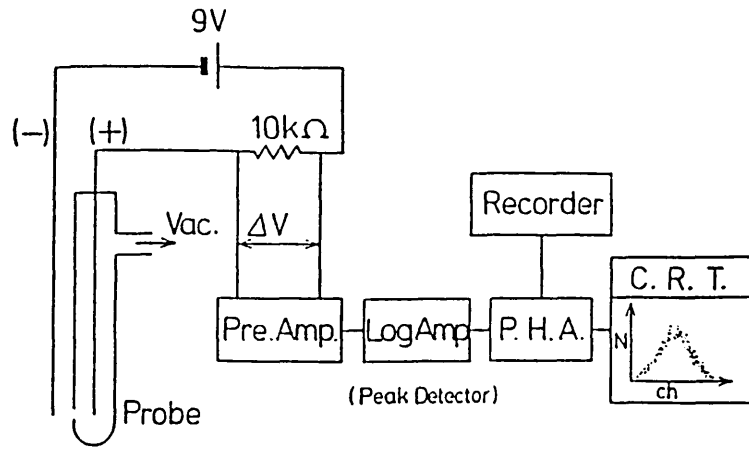
The E.S.Z. system is shown schematically in figure 2.12.^[90] It consists of a sampling probe, an electrical circuit, a pre-amplifier, a pulse height analyser (P.H.A.), and a recording system. In their studies, glass orifices of 480 μm were fitted to sampling probes, then the glass probe was shielded with a stainless steel flexible hose, as shown in figure 2.13.^[90] By applying this technique, Nakajima et al.^[90] studied the inclusion separation from tundishes

Figure 2.11



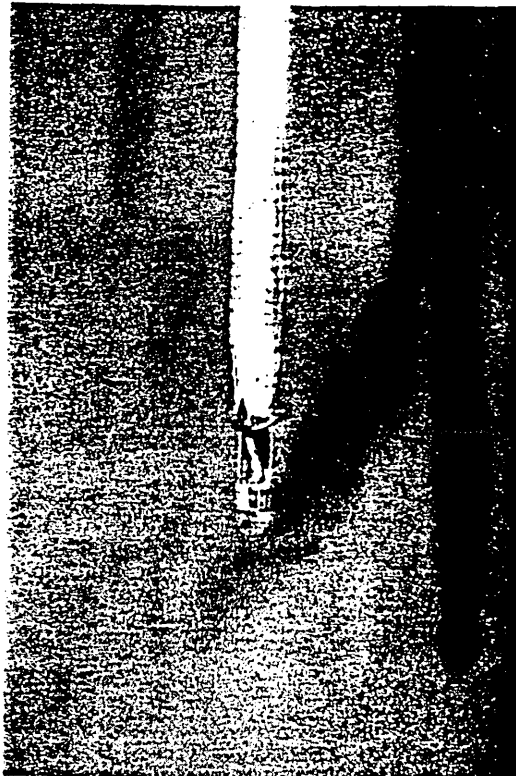
Principle of particle detection by the E.S.Z. method. [90]

Figure 2.12



Schematic of the E.S.Z. system. [90]

Figure 2.13



Photograph of E.S.Z. probe developed. [90]

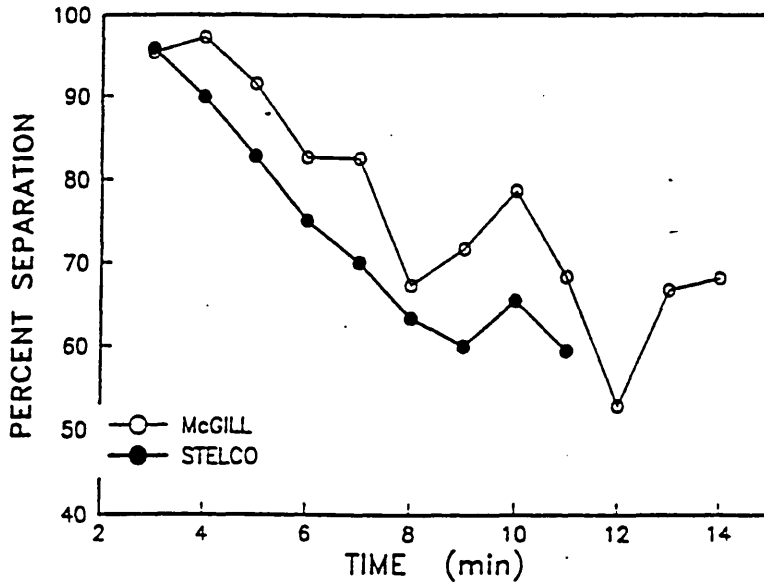
and found that this technique was compatible with the method used by Sahai and Ahuja.^[89] Both methods showed that for the particular tundish under study, steady state conditions with regard to inclusion float out behaviour were only achieved after some 2-3 nominal residence times, as shown in figure 2.14 and figure 2.15.

In a 1/4-scale tundish water model, Martinez et al.^[91] studied the inclusion separation from tundish. Once again, glass microspheres were selected as non-metallic inclusion simulators (wetting) because the physical properties of this material are very favourable to simulate non-metallic inclusions. A measured amount of glass microspheres were mixed with water and injected through the submerged nozzle. The recovery of these particles was then measured at the exit nozzle at various sampling times. The samples obtained were weighed and then the particle size distribution measured with the assistance of a computer. The data yielded the total percentage of separation as well as the separation with respect to certain sizes of the glass microsphere.

2.3.3. Theoretical approach.

Inclusion separation in continuous casting processes has a very strong influence on steel cleanliness and overall quality of continuously cast products. This has stimulated much recent theoretical investigation into the behaviour of inclusions in liquid steel, mainly through mathematical models. But just like in the case of empirical studies, most of the work^[66,92-95] were done in continuous casting tundishes, not in moulds. So in the following, only some aspects about the theoretical investigations of inclusion

Figure 2.14



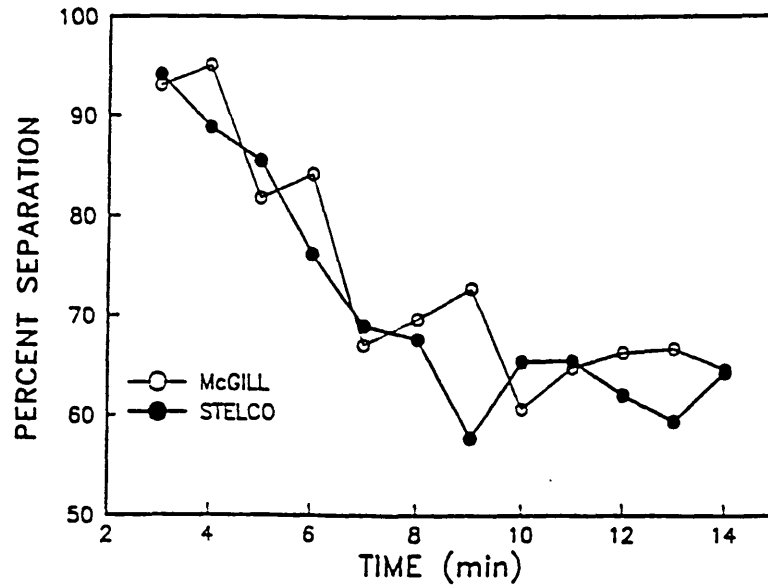
Comparison of weight-based separation ratios using the weighing method and the E.S.Z. method. [90]

Conditions: no flow controls,
hydrophillic particles,
straight shroud.

McGill: weighing method;

STELCO: E.S.Z. method.

Figure 2.15



Comparison of weight-based separation ratios
using the weighing method and the E.S.Z. method.^[90]

Conditions: flow controls,

hydrophillic particles,

straight shroud.

McGill: weighing method;

STELCO: E.S.Z. method.

separation from tundishes will be mentioned.

Hsu and Chou^[92] developed a mathematical model to represent the fluid flow phenomena and inclusion behaviour in a slab tundish. The mathematical model included the solution of two-dimensional Navier-Stokes equations. Prandtl's mixing length hypothesis^[68] was used to calculate the turbulent viscosity. Inclusion behaviour was studied through inclusion trajectories determined by accounting for buoyancy effects.

Nakajima and Kawasaki^[93] studied the floating behaviour of inclusions in a tundish in conjunction with the fluid flow state of the molten steel. Their mathematical model postulated that the tundish bath consists of three regions: a mixing flow region, a plug flow region and a stagnant region. In the mixing flow region, dominated by inertial force or turbulent viscous force, inclusions are transferred by various sized vortices. In the plug flow region, dominated by viscous force, inclusions are transferred approximately according to Stokes' law. The stagnant region is by-passed by the steel stream and is therefore not involved in inclusion transfer. Their model was found to be in good agreement with the results of physical model experiments and with actual operations. The model showed that the use of a longer and deeper tundish bath was effective for promoting the floating removal of inclusions owing to the resulting increase in the plug flow region. In addition, placing dams in the tundish reduced the efficiency of inclusion removal by floatation, since the dam increased the mixing flow region.

In another paper,^[94] Nakajima and Kawasaki further extended their

model to study the effectiveness of gas bubbling as a means of increasing inclusion removal efficiencies in a tundish at high casting speeds. The model was modified by including a recirculatory region related to the gas bubbling in which inclusion are mainly transferred by upward flow. Once again, the stagnant region is not involved in inclusion transfer. The model showed that a uniform bubbling flow, which occurred at low gas flow rates, was effective in promoting the floating removal of inclusions; the effect becoming stronger as the casting rate was increased.

Ilegbusi and Szekely^[66,95] studied fluid flow, tracer dispersion and inclusion behaviour in tundishes using a mathematical model. They employed the PHOENICS computational package to solve the Navier-Stokes equations together with the tracer conservation equation and the particle transport equation based on buoyancy effects. They found that there were significant differences between the behaviour of the tracer and the behaviour of the inclusion particles, principally due to the finite rising velocity of the inclusions.

Inclusion separation phenomena have also been studied in other metal treatment processes. From the fluid mechanical point of view, Engh and Lindskog^[96] developed a mathematical model to describe the separation of slag inclusions, as a function of the specific stirring power, during ladle treatment. The model is based on the use of the eddy diffusivity concept to calculate the inclusion removal rate to the ladle walls. The removal velocity of a given particle is obtained as a function of the specific stirring power and the particle size. However, the inclusion removal to the top slag, the only mechanism that can operate in a continuous casting mould, was not discussed in

their paper.

2.3.4. Factors affecting inclusion separation.

As expected, the factors, mentioned in section 2.2.3., affecting the fluid flow patterns have been shown to have some effect on the inclusion separation process. However, very little direct work has been carried out on the mechanisms of inclusion removal in the continuous casting mould. The present work has therefore been undertaken to elucidate which aspects of fluid flow in the sump have the greatest effect on inclusion removal, and hence what control strategies can be adopted to maximize inclusion removal in the sump. And this will be discussed later in the discussions.

3. EXPERIMENTAL TECHNIQUES.

3.1. Development and control of water model system.

3.1.1. Introduction.

The previous literature review has already identified the main area of interest of the research as the study of fluid flow patterns in the sump and their influences on the inclusion removal in the mould during continuous casting.

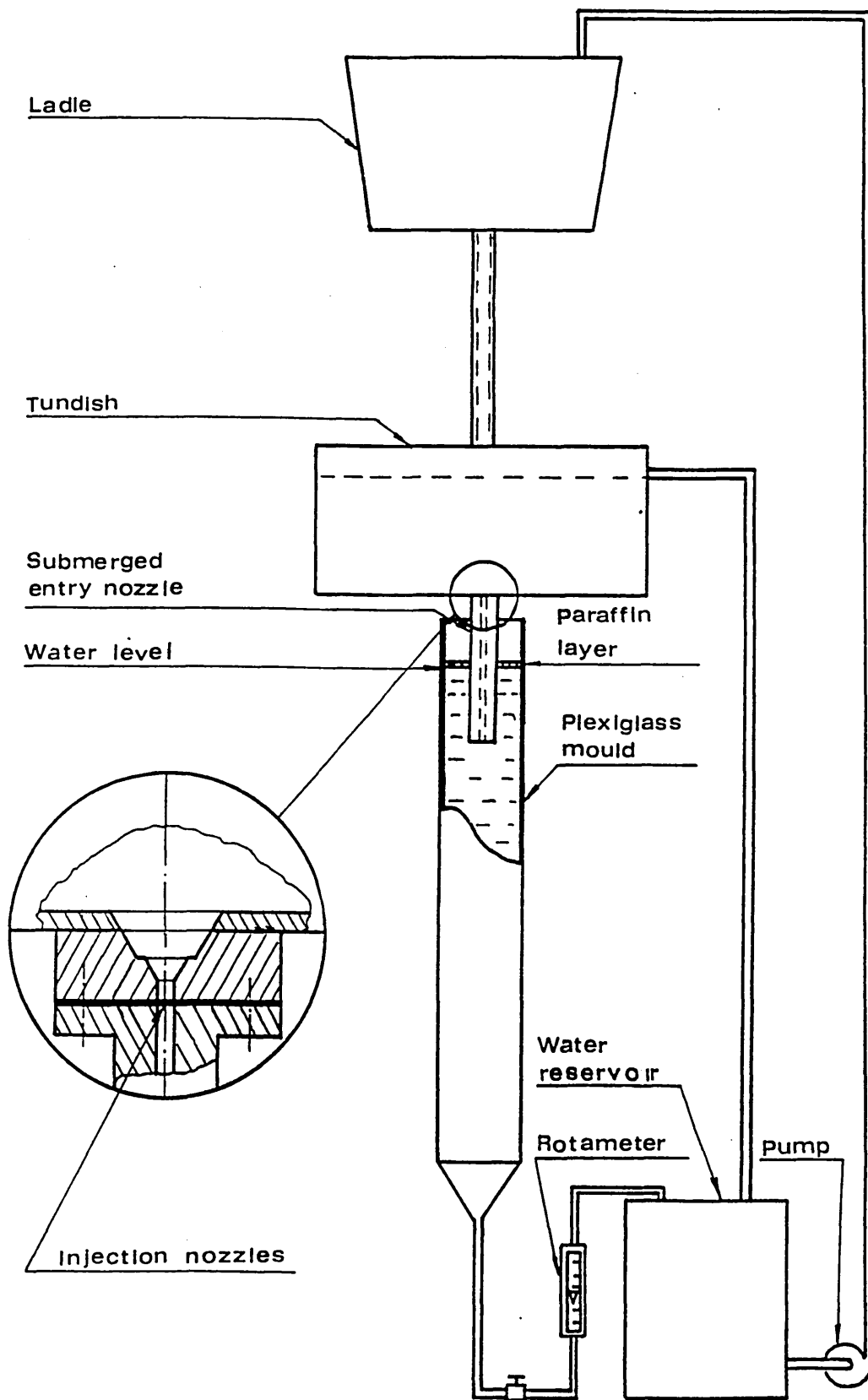
The aim of the experimental work was to develop water models of continuous casting systems and used them to observe fluid flow patterns and inclusion behaviour in the sump during continuous casting operations.

In order to achieve this purpose, continuous casting system water models have been developed, as shown schematically in figure 3.1, which consist of ladle, tundish, mould and a part of the strand. Two kinds of continuous caster have been simulated in this study. The first one is a vertical straight mould billet caster, with a mould cross section of 140 mm x 140 mm. The second one simulates a vertical straight mould bloom caster with a mould cross section of 425 mm x 305 mm.

3.1.2. Choice of scale.

The present study will be restricted to the treatment of submerged entry nozzles and only fluid flow patterns in the upper portion of the sump will be considered. The fluid flow in this region is governed by the action of the high momentum jet and by gravity driven

Figure 3.1



Experimental set up for recirculatory mode

flows at the exit of the nozzle. The expansion of the jet flow is also involved, a phenomenon influenced by viscous and inertial forces, making both Froude and Reynolds numbers important. Both the Froude and Reynolds criteria must be satisfied. The Froude number and Reynolds number expressions were given in section 2.2.1.2. but are rewritten below:-

$$\text{Froude No } Fr = \frac{V^2}{gL} = \frac{\textit{inertial force}}{\textit{gravity force}}$$

$$\text{Reynolds No } Re = \frac{VL}{\nu} = \frac{\textit{inertial force}}{\textit{viscous force}}$$

After considering the physical properties of water and liquid steel, given in table 3.1^[23], it is known that full-scale water models must be selected in order to satisfy the Froude and Reynolds criteria simultaneously. Therefore the length scale factor is equal to one, i.e.

$$L_f = \frac{L_m}{L_p} = 1 \quad (3.1)$$

where: subscript

m : model;

p : prototype (steel casting system);

L_f : length scale factor;

L_m : length in the model;

L_p : corresponding length in the prototype.

TABLE 3.1. Physical properties of water at 20°C and steel at 1600°C.

Property	Water (20°C)	Steel (1600°C)
Absolute Viscosity (cp)	1.0	6.4
Density (g.cm ⁻³)	1.0	6.95
Kinematic Viscosity (cs)	1.0	0.92
Surface Tension (dyne.cm ⁻¹)	74	1350

TABLE 3.2. Billet Tundish nozzle dimensions.

Dimensions	d _z (mm)	D _z (mm)	L (mm)	Others
Nozzle 1	15	50	280	Metering nozzle
Nozzle 2	15	70	280	Metering nozzle
Nozzle 3	19	50	280	Slide gate nozzle

However, because of the limitation of the water supply in the laboratory, it was only possible to run bloom caster water model using a full scale slice mould. Full scale slice mould means here that the mould used in the model is a slice cut off vertically from the centre of the bloom mould. This model, in fact, was a truncated model - truncated in the direction normal to the plane of the nozzle axes. Therefore the mould used in the experiments on the bloom caster model has a cross section of 425 mm x 65 mm. The mould used in the experiment on the billet caster model was a full scale three-dimensional one, having a cross section of 140 mm x 140 mm.

3.1.3. Model design calculations.

The fluid flow coming into the sump are mainly gravity driven flows. For gravity driven flow through an orifice, the velocity can be expressed as:-

$$V \propto \sqrt{h} \quad (3.2)$$

where: V: velocity;

h: fluid hydraulic head above the orifice.

Equation (3.2) may be written for both model and prototype as:-

$$V_m \propto \sqrt{h_m}$$

$$V_p \propto \sqrt{h_p}$$

Thus, the velocity scale factor, V_f , may be written as

$$V_f = \frac{V_m}{V_p} = \left(\frac{h_m}{h_p}\right)^{0.5} = h_f^{0.5} \quad (3.3)$$

where h_f is termed as fluid hydraulic head scale factor.

In the water model developed, h_f has been chosen to be equal to L_f , i.e.

$$h_f = L_f \quad (3.4)$$

So

$$V_f = L_f^{0.5} = 1 \quad (3.5)$$

Thus the velocity used in the model will be the same as that presented in the prototype.

The time scale factor, t_f , may be calculated with the aid of the following relation,

$$t_f = \frac{L_f}{V_f} \quad (3.6)$$

Substituting equation (3.5) into equation (3.6), equation (3.6) can be expressed in terms of the length scale factor as:-

$$t_f = L_f^{0.5} = 1. \quad (3.7)$$

So the time involved in the model will be the real time.

Similarly, the volume flow rate scale factor, Q_f , can be derived from the length scale factor and the time scale factor as:-

$$Q_f = \frac{L_f^3}{t_f} \quad (3.8)$$

which may be written in terms of the length scale factor after substitution from equation (3.7) as:-

$$Q_f = L_f^{2.5} = 1. \quad (3.9)$$

Therefore the volume flow rate employed in the model will be the same as that used in the prototype. But in the case of bloom caster model, because a truncated model was used, the volume flow rate employed in the model will be the same as that of the slice of mould simulated.

3.1.4. Mould.

Billet caster mould.

6 mm thick perspex sheets were used to build the model of the billet caster mould and a part of the strand. Two pieces of perspex sheets with dimensions of 140 mm x 1150 mm and two pieces with dimensions of 152 mm x 1150 mm were glued together to make a square tube of internal dimensions of 140 mm x 140 mm and length of 1150 mm. One end of the square tube was left open and the other end of the tube was glued onto a perspex square flange plate of internal dimensions of 140 mm x 140 mm and outside dimensions of 210 mm x 210 mm. At the bottom of the model, a perspex square funnel was glued onto a perspex flange plate (having the same dimensions as that at the bottom of the tube) which was then flanged onto the tube. A piece of perspex pipe, internal diameter 25 mm, was glued onto the bottom of the funnel to

form the water outlet of the mould. This arrangement ensures that water flows out of the mould evenly. Figure 3.2 shows the mould assembly for the model billet caster.

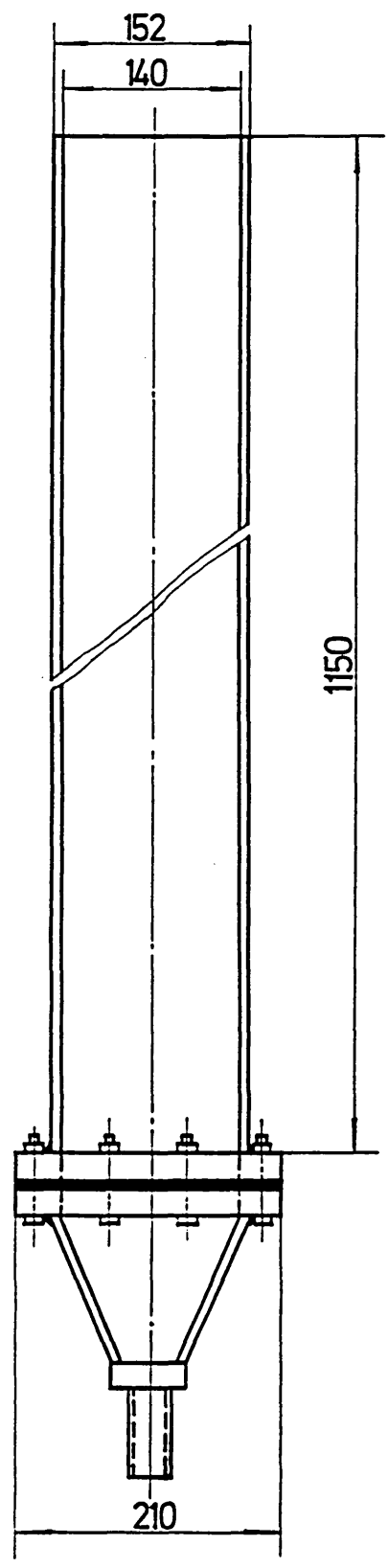
Bloom caster mould.

The bloom caster model mould was built using the same kind of materials as the billet caster model mould. 6 mm thick perspex sheets were cut into four pieces, two of them having dimensions of 437 mm x 650 mm and the other two having dimensions of 65 mm x 650 mm. These four pieces were glued together to form a square tube of internal dimensions of 425 mm x 65 mm 650 mm in length. A similar perspex square funnel to that used in the billet caster model was built and flanged onto the bottom of the mould model through a similar arrangement. A piece of perspex pipe, internal diameter 25 mm and wall thickness 3 mm, was again glued onto the bottom of the funnel to form the water outlet of the mould. Figure 3.3 shows the mould assembly for the model bloom caster.

3.1.5. Tundish and tundish nozzles.

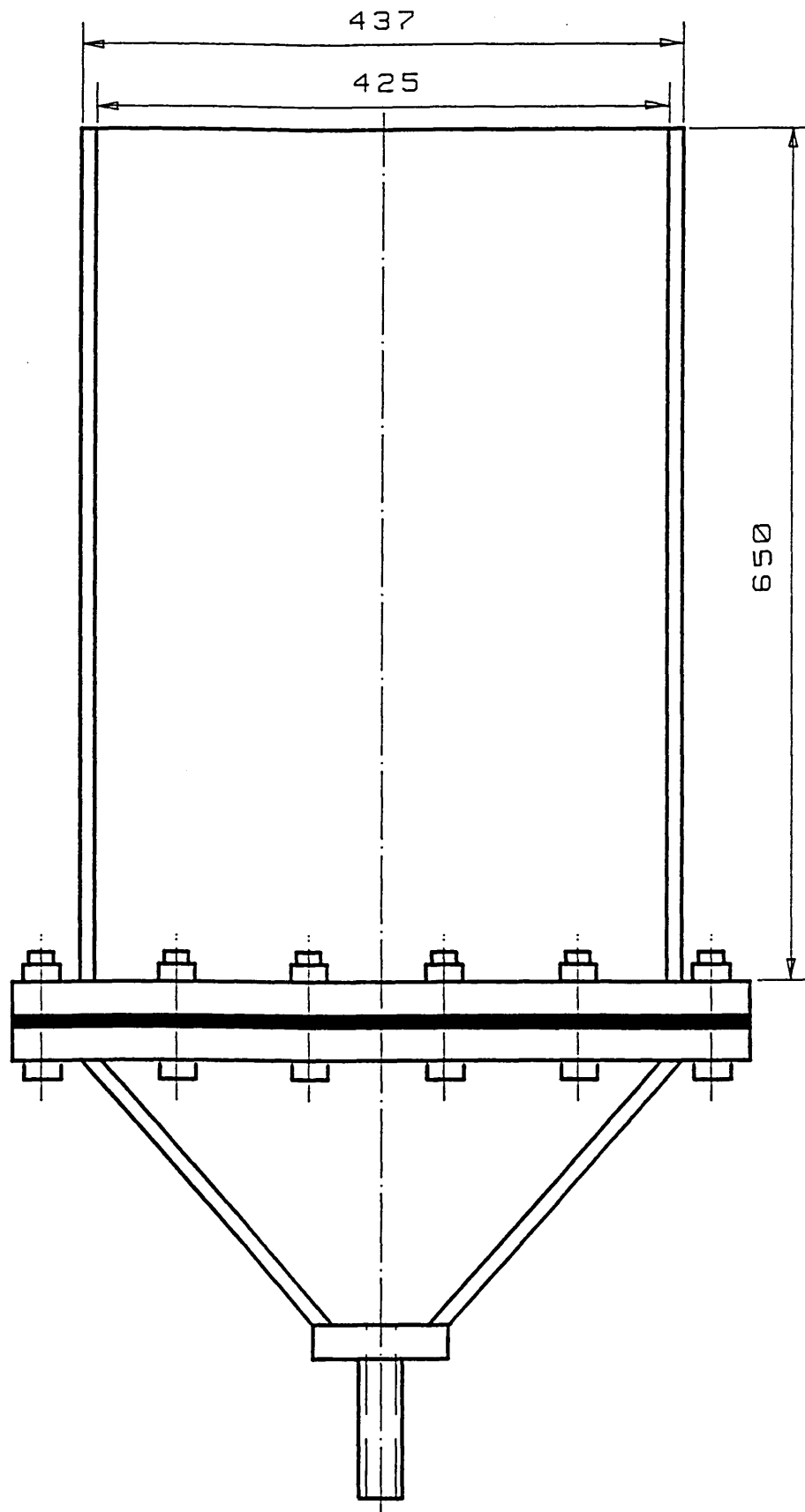
No observations were made within the tundish. The tundish was, therefore, only built as a distributor: to reduce the turbulence caused by entry stream and to eliminate gas bubbles contained in the water. A narrow tundish model made of perspex was used, provision being made to control the water level in the tundish and to mount different nozzles. Figure 3.4 schematically shows the tundish assembly.

Figure 3.2



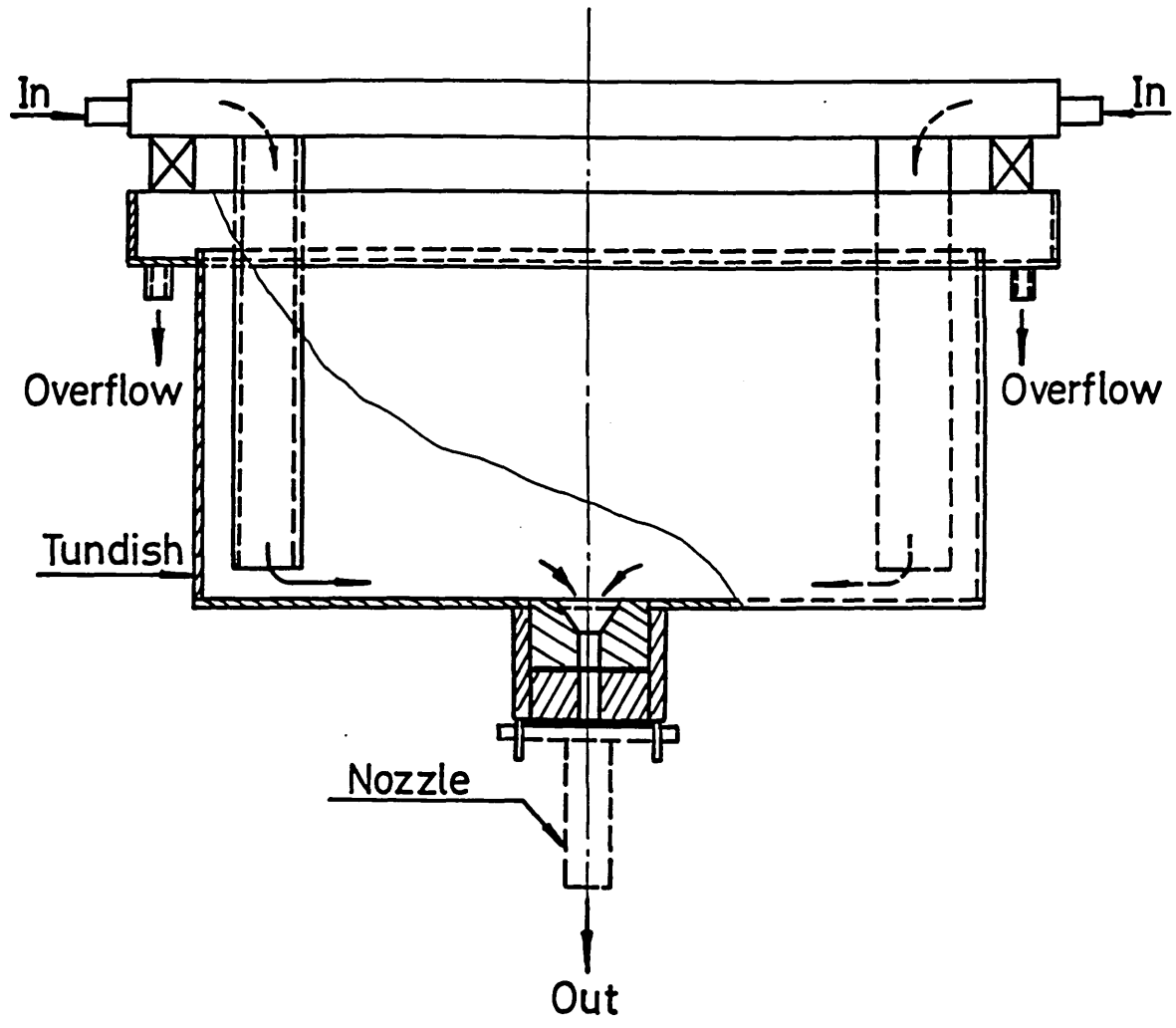
Sketches of the billet mould assembly.

Figure 3.3



Sketches of the bloom mould assembly.

Figure 3.4



Sketches of the tundish assembly.

Three tundish nozzles were used during the experiments on billet caster model. All of them have a vertical outlet, as shown schematically in figure 3.5. Two are metering nozzles and the other one is a slide gate nozzle. Their dimensions are given in table 3.2.

Eight tundish nozzles were used during the experiments on bloom caster model. All have bifurcated outlets with different outlet angles, as schematically shown in figure 3.6, 3.7 and 3.8. They are all metering nozzles. Their dimensions are given in table 3.3. The nozzle diameters were decided according to the volume flow rate required by the bloom caster model. The volume flow rate through the model was determined in such a way that downward fluid flow velocity will be the same in both the model and the prototype.

A centimeter scale was stuck onto the side of the nozzle, allowing the submerged depth to be easily read.

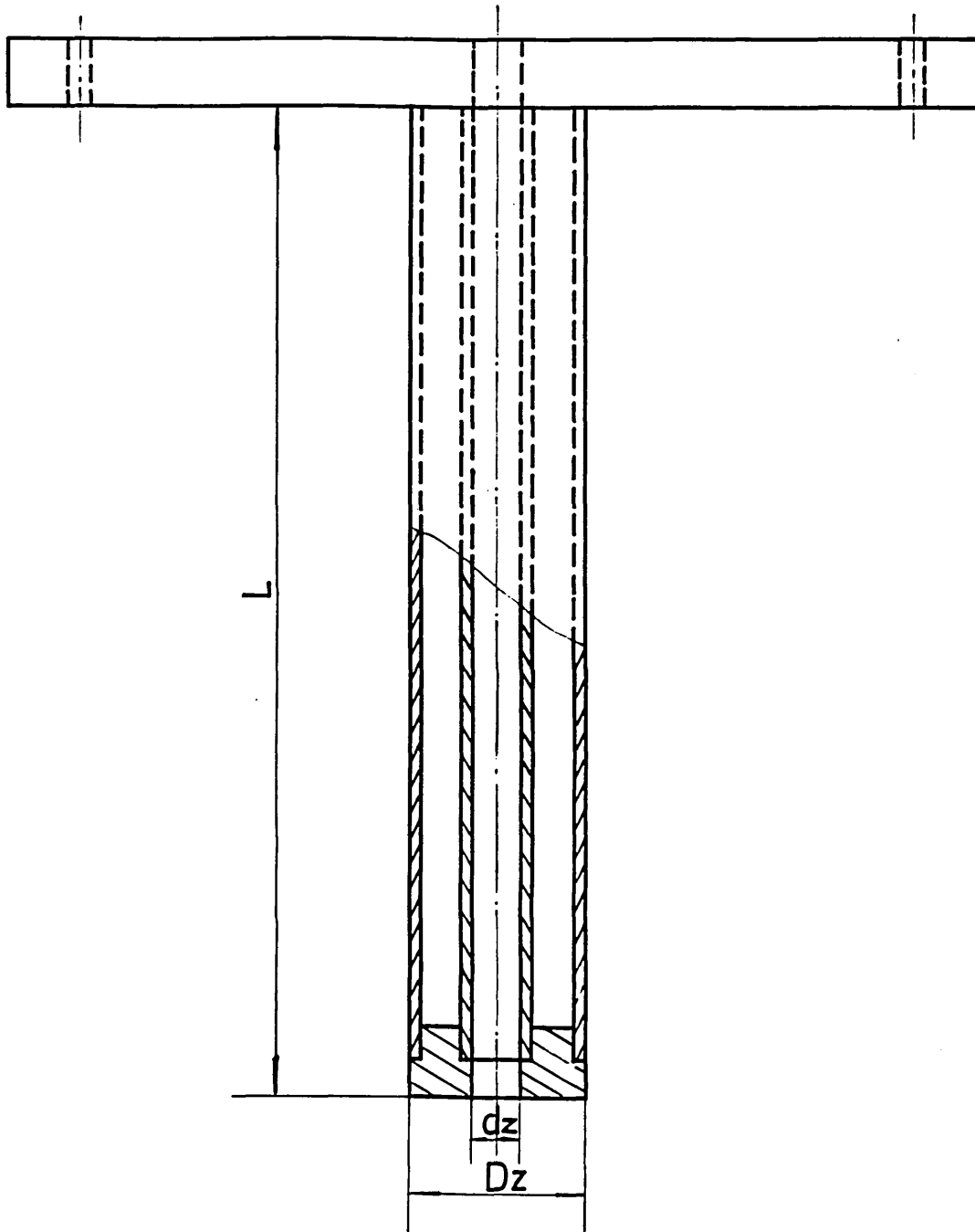
3.1.6. Ladle.

The ladle model was a simple plastic tank of 45 litre capacity, supported 2250 mm above the tundish water level. An overflow pipe was connected to the tank to control the water level.

3.1.7. Water flow modes.

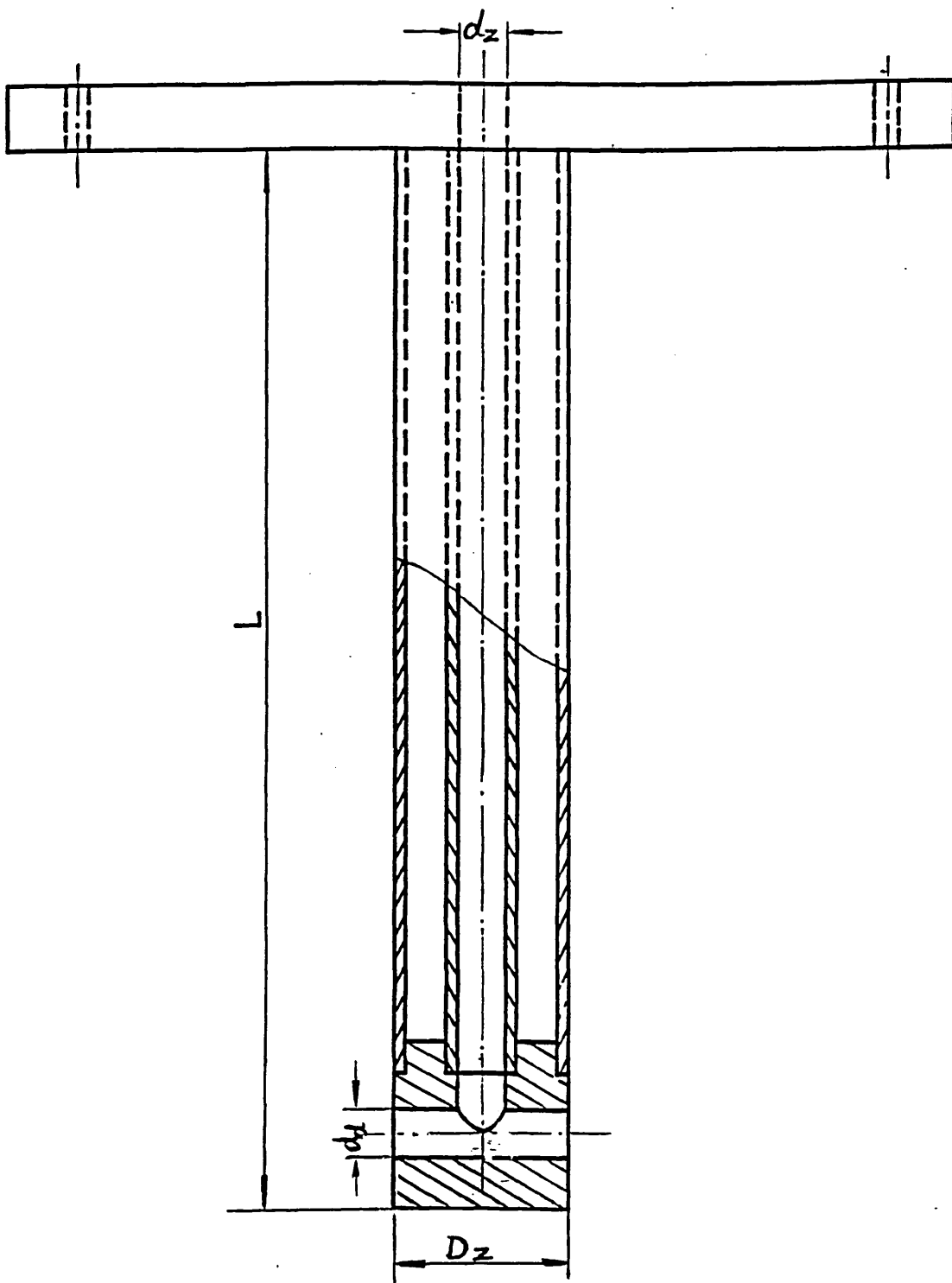
Two kinds of water flow modes were employed during the experiments, namely a recirculatory mode and a through-flow mode, as shown in figure 3.9. The water recirculatory mode was used during the experiments for fluid flow pattern visualization. In this mode, 70 litres of tap water were first fed into the water reservoir, and a

Figure 3.5



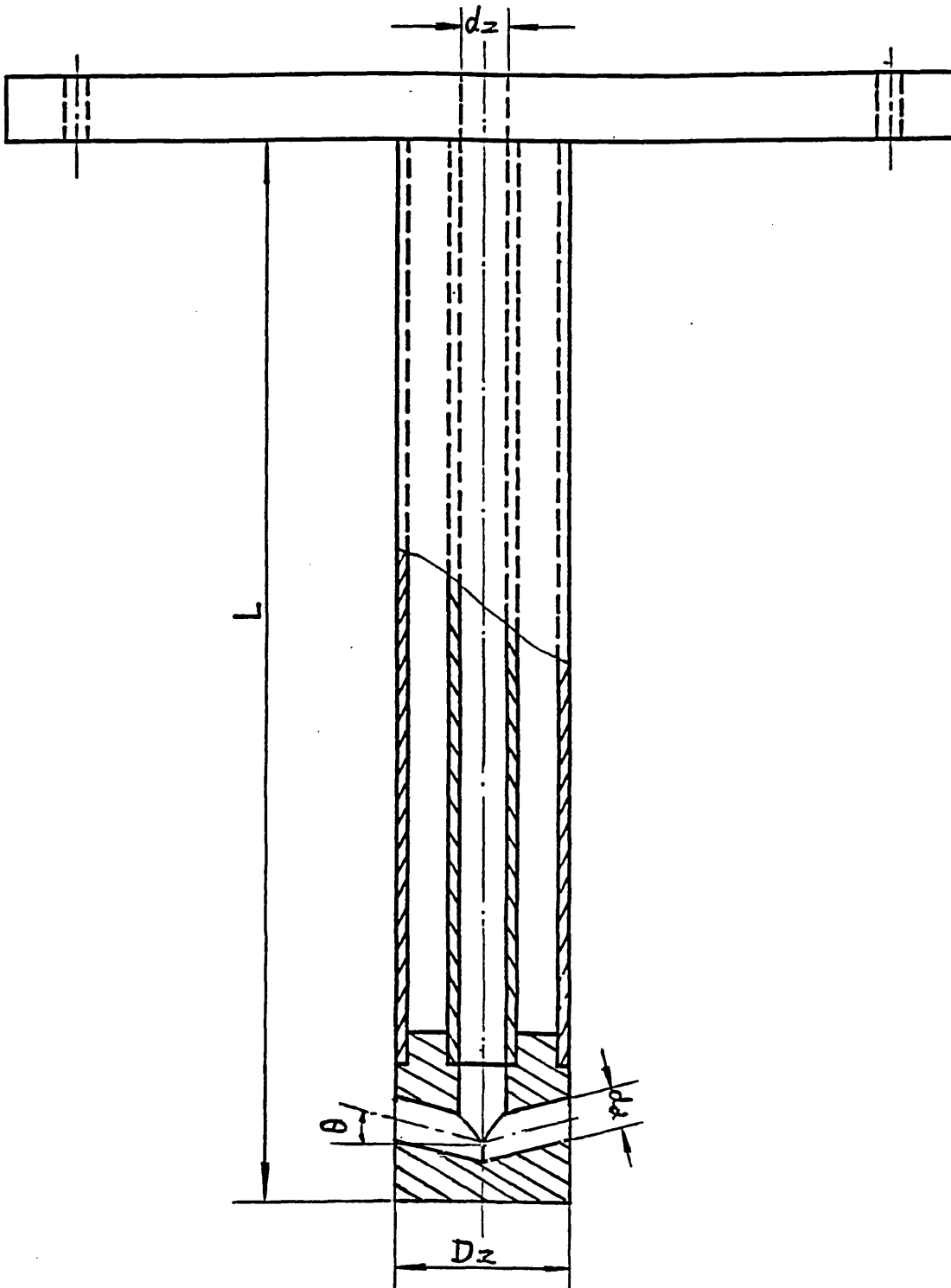
Design of submerged entry nozzle. (see Table 3.2.)

Figure 3.6



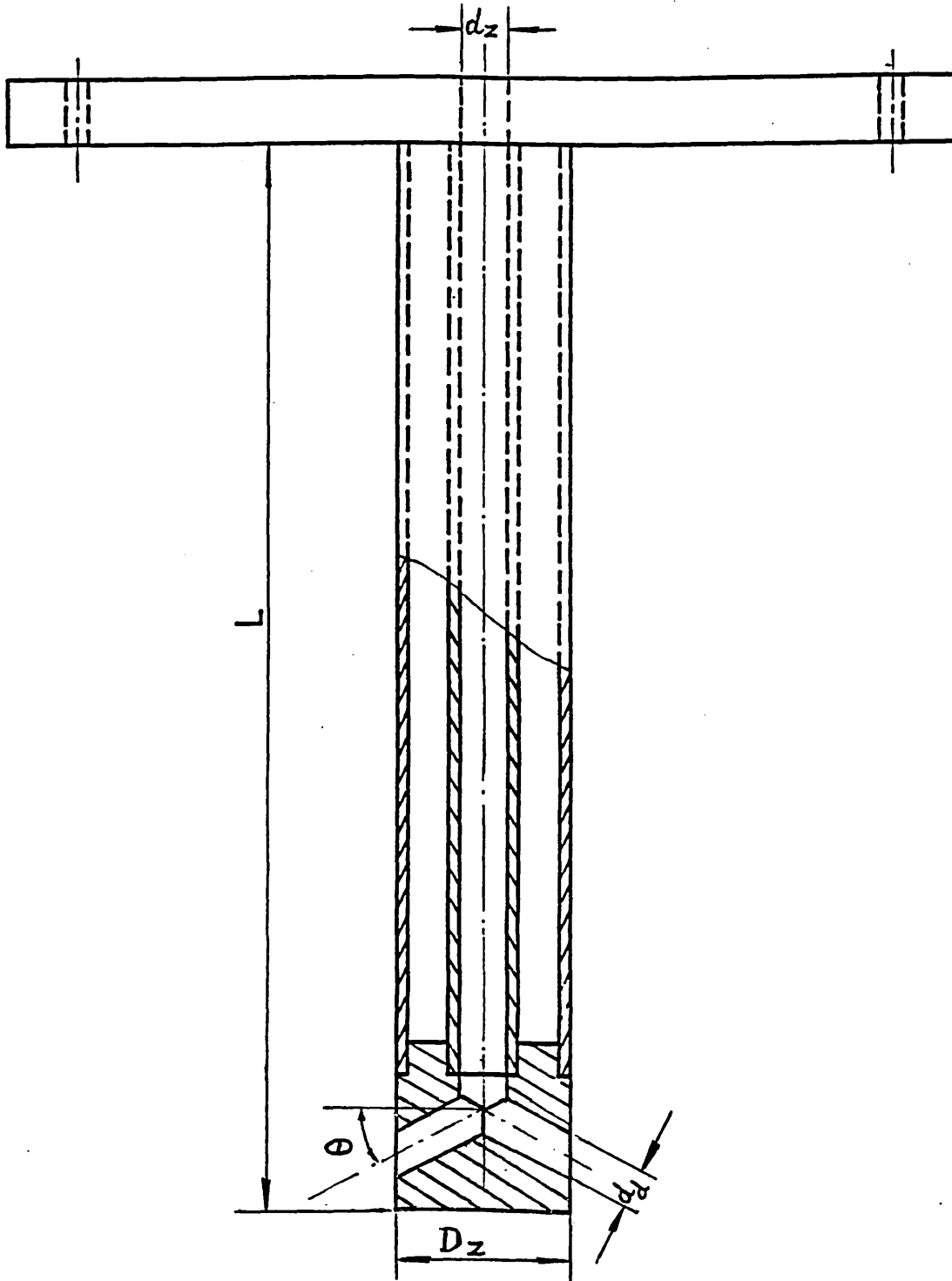
Design of submerged entry nozzle with horizontal outlets. (see Table 3.3.)

Figure 3.7



Design of submerged entry nozzle with upward outlets. (see Table 3.3.)

Figure 3.8

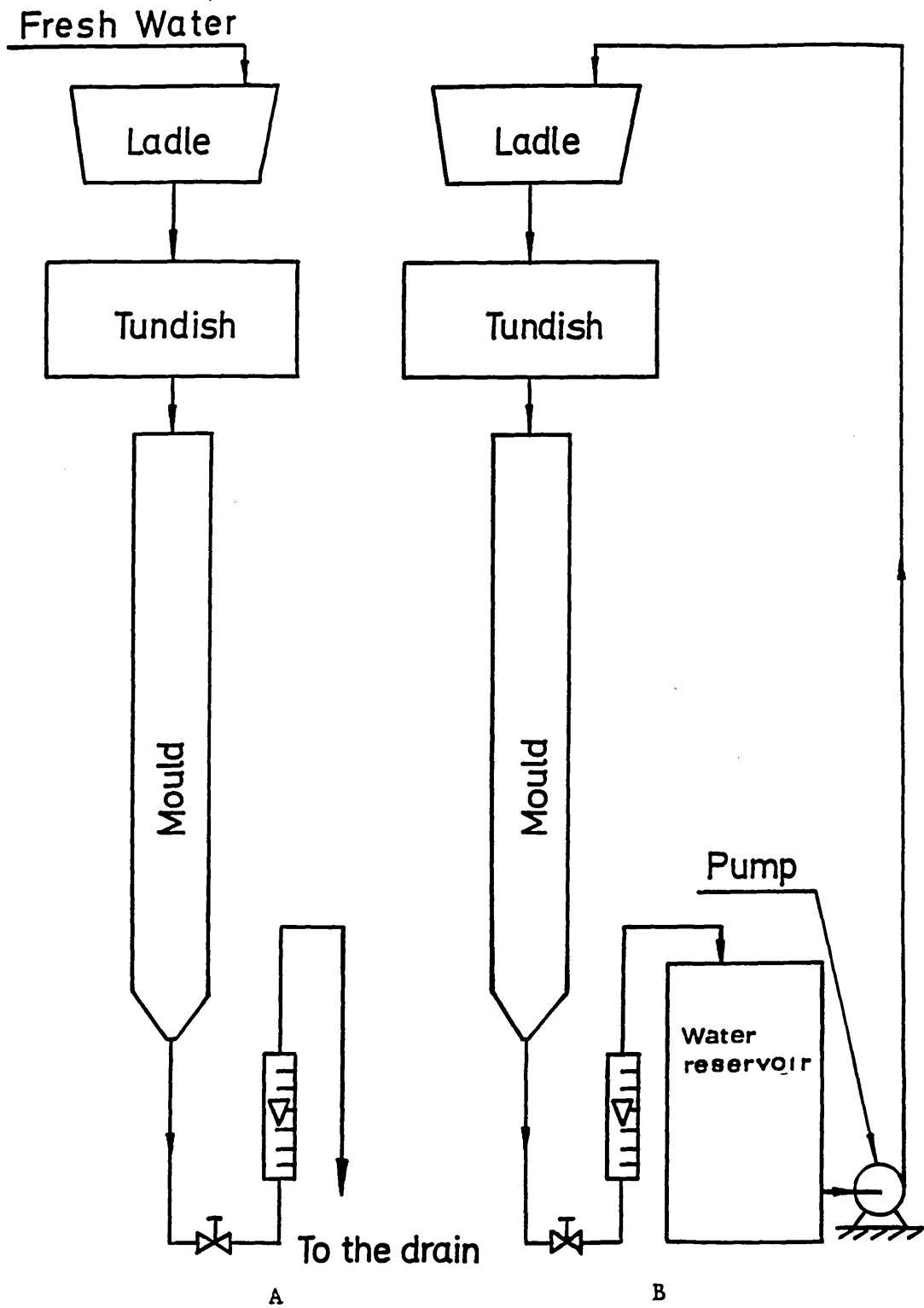


Design of submerged entry nozzle
with downward outlets. (see Table 3.3.)

TABLE 3.3. Bloom Tundish nozzle dimensions.

Dimensions	D_Z (mm)	d_Z (mm)	d_d (mm)	θ ($^\circ$)	L (mm)	Others
Nozzle 4	32	15	13	0	280	Horizontal
Nozzle 5	32	15	13	25	280	Upward
Nozzle 6	32	15	13	5	280	Upward
Nozzle 7	32	15	13	5	280	Downward
Nozzle 8	32	15	13	10	280	Downward
Nozzle 9	32	15	13	15	280	Downward
Nozzle 10	32	15	13	20	280	Downward
Nozzle 11	32	15	13	25	280	Downward

Figure 3.9



Sketches of the water flow modes employed.

A — through-flow mode,

B — recirculatory mode

pump was used to circulate the water within the model system. The through-flow mode was employed during the experiments simulating inclusion separation. In this mode, fresh water was continuously fed into the ladle, through the model system and then into the drain.

3.1.8. Control of water levels.

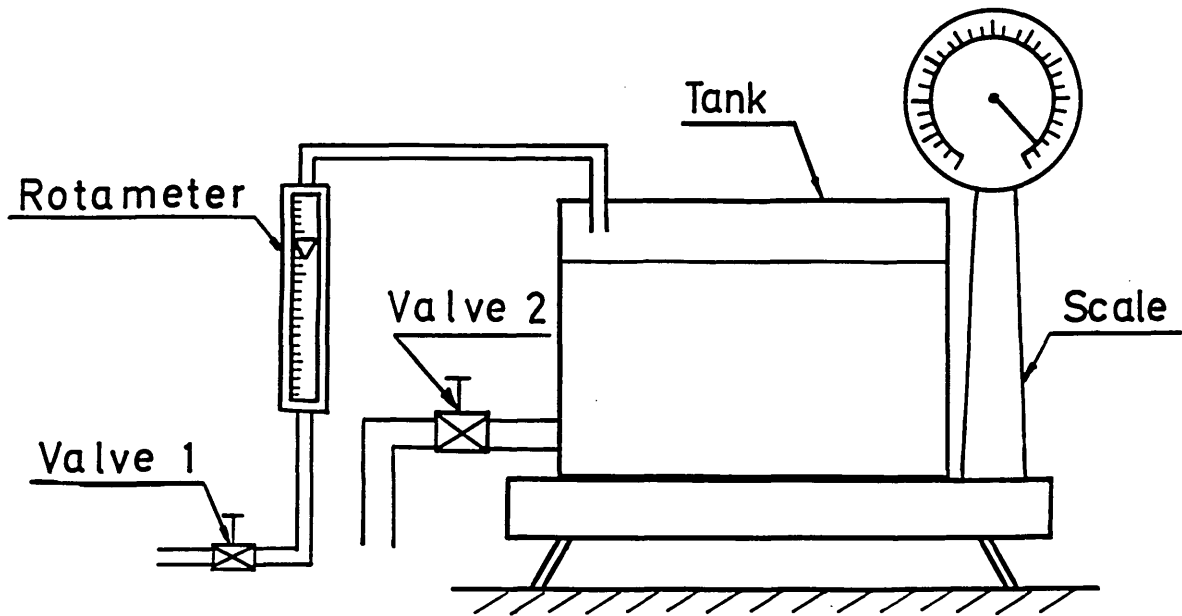
The water levels in the ladle and the tundish were controlled to be constant, thus keeping a constant water flow rate through the mould. The water level in the mould was thus easily controlled by controlling the water flow rate out of the mould. This control was provided by the valve below the mould set to a fixed position and allowed the water level in the mould to be controlled to within ± 2 mm during a typical run of 20-30 minutes.

3.1.9. Water flow rate measurement.

The water flow rate through the model system was measured by a rotameter, which was installed below the mould and after the flow control valve, as shown in figure 3.1. A rotameter 2000 made by GEC-Elliott Process Instruments Ltd, Model: Metric 47XE, was used, having a scale of graduated 0 - 27. The rotameter was calibrated using a tank, a platform scale and a stop watch, the experimental set-up being shown in figure 3.10. The calibration procedure is as follows:

- a) open valve 2;
- b) use valve 1 to set the rotameter to a certain reading;
- c) shut off valve 2;
- d) when the scale reaches a certain reading (e.g. 10 Kg),

Figure 3.10



Experimental set-up for the rotameter calibration.

- start the stop watch;
- e) when the scale reaches another reading (e.g. 25 Kg), stop the stop watch followed by opening Valve 2;
 - f) record the time and two readings from the scale;
 - g) set the rotameter to another reading and repeat steps a) to f) and use the following expression to calculate the actual flow rate.

$$\text{Actual flow rate} = \frac{W_{stop} - W_{start}}{t \rho}$$

- where: W_{start} : the scale reading when starting the stop watch;
 W_{stop} : the scale reading when stopping the stop watch;
t: the time recorded;
 ρ : density of water at room temperature.

The calibration curve such obtained is shown in figure 3.11.

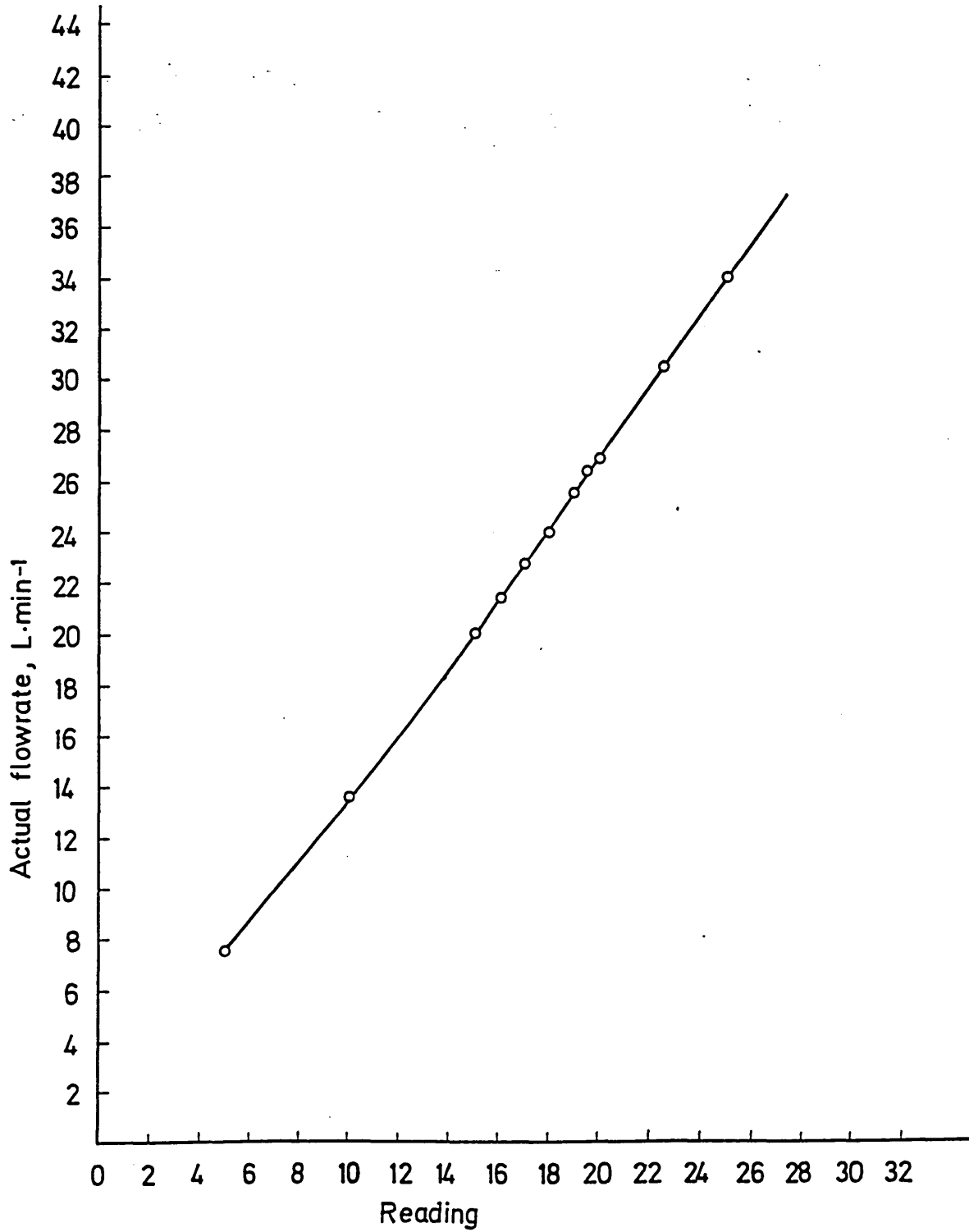
3.2. Experimental techniques for fluid flow pattern visualization.

Techniques used for visualizing the fluid flow pattern have mainly involved making additions to the water and selecting a suitable light source for visibility and clarity. These additions, termed tracers, allow the water flow patterns to be easily seen and photographically recorded.

3.2.1. Choice of tracers.

Several materials have been tried as the tracers, including plastic particles, glass microspheres, fine alumina flakes, star glitter,

Figure 3.11



Rotameter calibration curve.

Chapter 3

small air bubbles and coloured liquid. It was found that fine alumina flakes and small air bubbles gave very good and clear visualization of the fluid flow patterns and injection of coloured liquid into the entry nozzle stream gave a perfect visualization of the shape of the entry jet and of its penetration. So in the later experiments, fine alumina flakes, small air bubbles and coloured liquid were chosen as the tracers.

3.2.2. Preparation and addition of the tracers.

a) Preparation and addition of the fine alumina flakes.

15 grams of the alumina flakes were mixed with 50 ml of alcohol to make a slurry at least 10 minutes before use. This changed the surface characteristics of fine alumina flakes; otherwise they would float on the water surface instead of mixing with the water.

When fluid flow conditions in the mould reached a steady-state and the fine alumina flakes-alcohol slurry was ready to use, 15 ml of the slurry was injected into the mould by using a surgical syringe. Observations were then begun after the water had been allowed to recirculate within the model system for a further 10 minutes.

b) Preparation and addition of small air bubbles.

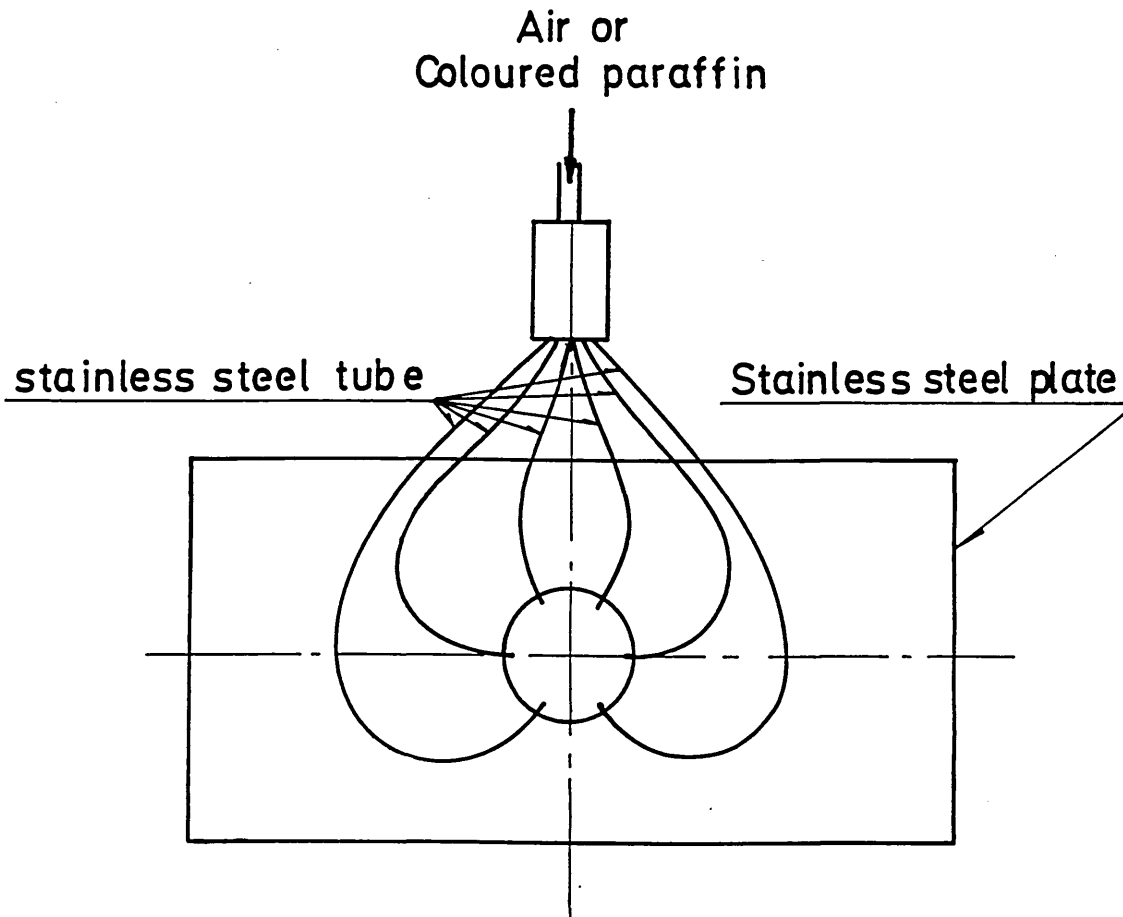
Pre-treatment was unnecessary for the air which was sucked into the entry stream from the atmosphere of the room through nozzles which were placed in the entry stream, as shown in figure 3.1. There were six nozzles altogether, formed from stainless steel small-bore tubing of internal diameter 200 μm and soldered onto a stainless steel plate to make a set of nozzles, as shown in figure 3.12. The size of the

hole on the plate exactly matched the internal diameter of the tundish nozzles given in table 3.2 and 3.3.

3.2.3. Illumination of fluid flow domain.

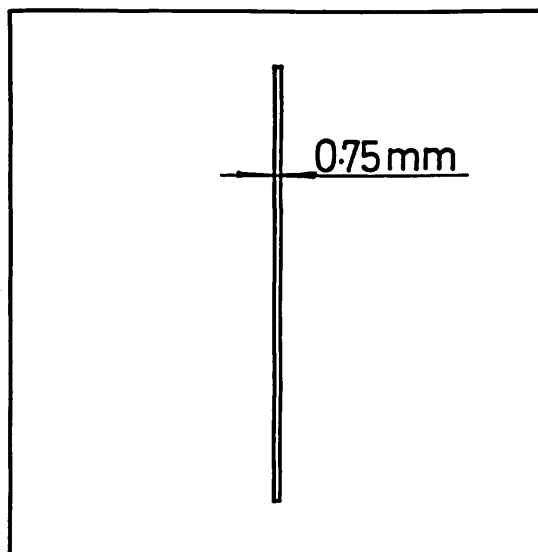
The model moulds have thickness of 140 mm and 65 mm respectively. They can, in respect to their thickness, be considered as three-dimensional models. It is obviously very difficult to view or record the fluid flow patterns three-dimensionally, so, a method must be developed that could allow two-dimensional patterns to be viewed or recorded. First the fluid flow domain must be illuminated two-dimensionally: in the present study, two slide projectors were employed with narrow slits at their planes of focus. Each slit, as shown in figure 3.13, has a width of 0.75 mm. PRADO UNIVERSAL projectors of slide size of 70 mm x 70 mm being used. By arranging the projectors, as shown in figure 3.14, a slit light band of approximate 8 mm width was obtained in the fluid flow domain in the mould. Any vertical plane within the fluid flow domain could be illuminated by moving the projectors. By turning the slit 90°, horizontal planes in the domain could also be illuminated. This allowed the fluid flow pattern developed in any plane within the mould to be observed or photographically recorded without interference from and disturbance to the rest of the domain. This method of illuminating planes in the fluid flow domain has been proved to be very successful, all the observations reported in this work being made with its aid.

Figure 3.12



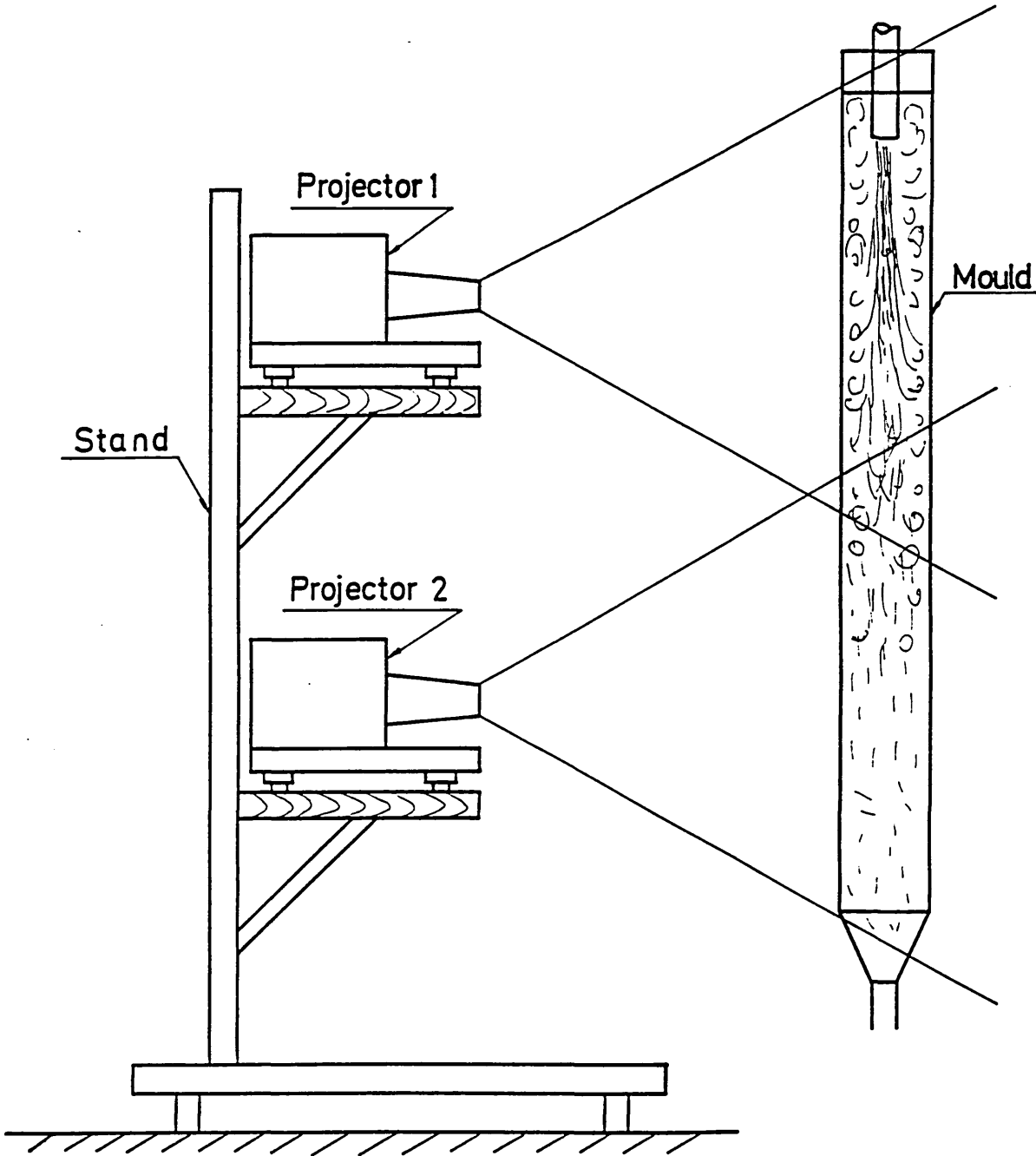
Injection nozzle set-up.

Figure 3.13



Sketches of the slide slit used in the projector.

Figure 3.14



Sketches of the plane light source arrangement.

3.2.4. Recording of the fluid flow patterns.

The fluid flow patterns were photographically recorded using a NIKON F3 camera with 50 mm lens. The aperture of the camera was set to 1.8. Three exposure settings were employed for each flow pattern, i.e. 1/8 s, 1/15 s and 1/30 s, two frames being taken at each exposure.

3.3. Experimental technique for simulating inclusion separation.

3.3.1. Introduction.

The literature survey showed that no experimental techniques have yet been developed to simulate inclusion separation in continuous casting moulds. Thus an important aspect of the present investigation is the development of a suitable method. An experimental technique had been developed after a series of careful studies and trials.

3.3.2. Method of simulation.

A colourless paraffin layer on the top of the water in the model mould together with the injection of coloured paraffin into the nozzle entry stream was used to simulate inclusion separation. After injection, the whole paraffin layer was removed as a sample. By measuring the colour change of this sample, the distribution of the injected coloured paraffin between the top layer and the exit water flow (representing the strand in continuous casting operation) was determined with the aid of a calibration curve.

3.3.3. Preparation of the coloured paraffin.

Colourless paraffin oil was coloured by organic dye, SUDAN III being

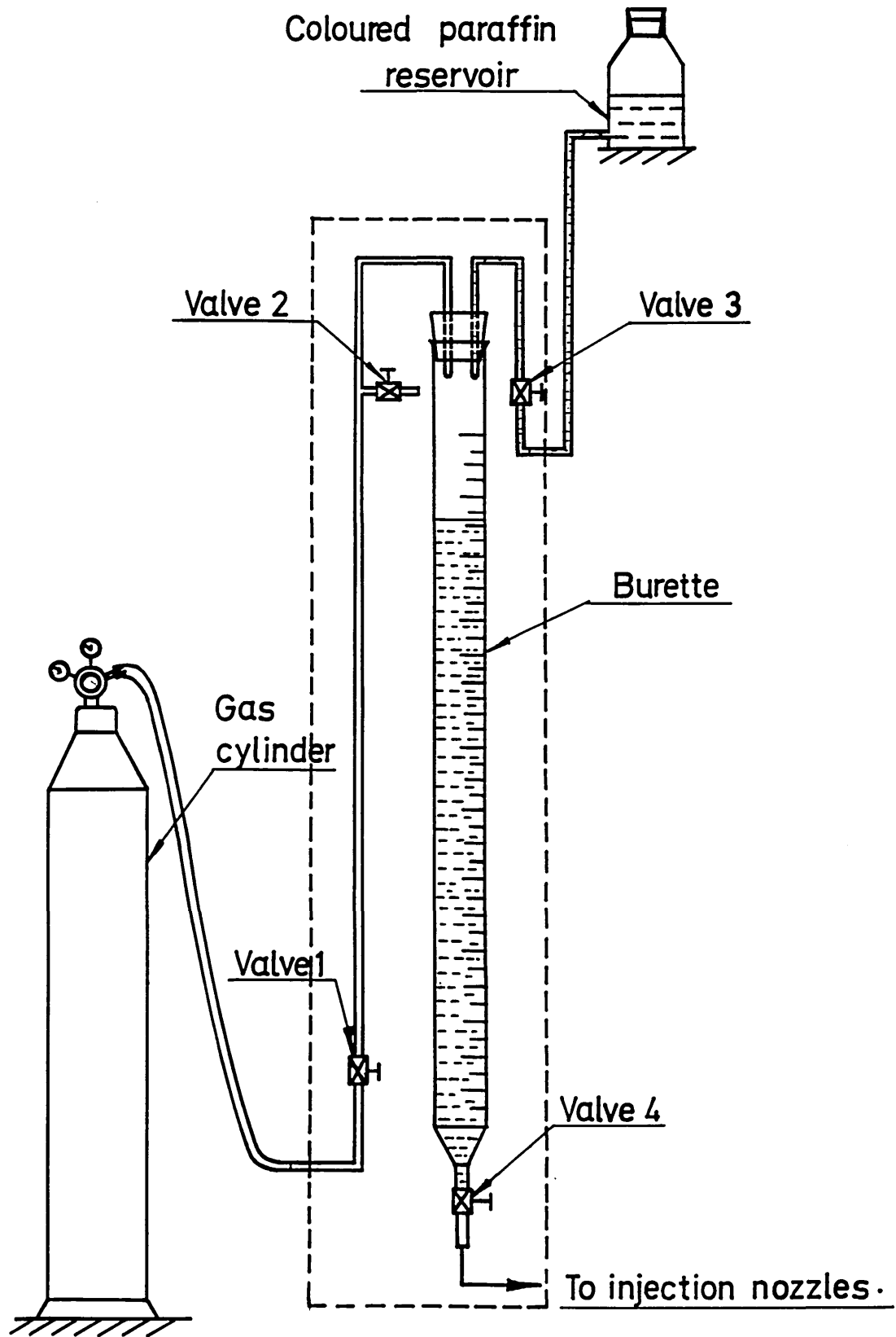
chosen as the dye after many trials. 5.9864 grams SUDAN III were dissolved in 4000 ml colourless paraffin oil. The solution was heated to 110°C for an hour to assist the dissolution process. The resulting solution, after being allowed to cool naturally, was stored in a bottle for future uses.

3.3.4. Coloured paraffin injection system.

3.3.4.1. Injection assembly.

Coloured paraffin oil was injected into the tundish nozzle using the injection system shown schematically in figure 3.15, which is a pressure-injection system. It consists of a reservoir for the coloured paraffin, a burette (acting as the measuring tube), a gas cylinder (acting as the pressure source), and valves and pipes. The bottom end of the burette was connected to the injection nozzle through a pipe. The burette and the valves were fixed onto a panel. The gas pressure from the gas cylinder was regulated to 1.8×10^6 dyne/cm² and this pressure was applied onto the surface of the paraffin in the burette. The coloured paraffin was fed into the burette from the reservoir by closing Valve 1 and Valve 4, and then opening Valve 2 and Valve 3. When the burette was filled to the desired position (usually to the zero reading), Valve 3 was closed followed by Valve 2. During the injection operation, all the valves were initially closed; Valve 1 being slowly opened to let pressure build up inside the burette. Valve 4 was then opened to force the coloured paraffin through the injection nozzles. After injection, Valve 4 was first closed followed by Valve 1, and finally Valve 2 was opened to release the pressure inside the burette.

Figure 3.15



Sketches of the coloured paraffin injection System.

3.3.4.2. Injection nozzles.

The nozzles already described in section 3.2.2. were used to inject the coloured paraffin. Two sets of nozzles have been employed in the present investigation. The first set of nozzles is made of 6 large capillary stainless tubes having a inside diameter of 0.200 mm and a outside diameter of 0.410 mm, and termed as 'big injection nozzle'. The second set of nozzles is made of 10 smaller stainless tubes of inside diameter of 0.127 mm and outside diameter of 0.229 mm, and therefore termed as 'small injection nozzle'.

3.4. Analytical techniques.

The technique used for analysing the samples from the inclusion separation simulation experiment will be described in the following section.

3.4.1. Analytical equipment.

The samples were analysed colorimetrically. A spectrophotometer made by Phillips Scientific Ltd, model: PU8625 UV/VIS was employed, this instrument being capable of single beam absorptiometric measurements within the wavelength range 195 to 1100 nm. Measurements can be obtained in absorbance, transmission and concentration modes with the liquid crystal display of the readings. The absorbance mode was found to be suitable for the current investigation. All of the measurements were therefore carried out in the absorbance mode.

3.4.2. Sampling technique.

After each experiments, the paraffin layer on the top of water in the

mould was sucked out using the suction system illustrated in figure 3.16. A vacuum was created within the sampling bottle using a vacuum pump. A sampling probe made of glass was connected to the bottle through a piece of rubber tube. By carefully moving the sampling probe on the surface of liquid layer in the mould, the whole paraffin layer could be sucked into the bottle although with a certain amount of water. The liquid was left in the bottle for a period to allow the paraffin to separate from the water, samples of paraffin being subsequently decanted.

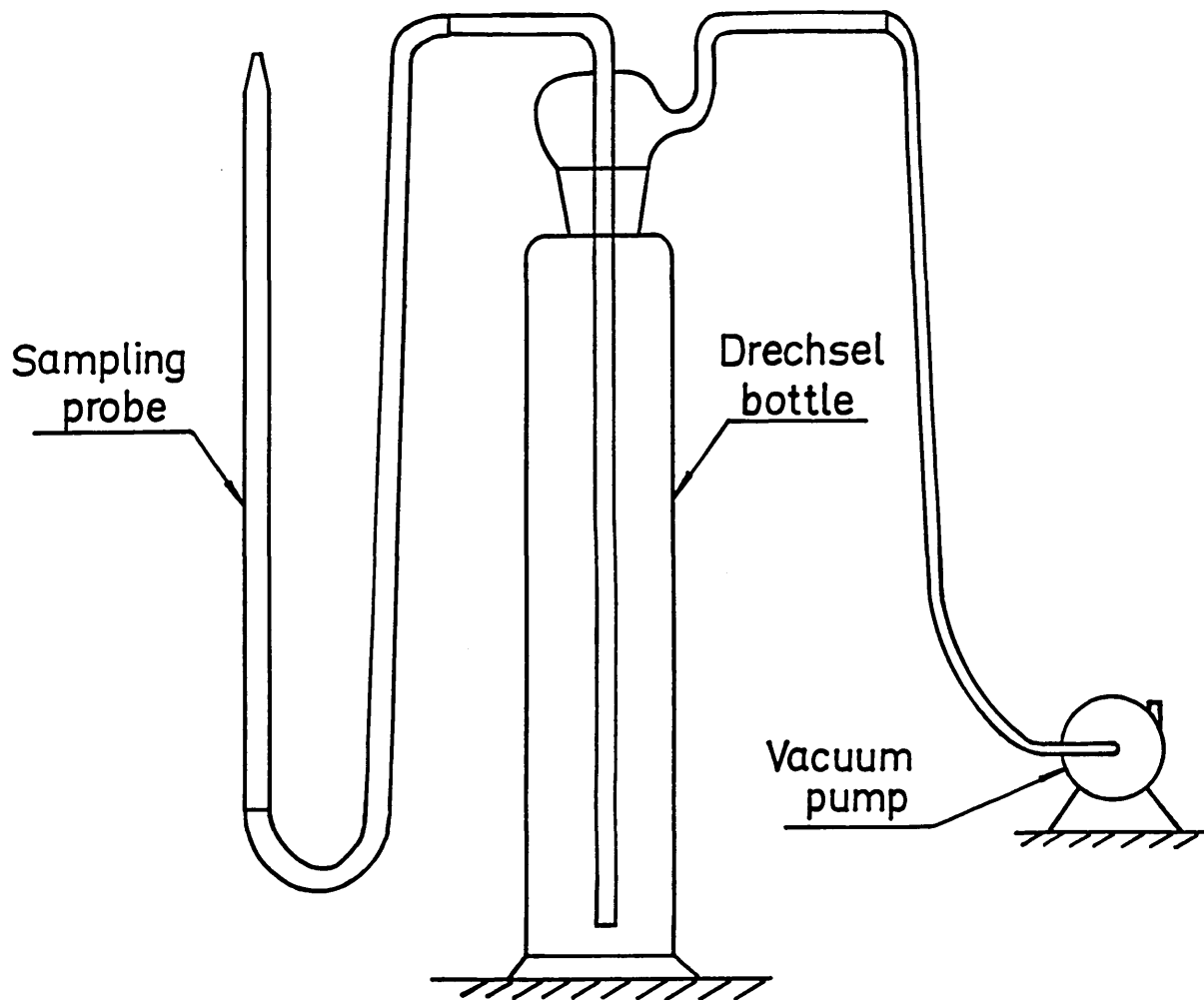
3.4.3. Sample preparation.

The samples taken from the sampling bottle were slightly opaque due to the presence of fine water droplets. These droplets had to be removed before absorbance measurements could be made with the spectrophotometer. Two methods were tried: samples were left for about ten days to allow the water to settle to the bottom, and, alternatively, samples were heated up to 110-120°C for two hours to remove the water. Experiments were conducted to check whether heating in this temperature range affected the colour of the samples. The data obtained, table 3.4, showed that the heating process had no effect on the colour of the samples, so this heating method is the one that has been used to pre-treat the samples.

3.4.4. Calibration curve.

In order to determine how much of the coloured paraffin had entered the top layer, the calibration curve, shown in figure 3.17, was obtained by measuring the absorbance of a series of samples

Figure 3.16



Sketches of the sample suction system.

TABLE 3.4. Effect of heating process on the colour changes of the samples.

Sample No	Absorbance at wavelength of 530 nm									
	Before heating					After heating				
	X ₁	X ₂	X ₃	X	X ₁	X ₂	X ₃	X		
C1	0.063	0.062	0.063	0.063	0.062	0.063	0.063	0.063	0.063	0.063
C2	0.095	0.096	0.096	0.096	0.095	0.095	0.096	0.096	0.095	0.095
C3	0.118	0.119	0.118	0.118	0.118	0.118	0.118	0.118	0.118	0.118
C4	0.151	0.154	0.152	0.152	0.151	0.152	0.152	0.152	0.152	0.152
C5	0.171	0.173	0.171	0.172	0.172	0.171	0.171	0.171	0.171	0.171
C6	0.217	0.217	0.217	0.217	0.217	0.217	0.217	0.217	0.217	0.217
C7	0.282	0.282	0.282	0.282	0.282	0.282	0.282	0.282	0.282	0.282
C8	0.329	0.329	0.329	0.329	0.329	0.329	0.329	0.329	0.329	0.329
C9	0.411	0.411	0.411	0.411	0.411	0.411	0.411	0.411	0.411	0.411
C10	0.512	0.511	0.514	0.512	0.511	0.514	0.512	0.512	0.511	0.512
C11	0.781	0.785	0.785	0.784	0.782	0.783	0.782	0.782	0.782	0.782
C12	1.00	1.00	1.00	1.00	1.00	0.998	1.00	1.00	0.998	0.999

Figure 3.17

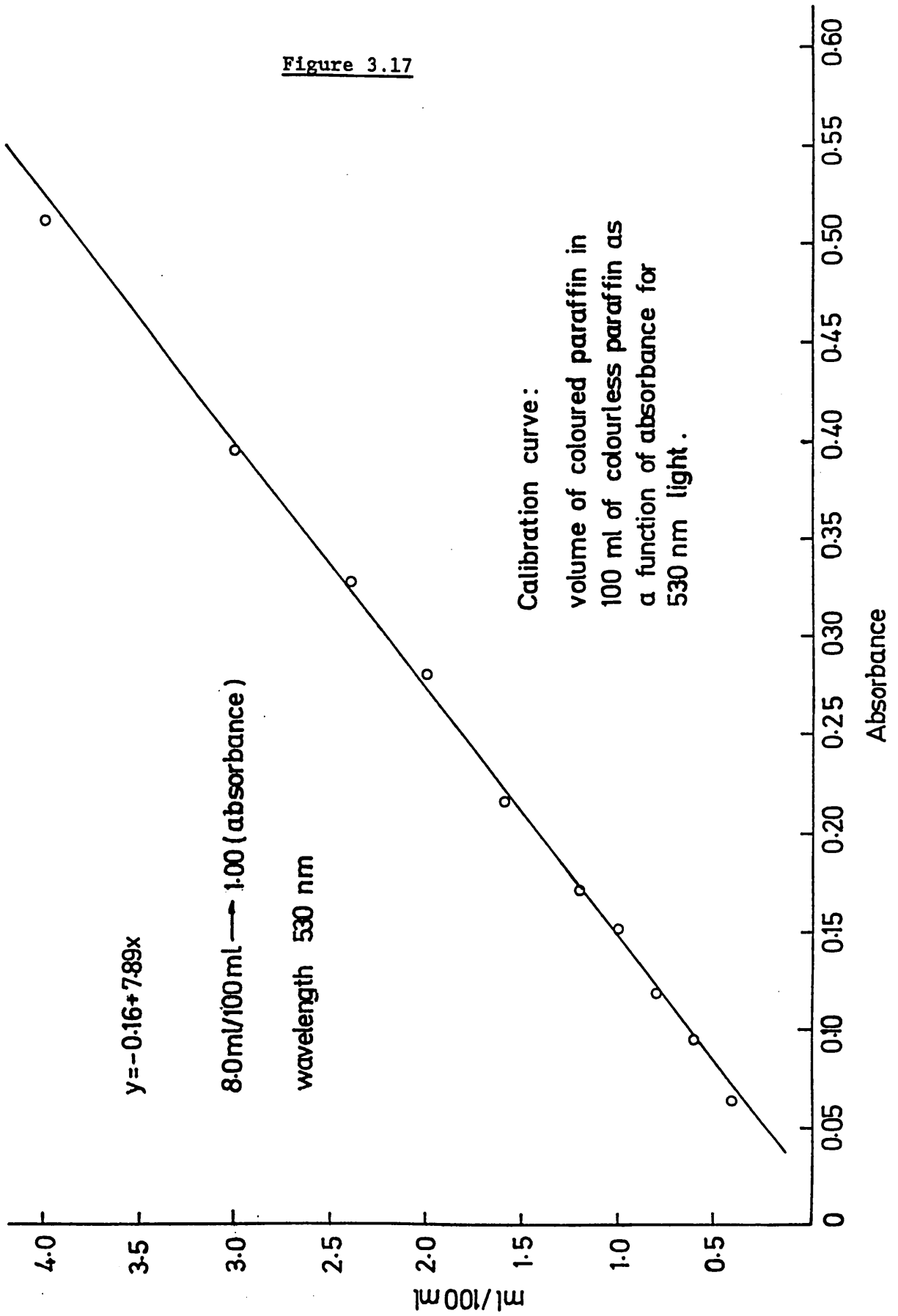


TABLE 3.5. Calibration Data.

Sample No.	Volume of coloured paraffin in 100 ml colourless paraffin	Absorbance at wavelength of 530 nm			
		X ₁	X ₂	X ₃	X
C1	0.40	0.063	0.062	0.063	0.063
C2	0.60	0.095	0.096	0.096	0.096
C3	0.80	0.118	0.119	0.118	0.118
C4	1.00	0.151	0.154	0.152	0.152
C5	1.20	0.171	0.173	0.171	0.172
C6	1.60	0.217	0.217	0.217	0.217
C7	2.00	0.282	0.282	0.282	0.282
C8	2.40	0.329	0.329	0.329	0.329
C9	3.00	0.411	0.411	0.411	0.411
C10	4.00	0.512	0.511	0.514	0.512
C11	6.00	0.781	0.785	0.785	0.784
C12	8.00	1.00	1.00	1.00	1.00

containing known quantities of the coloured paraffin added to 100 ml of the colourless paraffin. The wavelength of the instrument was set to 530 nm, at which wavelength the absorbance of a sample containing 8.0 ml of the coloured paraffin in 100 ml of the colourless paraffin was 1.00. All the data obtained about the calibration curve are given in table 3.5.

3.4.5. Absorbance analyses.

The absorbance analyses of the samples were carried out on the spectrophotometer described in section 3.4.1., the operating instructions given in the instrument menu being followed. With the wavelength set to 530 nm, the colourless paraffin was used as the reference solution. Before analysing the samples, calibration samples were used to test and calibrate the instrument. Three readings were taken for each sample.

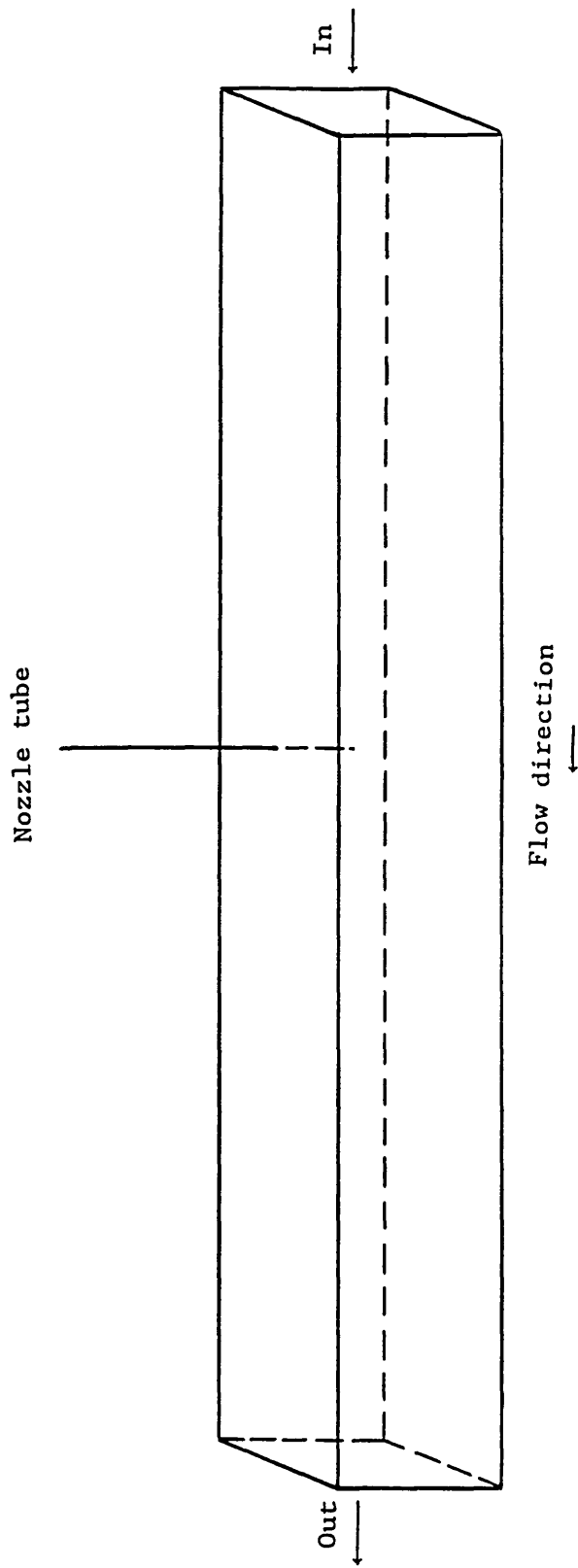
3.5. Experimental technique for measuring inclusion particle sizes.

The technique used to measure particle diameters just as they were being generated from the nozzle tube has mainly involved the photography of the nozzle tip area with the aid of a micro-flash.

A square tube made of perspex with an inner section size of 12 mm x 12 mm and a length of 300 mm, as shown in figure 3.18, was used in the measurement of particle diameters. A piece of stainless tube of the same size as the injection nozzles was placed in the middle point of the middle section of the perspex tube. Coloured paraffin was injected through the stainless tube into the perspex tube using the injection system that was used in the inclusion removal experiments -

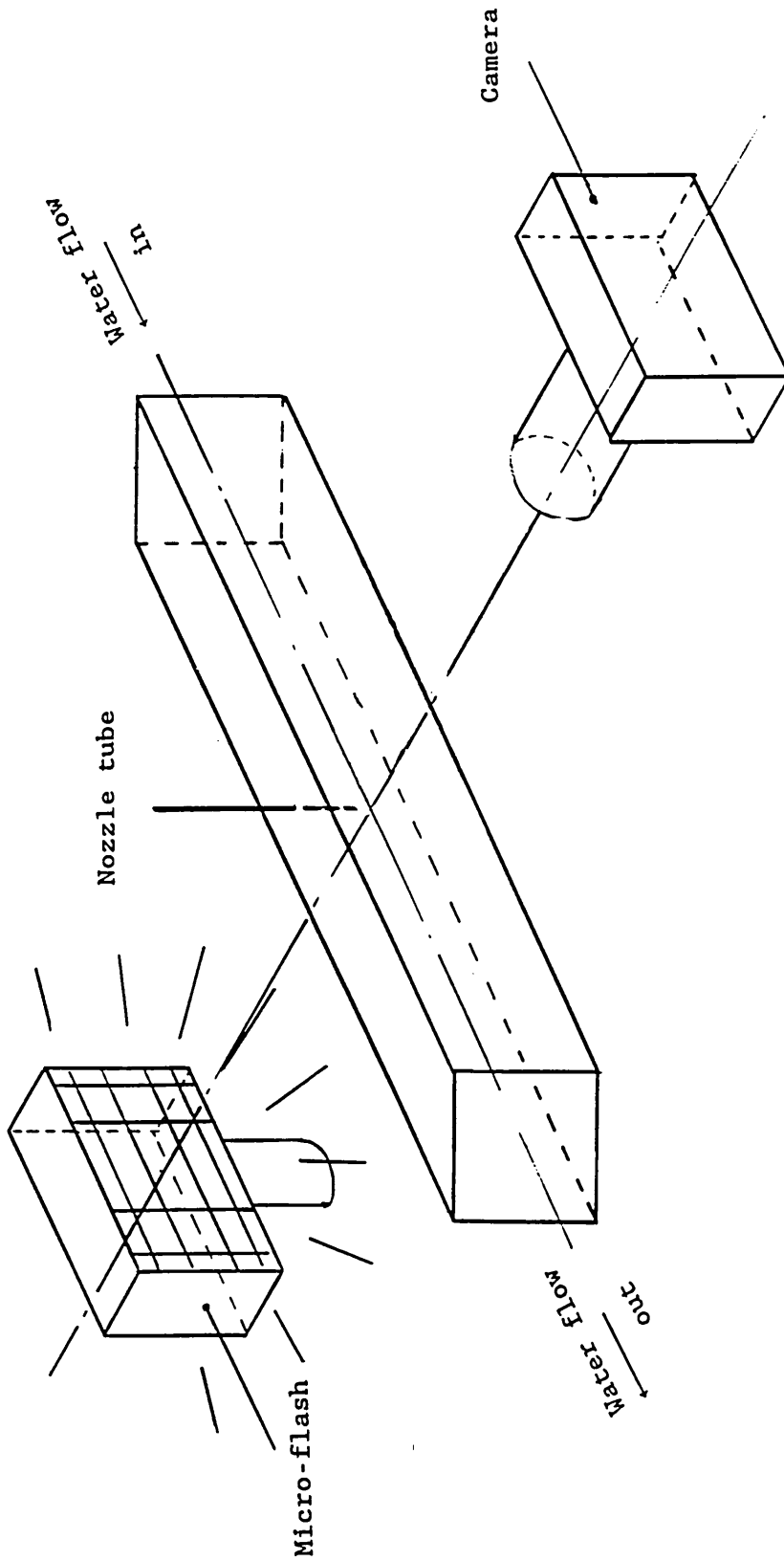
see section 3.3.4, operated at the same injection pressure. Water was caused to flow through the perspex tube at a velocity of 1.43 m.min^{-1} - identical to the velocity at which the water flowed past the injection nozzles in the bloom caster model system. Pictures were taken of the views of the tip area of the stainless tube with the aid of the micro-flash. Two arrangements were used for taking pictures. The first arrangement, as shown in figure 3.19, provided a general view of the nozzle tip area, pictures being taken directly using a standard camera lens. The second arrangement, as shown in figure 3.20, provided a close-up view, in which the pictures were taken through a microscope. The value of the magnification factor was not important in either arrangement, since the particle size could be measured by reference to the known outer diameter of the stainless tube. The particle diameters were measured by projecting negatives obtained using the standard camera lens onto a screen and making direct measurements.

Figure 3.18



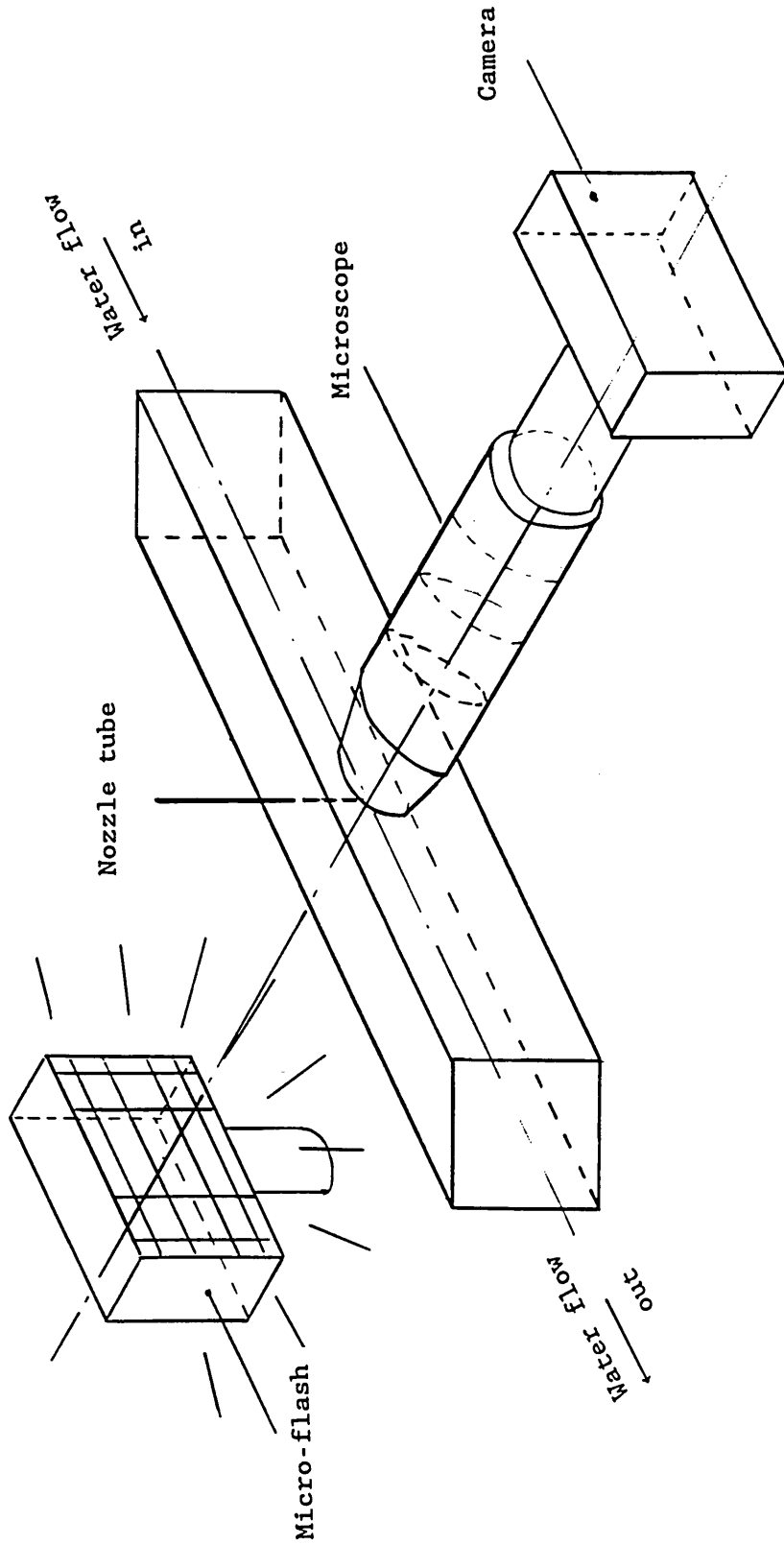
Sketch of the tube assembly for viewing the particle generation

Figure 3.19



Experimental arrangement for general viewing

Figure 3.20



Experimental arrangement for close-up viewing

4. THEORETICAL DEVELOPMENT

4.1. Inclusion mass transfer coefficient at the meniscus surface
incorporating the effect of Stokes rise.

4.1.1. Introduction.

Inclusions, being less dense than liquid steel, experience a buoyancy force causing them to rise towards the steel surface. Relative accelerations between inclusions and the liquid steel are fully damped out because small size of inclusions, so friction effects dominate over inertial effects. Therefore, only velocity difference between inclusions and the liquid steel due to balance between gravity driven buoyancy force and friction force is normally considered. The velocity at which inclusions rise relatively to the liquid steel is determined by a balance between this buoyancy force and the drag force:-

$$[V_{St}]_d = \frac{D_p^2 (\rho_S - \rho_p) g}{18 \mu_s f(Re)} \quad (4.1)$$

where: $[V_{St}]_d$: relative rising velocity of inclusion whose diameter is D_p , m.s⁻¹;

D_p : diameter of inclusion particle, m;

ρ_S : density of liquid steel Kg.m⁻³;

ρ_p : density of inclusion, Kg.m⁻³

g : gravitational acceleration, m.s⁻²;

μ_s : viscosity of liquid steel, N.s.m⁻²;

where $f(Re)$ can be taken as unity if the inclusions are assumed to

obey Stokes Law. This assumption will be made throughout this work so that $f(\text{Re})$ is set equal to one, and the velocity predicted by equation (4.1) will be termed the 'Stokes rise' velocity.

Inclusions will also be transported to the steel surface through the action of the turbulent mixing in the liquid steel resulting from the random motion of turbulent eddies. The scale of the eddies is considerable greater than the inclusion size, so that inclusion mixing will be the summation of a series of individual translations over random finite steps. Mathematically, this is the same process as molecular diffusion and can therefore be described by Fick's first law of diffusion:-

$$\dot{m}_d'' = -\rho_S D_T \left[\frac{\partial f_d}{\partial y} \right]_{y=0} \quad (4.2)$$

where: \dot{m}_d'' : mass flux of inclusions whose diameters are D_p ,
Kg.m⁻².s⁻¹;

ρ_S : density of liquid steel Kg.m⁻³;

D_T : turbulent diffusivity, m².s⁻¹;

f_d : mass fraction of inclusions whose diameters are D_p in the liquid steel;

$\left[\frac{\partial f_d}{\partial y} \right]_{y=0}$: mass fraction gradient of inclusions at the steel meniscus, m⁻¹;

The suffix 'd' in the above equation and the following equations denotes that the equations are to be applied to inclusions whose diameter is D_p .

4.1.2. Transport equations and boundary conditions

The steel flow field in the sump includes a bulk flow of steel across the meniscus from the walls of the mould towards the submerged entry nozzle. On a scale that is small compared with the overall dimensions of the flow field but large compared with the scale of turbulence, we can assume that the inclusion mass fraction within the horizontal bulk flow immediately below the steel meniscus will obey the diffusion equation:-

$$D_T \frac{\partial^2 f_d}{\partial y^2} + [V_{St}]_d \frac{\partial f_d}{\partial y} = \frac{\partial f_d}{\partial \tau} \quad (4.3)$$

where the equation has been written down in relation to a co-ordinate system travelling horizontally across the steel meniscus with each bulk steel flow packet, directions downwards into the liquid steel being taken as positive. The time, τ , in equation (4.3) is the time for which a flow packet has been exposed to the surface.

If we assume that inclusions arriving at the steel surface are immediately absorbed by the molten flux, we can assume that their mass fraction at the surface is zero so that the boundary conditions for the solution of equation (4.3) are:-

$$\tau > 0 ; y = 0 : f_d = 0 \quad (4.4)$$

$$\tau = 0 ; y > 0 : f_d = [f_d]_R \quad (4.5)$$

$$\tau > 0 ; y \rightarrow \infty : f_d = [f_d]_R \quad (4.6)$$

$[f_d]_R$ in equations (4.5) and (4.6) is the mass fraction of inclusions of diameter D_p in the recirculation region above the submerged entry nozzle. The equations assume that each bulk volume packet of liquid steel contains this average content of inclusions at the moment it starts its traverse of the steel meniscus. At this same moment, the inclusion content at the surface is reduced to zero - equation (4.4) - and inclusions are thereafter brought to the steel surface by a combination of Stokes rise and turbulent diffusion.

4.1.3. Solution of transport equations

Solution^[97] of the diffusion equation over a length scale that is small compared with the dimensions of the flow field but large compared with the scale of the turbulence gives the inclusion mass fraction in the flow packet during the time of its passage across the steel meniscus as:-

$$f_d = [f_d]_R - [f_d]_R/2 \left\{ \operatorname{erfc} \left[\frac{y + [V_{St}]_d \tau}{\sqrt{(4D_T \tau)}} \right] + \exp \left[\frac{-[V_{St}]_d y}{D_T} \right] \operatorname{erfc} \left[\frac{y - [V_{St}]_d \tau}{\sqrt{(4D_T \tau)}} \right] \right\} \quad (4.7)$$

Evaluating the differential of this equation at the surface gives:-

$$\frac{1}{[f_d]_R} \left[\frac{\partial f_d}{\partial y} \right]_{y=0} = \frac{\exp[-[V_{St}]_d^2 \tau / (4D_T)]}{\sqrt{(\pi D_T \tau)}} + \frac{[V_{St}]_d}{D_T} - \frac{[V_{St}]_d}{2D_T} \operatorname{erfc} \left[\frac{[V_{St}]_d \tau}{\sqrt{(4D_T \tau)}} \right] \quad (4.8)$$

so that equation (4.2) gives the diffusion flux as:-

$$\frac{-\dot{m}_d}{\rho_S [V_{St}]_d [f_d]_R} = \frac{\sqrt{[D_T/(\pi r)]}}{[V_{St}]_d} \exp\left[\frac{-[V_{St}]_d^2 r}{4D_T}\right] + 1 - \frac{1}{2} \operatorname{erfc}\left[\frac{[V_{St}]_d \sqrt{r}}{\sqrt{4D_T}}\right] \quad (4.9)$$

where the minus sign before the flux appears because directions downwards into the steel are taken as positive.

The following limiting values from equation (4.9) are worth noting:-

$$\lim_{V_{St} \rightarrow 0} \left[\frac{-\dot{m}_d}{\rho_S [f_d]_R} \right] = \sqrt{D_T/(\pi r)} \quad (4.10)$$

$$\lim_{D_T \rightarrow 0} \left[\frac{-\dot{m}_d}{\rho_S [f_d]_R} \right] = [V_{St}]_d \quad (4.11)$$

Equation (4.10) is the flux predicted by the penetration theory of mass transfer, in which diffusion is the only transport mechanism, and equation (4.11) gives the flux brought about by Stokes' rise alone.

4.1.4. Average inclusion diffusion flux

Equations (4.9) to (4.11) give the flux from any given fluid packet at a specific moment during the period of its exposure at the steel meniscus. If we assume that the flow field is steady, this moment

will correspond to a fixed position on the surface allowing the average flux from the surface to be evaluated as:-

$$\frac{-\tau_e \bar{m}_d''}{\rho_S [V_{St}]_d [f_d]_R} = \int_0^{\tau_e} \left\{ \frac{\sqrt{[D_T/(\pi r)]}}{[V_{St}]_d} \exp\left[\frac{-[V_{St}]_d^2 r}{4D_T}\right] + 1 - \frac{1}{2} \operatorname{erfc}\left[\frac{[V_{St}]_d \sqrt{r}}{\sqrt{4D_T}}\right] \right\} dr \quad (4.12)$$

where τ_e is the total time for which a fluid packet is exposed at the steel meniscus - equal to the average length of the fluid path across the surface divided by the average surface velocity.

Evaluation of equation (4.12) is most conveniently carried out in relation to a dimensionless exposure time defined as:-

$$\tau_e^* = \frac{[V_{St}]_d^2 \tau_e}{D_T} \quad (4.13)$$

In addition, the integration variable, $\psi = \frac{1}{2}\sqrt{[\tau_e^* \cdot r / \tau_e]}$, aids formulation of the integral, allowing equation (4.12) to become:-

$$\frac{-\bar{m}_d''}{\rho_S [V_{St}]_d [f_d]_R} = \frac{4}{\tau_e^*} \int_0^{\frac{1}{2}\sqrt{\tau_e^*}} \left\{ \frac{\exp(-\psi^2)}{\sqrt{\pi}} + 2\psi - \psi \operatorname{erfc}(\psi) \right\} d\psi \quad (4.14)$$

which, on integration, gives:-

$$\frac{-\overline{\dot{m}}_d''}{\rho_S [V_{St}]_d [f_d]_R} = \frac{2}{\tau_e^*} \operatorname{erf}\left(\frac{1}{2}\sqrt{\tau_e^*}\right) + 1 - \frac{4}{\tau_e^*} \int_0^{\frac{1}{2}\sqrt{\tau_e^*}} \left[\psi \cdot \operatorname{erfc}(\psi) \right] d\psi \quad (4.15)$$

The final integral in equation (4.15) cannot be evaluated analytically. As a later section demonstrates, the contribution that it makes to equation (4.15) is always relatively minor, however, so that at a level of analysis appropriate to the semi-quantitative treatment that the available data will support, we can write:-

$$\overline{\dot{m}}_d'' = \rho_S [V_{St}]_d [f_d]_R \left[(2/\tau_e^*) \operatorname{erf}\left(\frac{1}{2}\sqrt{\tau_e^*}\right) + 1 \right] \quad (4.16)$$

where minus sign has been omitted to denote that the mass flux of inclusions is the rate at which they are being removed through the meniscus.

4.1.5. Effective mass transfer coefficient for inclusion removal

Inclusions are removed from a steel packet to the meniscus through the action of eddy diffusion and Stokes rise. This is a mass transfer process and could be represented by an equation of the form:-

$$\overline{\dot{m}}_d'' = \rho_S \alpha_d ([f_d]_R - [f_d]_m) \quad (4.17)$$

where: $\overline{\dot{m}}_d''$: average inclusion removal flux
 α_d : effective mass transfer coefficient for the removal of inclusions of diameter D_p to the

meniscus

ρ_S : density of liquid steel

$[f_d]_R$: mass fraction of inclusions of diameter D_p in the recirculation region above the submerged entry nozzle

$[f_d]_m$: mass fraction of inclusions of diameter D_p at the meniscus surface

According to the assumptions made in Section 4.1.2 $[f_d]_m$ could be taken as zero, i.e. $[f_d]_m = 0$. Therefore equation (4.17) becomes:-

$$\bar{m}_d'' = \rho_S \alpha_d ([f_d]_R) \quad (4.18)$$

Equations (4.16) and (4.18) allow us to define the effective mass transfer coefficient for the removal of inclusions of diameter D_p to the meniscus surface:-

$$\alpha_d = \frac{\bar{m}_d''}{\rho_S [f_d]_R} = [V_{St}]_d \left[(2/r_e^*) \operatorname{erf}(\frac{1}{2} r_e^*) + 1 \right] \quad (4.19)$$

Examining the limits of equation (4.19) for complete diffusion control and for complete Stokes rise control allows us to assess the effect of omitting the final integral in the equation (4.15). Using the series expansion for the error function:-

$$\operatorname{erf}(x) = \frac{2}{\sqrt{\pi}} \left[x - \frac{x^3}{3.1!} + \frac{x^5}{5.2!} - \frac{x^7}{7.3!} + \dots \right] \quad (4.20)$$

allows the value of the mass transfer coefficient resulting from diffusion alone to be derived as:-

$$\lim_{[V_{St}]_d \rightarrow 0} [\alpha_d] = \sqrt{[4D_T/(\pi\tau_e)]} \quad (4.21)$$

which is the result to be expected from the penetration theory.

Since $\operatorname{erf}(\infty) = 1$, the limiting value of equation (4.19) in the absence of effects due to turbulent diffusion, is:-

$$\lim_{D_T \rightarrow 0} [\alpha_d] = [V_{St}]_d \quad (4.22)$$

which is the result to be expected from Stokes rise alone.

Thus equation (4.19) behaves at its limits in the manner to be expected — further confirming that the omission of the final integral in equation (4.15) produces no significant error.

Accurate data from which the parameters in equation (4.19) can be evaluated are not available but it is nevertheless useful to consider order of magnitude values of $[V_{St}]_d$, τ_e^* and α_d as functions of inclusion size. Plots showing these functions for alumina inclusions in steel and simulated paraffin inclusion in water are plotted in

figure 4.1 for a range of conditions corresponding to this work.

The ordinate used in the figure is the diameter of the simulated paraffin inclusions, the equivalent diameter of alumina inclusions in steel being defined as:-

$$[D_p]_S = \left[\frac{\mu_S(\rho_W - \rho_P)}{\mu_W(\rho_S - \rho_A)} \right]^{\frac{1}{2}} [D_p]_W = 0.6[D_p]_W \quad (4.23)$$

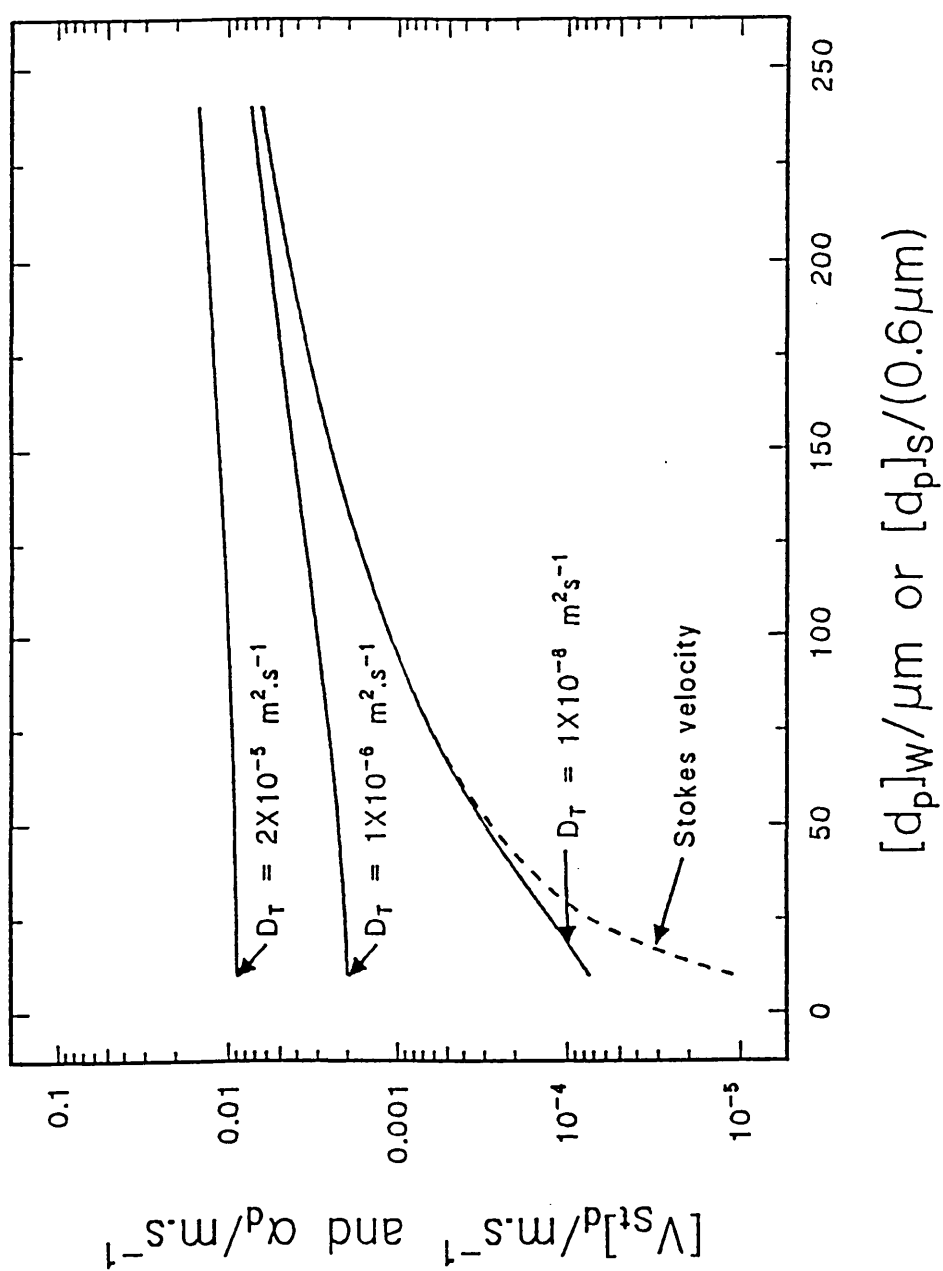
The value of the exposure time used to plot the data in the figure — 0.32 — has been calculated on the assumption that the surface velocity is about 15% of the nozzle exit velocity, this fraction having been estimated from the computer simulation of Thomas, Mika and Najjar^[98]. This simulation was carried out for a bifurcated nozzle, the exit stream directions of which are close to the horizontal. The value of 15% is therefore likely to over-estimate surface velocities in the billet caster in which the nozzle exit stream is directed vertically downwards.

Values of the effective turbulent diffusivity are more difficult to estimate than values of the surface velocity. The computer simulation of Thomas et al use the $K-\epsilon$ model to estimate the turbulent component of the effective diffusivity, and the value of this component can be used to estimate the turbulent diffusivity:-

$$D_T = C_\mu K^2 / \epsilon \quad (4.24)$$

where the standard^[68] value of 0.09 is taken for the empirical constant C_μ , K is the turbulent kinetic energy, and ϵ is its rate of

Figure 4.1



Stokes velocity and mass transfer coefficients as a function of inclusion size.

dissipation. Thomas, Mika and Najjar only present values of K and ϵ for the nozzle stream, these values giving a diffusion coefficient of about $6.3 \times 10^{-4} \text{ m}^2 \cdot \text{s}^{-1}$. Turbulence levels at the surface will be very much less, indeed the surface flow might even appear laminar in nature for the billet caster with deep penetration. For this reason, the curves in figure 4.1 have been calculated for three diffusion coefficient values:-

a 'laminar' diffusion coefficient: $D_T = 1 \times 10^{-8} \text{ m}^2 \cdot \text{s}^{-1}$

a low value 'turbulent' diffusion coefficient: $D_T = 1 \times 10^{-6} \text{ m}^2 \cdot \text{s}^{-1}$

a high value 'turbulent' diffusion coefficient: $D_T = 2 \times 10^{-5} \text{ m}^2 \cdot \text{s}^{-1}$

The effective 'laminar' diffusion coefficient is the molecular diffusion coefficient which has roughly the same value for both liquid steel and water. A single value can also be used for the turbulent diffusion coefficient since both liquids have very similar values of kinematic viscosity.

For the removal of large inclusions, however, diffusion will play a relatively minor role so that r_e^* , defined by equation (4.13) will be a large number. The error function in equation (4.16) will be close to unity and we can write the flux as:-

$$\bar{m}_d'' = \rho_S [V_{St}]_d [f_d]_R \left[1 + 2/r_e^* \right] \quad (4.25)$$

This equation is easier to use in the analysis of the experimental results and is accurate to better than 5% for values of r_e^* greater than 4. Thus the mass transfer coefficient for combined Stokes rise

and turbulent diffusion is:-

$$\alpha_d = [V_{St}]_d \left[1 + 2/r_e^* \right] \quad (4.26)$$

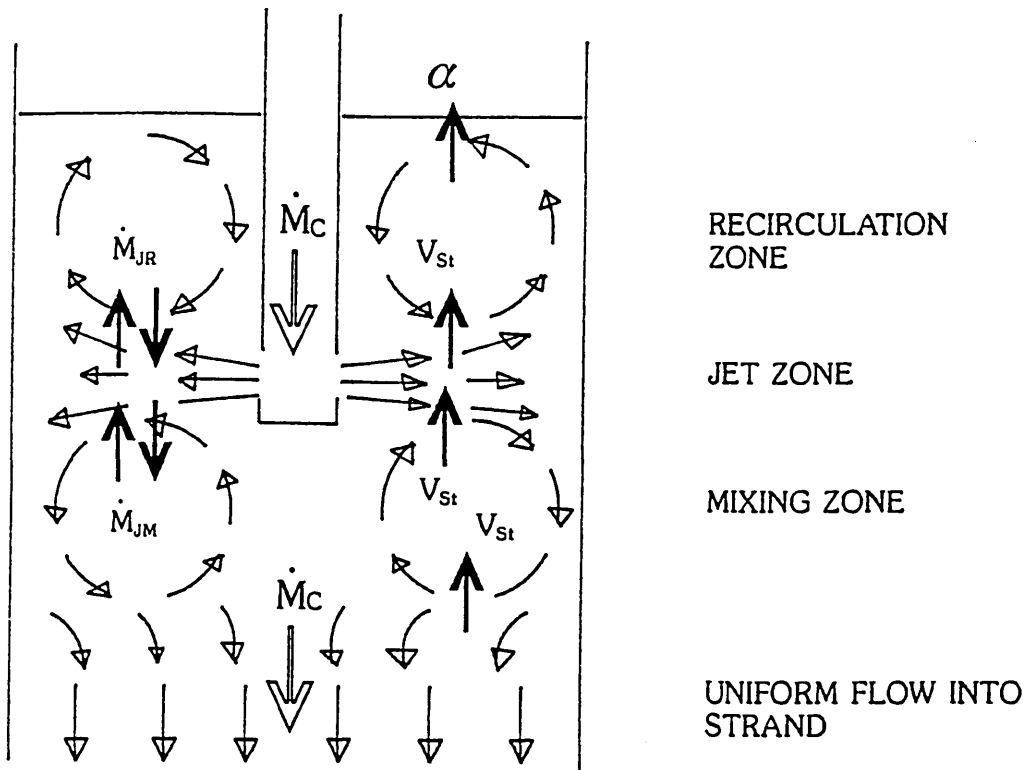
This equation will be used later in analysis the experimental results.

4.2. Zonal sump flow model used to analyse inclusion removal.

4.2.1. Description of the flow field

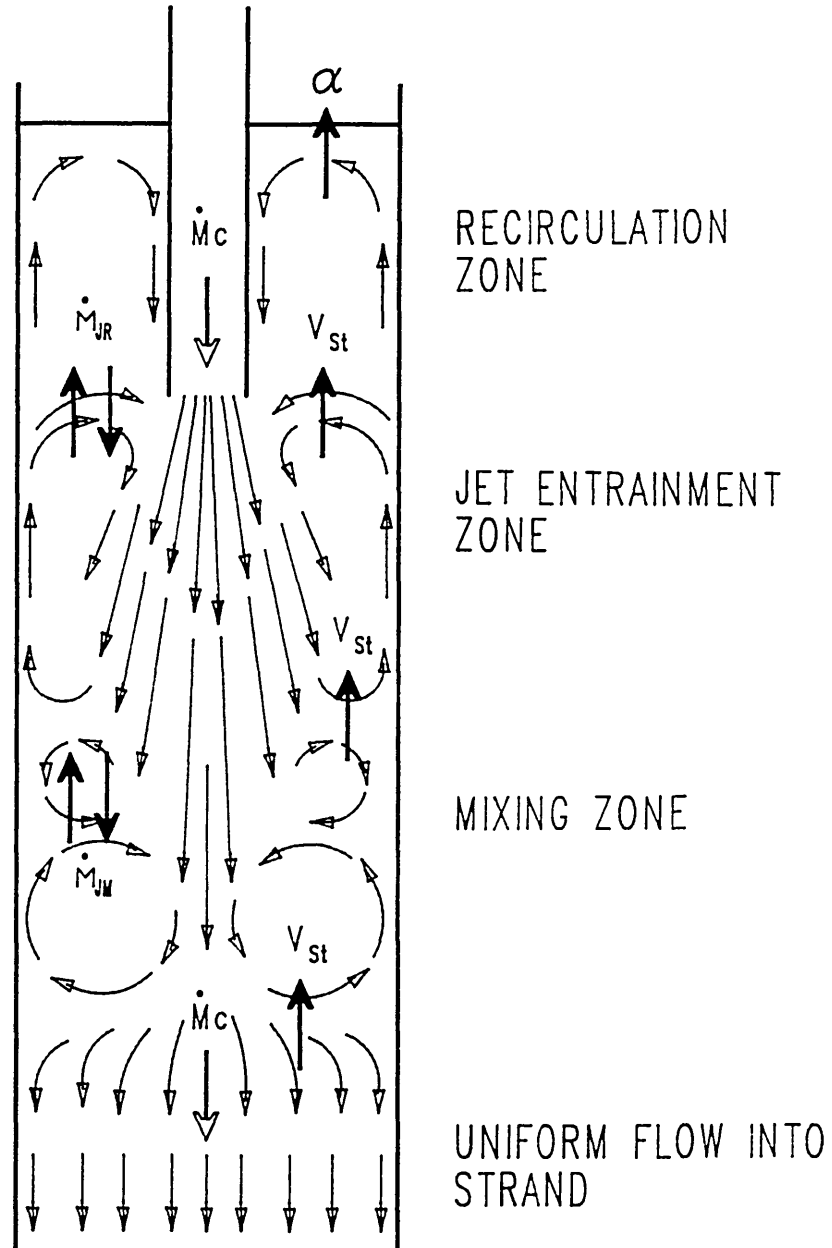
Analysis of the flow field in the sump shows that it can be considered to consist of three principal components, as far as the removal of inclusions is concerned - the jet entrainment zone, the recirculation zone above the submerged nozzle exit ports and the mixing zone below the submerged nozzle exit port - see figure 4.2 and figure 4.3. The fluid leaving the submerged nozzle flows into the jet entrainment zone, then mixes with the fluid in the recirculation and mixing zones. Thereafter the fluid flows into the strand with an, eventually, uniform velocity. The fluid flow pattern in the recirculation zone is due to momentum entrainment from the jet zone. A lazy circulation pattern is therefore set up in the billet caster, but a vigorous pattern is set up in the bloom caster through the action of the horizontal, or near horizontal, flows from bifurcated nozzle. The flow field in the recirculation zone takes inclusions up, close to the wall of the sump, and horizontally across the surface

Figure 4.2



Schematic diagram of mixing regions in the sump of a continuous casting machine showing the interchange fluxes.

Figure 4.3



Schematic diagram of mixing regions in the sump of a continuous casting machine showing the interchange fluxes

just beneath the meniscus. It is while the inclusions are crossing just below the meniscus that they can escape into the slag layer through the combined action of Stokes' law rise and eddy diffusion.

4.2.2. Description of the mass fluxes in the sump

As described in the previous section the sump consists of 3 interacting zones, namely:-

J : Jet entrainment zone.

M : Mixing zone.

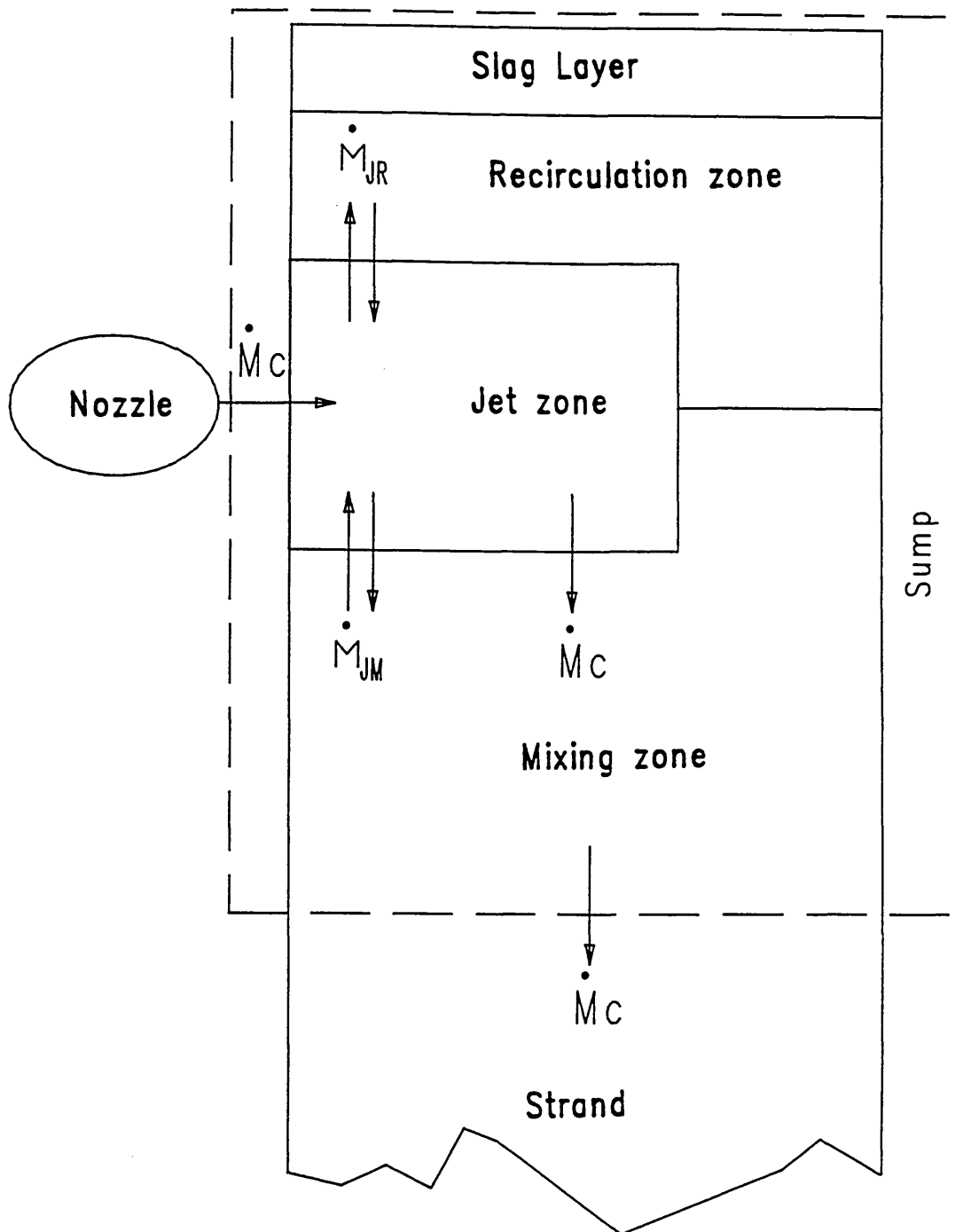
R : Recirculation zone.

These zones are schematically represented in figure 4.4 together with the liquid metal interchange mixing fluxes between them. These fluxes are defined below:-

\dot{M}_{JR} is the liquid metal interchange mass flux between the jet entrainment zone and the recirculation zone, being mainly brought about by jet entrainment. This is a vigorous process for the bifurcated bloom SEN, but a gentle process for the billet SEN.

\dot{M}_{JM} is the liquid metal interchange mass flux between the jet entrainment zone and the mixing zone, which is also mainly caused by jet entrainment in the bloom caster, but in the billet caster, is mainly due to the uneven velocity distribution that exists at the bottom of the jet entrainment zone.

Figure 4.4



Schematic Representation of Mixing Zones
in the Sump of a Continuous Casting Machine

The values of \dot{M}_{JM} and \dot{M}_{JR} are similar for the bloom caster, but, in the billet caster, \dot{M}_{JR} is caused by the lazy flow pattern above the jet entrainment and so is much less than \dot{M}_{JM} .

\dot{M}_c is the net liquid metal mass flux from the nozzle 'N' into the jet entrainment zone J, then into the mixing zone, and afterwards into the strand. Overall mass conservation considerations show that:-

$$\dot{M}_c = V_c \rho_S A_B \quad (4.27)$$

where V_c : machine casting speed;

ρ_S : density of liquid steel;

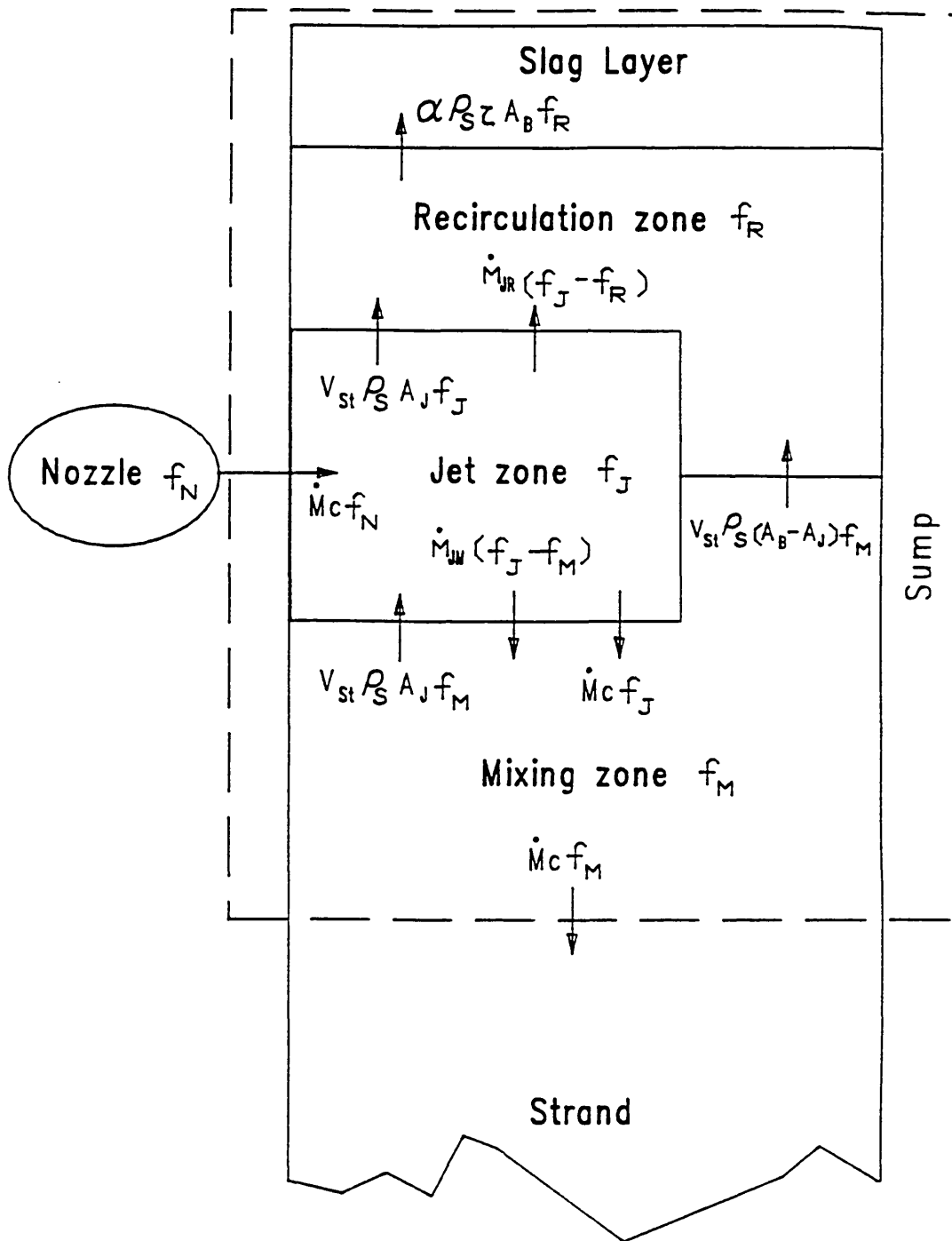
A_B : mould cross area at meniscus.

4.2.3. Description of the inclusion fluxes

As the inclusion effective mass transfer coefficient at the meniscus has been determined in Section 4.1 for inclusions having a certain diameter D_p , the analysis described below has been carried out for a mono-sized inclusions distribution, the diameter being represented as D_p . Because the discussions have been confined to the mono-sized inclusions, the suffix 'd' used in the above section has been omitted here.

Assuming each separate zone in the sump is a completely stirred reactor, as schematically indicated in figure 4.5, we can assume that each zone has its own bulk uniform inclusion concentration. The

Figure 4.5



Schematic Diagram of Inclusion Interchange Fluxes between Zones

following symbols will be used to represent the inclusion mass fraction in each zone:-

f_J : The inclusion mass fraction present in the jet entrainment zone.

f_R : The inclusion mass fraction present in the recirculation zone.

f_M : The inclusion mass fraction present in the mixing zone (equal to the inclusion mass fraction in the withdrawn strand).

f_N : The inclusion mass fraction present in the nozzle stream.

These symbols are used in figure 4.5 and in the following sections to analyse inclusion removal in the sump.

The inclusion flux from the nozzle stream into the jet entrainment zone:-

Inclusions will be carried into the mould sump by bulk liquid metal flow through the nozzle. Thus the inclusion mass flux into the sump is:-

$$\dot{M}_c f_N$$

The inclusion flux from the recirculation zone into the slag layer:-

Through the actions of Stokes rise and eddy diffusion, inclusions in the recirculation zone are removed to the slag layer. If we assume perfect capture efficiency at the steel/slag interface, we can take the inclusion mass fraction at the steel meniscus to be zero. we can therefore represent the inclusion flux into the slag layer as:-

$$\alpha \rho_S \zeta A_B f_R$$

where α : inclusion effective mass transfer coefficient at the meniscus;

ρ_S : density of liquid steel;

A_B : mould cross section area at meniscus.

ζ : a geometric factor less than 1, which describes the obscuration of the upper surface of the meniscus due to the insertion of the nozzle, and the denuding of the liquid steel surface when vigorous steel flowing in the recirculation zone sweep the liquid slag away from the walls of the mould.

The inclusion fluxes from the jet entrainment zone into the recirculation zone:-

Two mechanisms move inclusions from the jet entrainment zone into recirculation zone. One is caused by liquid metal interchange between the two zones, the other by Stokes' rise. The resulting fluxes are as follows:-

by interchange : $\dot{M}_{JR}(f_J - f_R)$

by Stokes rise : $V_{St} \rho_S A_J f_J$

where V_{St} : Stokes rise velocity of inclusions of diameter D_p ;

A_J : Area of contact between the jet entrainment zone and the recirculation zone projected onto a horizontal plane.

The inclusion fluxes from the jet entrainment zone to the mixing zone:-

Two processes carry inclusions from the jet entrainment zone into mixing zone. One is the liquid metal bulk flow and the other is the liquid metal interchange flux between the two zones. The inclusion fluxes due to these two mechanisms are as follows:-

$$\text{due to bulk flow} \quad : \quad \dot{M}_c f_J$$

$$\text{due to interchange} \quad : \quad \dot{M}_{JM}(f_J - f_M)$$

The inclusion fluxes from the mixing zone to the jet entrainment zone:-

The inclusion flux from the mixing zone to the jet entrainment zone, due to Stokes' Law, is:-

$$V_{St} \rho_S A_J f_M$$

The inclusion flux from the mixing zone to the recirculation zone:-

Inclusions move from the mixing zone to the recirculation zone by Stokes rise. The inclusion flux is:-

$$V_{St} \rho_S (A_B - A_J) f_M$$

The interface between the mixing zone and the recirculation zone lies outside the jet entrainment zone and is thus relatively quiescent. It is therefore valid to assume that the mixing interchange between these two zones is negligible.

The inclusion flux from the mixing zone into the strand:-

The inclusion flux from the mixing zone into the strand is caused by the liquid metal bulk flow and is:-

$$\dot{M}_c f_M$$

4.2.4. Inclusion removal model

Figure 4.6 shows the inclusion fluxes in the sump in a conductance net-work form. The nodes J, R and M represent, respectively, the bulk condition in the jet entrainment, recirculation and mixing zones. The connecting arrows represent the inclusion mass fluxes between the zones. A negative sign preceding a flux means that the direction of that flux is opposite to the direction indicated by the arrow in the diagram.

We will now consider inclusion mass balances over unit time within jet entrainment and recirculation zones and within the sump as a whole.

Consideration will be limited to the steady state conditions which are built up very rapidly once the machine starts operation.

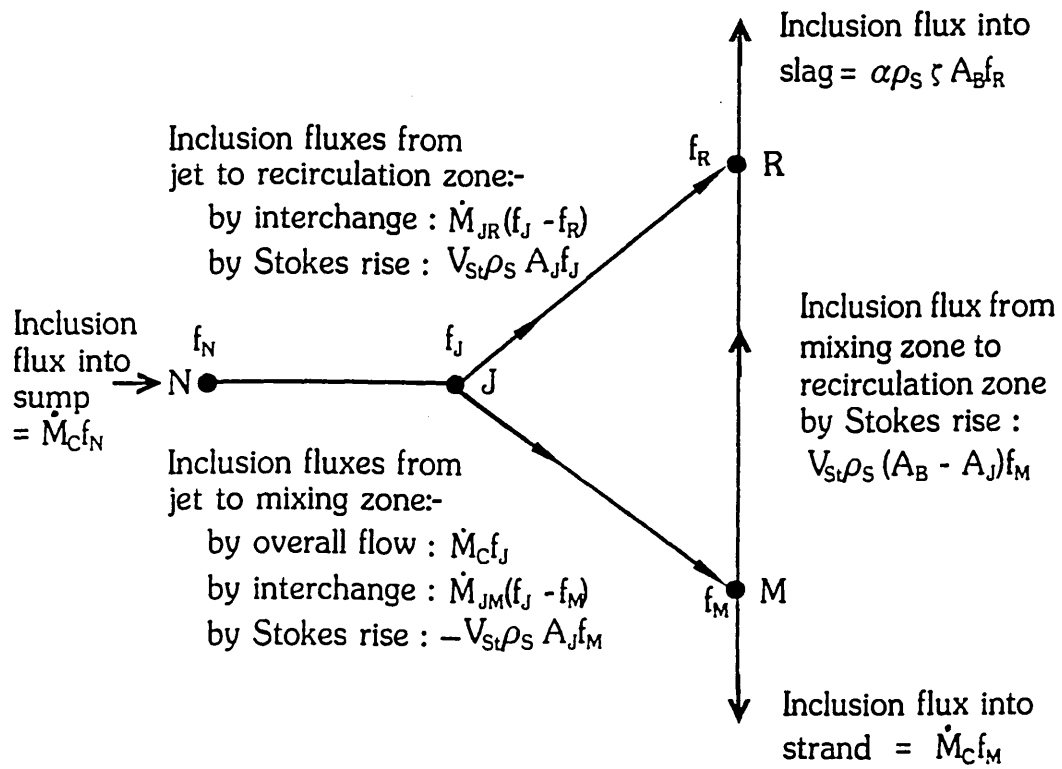
Overall mass balance within the sump:-

$$\text{Mass flux of inclusions into the sump} = \dot{M}_c f_N$$

$$\text{Mass flux of inclusions out of the sump} = \dot{M}_c f_M + \alpha \rho_S \zeta A_B f_R$$

Therefore the inclusion mass balance on the sump gives:-

Figure 4.6



Schematic diagram of inclusion interchange fluxes - in conductance network form.

$$\dot{M}_c f_N = \dot{M}_c f_M + \alpha \rho_S \zeta A_B f_R \quad (4.28)$$

Rearranging equation (4.28) gives:-

$$\dot{M}_c (f_N - f_M) = \alpha \rho_S \zeta A_B f_R \quad (4.29)$$

Mass balance on the jet entrainment zone:-

$$\text{Mass flux of inclusions into the zone} = \dot{M}_c f_N + V_{St} \rho_S A_J f_M$$

$$\begin{aligned} \text{Mass flux of inclusions out of the zone} &= \dot{M}_c f_J + \dot{M}_{JM} (f_J - f_M) \\ &+ \dot{M}_{JR} (f_J - f_R) + V_{St} \rho_S A_J f_J \end{aligned}$$

So the mass balance on the jet entrainment zone gives:-

$$\dot{M}_c f_N + V_{St} \rho_S A_J f_M = \dot{M}_c f_J + \dot{M}_{JM} (f_J - f_M) + \dot{M}_{JR} (f_J - f_R) + V_{St} \rho_S A_J f_J \quad (4.30)$$

Mass balance on the recirculation zone:-

$$\begin{aligned} \text{Mass flux of inclusions into the zone} &= \dot{M}_{JR} (f_J - f_R) + V_{St} \rho_S A_J f_J \\ &+ V_{St} \rho_S (A_B - A_J) f_M \end{aligned}$$

$$\text{Mass flux of inclusions out of the zone} = \alpha \rho_S \zeta A_B f_R$$

Thus the mass balance on the recirculation zone gives:-

$$\dot{M}_{JR}(f_J - f_R) + V_{St}\rho_S A_J f_J + V_{St}\rho_S (A_B - A_J) f_M - \alpha\rho_S \zeta A_B f_R \quad (4.31)$$

\dot{M}_c is the basic parameter determining the magnitude of all the flows, and will therefore be used to render the variables in equation (4.29) to (4.31) dimensionless. The three equations will thus be reformulated in terms of the following normalising terms:-

$$\Gamma_{xx} = \frac{\dot{M}_{xx}}{\dot{M}_c} \quad (4.32)$$

$$\alpha^* = \frac{\alpha\rho_S \zeta A_B}{\dot{M}_c} = \frac{\alpha\rho_S \zeta A_B}{A_B \rho_S V_c} = \frac{\zeta\alpha}{V_c} \quad (4.33)$$

$$v = \frac{V_{St}}{V_c} \quad (4.34)$$

$$a = \frac{A_J}{A_B} \quad (4.35)$$

where Γ_{xx} : dimensionless liquid metal interchange flux between zones;

\dot{M}_{xx} : liquid metal mass fluxes, \dot{M}_{xx} could be \dot{M}_{JR} , \dot{M}_{JM} or \dot{M}_J ;

α^* : dimensionless effective inclusion mass transfer coefficient;

v : dimensionless Stokes rise velocity as defined
in equation (4.34);

a : fractional jet projected area as defined in
equation (4.35).

To reformulate equations (4.29) to (4.31) we divide both sides of
these equations by \dot{M}_c , therefore equations (4.29) to (4.31) become :-

$$f_N - f_M = \alpha f_R \quad (4.36)$$

$$f_N + avf_M = f_J + \Gamma_{JM}(f_J - f_M) + \Gamma_{JR}(f_J - f_R) + avf_J \quad (4.37)$$

$$\Gamma_{JR}(f_J - f_R) + avf_J + (1 - a)vf_M = \alpha f_R \quad (4.38)$$

Rearranging equation (4.36), we have:-

$$f_M = f_N - \alpha f_R \quad (4.39)$$

From equation (4.37) we obtain the following equation:-

$$(1 + \Gamma_{JM} + \Gamma_{JR} + av)f_J = f_N + (\Gamma_{JM} + av)f_M + \Gamma_{JR}f_R \quad (4.40)$$

From equation (4.38) we have:-

$$(\Gamma_{JR} + av)f_J = (\Gamma_{JR} + \alpha)f_R - (1 - a)vf_M \quad (4.41)$$

Subtracting equation (4.41) from equation (4.40), we get:-

$$(1 + \Gamma_{JM})f_J = f_N + (\Gamma_{JM} + v)f_M - \alpha^*f_R \quad (4.42)$$

Dividing equation (4.41) by equation (4.42) to eliminate f_J from equations, we have:-

$$\frac{(\Gamma_{JR} + av)}{(1 + \Gamma_{JM})} = \frac{(\Gamma_{JR} + \alpha^*)f_R - (1 - a)v f_M}{f_N + (\Gamma_{JM} + v)f_M - \alpha^*f_R} \quad (4.43)$$

Therefore:-

$$\begin{aligned} & (\Gamma_{JR} + av)f_N + (\Gamma_{JR} + av)(\Gamma_{JM} + v)f_M - (\Gamma_{JR} + av)\alpha^*f_R \\ & = (1 + \Gamma_{JM})(\Gamma_{JR} + \alpha^*)f_R - (1 + \Gamma_{JM})(1 - a)v f_M \end{aligned} \quad (4.44)$$

or in another form:-

$$\begin{aligned} (\Gamma_{JR} + av)f_N & = \left[(1 + \Gamma_{JM})(\Gamma_{JR} + \alpha^*) + (\Gamma_{JR} + av)\alpha^* \right] f_R \\ & \quad - \left[(\Gamma_{JR} + av)(\Gamma_{JM} + v) + (1 + \Gamma_{JM})(1 - a)v \right] f_M \end{aligned} \quad (4.45)$$

Substituting from equation (4.39) for f_M , we get:-

$$\begin{aligned} (\Gamma_{JR} + av)f_N & = \left[(1 + \Gamma_{JM})(\Gamma_{JR} + \alpha^*) + (\Gamma_{JR} + av)\alpha^* \right] f_R \\ & \quad - \left[(\Gamma_{JR} + av)(\Gamma_{JM} + v) + (1 + \Gamma_{JM})(1 - a)v \right] (f_N - \alpha^*f_R) \end{aligned} \quad (4.46)$$

We shall now simplify the above equation. Define Φ as:-

$$\Phi = (1 + \Gamma_{JM})(\Gamma_{JR} + \nu) + (\Gamma_{JR} + \alpha\nu)\nu. \quad (4.47)$$

Then, equation (4.46) can be rewritten as:-

$$\Phi f_N = \left[(1 + \Gamma_{JM})(\Gamma_{JR} + \alpha^*) + \Phi\alpha^* \right] f_R \quad (4.48)$$

Therefore

$$\frac{f_R}{f_N} = \frac{\Phi}{\Phi\alpha^* + (1 + \Gamma_{JM})(\alpha^* + \Gamma_{JR})} \quad (4.49)$$

We shall now define the efficiency of inclusion removal from liquid bath into slag layer as the inclusion removal ratio $\eta_{inclusion}$, which can be expressed as:-

$$\eta_{inclusion} = \frac{\alpha \rho_S \gamma_B^A f_R}{\dot{M}_c f_N} = \alpha^* \frac{f_R}{f_N} \quad (4.50)$$

Substituting from equation (4.49) for $\frac{f_R}{f_N}$, we have:-

$$\eta_{inclusion} = \frac{\alpha^*\Phi}{\alpha^*\Phi + (1 + \Gamma_{JM})(\alpha^* + \Gamma_{JR})} \quad (4.51)$$

Rewriting equation (4.51) in a simpler form, we have:-

$$\eta_{inclusion} = \frac{1}{1 + (1 + \Gamma_{JM})(1 + \Gamma_{JR}/\alpha^*)/\Phi} \quad (4.52)$$

Γ_{JM} , Γ_{JR} and a in the above equations are functions of the fluid flow field. v and α^* are strong functions of the inclusions and, possible, weak functions of the fluid flow field.

Equations (4.52) and (4.47) would allow the inclusion removal efficiency to be calculated for a given casting speed, provided values could be provided for the interchange fluxes between the different zones, for the geometric factor, for the Stokes rise velocity and for the inclusion mass transfer coefficient at the liquid steel meniscus. As Appendix 1 shows, the interchange fluxes can be estimated from jet entrainment theory and the geometric factor can be determined from the geometry of the SEN and the mould and from observation of the slag surface during casting.

Estimation of the Stokes rise velocity and the surface mass transfer coefficient is much more complicated since it depends, as figure 4.1 shows, upon the diameter of the inclusions. Although the inclusion population entering the sump from the SEN could be assumed to be known, inclusion agglomeration in the sump flows could increase the mean inclusion diameter quite significantly, thus changing both the Stokes rise velocity and the meniscus mass transfer coefficient. Indeed, it is understanding the extent to which this can occur that is one of the principal aims of the current investigation.

The average inclusion size in the SEN stream has been determined as described in section 5.3, but it is not possible to measure the inclusion size in the sump. The experiments have, however, measured the inclusion efficiencies directly, so that the left hand side of

equation (4.52) is known. In principle, then, the measured inclusion efficiencies could be used to determine the effective Stokes rise velocity and meniscus mass transfer coefficient. The manipulation of the equations to allow this to be done is described in the next section.

4.2.5. Γ equation.

We will temporarily omit subscript "inclusion" in the following discussions for the reason of clarity. Therefore, we can write equation (4.51) as:-

$$\eta = \frac{\alpha^* \bar{\phi}}{\alpha^* \bar{\phi} + (1 + \Gamma_{JM})(\alpha^* + \Gamma_{JR})} \quad (4.53)$$

Substituting equation (4.47) into equation (4.53) and rearranging gives:-

$$\begin{aligned} \eta \alpha^* (1 + \Gamma_{JM})(\Gamma_{JR} + v) + \eta \alpha^* (\Gamma_{JR} + av)v + \eta (1 + \Gamma_{JM})(\alpha^* + \Gamma_{JR}) \\ = \alpha^* (1 + \Gamma_{JM})(\Gamma_{JR} + v) + \alpha^* (\Gamma_{JR} + av)v \end{aligned} \quad (4.54)$$

or in the form of:-

$$\begin{aligned} (\eta - 1) \alpha^* \left[(1 + \Gamma_{JM})(\Gamma_{JR} + v) + (\Gamma_{JR} + av)v \right] \\ + \eta (1 + \Gamma_{JM})(\alpha^* + \Gamma_{JR}) = 0 \end{aligned} \quad (4.55)$$

We will simplify the above equation using the following assumptions.

$$1) \quad \Gamma_{JR} = \Gamma \quad (4.56)$$

where Γ can be estimated from the flow field in the sump.

$$2) \quad \Gamma_{JM} = \beta \cdot \Gamma_{JR} = \beta \cdot \Gamma \quad (4.57)$$

where $\beta \approx 1$ for the nozzle flows from nozzles with horizontal and near horizontal port angles, since the jet entrains more or less equally from both sides of the jet, i.e. from the recirculation zone and from the mixing zone.

$\beta \gg 1$ for the nozzle flows from nozzles with vertical outlets, since very little entrainment occurs from the upper recirculation zone.

Thus equation (4.55) becomes:-

$$(\eta - 1)\alpha^* \left[(1 + \beta\Gamma)(\Gamma + \nu) + (\Gamma + a\nu)\nu \right] + \eta(1 + \beta\Gamma)(\alpha^* + \Gamma) = 0 \quad (4.58)$$

β and a in this equation can be estimated reliably from the fluid flow characteristics in the sump, and η can be obtained from the experiment carried out in the present investigation. ν and α^* are strongly dependent on inclusion size and are therefore unknown if a substantial amount of agglomeration occurs in the sump. Γ is also unknown in the enclosed flow field in the sump, although the theory of entrainment into free jets will indicate its order of magnitude.

The theoretical analysis in section 4.1.5 suggested that moderate turbulent diffusion has a relatively small effect on the meniscus

mass transfer coefficient, so that equation (4.26) could be used to determine the value of the meniscus mass transfer coefficient.

Thus:-

$$\alpha_d = e \cdot [V_{St}]_d$$

where 'e' is termed as enhancement factor, which, according to equation (4.26), is expressed as:-

$$e = 1 + 2/\tau_e^* \quad (4.59)$$

So according to equation (4.33) and (4.34), we have:-

$$\alpha^* = e\zeta \cdot v \quad (4.60)$$

so that equation (4.58) could be written as:-

$$\begin{aligned} & (\eta - 1)e\zeta v \left[(1 + \beta\Gamma)(\Gamma + v) + (\Gamma + av)v \right] \\ & + \eta(1 + \beta\Gamma)(e\zeta v + \Gamma) = 0 \end{aligned} \quad (4.61)$$

or

$$\begin{aligned} & (\eta - 1)e\zeta v(1 + \beta\Gamma)(\Gamma + v) + (\eta - 1)e\zeta v^2(\Gamma + av) \\ & + \eta(1 + \beta\Gamma)(e\zeta v + \Gamma) = 0 \end{aligned} \quad (4.62)$$

where Γ and v are two unknowns.

It may be seen that equation (4.62) is a cubic equation in v and a quadratic equation in Γ . Because there are two unknowns and we only have one equation, it seems that we could not have a definite solution from the above equation. However we know that Γ is real and positive and jet theory suggests, for the bloom mould model, that it will be some where between 1 and 2 (see Appendix 1). Thus we can

rewrite the equation as a quadratic equation in Γ , and find values of v , for which this equation has a real solution.

Rearranging equation (4.61), we have:-

$$(\eta - 1)e\zeta v \left[\Gamma + \beta\Gamma^2 + v + \beta\Gamma v + \Gamma v + av^2 \right] + \eta(e\zeta v + \beta\Gamma e\zeta v + \beta\Gamma^2 + \Gamma) = 0 \quad (4.63)$$

Therefore

$$\beta \left[e\zeta v(\eta - 1) + \eta \right] \Gamma^2 + \left[e\zeta v(\eta - 1)(1 + \beta v + v) + \eta(1 + e\beta\zeta v) \right] \Gamma + e\zeta v^2(\eta - 1) + ae\zeta v^3(\eta - 1) + e\eta\zeta v = 0 \quad (4.64)$$

This is a quadratic equation in Γ , which can be expressed in the form:-

$$A\Gamma^2 + B\Gamma + C = 0 \quad (4.65)$$

where:-

$$A = \beta \left[e\zeta v(\eta - 1) + \eta \right] \quad (4.66)$$

$$B = e\zeta v(\eta - 1)(1 + \beta v + v) + \eta(1 + e\beta\zeta v) \quad (4.67)$$

$$C = e\zeta v \left[v(\eta - 1)(1 + av) + \eta \right] \quad (4.68)$$

If A, B and C are known, Γ could be obtained from the following expression:-

$$\Gamma = \frac{-B \pm \sqrt{B^2 - 4AC}}{2A} \quad (4.69)$$

The use of this equation will be considered further in the discussion section

5. EXPERIMENTAL RESULTS.

5.1. Fluid flow studies.

5.1.1. Introduction.

Fluid flow patterns in the sump of a billet caster and a bloom caster were studied by using the water models described in Chapter 3. Two tracers, fine alumina flakes and small air bubbles, were used. Three different nozzles, table 3.2, were employed for the billet caster model studies and eight different bifurcated nozzles (see table 3.3) were used for the bloom caster model investigations. The fluid flow patterns developed in three different planes within the billet mould, namely plane 1, 2 and 3, shown in figure 5.1, were photographed with the aid of the plane light source described in section 3.2.3. However, in the case of the bloom caster model which has a mould thickness of 65 mm, only the fluid flow patterns developed in the centre plane were photographically recorded. The results obtained are reported in the following sections.

5.1.2. Effect of SEN geometry.

On the billet caster model:-

Plate 5.1 shows the fluid flow patterns developed on plane 1 when different SENs were employed on the billet caster model. The fluid flow patterns obtained are almost identical except in the top region, where the use of Nozzle 2 results in less fluid movement. The flow from the outlet is directed strongly downwards and the streams from all the nozzles penetrate deeply into the sump, and the penetration depth being very nearly the same. Some vortex regions

around the jet were observed and the jet mixes with the surrounding fluid during its penetration. The fluid flow patterns developed on plane 2 and plane 3 when the different SENs were used are shown respectively in plates 5.2 and 5.3. Plates 5.4 to 5.6 show the same flow fields when fine alumina flakes are used as tracer.

On the bloom caster model:-

Plate 5.7 shows the fluid flow patterns developed on the centre plane when Nozzle 11 (25° downward), Nozzle 9 (15° downward), Nozzle 4 (0°) and Nozzle 5 (25° upward) were used. It can be seen from the pictures that the fluid flow patterns obtained consist of three regions, namely the jet entrainment region, the recirculation region above the jet and the mixing region below the jet. The fluid flow patterns obtained are almost the same except in the case when using Nozzle 5, where more fluid is directed towards the meniscus. Plates 5.8 to 5.11 shows the fluid flow patterns developed when the same types of nozzles (as those used in plate 5.7) with different SEN submerged depth are used.

5.1.3. Effect of SEN submerged depth.

On the billet caster model:-

The fluid flow patterns developed on plane 1 using Nozzle 1 at different submerged depths are shown in plate 5.12. The basic features of the fluid flow patterns are almost identical but there are some differences. In the first place, when employing large SEN submerged depths, the stream penetrates somewhat more deeply into the sump than is the case with small submerged depths, but the increase in the depth to which its stream penetrates is not as great as the

increase in the submerged depth of the SEN. When small SEN submerged depths are used, the flow field near the meniscus shows intensive mixing and vortex flow, but when large SEN submerged depths are employed, the fluid flow in the same region was quiescent — mainly a slowly upward flow close to the periphery. The fluid flow patterns developed on plane 2 and plane 3 when Nozzle 1 with different SEN submerged depth being used are shown in plates 5.13 and 5.14 respectively. A similar effect due to different submerged depths of SEN on the stream penetration depth was observed. And as the observing plane moves towards the mould wall (the solidification front), the stirring of the fluid becomes more uniformly distributed. Plates 5.15 to 5.17 shown the fluid flow patterns as disclosed for the same conditions when fine alumina flakes are used as the tracer. The fluid flow patterns obtained are nearly the same.

The comparison of the fluid flow patterns developed when using Nozzle 2 with different SEN submerged depth are shown in plates 5.18 to 5.23. The basic patterns of the fluid flow are similar to those described for Nozzle 1 except that the movement of the fluid close to the meniscus is less intensive.

The fluid flow patterns developed when employing Nozzle 3 with different SEN submerged depth are given in plate 5.24 to plate 5.29. Once again, the similar fluid flow patterns are observed.

On the bloom caster model:-

The fluid flow patterns developed on the centre plane when using Nozzle 4 at different SEN submerged depth are shown in plate 5.30. The basic features of the fluid flow patterns are almost identical

but there are some differences. When employing small SEN submerged depth the fluid flow in the mixing region below the jet is very intensive and full of vortex, but when large SEN submerged depth is used, the fluid flow in the same region was very quiescent, mainly a slowly moving downward flow.

The fluid flow patterns developed on the centre plane when using Nozzle 5 at different SEN submerged depth are shown in plate 5.31. The same for Nozzle 9 and 11 are shown in plate 5.32 and plate 5.33 respectively.

5.1.4. Effect of casting speed.

The effect of casting speed on the fluid flow patterns developed in the billet mould when using Nozzle 3 with submerged depth of 125 mm is shown in plate 5.34. As can be seen from the plate, the change of casting speed has a little effect on the fluid flow patterns developed within the billet mould sump.

5.1.5. Entry nozzle stream penetration.

As mentioned in section 5.1.3., increasing submerged depth of the SEN increased the depth to which the nozzle stream penetrated. This depth was measured for different submerged depth of SEN, the data being shown in Table 5.1 and presented in figure 5.2.

5.2. Inclusion separation studies.

5.2.1. Introduction.

The inclusion behaviour in the sump was studied by applying the

methods described in Chapter 3. The distribution of the inclusions in the sump was expressed as the fraction of the inclusions removed into the slag layer, termed the removal ratio, which is defined as:-

$$\eta_{inclusion} = \frac{V_{in\ slag}}{V_{injected}} \times 100 \quad (5.1)$$

where: $\eta_{inclusion}$: the inclusion removal ratio;

$V_{injected}$: volume of coloured paraffin injected;

$V_{in\ slag}$: volume of coloured paraffin absorbed into the slag layer.

The data obtained are reported in the following sections.

5.2.2. Effect of SEN submerged depth.

On the billet caster model:-

The effect of SEN submerged depth on the inclusion removal for Nozzle 1 was recorded in table 5.2 and presented in figure 5.3. As shown in the figure, the removal ratio increases with increasing SEN submerged depth. The data obtained for Nozzle 2 and Nozzle 3 were recorded in table 5.3 and table 5.4 and presented in figure 5.4 and figure 5.5 respectively. Once again, the figures shown that the removal ratio increases with increasing submerged nozzle depth.

On the bloom caster model:-

The effect of SEN submerged depth on the inclusion removal into "slag" layer for Nozzle 4 was recorded in table 5.5 and shown in figure 5.6. As seen in the figure, the removal ratio increases with the increasing SEN submerged depth. The data obtained for Nozzle 5 to

Nozzle 11 were recorded in table 5.6 to table 5.12 and presented in figure 5.7 to figure 5.13. Once again, The figures shown that the removal ratio increases with the increases of the SEN submerged depth.

5.2.3. Effect of SEN geometry.

Figure 5.14 shows the effect of SEN geometry on the removal of inclusion in the billet mould sump. As can be seen in the figure, the removal ratio increases as the outside diameter of the SEN decreases. Figure 5.15 shows the effect of SEN geometry (port angle) on the removal of inclusion in the bloom mould sump when employing different SEN submerged depth. As shown in the figure, the removal ratio decreases as the port angle decreases from upward angle, and the minimum value is reached when the port angle is 5° (downward) in the case of using SEN submerged depth of 175 mm. After this angle, the removal ratio increases with the increasing SEN port downward angle. As can be seen from the figure, the SEN port angle at which the minimum removal ratio was achieved shifts towards downward angle when employing a smaller SEN submerged depth, i.e. when SEN submerged depth was reduced to 75 mm, this angle is 10° downward. And also when small SEN submerged depth was employed, too large downward angle is not beneficial to the inclusion removal.

5.2.4. Effect of gas bubbling.

Argon gas was introduced into the nozzle stream to elucidate its effect on the inclusion removal ratio. The results obtained in the billet mould model are recorded in table 5.13 and presented in figure 5.16. The removal ratio decreases as the gas flow rate increases.

Once the gas flow rate was raised to 1.0 L.min^{-1} , the removal ratio was found to be very low and to be virtually insensitive to submerged depth of the SEN.

The effects of argon gas injection into the nozzle stream on the inclusion removal ratio in the bloom mould model when using Nozzle 4 are recorded in table 5.14 and presented in figure 5.17. As shown in the figure, the removal ratio increases when a small amount of gas ($< 0.50 \text{ L.min}^{-1}$) is injected into the nozzle stream. When employing small SEN submerged depth, any amount of gas injection will improve the inclusion removal ratio, but the problem is that when employing small SEN submerged depth it is not possible to keep the meniscus fully covered.

The same effects of argon injection in the bloom mould model when using Nozzle 5 are recorded in table 5.15 and presented in figure 5.18. As can be seen in the figure, argon gas injection into the nozzle stream has little effect on the inclusion removal. At this SEN port angle (25° upward) the introduction of argon gas into the nozzle stream is not practicable when using a SEN submerged depth less than 125 mm because of the meniscus exposure and the mould powder entrainment.

The same results for Nozzle 10 in the bloom mould model are recorded in table 5.16 and presented in figure 5.19. The removal ratio decreases as the increase of the gas flow rate.

5.2.5. Effect of casting speed.

Figure 5.20 shows the effect of casting speed on the removal of inclusion in the billet mould sump. As can be seen in the figure, the removal ratio slightly decreases as the casting speed increases. The results obtained are also recorded in table 5.17.

5.2.6. Effect of the size of injection nozzle.

Figure 5.21 shows the effect of the size of the injection nozzles on the removal of inclusion in the bloom mould sump. As can be seen, the inclusion removal ratio increases dramatically as the increase of the injection nozzle size. The results obtained are also listed in tables 5.18 and 5.19.

5.3. Inclusion particle size measurement.

The generation of the inclusion particles has been recorded photographically by the methods described in section 3.5. Plates 5.35 and 5.36 show examples of the pictures taken.

The diameters of the inclusion particles immediately after they had been generated were measured employing the methods described in section 3.5. The data are listed in table 5.20 and 5.21. The average diameter of particles produced from the nozzle with an internal diameter of 200 μm was 150 μm . The nozzle with an internal diameter of 127 μm produced particles with an average particle diameter of 95 μm .

Relating the above values to the inner diameters of the tubes, the following approximation holds:-

$$\frac{d_o}{d_n} = 0.95(0.5)^{\frac{1}{3}} \quad (5.2)$$

where d_o : particle diameter when generated;

d_n : nozzle tube inner diameter.

TABLE 5.1. Effect of SEN submerged depth on nozzle stream penetration.

SEN submerged depth mm	Nozzle stream penetration mm
25	520 - 660
50	530 - 680
75	550 - 690
100	540 - 700
125	570 - 720
150	580 - 740
175	590 - 750

Note: The values of the stream penetration depth were read from a centimeter scale attached to the side wall of the model mould, during the experimental observations of the fluid flow patterns. The depth was taken as the distance from the meniscus to the point where the downward velocity of the nozzle stream could no longer be clearly discerned. Examples of this point are marked on plate 5.1.

TABLE 5.2. Effect of SEN submerged depth on inclusion removal.

Sample No	Submerged depth (mm)	Volume of colourless paraffin in the top layer (ml)	Volume of coloured paraffin injected $V_{injected}$ (ml)	Injection time (min)	Absorbance	Volume into top layer $V_{in\ slag}$ (ml)	Removal ratio η (%)
1	175	50	10.0	14.61	0.234	0.843	8.43
2	150	50	10.0	14.52	0.232	0.835	8.35
3	125	50	10.0	14.75	0.221	0.792	7.92
4	100	50	10.0	14.67	0.202	0.717	7.17
5	75	50	10.0	14.80	0.191	0.673	6.73
6	50	50	10.0	14.73	0.162	0.559	5.59
7	25	50	10.0	14.73	0.147	0.500	5.00
8	150	50	10.0	14.51	0.228	0.819	8.19
9	125	50	10.0	14.48	0.219	0.784	7.84
10	100	50	10.0	14.71	0.210	0.748	7.48
11	75	50	10.0	14.42	0.189	0.666	6.66
12	50	50	10.0	14.64	0.169	0.587	5.87
13	25	50	10.0	14.56	0.150	0.512	5.12

SEN: Nozzle 1;

Casting speed: 1.33 m.min⁻¹;

No gas bubbling.

TABLE 5.3. Effect of SEN submerged depth on inclusion removal.

Sample No	Submerged depth (mm)	Volume of colourless paraffin in the top layer (ml)	Volume of coloured paraffin injected $V_{injected}$ (ml)	Injection time (min)	Absorbance	Volume into top layer $V_{in\ slag}$ (ml)	Removal ratio η (%)
14	175	50	10.0	13.55	0.150	0.512	5.12
15	150	50	10.0	13.75	0.149	0.508	5.08
16	125	60	10.0	14.35	0.123	0.486	4.86
17	100	50	10.0	14.25	0.134	0.449	4.49
18	75	50	10.0	13.93	0.118	0.386	3.86
19	50	50	10.0	13.70	0.100	0.315	3.15
20	25	50	10.0	13.13	0.092	0.283	2.83
21	150	50	10.0	13.53	0.146	0.496	4.96
22	125	50	10.0	14.12	0.148	0.504	5.04
23	100	50	10.0	13.65	0.140	0.472	4.72
24	75	50	10.0	13.05	0.123	0.405	4.05
25	50	50	10.0	14.13	0.104	0.330	3.30
26	25	50	10.0	13.76	0.096	0.299	2.99

SEN: Nozzle 2:

Casting speed: 1.33 m.min⁻¹;

No gas bubbling.

TABLE 5.4. Effect of SEN submerged depth on inclusion removal.

Sample No	Submerged depth (mm)	Volume of colourless paraffin in the top layer (ml)	Volume of coloured paraffin injected $V_{injected}$ (ml)	Injection time (min)	Absorbance	Volume into top layer $V_{in\ slag}$ (ml)	Removal ratio η (%)
27	175	50	10.0	9.25	0.200	0.709	7.09
28	150	50	10.0	9.42	0.181	0.634	6.34
29	125	50	10.0	9.40	0.163	0.563	5.63
30	100	50	10.0	9.18	0.153	0.524	5.24
31	75	50	10.0	9.18	0.138	0.464	4.64
32	50	50	10.0	8.94	0.113	0.366	3.66
33	25	50	10.0	9.22	0.087	0.263	2.63

SEN: Nozzle 3;

Casting speed: 1.33 m.min⁻¹;

No gas bubbling.

TABLE 5.5. Effect of SEN submerged depth on inclusion removal.

Sample No	Submerged depth (mm)	Volume of colourless paraffin in the top layer (ml)	Volume of coloured paraffin injected $V_{injected}$ (ml)	Injection time (min)	Absorbance	Volume into top layer $V_{in\ slag}$ (ml)	Removal ratio η (%)
70	175	150	10.0	13.48	0.480	5.441	54.41
71	150	150	10.0	13.52	0.363	4.056	40.56
72	125	150	10.0	14.25	0.299	3.299	32.99
73	100	150	10.0	13.67	0.272	2.979	29.79
74	75	150	10.0	14.20	0.227	2.447	24.47

SEN: Nozzle 4; Port Angle: 0° Horizontal

Casting speed: 0.55 m.min⁻¹;

No gas bubbling.

TABLE 5.6. Effect of SEN submerged depth on inclusion removal.

Sample No	Submerged depth (mm)	Volume of colourless paraffin in the top layer (ml)	Volume of coloured paraffin injected $V_{injected}$ (ml)	Injection time (min)	Absorbance	Volume into top layer $V_{in\ slag}$ (ml)	Removal ratio η (%)
88	175	150	5.0	9.30	0.341	3.796	75.92
89	150	150	5.0	9.55	0.292	3.216	64.32
90	125	150	5.0	10.10	0.238	2.577	51.54
91	100	150	5.0	10.15	0.140	1.417	28.34
92	75	150	5.0	10.00	0.090	0.825	16.50

SEN: Nozzle 5: Port Angle: 25° Upward

Casting speed: 0.55 m.min⁻¹;

No gas bubbling.

TABLE 5.7. Effect of SEN submerged depth on inclusion removal.

Sample No	Submerged depth (mm)	Volume of colourless paraffin in the top layer (ml)	Volume of coloured paraffin injected $V_{injected}$ (ml)	Injection time (min)	Absorbance	Volume into top layer $V_{in\ slag}$ (ml)	Removal ratio η (%)
93	175	150	5.0	9.70	0.248	2.695	53.90
94	150	150	5.0	9.42	0.208	2.222	44.44
95	125	150	5.0	9.40	0.164	1.701	34.02
96	100	150	5.0	9.18	0.133	1.334	26.68
97	75	150	5.0	9.30	0.124	1.228	24.56

SEN: Nozzle 6; Port Angle: 5° Upward

Casting speed: 0.55 m.min⁻¹;

No gas bubbling.

TABLE 5.8. Effect of SEN submerged depth on inclusion removal.

Sample No	Submerged depth (mm)	Volume of colourless paraffin in the top layer (ml)	Volume of coloured paraffin injected $V_{injected}$ (ml)	Injection time (min)	Absorbance	Volume into top layer $V_{in\ slag}$ (ml)	Removal ratio η (%)
108	175	150	6.1	12.25	0.290	3.192	52.33
109	150	150	5.0	9.42	0.169	1.760	35.20
110	125	150	5.0	9.40	0.119	1.168	23.36
111	100	150	5.0	9.18	0.093	0.861	17.22
112	75	150	5.0	9.35	0.067	0.553	11.06

SEN: Nozzle 7; Port Angle: 5° Downward

Casting speed: 0.55 m.min⁻¹;

No gas bubbling.

TABLE 5.9. Effect of SEN submerged depth on inclusion removal.

Sample No	Submerged depth (mm)	Volume of colourless paraffin in the top layer (ml)	Volume of coloured paraffin injected $V_{injected}$ (ml)	Injection time (min)	Absorbance	Volume into top layer $V_{in\ slag}$ (ml)	Removal ratio η (%)
113	175	150	5.1	12.00	0.287	3.157	61.89
114	150	150	5.0	11.85	0.205	2.186	43.72
115	125	150	5.2	11.90	0.131	1.310	25.20
116	100	150	5.0	12.18	0.084	0.754	15.08
117	75	150	5.0	12.35	0.052	0.375	7.50

SEN: Nozzle 8; Port Angle: 10° Downward

Casting speed: 0.55 m.min⁻¹;

No gas bubbling.

TABLE 5.10. Effect of SEN submerged depth on inclusion removal.

Sample No	Submerged depth (mm)	Volume of colourless paraffin in the top layer (ml)	Volume of coloured paraffin injected $V_{injected}$ (ml)	Injection time (min)	Absorbance	Volume into top layer $V_{in\ slag}$ (ml)	Removal ratio η (%)
98	175	150	5.0	10.10	0.255	2.778	55.56
99	150	150	5.1	10.35	0.202	2.151	42.18
100	125	150	5.0	11.00	0.143	1.452	29.04
101	100	150	5.0	10.48	0.121	1.192	23.84
102	75	150	5.1	11.18	0.106	1.015	19.89

SEN: Nozzle 9; Port Angle: 15° Downward

Casting speed: 0.55 m.min⁻¹;

No gas bubbling.

TABLE 5.11. Effect of SEN submerged depth on inclusion removal.

Sample No	Submerged depth (mm)	Volume of colourless paraffin in the top layer (ml)	Volume of coloured paraffin injected $V_{injected}$ (ml)	Injection time (min)	Absorbance	Volume into top layer $V_{in\ slag}$ (ml)	Removal ratio η (%)
103	175	150	5.0	8.95	0.255	2.778	55.56
104	150	150	5.0	9.20	0.197	2.091	41.82
105	125	150	5.0	9.40	0.153	1.571	31.42
106	100	150	5.0	9.18	0.129	1.287	25.74
107	75	150	5.0	9.25	0.097	0.908	18.16

SEN: Nozzle 10; Port Angle: 20° Downward

Casting speed: 0.55 m.min⁻¹;

No gas bubbling.

TABLE 5.12. Effect of SEN submerged depth on inclusion removal.

Sample No	Submerged depth (mm)	Volume of colourless paraffin in the top layer (ml)	Volume of coloured paraffin injected $V_{injected}$ (ml)	Injection time (min)	Absorbance	Volume into top layer $V_{in\ slag}$ (ml)	Removal ratio η (%)
82	175	150	5.0	9.90	0.280	3.074	61.48
83	150	150	5.0	10.20	0.265	2.744	54.87
84	125	150	5.0	10.23	0.223	2.400	48.00
85	100	150	5.0	10.65	0.191	2.020	40.40
86	75	150	5.0	9.95	0.126	1.251	25.02
87	50	150	5.0	9.65	0.066	0.541	10.82

SEN: Nozzle 11; Port Angle: 25° Downward

Casting speed: 0.55 m.min⁻¹;

No gas bubbling.

TABLE 5.13. Effect of gas bubbling on inclusion removal.

Sample No	Submerged depth (mm)	Argon gas flow rate (L.min ⁻¹)	Volume of coloured paraffin injected V _{injected} (ml)	Injection time (min)	Absorbance	Volume into top layer V _{in slag} (ml)	Removal ratio η (%)
34	175	1.00	10.0	14.75	0.051	0.121	1.21
35	150	1.00	10.0	14.80	0.050	0.117	1.17
36	125	1.00	10.0	14.35	0.048	0.109	1.09
37	100	1.00	10.0	14.91	0.045	0.098	0.98
38	75	1.00	10.0	14.80	0.043	0.090	0.90
39	50	1.00	10.0	14.92	0.046	0.101	1.01
40	175	0.50	10.0	14.62	0.120	0.393	3.93
41	150	0.50	10.0	14.58	0.110	0.354	3.54
42	125	0.50	10.0	14.90	0.109	0.350	3.50
43	100	0.50	10.0	14.67	0.105	0.334	3.34
44	75	0.50	10.0	14.59	0.098	0.307	3.07
45	50	0.50	10.0	14.26	0.082	0.243	2.43
46	175	0.25	10.0	14.82	0.181	0.634	6.34
47	150	0.25	10.0	14.61	0.152	0.520	5.20
48	125	0.25	10.0	14.36	0.131	0.437	4.37
49	100	0.25	10.0	14.64	0.119	0.389	3.89
50	75	0.25	10.0	14.47	0.102	0.322	3.22
51	50	0.25	10.0	14.58	0.082	0.243	2.43

continued on next page.

TABLE 5.1.3. Continued.

Sample No	Submerged depth (mm)	Argon gas flow rate (L.min ⁻¹)	Volume of coloured paraffin injected V _{injected} (ml)	Injection time (min)	Absorbance	Volume into top layer V _{in slag} (ml)	Removal ratio η (%)
1	175	0.00	10.0	14.61	0.234	0.843	8.43
2	150	0.00	10.0	14.52	0.232	0.835	8.35
3	125	0.00	10.0	14.75	0.221	0.792	7.92
4	100	0.00	10.0	14.67	0.202	0.717	7.17
5	75	0.00	10.0	14.80	0.191	0.673	6.73
6	50	0.00	10.0	14.73	0.162	0.559	5.59
7	25	0.00	10.0	14.73	0.147	0.500	5.00
8	150	0.00	10.0	14.51	0.228	0.819	8.19
9	125	0.00	10.0	14.48	0.219	0.784	7.84
10	100	0.00	10.0	14.71	0.210	0.748	7.48
11	75	0.00	10.0	14.42	0.189	0.666	6.66
12	50	0.00	10.0	14.64	0.169	0.587	5.87
13	25	0.00	10.0	14.56	0.150	0.512	5.12

Volume of colourless paraffin in the top layer: 50 ml;

SEN: Nozzle 1;

Casting speed: 1.33 m.min⁻¹.

TABLE 5.14. Effect of gas bubbling on inclusion removal.

Sample No	Submerged depth (mm)	Argon gas flow rate (L.min ⁻¹)	Volume of coloured paraffin injected V _{injected} (ml)	Injection time (min)	Absorbance	Volume into top layer V _{in slag} (ml)	Removal ratio η (%)
174	200	1.00	5.0	12.33	0.247	2.68	53.66
175	175	1.00	5.0	12.33	0.185	1.95	38.99
176	150	1.00	5.0	12.50	0.135	1.36	27.15
177	125	1.00	6.0	13.60	0.147	1.50	25.00
178	100	1.00	5.0	11.85	0.131	1.31	26.21
179	75	1.00	5.0	11.42	0.217	2.33	46.56
168	200	0.50	5.0	10.40	0.248	2.70	53.90
169	175	0.50	5.0	10.66	0.217	2.33	46.56
170	150	0.50	5.0	11.00	0.207	2.21	44.20
171	125	0.50	5.0	11.25	0.174	1.82	36.39
172	100	0.50	5.0	11.33	0.155	1.59	31.89
173	75	0.50	5.0	11.42	0.205	2.19	43.72
180	200	0.25	5.0	10.85	0.303	3.35	67.04
181	175	0.25	5.0	10.25	0.296	3.26	65.26
182	150	0.25	5.0	10.60	0.270	2.96	59.11
183	125	0.25	5.0	11.20	0.203	2.16	43.25
184	100	0.25	5.0	11.83	0.171	1.78	35.68
185	75	0.25	5.0	11.50	0.214	2.29	45.85

Volume of colourless paraffin in the top layer: 150 ml;

SEN: Nozzle 4 (Horizontal);

Casting speed: 0.55 m.min⁻¹.

TABLE 5.15. Effect of gas bubbling on inclusion removal.

Sample No	Submerged depth (mm)	Argon gas flow rate (L.min ⁻¹)	Volume of coloured paraffin injected V _{injected} (ml)	Injection time (min)	Absorbance	Volume into top layer V _{in slag} (ml)	Removal ratio η (%)
190	200	1.00	5.0	12.25	0.376	4.21	84.20
191	175	1.00	5.0	12.30	0.350	3.90	78.05
192	150	1.00	5.0	12.41	0.264	2.88	47.51
193	125	1.00	5.0	12.50	0.240	2.60	52.01
186	200	0.50	5.0	11.30	0.292	3.22	64.32
187	175	0.50	5.0	11.66	0.282	3.10	61.95
188	150	0.50	5.0	11.00	0.273	2.99	59.82
189	125	0.50	5.0	11.25	0.196	2.08	41.59
194	200	0.25	5.0	13.00	0.304	3.36	67.16
195	175	0.25	5.0	12.25	0.307	3.39	67.87
196	150	0.25	5.0	11.60	0.274	3.00	60.06
197	125	0.25	5.0	11.30	0.263	2.87	57.45

Volume of colourless paraffin in the top layer: 150 ml;

SEN: Nozzle 5 (25° Upward);

Casting speed: 0.55 m.min⁻¹.

TABLE 5.16. Effect of gas bubbling on inclusion removal.

Sample No	Submerged depth (mm)	Argon gas flow rate (L.min ⁻¹)	Volume of coloured paraffin injected V _{injected} (ml)	Injection time (min)	Absorbance	Volume into top layer V _{in slag} (ml)	Removal ratio η (%)
156	200	1.00	5.0	11.56	0.270	2.96	59.11
157	175	1.00	5.0	11.50	0.215	2.30	46.09
158	150	1.00	5.0	11.80	0.148	1.51	30.23
159	125	1.00	6.0	13.33	0.103	0.98	16.32
160	100	1.00	5.0	11.15	0.076	0.66	13.19
161	75	1.00	5.0	11.35	0.051	0.36	7.27
150	200	0.50	5.0	11.40	0.274	3.00	60.06
151	175	0.50	5.0	10.50	0.238	2.58	51.53
152	150	0.50	5.0	11.15	0.178	1.87	37.33
153	125	0.50	5.0	11.30	0.128	1.27	25.50
154	100	0.50	5.0	11.33	0.096	0.90	17.92
155	75	0.50	5.0	11.32	0.061	0.48	9.64
162	200	0.25	5.0	11.85	0.303	3.35	67.04
163	175	0.25	5.0	11.55	0.245	2.65	53.00
164	150	0.25	5.0	11.60	0.190	2.01	40.17
165	125	0.25	5.0	11.40	0.136	1.37	27.39
166	100	0.25	5.0	11.63	0.095	0.88	17.96
167	75	0.25	5.0	11.10	0.068	0.56	11.30

Volume of colourless paraffin in the top layer: 150 ml;

SEN: Nozzle 10 (20° Downward)

Casting speed: 0.55 m.min⁻¹.

TABLE 5.17. Effect of casting speed on inclusion removal.

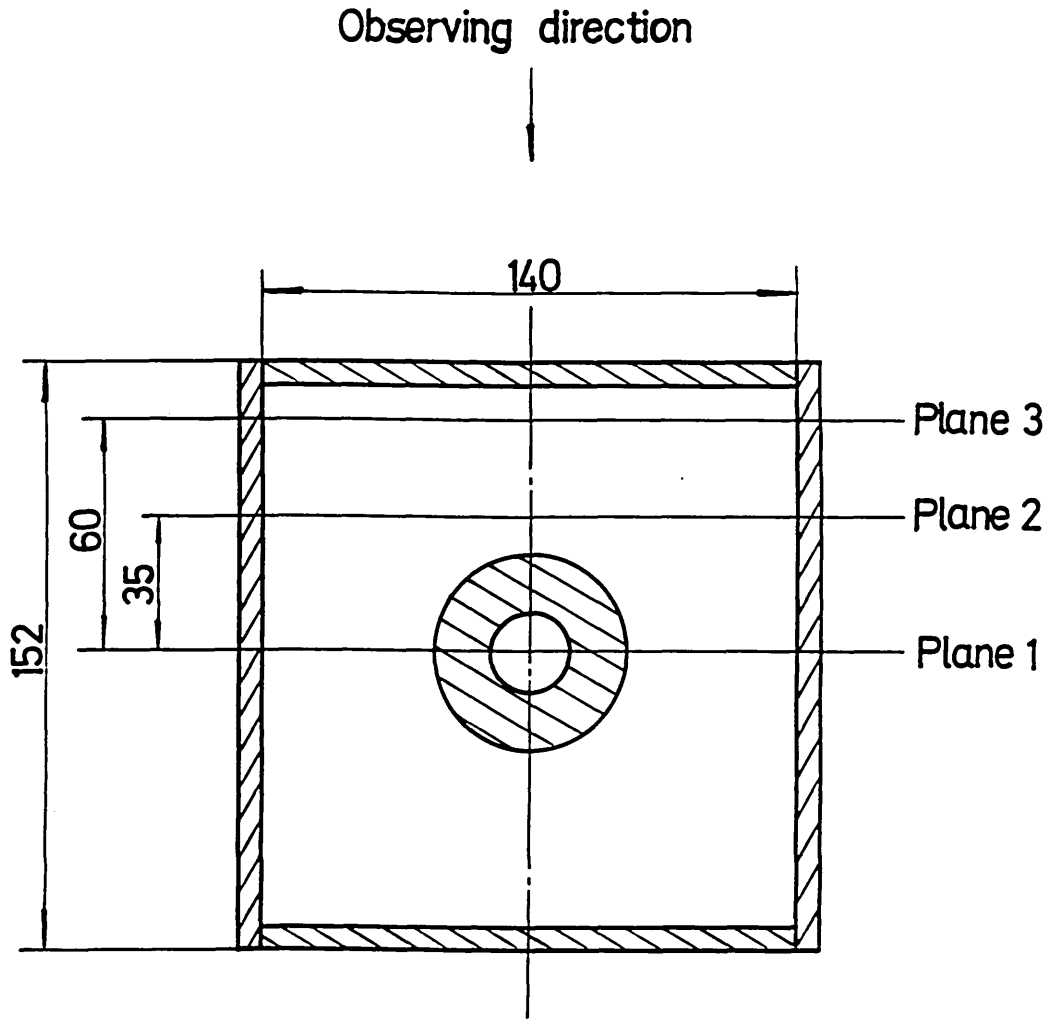
Sample No	Casting speed (m.min ⁻¹)	Volume of colourless paraffin in the top layer (ml)	Volume of coloured paraffin injected $V_{injected}$ (ml)	Injection time (min)	Absorbance	Volume into top layer $V_{in\ slag}$ (ml)	Removal ratio η (%)
52	1.00	50	10.0	9.40	0.186	0.654	6.54
53	1.25	50	10.0	9.34	0.167	0.579	5.79
54	1.50	50	10.0	9.88	0.157	0.539	5.39
55	1.75	50	10.0	9.50	0.151	0.516	5.16
56	2.00	50	10.0	9.57	0.147	0.500	5.00

SEN: Nozzle 3;

SEN submerged depth: 125 mm;

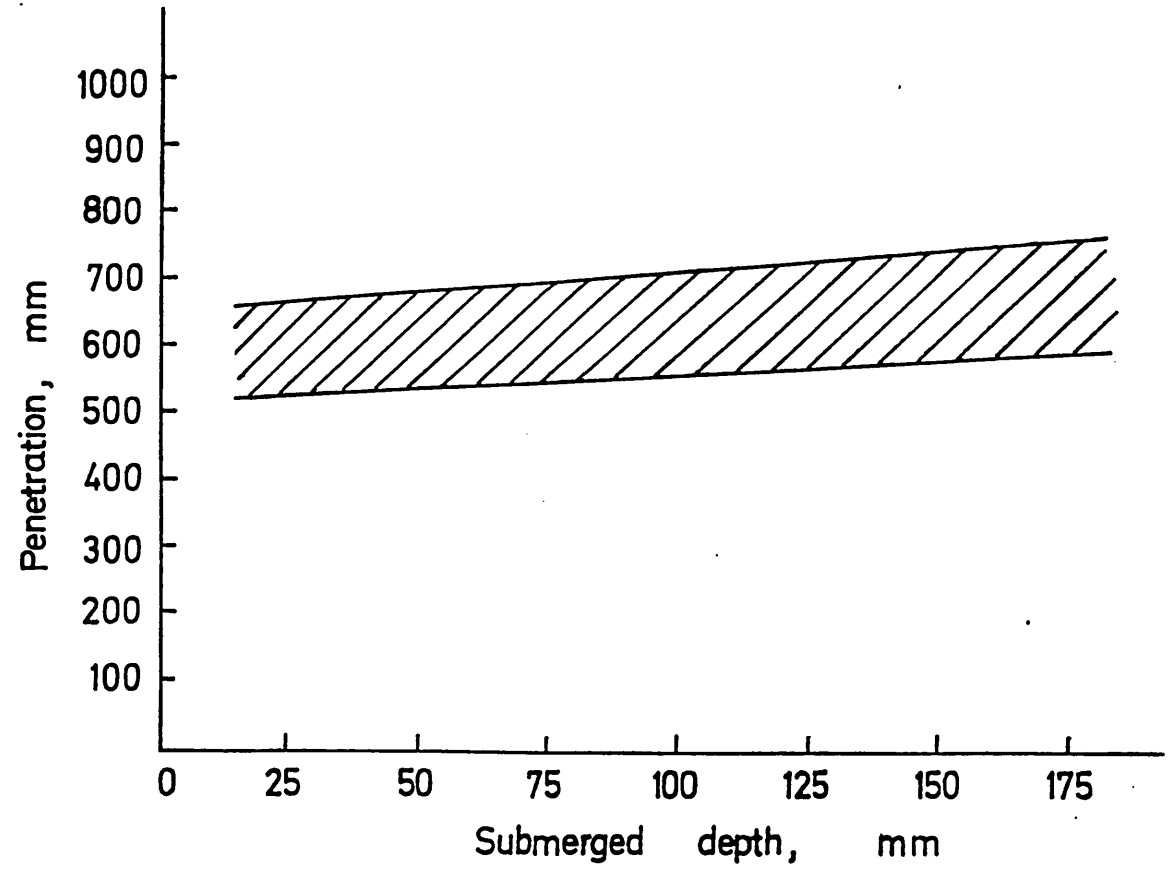
No gas bubbling.

Figure 5.1



The position of the view planes.

Figure 5.2

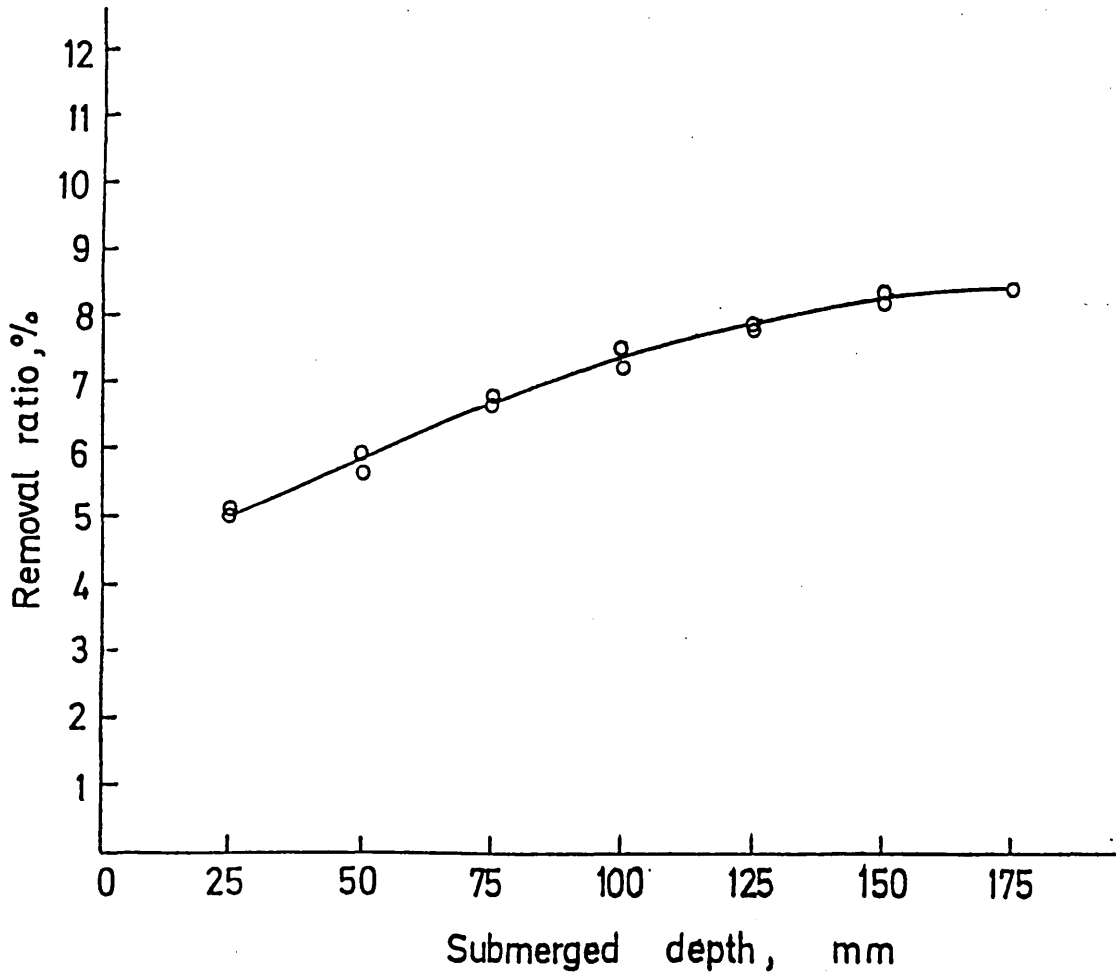


Effect of SEN submerged depth on length of jet penetration zone.

SEN: Nozzle 1;

Casting speed: 1.33 m.min⁻¹.

Figure 5.3



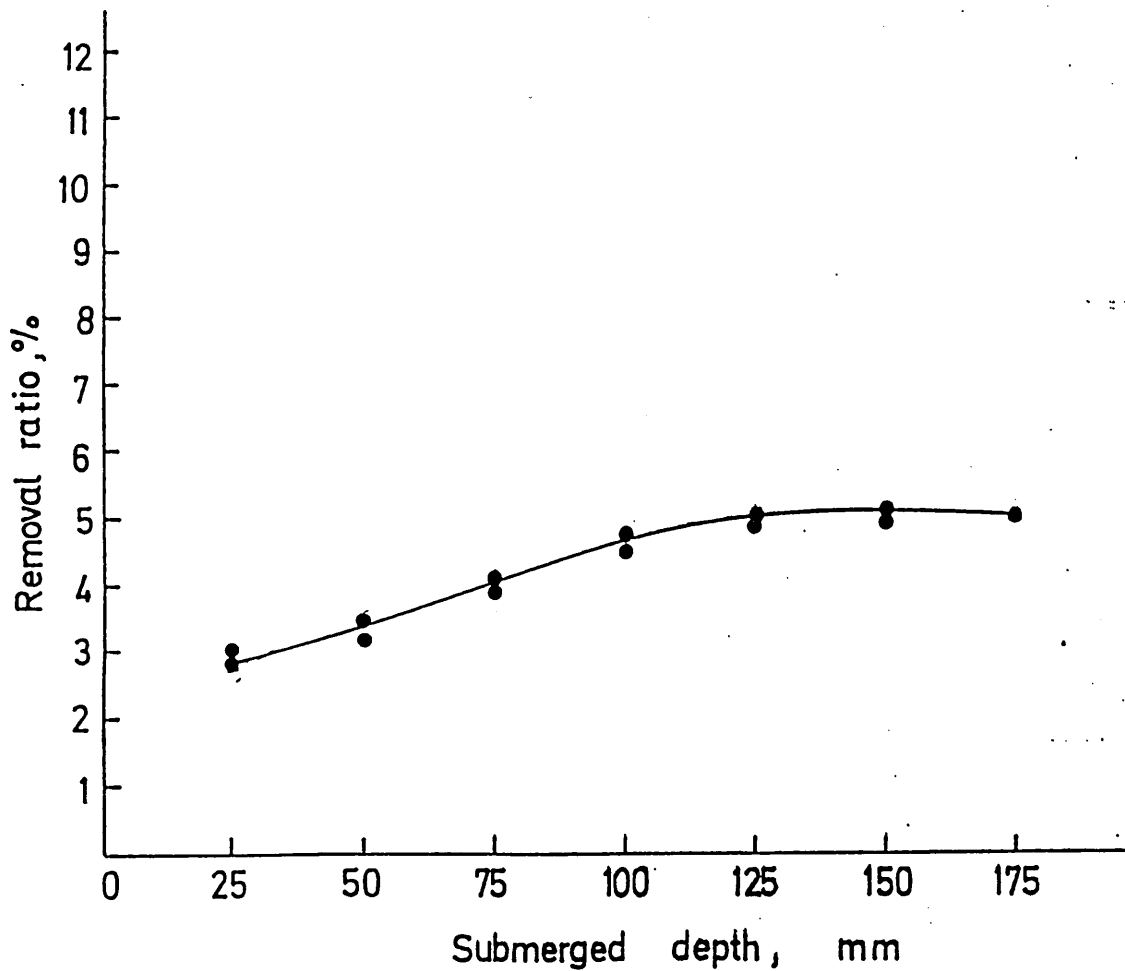
Effect of SEN submerged depth on the proportion of inclusion removed to the 'slag' layer.

SEN: Nozzle 1;

Casting speed: $1.33 \text{ m}\cdot\text{min}^{-1}$;

No gas bubbling.

Figure 5.4

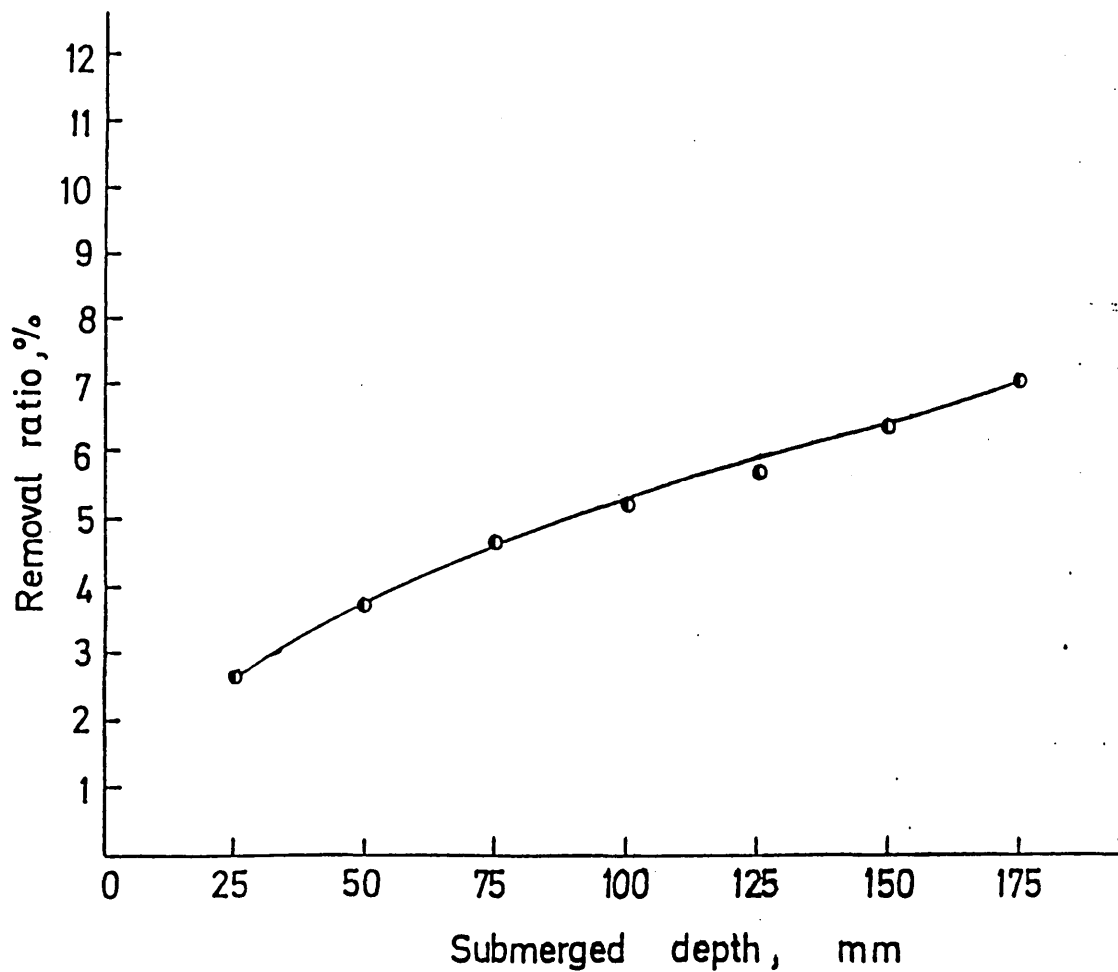


Effect of SEN submerged depth on the proportion of inclusion removed to the 'slag' layer.

SEN: Nozzle 2;

Casting speed: 1.33 m.min⁻¹;

No gas bubbling.

Figure 5.5

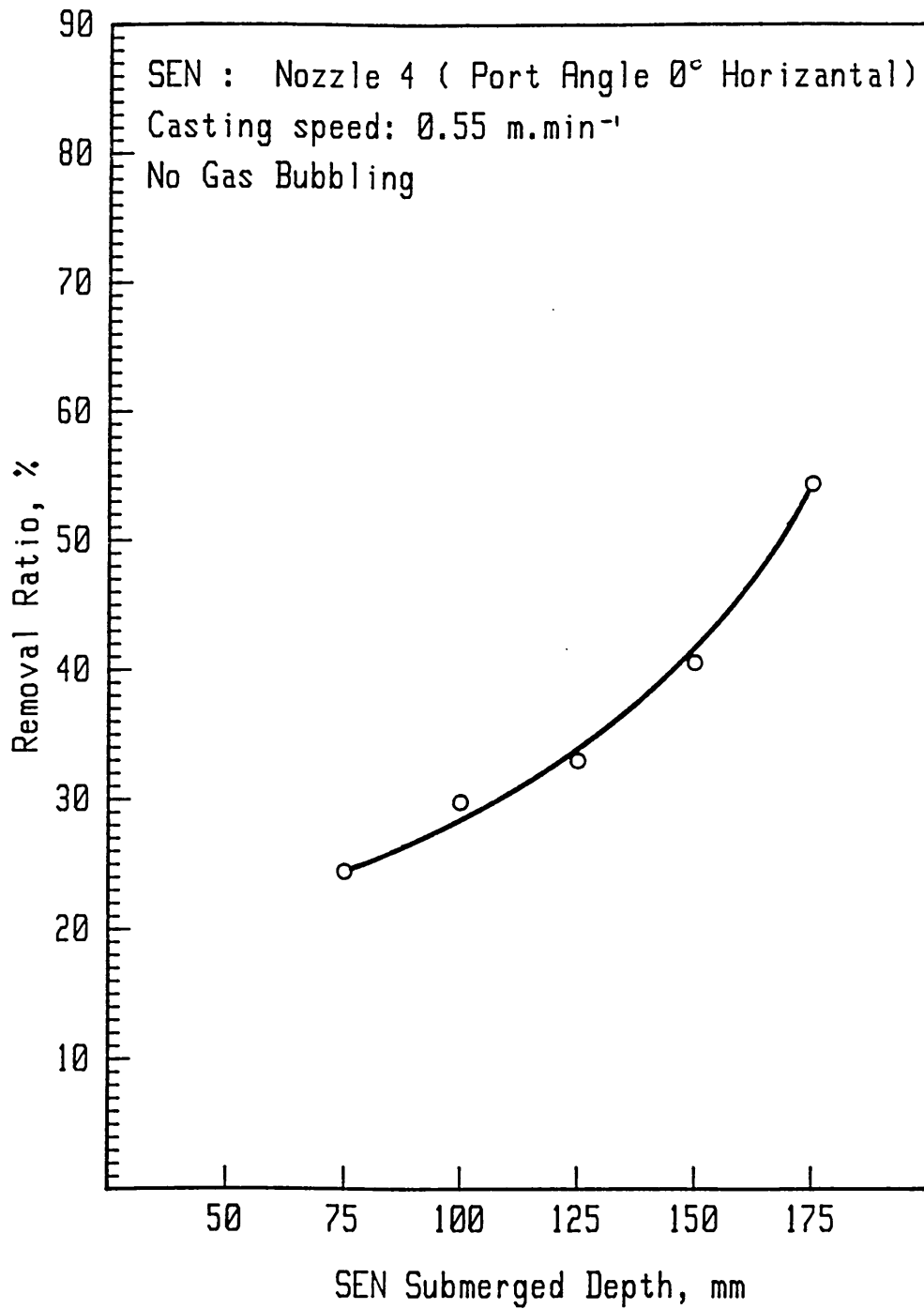
Effect of SEN submerged depth on the proportion of inclusion removed to the 'slag' layer.

SEN: Nozzle 3;

Casting speed: $1.33 \text{ m}\cdot\text{min}^{-1}$;

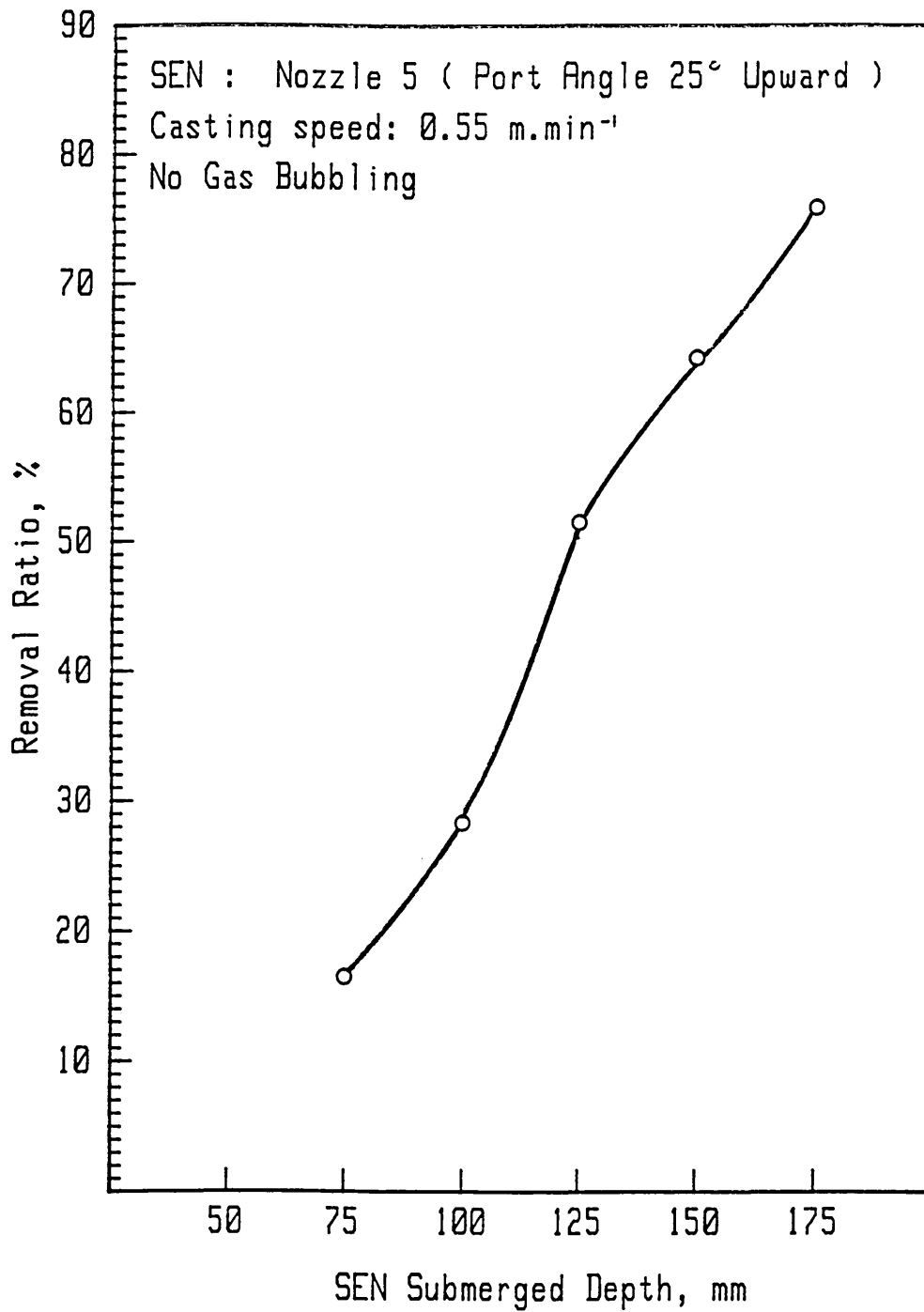
No gas bubbling.

Figure 5.6



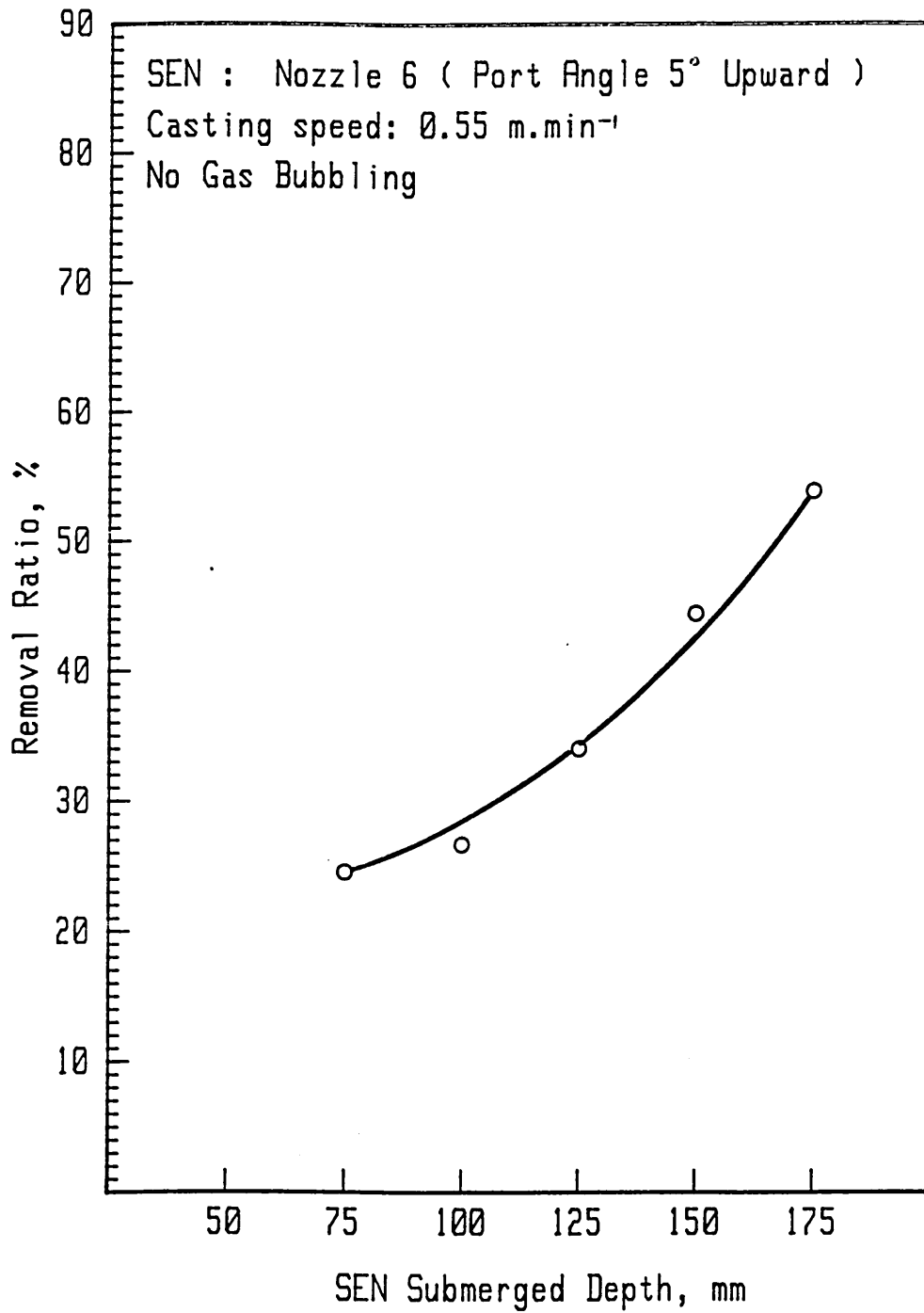
Effect of SEN Submerged Depth on the Proportion of Inclusion Removed into the 'slag' Layer

Figure 5.7



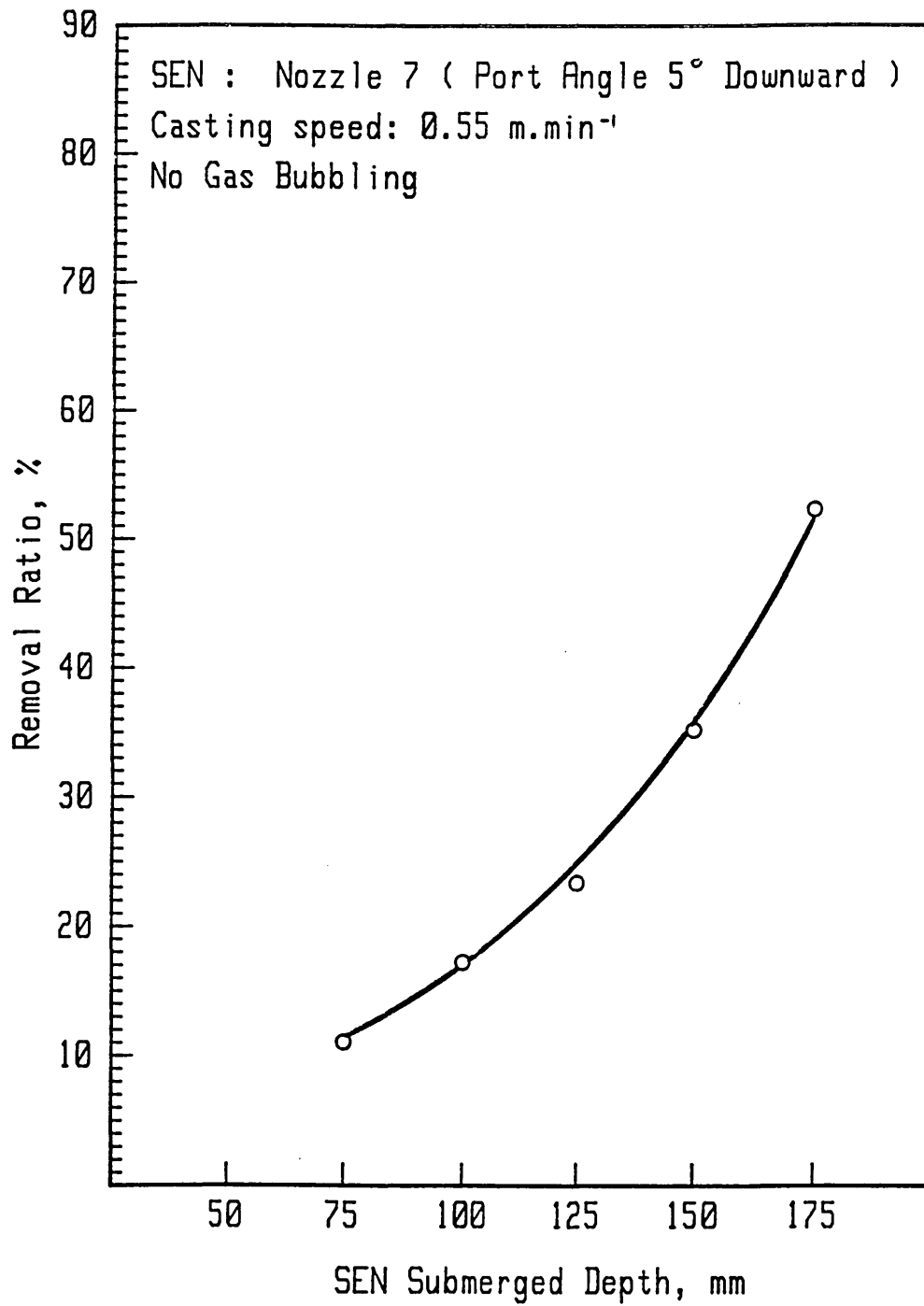
Effect of SEN Submerged Depth on the Proportion of
Inclusion Removed into the 'slag' Layer

Figure 5.8



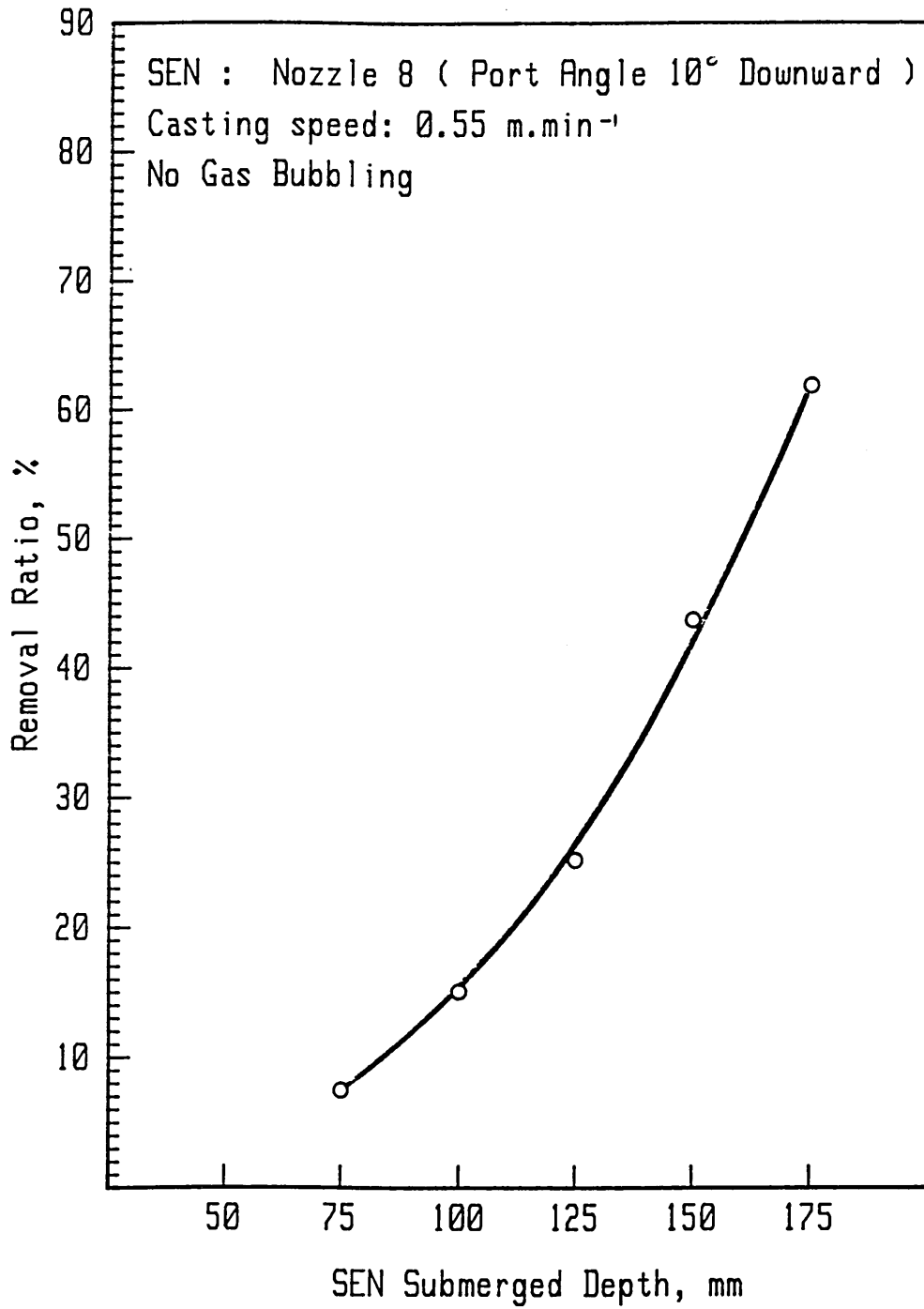
Effect of SEN Submerged Depth on the Proportion of
Inclusion Removed into the 'slag' Layer

Figure 5.9



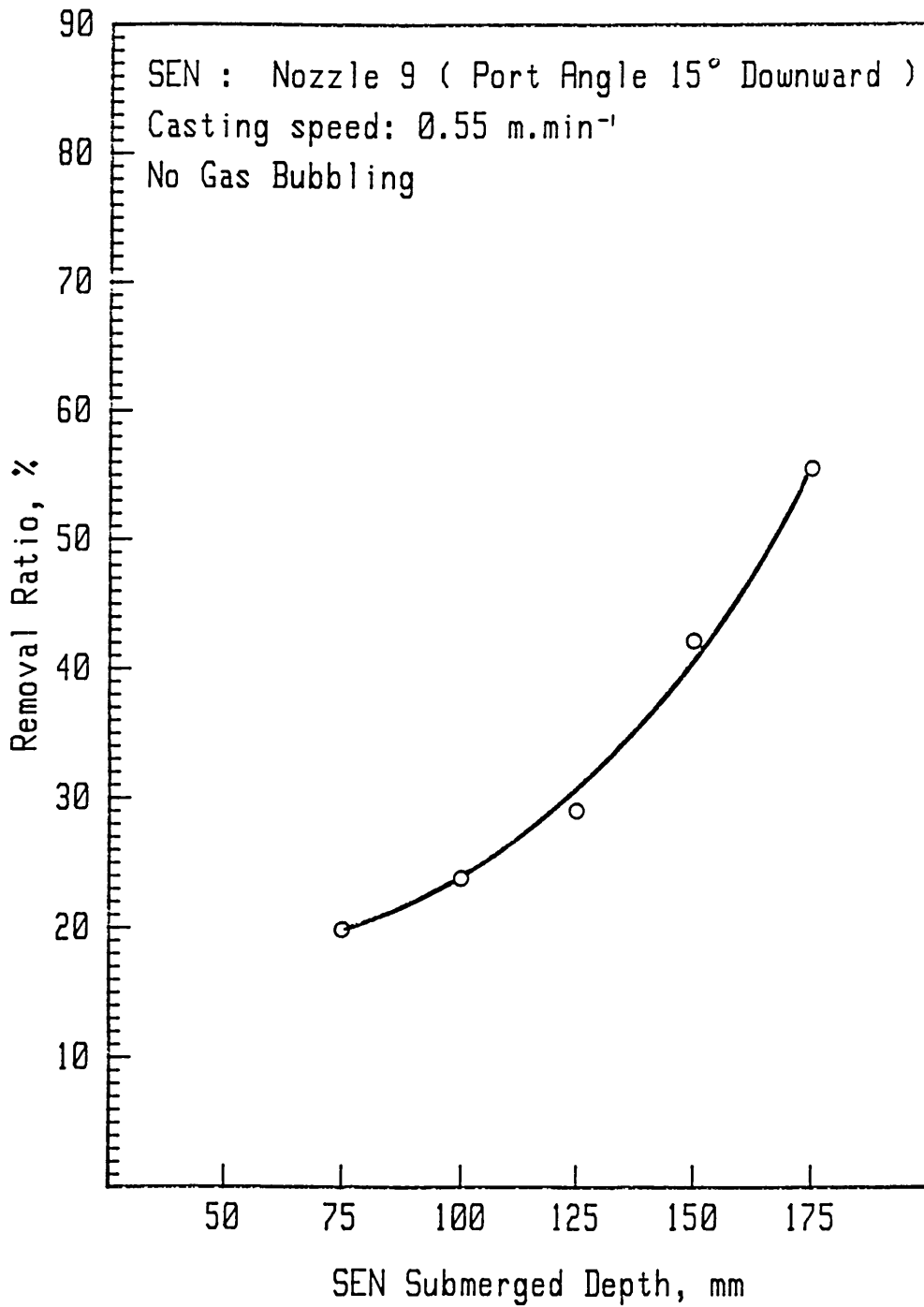
Effect of SEN Submerged Depth on the Proportion of Inclusion Removed into the 'slag' Layer

Figure 5.10



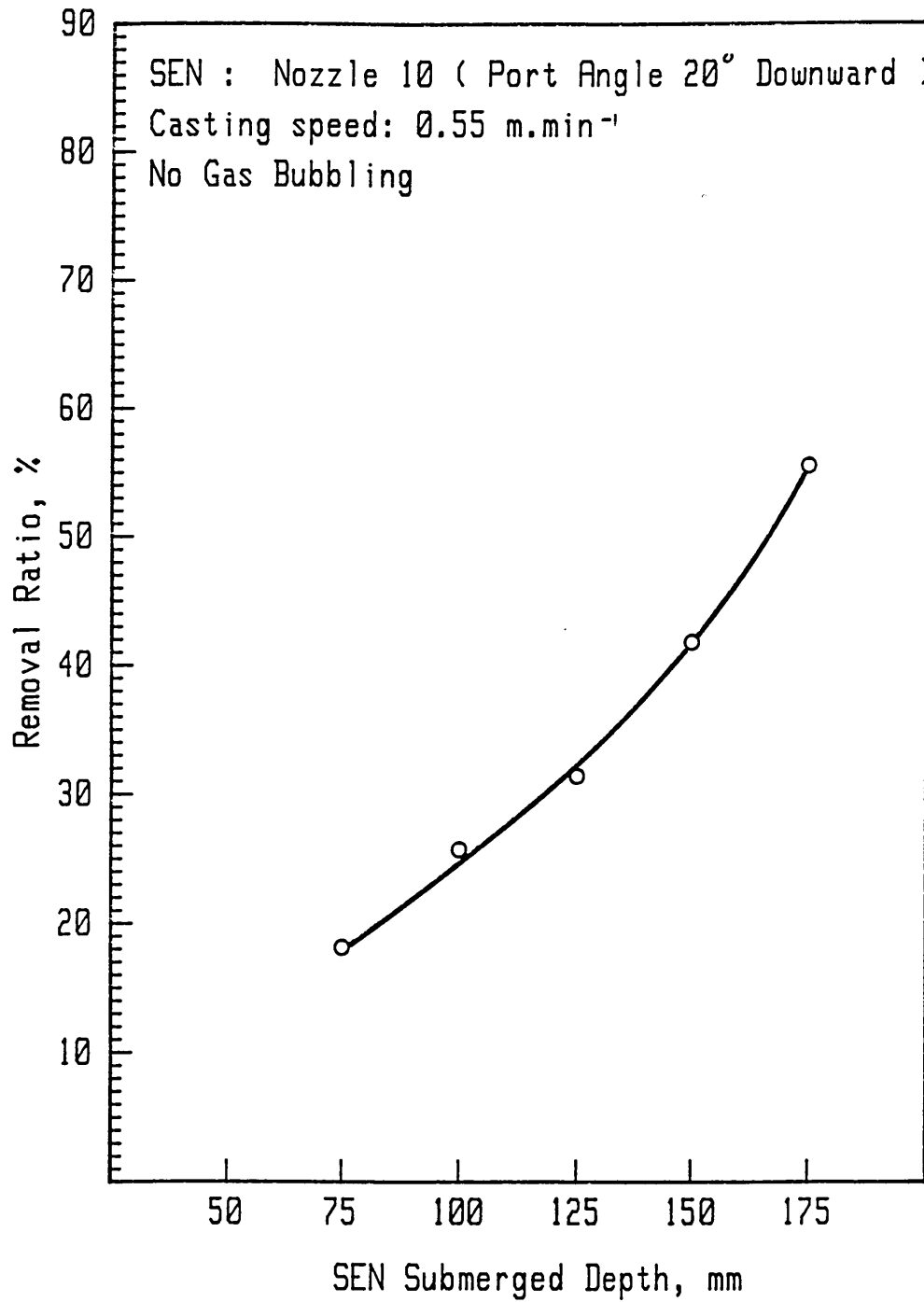
Effect of SEN Submerged Depth on the Proportion of Inclusion Removed into the 'slag' Layer

Figure 5.11



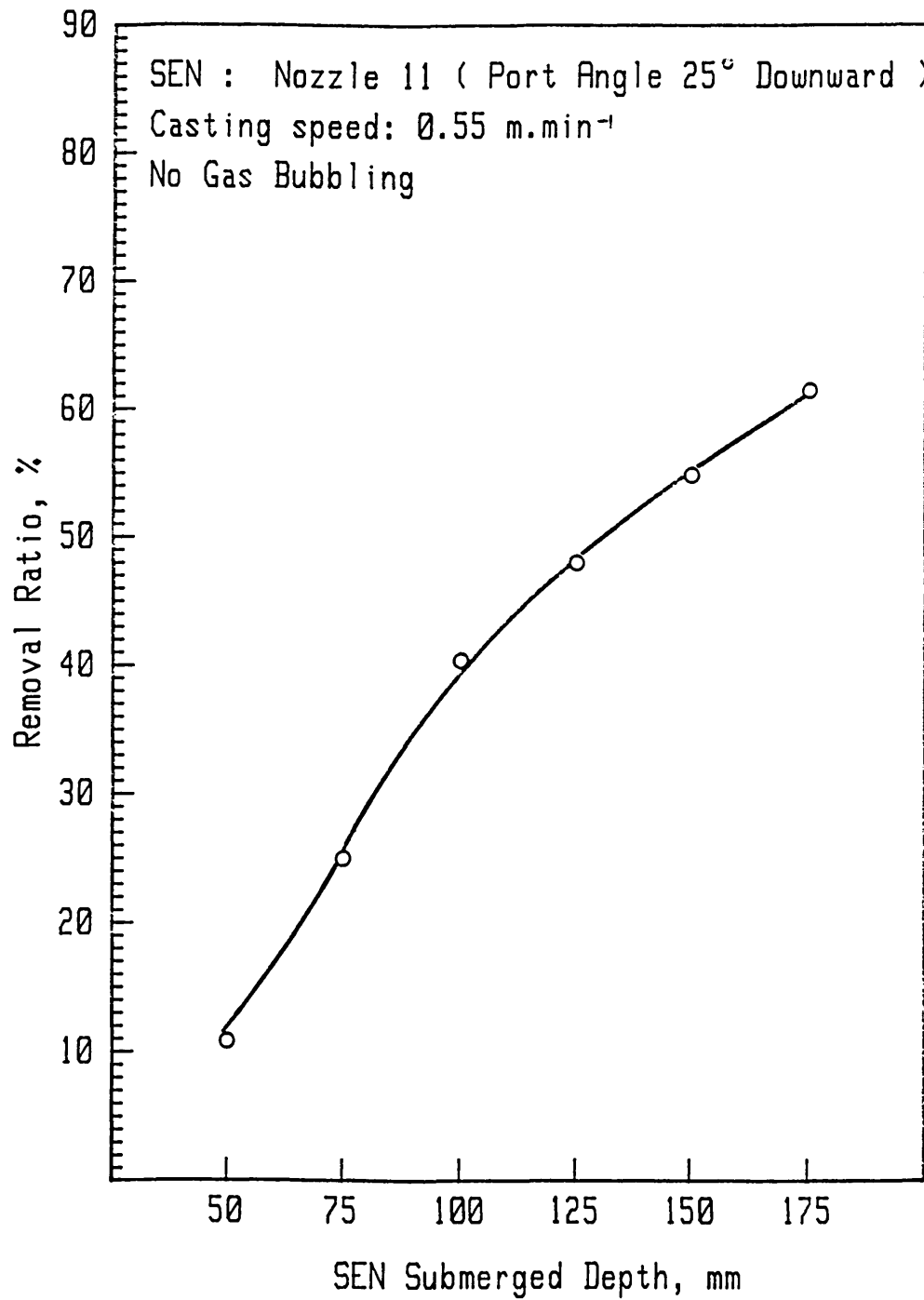
Effect of SEN Submerged Depth on the Proportion of Inclusion Removed into the 'slag' Layer

Figure 5.12



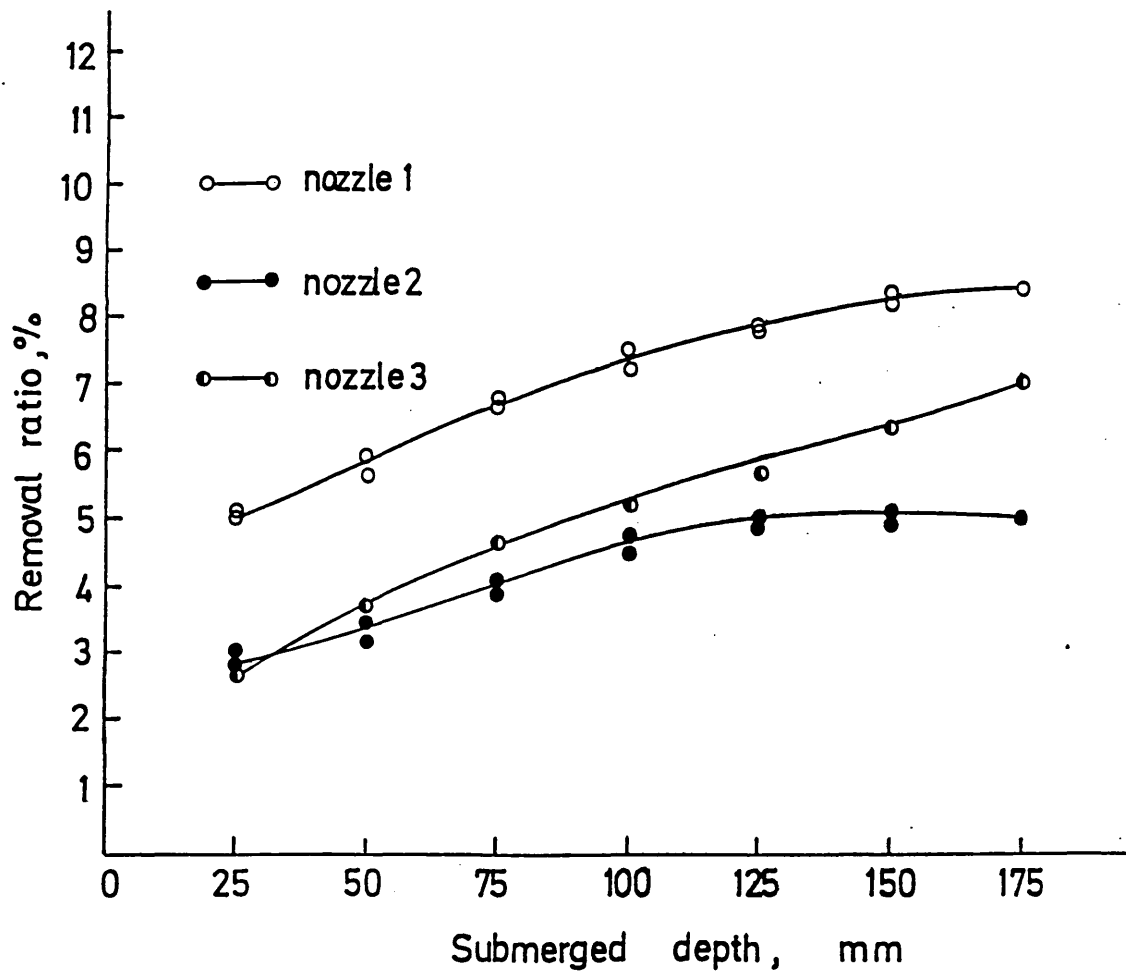
Effect of SEN Submerged Depth on the Proportion of
Inclusion Removed into the 'slag' Layer

Figure 5.13



Effect of SEN Submerged Depth on the Proportion of
Inclusion Removed into the 'slag' Layer

Figure 5.14

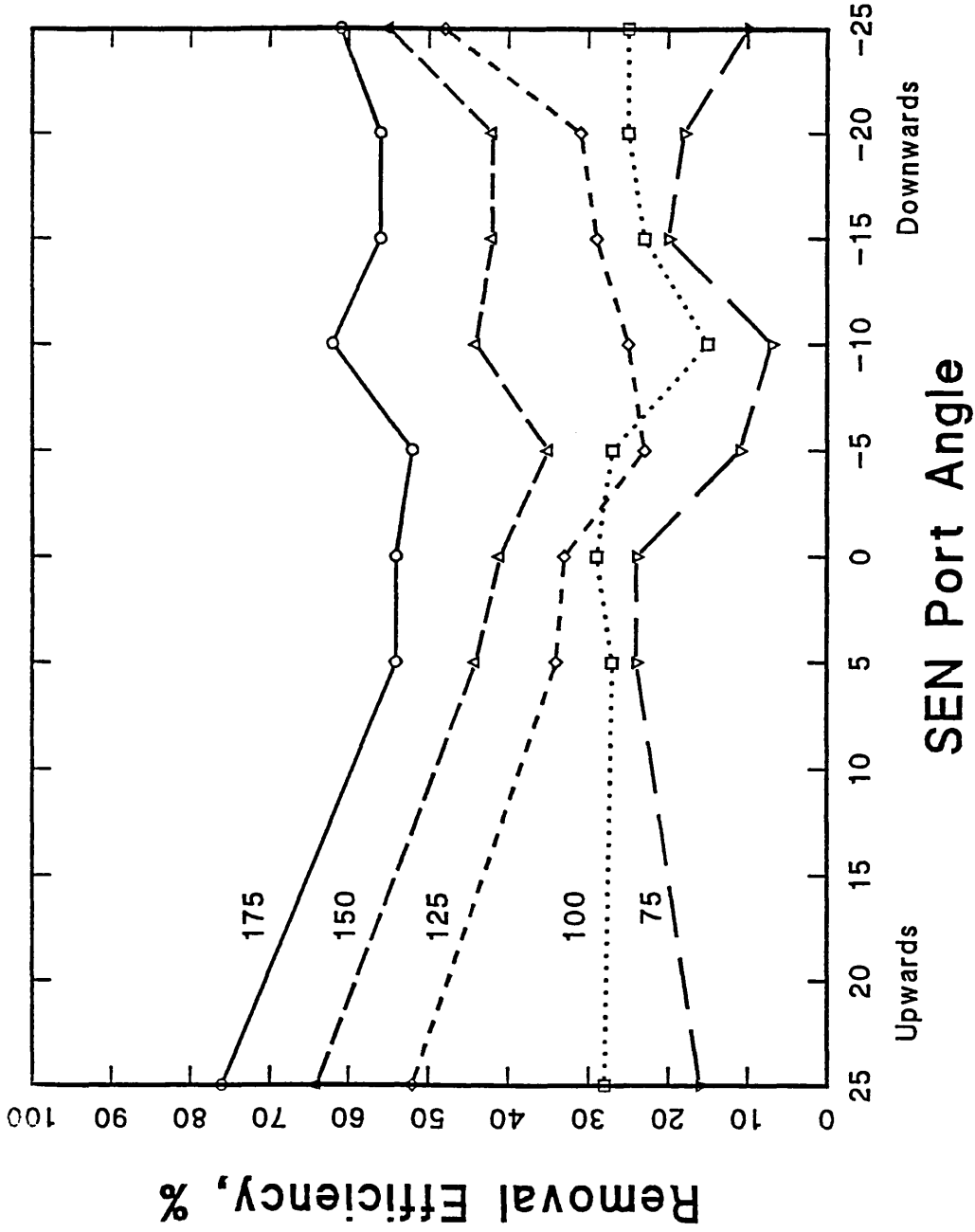


Effect of SEN geometry on the proportion of inclusion removed to the 'slag' layer.

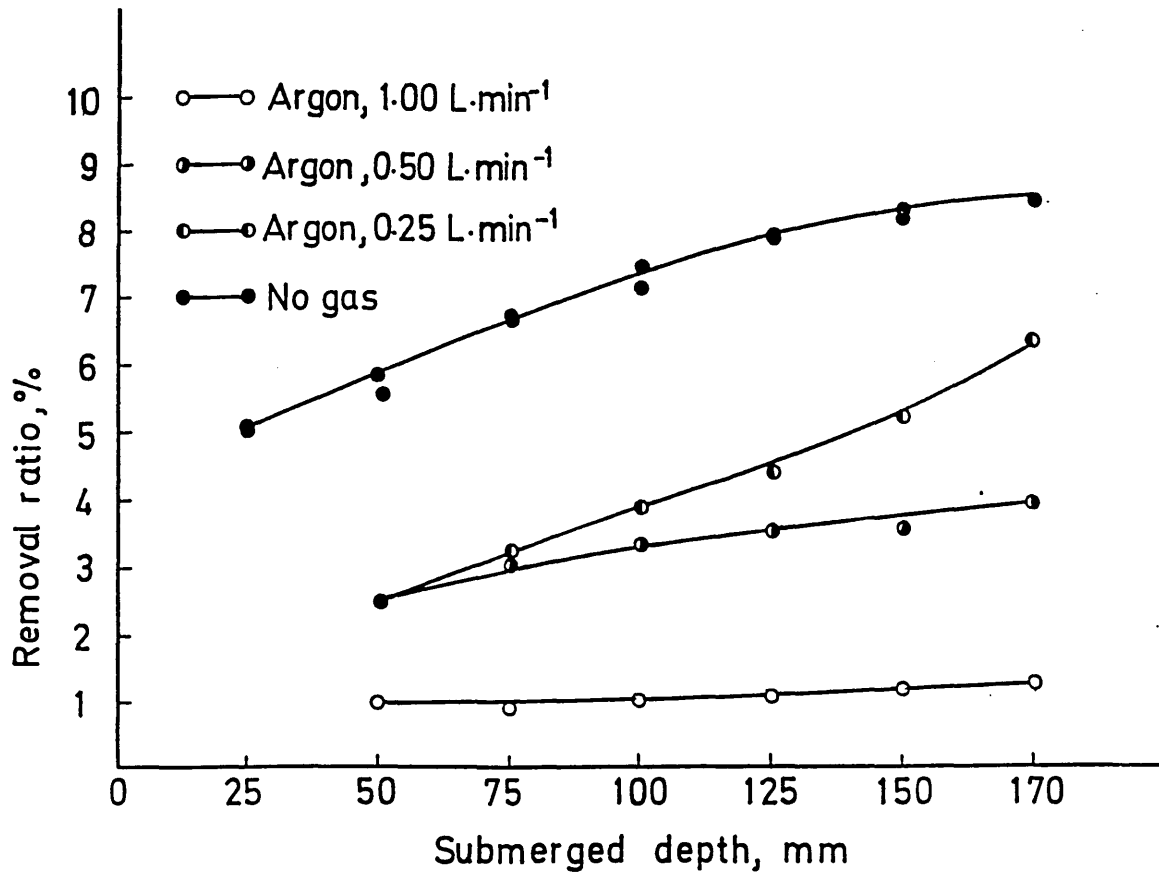
Casting speed: 1.33 m.min⁻¹;

No gas bubbling.

Figure 5.15



Effect of SEN port angle on the inclusion removal efficiency for different submerged depths (marked on each curve in mm)

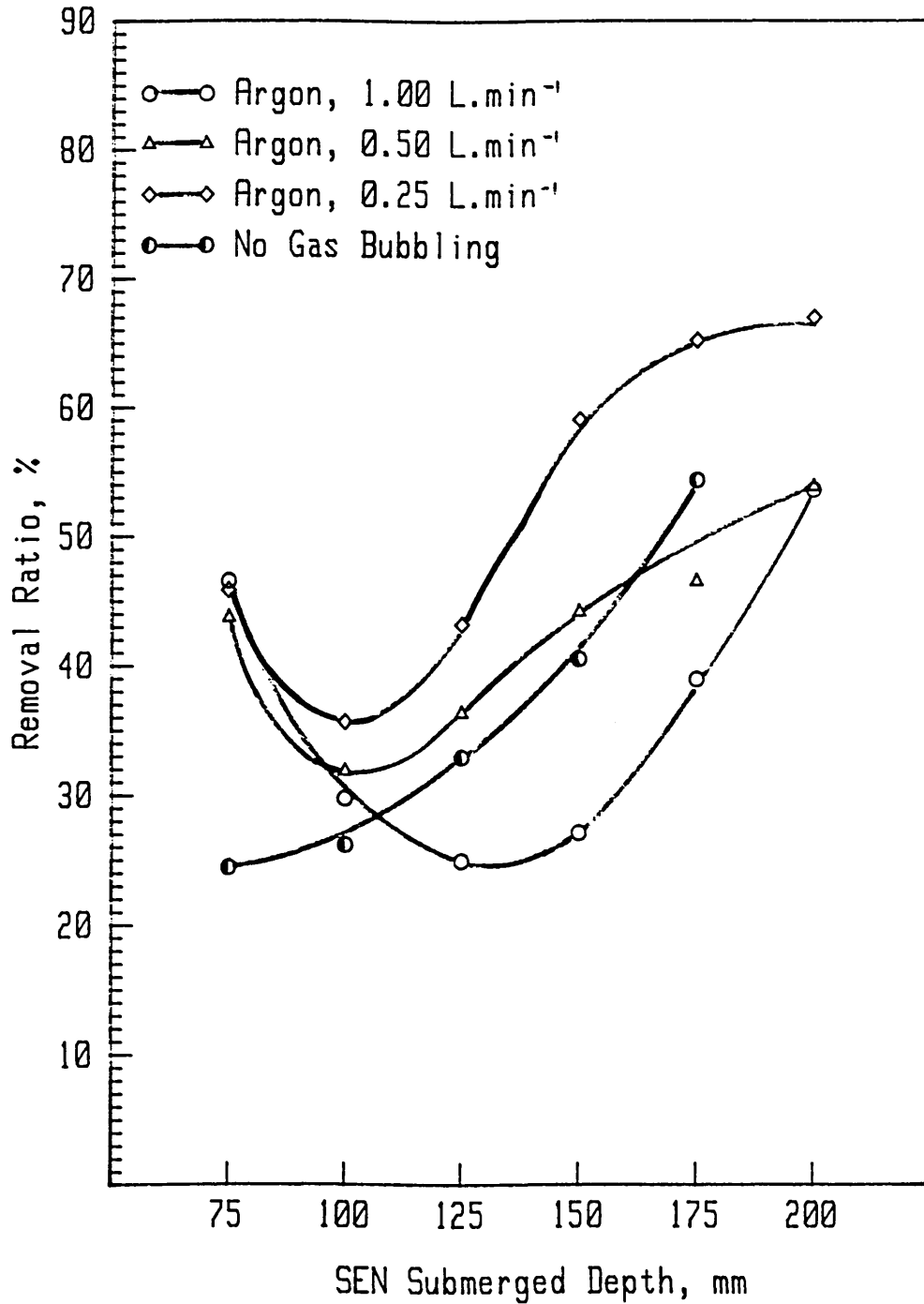
Figure 5.16

Effect of gas injection on the inclusion
removal ratio in the billet caster.

SEN: Nozzle 1;

Casting speed: 1.33 m·min⁻¹.

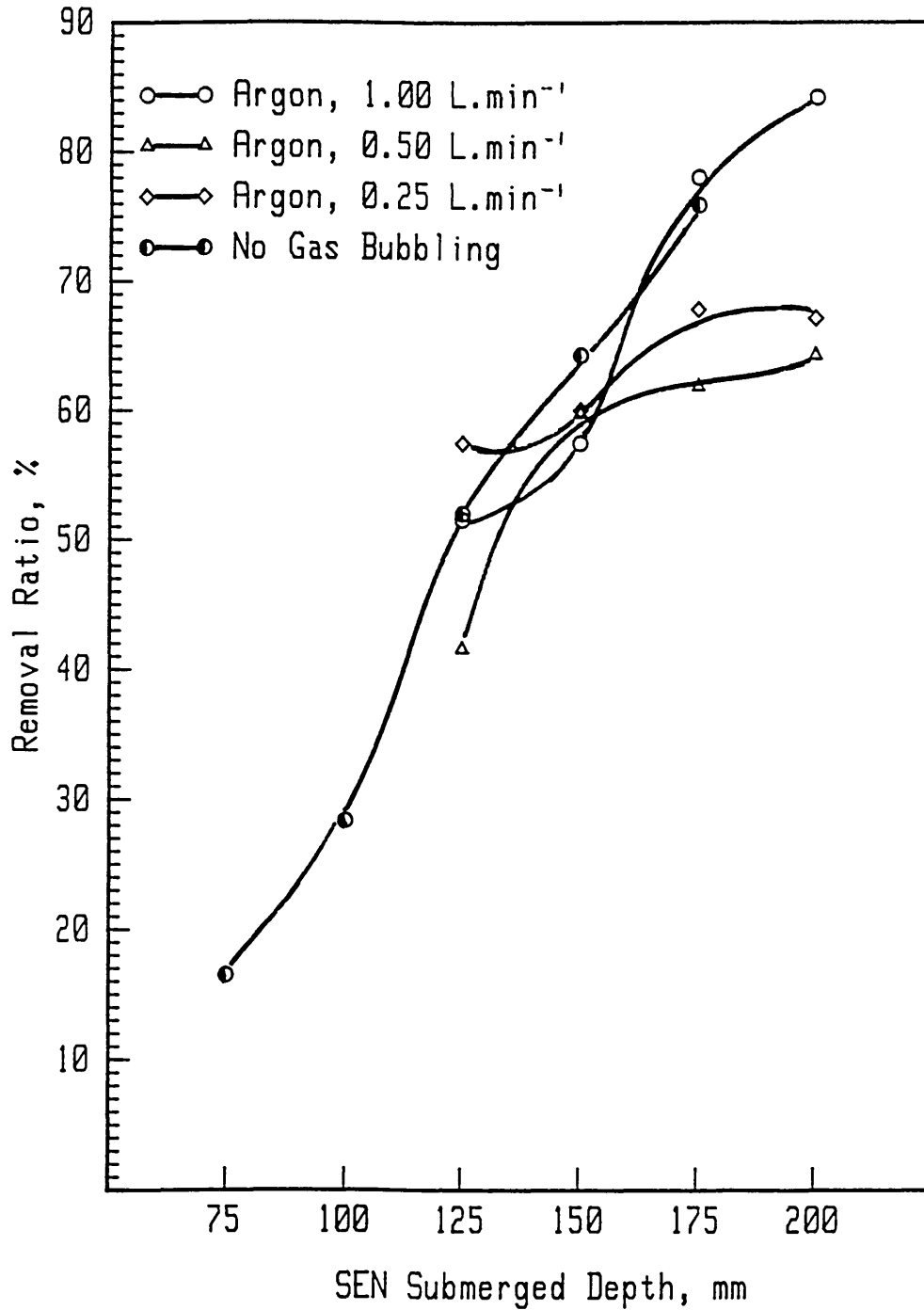
Figure 5.17



Effect of Gas Injection on the Inclusion
Removal Ratio in the Bloom Caster

SEN: Nozzle 4 (Port Angle 0 Horizontal)
Casting speed: 0.55 m.min⁻¹

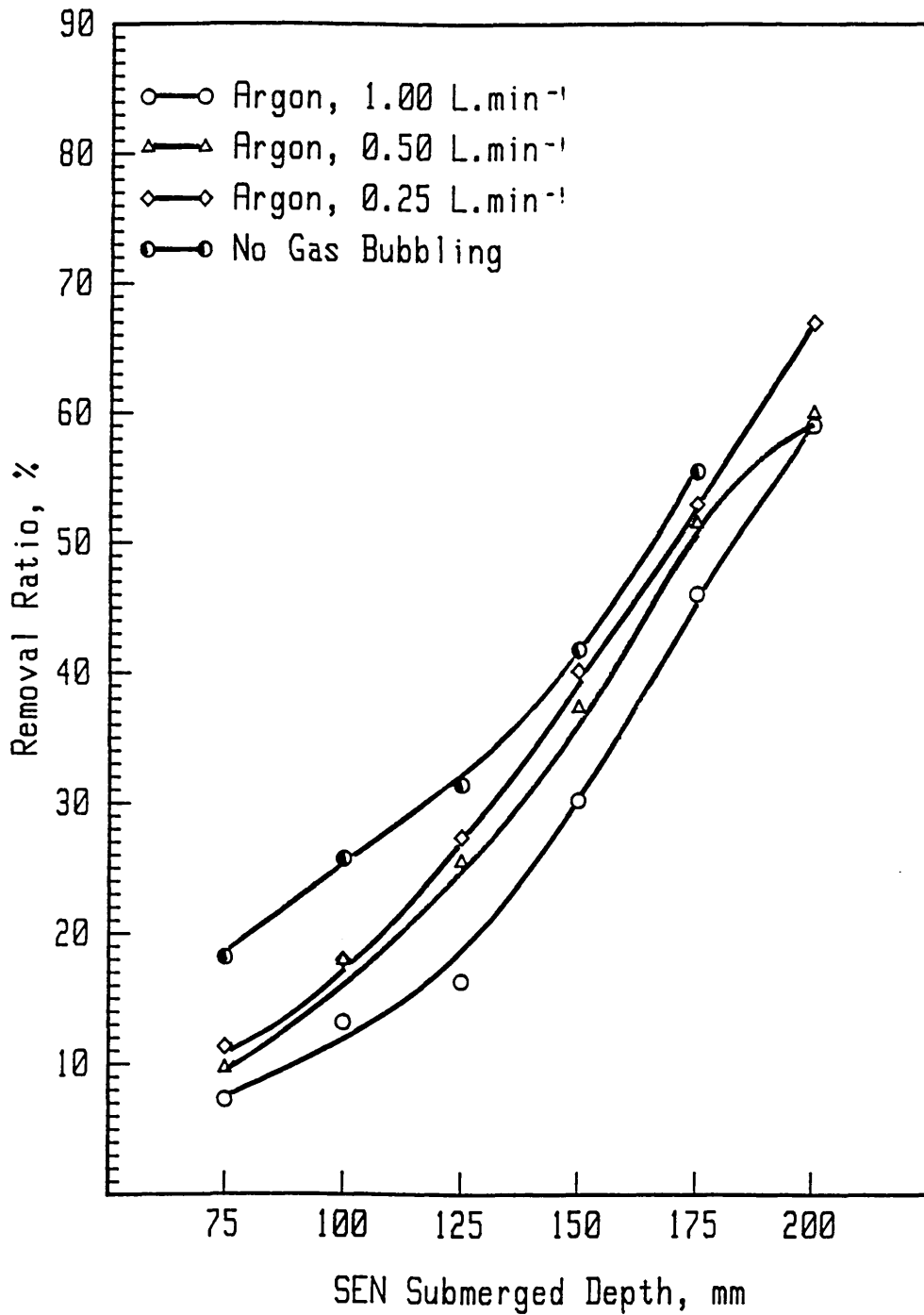
Figure 5.18



Effect of Gas Injection on the Inclusion
Removal Ratio in the Bloom Caster

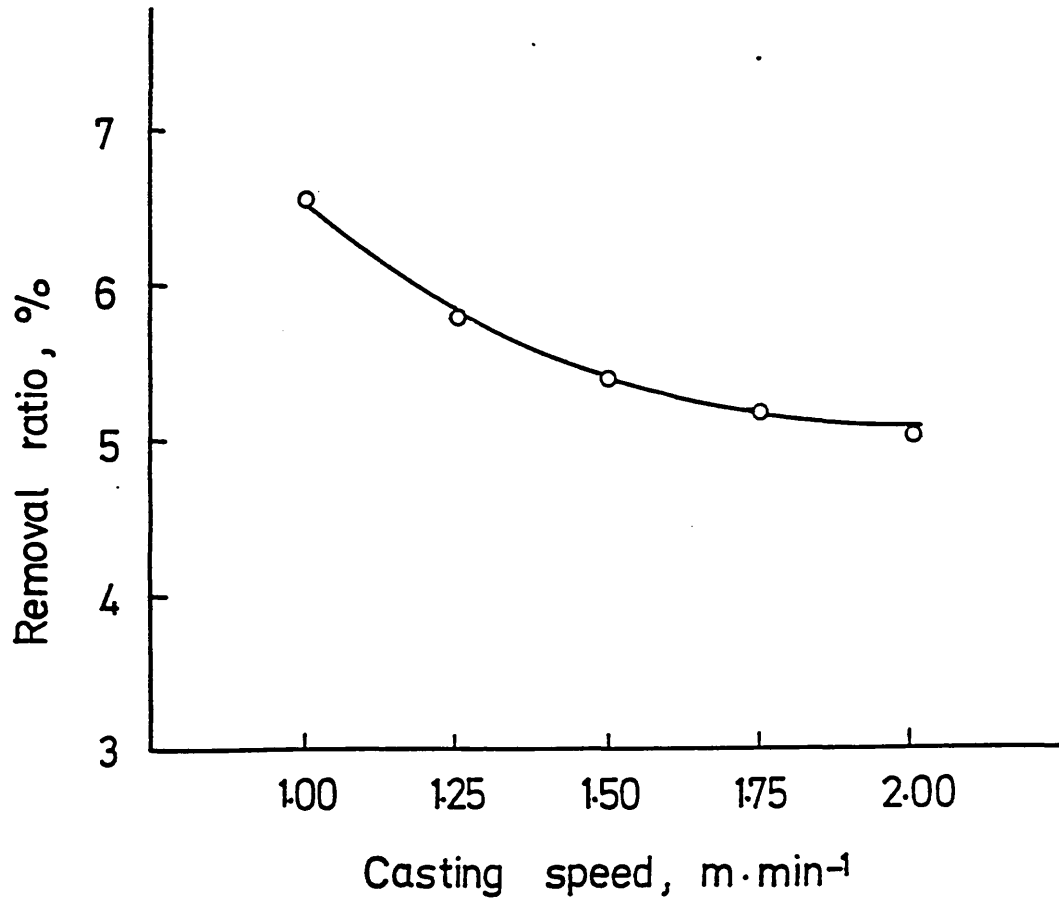
SEN: Nozzle 5 (Port Angle 25 Upward)
Casting speed: 0.55 m.min⁻¹

Figure 5.19



Effect of Gas Injection on the Inclusion Removal Ratio in the Bloom Caster

SEN: Nozzle 10 (Port Angle 20 Downward)
Casting speed: 0.55 m.min⁻¹

Figure 5.20

Effect of casting speed on the proportion of
inclusion removed to the 'slag' layer.

SEN: Nozzle 3;

No gas bubbling.

TABLE 5.18 Effect of SEN submerged depth on inclusion removal for big injection nozzle.

Sample No	Submerged depth (mm)	Volume of colourless paraffin in the top layer (ml)	Volume of coloured paraffin injected $V_{injected}$ (ml)	Injection time (min)	Absorbance	Volume into top layer $V_{in\ slag}$ (ml)	Removal ratio η (%)
200	220	150	5.0	13.30	0.344	3.831	76.62
201	200	150	5.0	13.20	0.318	3.524	70.48
202	175	150	5.0	13.01	0.260	2.837	56.74
203	150	150	5.0	13.06	0.195	2.062	41.24
204	125	150	5.0	13.05	0.163	1.689	33.78
205	100	150	5.0	13.07	0.121	1.192	23.84
206	75	150	5.0	13.25	0.096	0.896	17.92

SEN: Nozzle 4; Port Angle: 0° Horizontal

Casting speed: 0.55 m.min⁻¹;

No gas bubbling.

TABLE 5.19 Effect of SEN submerged depth on inclusion removal for small injection nozzle.

Sample No	Submerged depth (mm)	Volume of colourless paraffin in the top layer (ml)	Volume of coloured paraffin injected $V_{injected}$ (ml)	Injection time (min)	Absorbance	Volume into top layer $V_{in\ slag}$ (ml)	Removal ratio η (%)
210	220	150	3.0	20.33	0.064	0.518	17.25
211	200	150	3.0	19.83	0.059	0.458	15.28
212	175	150	3.0	19.92	0.051	0.364	12.12
213	150	150	3.0	20.00	0.032	0.230	7.67
214	125	150	3.0	20.25	0.032	0.230	7.67
215	100	150	3.0	19.80	0.020	0.140	4.67
216	75	150	3.0	20.16	0.017	0.120	4.00

SEN: Nozzle 4; Port Angle: 0° Horizontal

Casting speed: 0.55 m.min⁻¹;

No gas bubbling.

TABLE 5.20. Diameters of the particles generated from big injection nozzle.

No*	Diameters of the particles generated, μm							
1	147	136	81	157	101	177	121	154
	147	178	211	165	179	154	135	98
2	133	138	84	79	89	163	206	208
	149	111	156	86	137	114		
3	91	121	208	147	129	206	137	208
	123	135	142	171	129	178	136	
4	202	152	209	101	112	158	86	135
	129	212	158	197				
5	212	119	115	142	181	112	135	147
	158	145	152	202	115	167		
6	137	153	106	136	168	148	87	119
	152	148	207	109	156	213	201	
7	177	236	128	159	136	127	119	178
	148	146	135	108	95	146	153	
8	164	218	159	82	137	156	176	202
	94	108	178	153	168	162		
9	205	172	128	113	149	164	177	157
	130	146	208	90	163	117	167	172
10	165	144	138	108	126	158	178	165
	142	157	160	152	208			
11	182	169	118	133	159	173	119	98
	157	147	214	133	213	168	188	
12	98	214	182	178	139	129	198	154
	172	96	110	93	153	150	172	
13	171	138	122	188	95	168	153	161
	164	157	151	198	138			
14	143	183	161	114	156	149	153	204
	137	153	136	163	116	164	172	179
15	109	143	152	172	161	143		
	171	138	118	153	158	128	143	202
16	157	164	145	147	198	160	149	
	176	126	173	162	135	150	97	109
17	135	128	153	109	197	204	153	148
	153	147	162	163	169	129	134	128
18	106	145	147	91	206	128		
	136	135	153	154	142	167	143	143
19	147	176	116	119	138			
	168	126	141	153	197	101	204	176
20	135	162	183	164				
	158	153	128	137	161	184	162	150
21	143	118	140	172	208			

* Negative frame number

TABLE 5.21. Diameters of the particles generated from small injection nozzle.

No*	Diameters of the particles generated, μm							
1	107	96	81	87	101	117	121	124
	127	88	65	79	54	105		
2	93	118	94	109	99	87	65	125
	125	93	121					
3	108	97	69	109	120	85	73	106
	78	121	114	91	56	82	73	
4	115	97	124	83	54	101	109	85
	95	97	75	105				
5	98	93	106	56	125	74	82	91
	62	73	81	99	94	126	95	
6	65	78	114	101	95	65	79	115
	78	63	121	79				
7	93	104	65	79	125	97	104	
8	78	132	97	91	108	65	73	81
	85	95	94	74	114	116		
9	118	107	78	98	107	126	84	69
	96	97	104	101	95	68		
10	108	98	71	84	115	69	54	130
	96	97	85	109	116	73	78	119
11	96	95	76	89	106	124	108	131
	78	98	86	97	126	121		
12	84	114	79	83	95	104	109	97
	97	117	82	94	123	118		
13	93	78	71	64	92	94	85	86
	127	97	125	99	107			
14	68	98	73	92	87	108	59	86
	125	100	76	97	67	126		
15	97	92	76	71	108	123	105	74
	81	103	97	83	106			
16	96	95	74	118	93	71	112	82
	106	101	128	98	95	61	130	98
	68	79						
17	84	106	124	86	95	94	117	119
	76	107	118	73	58	99		
18	94	106	118	134	78	96	104	74
	84	117	108	129	62	126		
19	98	94	104	68	125	72	91	103
	68	84	76	115	113	106		
20	101	91	83	95	91	108	121	

* Negative frame number

Plate 5.1 Fluid flow patterns developed on plane 1 when different
SEN were used.

A - Nozzle 1; B - Nozzle 2; C - Nozzle 3.

Tracer: small air bubbles.

SEN submerged depth: 125 mm.

Casting speed: $1.33 \text{ m}\cdot\text{min}^{-1}$

(see facing page)



A

B

C

Plate 5.2 Fluid flow patterns developed on plane 2 when different SEN were used.

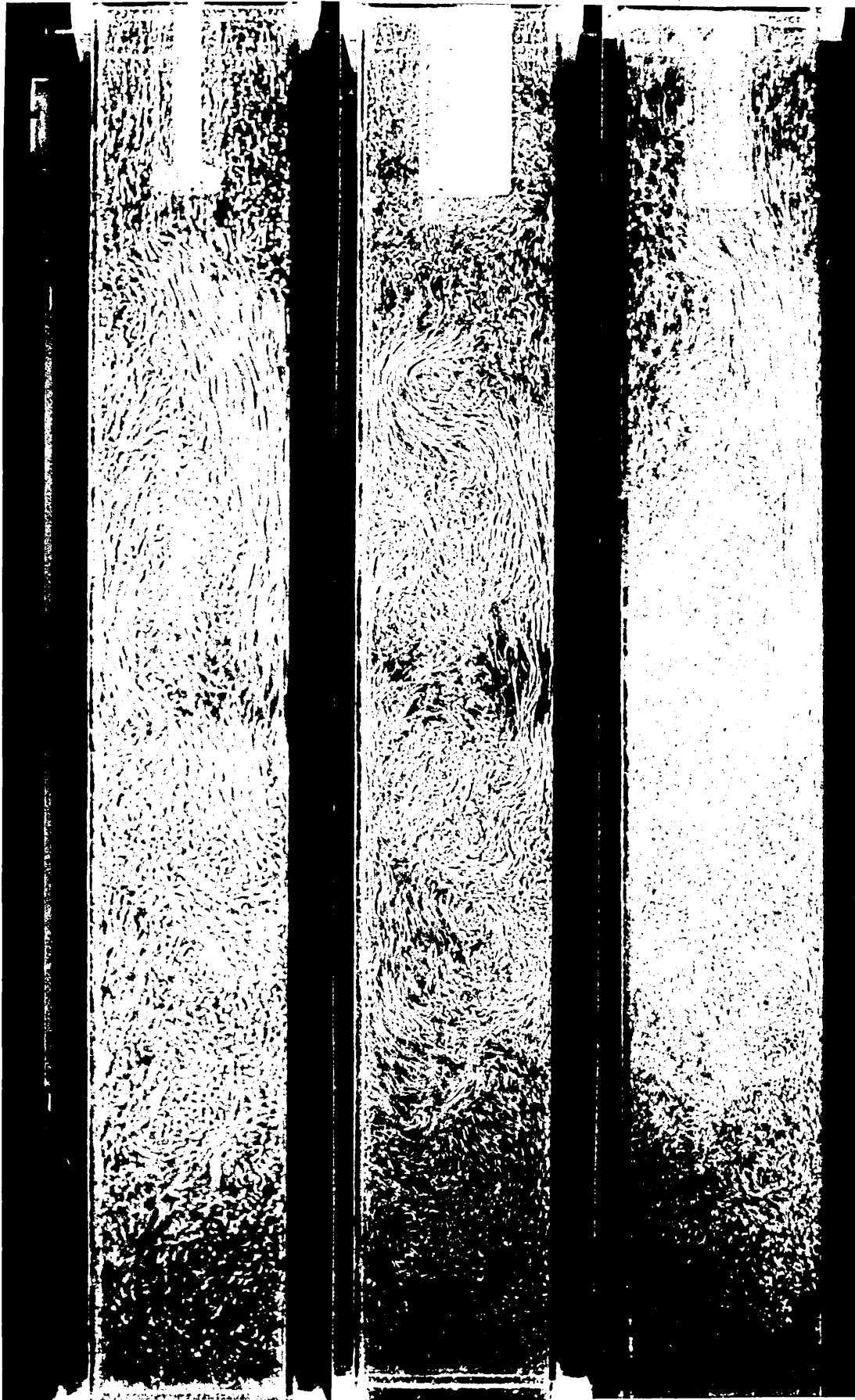
A - Nozzle 1; B - Nozzle 2; C - Nozzle 3.

Tracer: small air bubbles.

SEN submerged depth: 125 mm.

Casting speed: 1.33 m.min⁻¹

(see facing page)



A

B

C

Plate 5.3 Fluid flow patterns developed on plane 3 when different SEN were used.

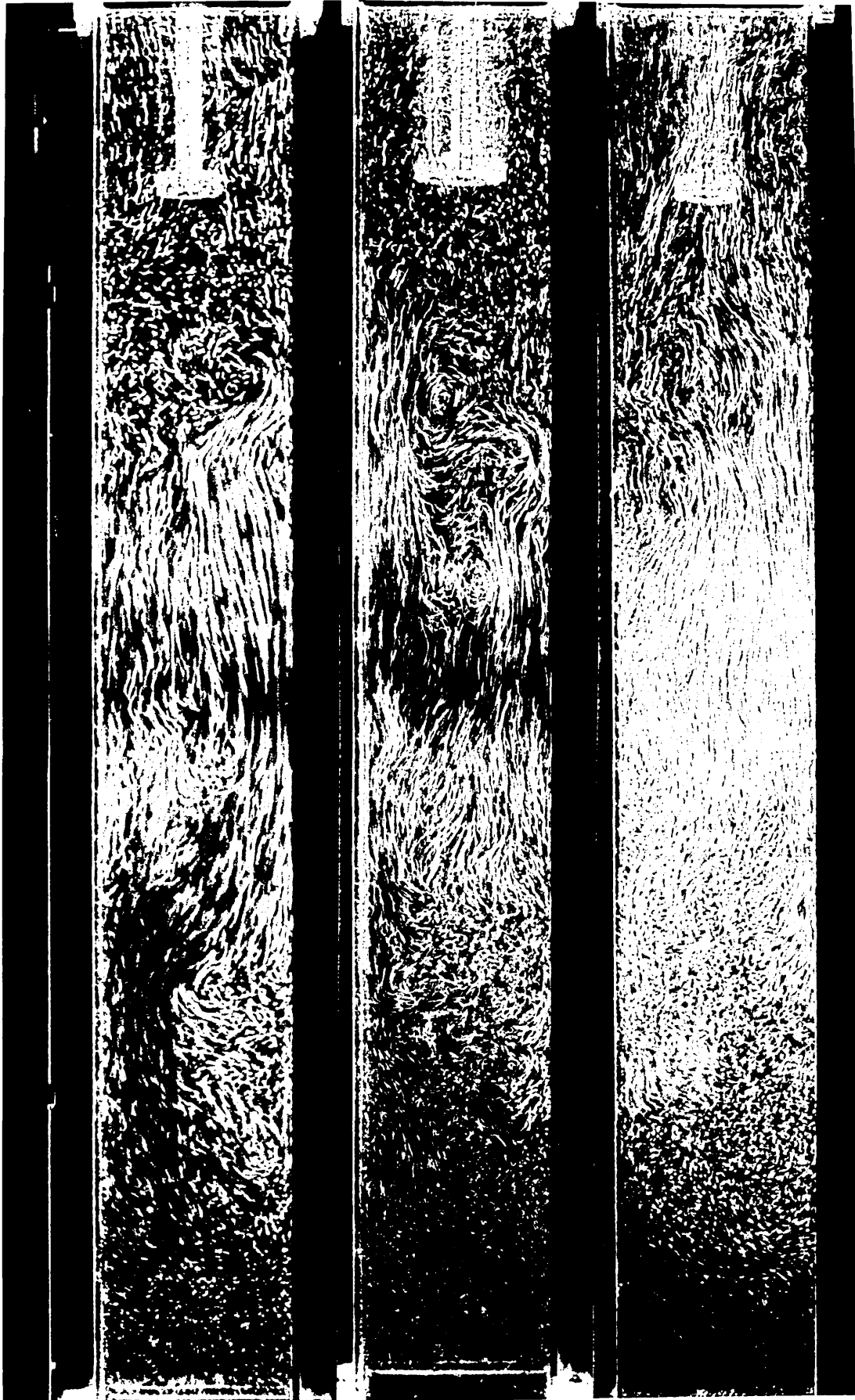
A - Nozzle 1; B - Nozzle 2; C - Nozzle 3.

Tracer: small air bubbles.

SEN submerged depth: 125 mm.

Casting speed: 1.33 m.min⁻¹

(see facing page)



A

B

C

Plate 5.4 Fluid flow patterns developed on plane 1 when different SEN were used.

A - Nozzle 1; B - Nozzle 2; C - Nozzle 3.

Tracer: fine alumina flakes.

SEN submerged depth: 125 mm.

Casting speed: 1.33 m.min⁻¹

(see facing page)



A

B

C

Plate 5.5 Fluid flow patterns developed on plane 2 when different SEN were used.

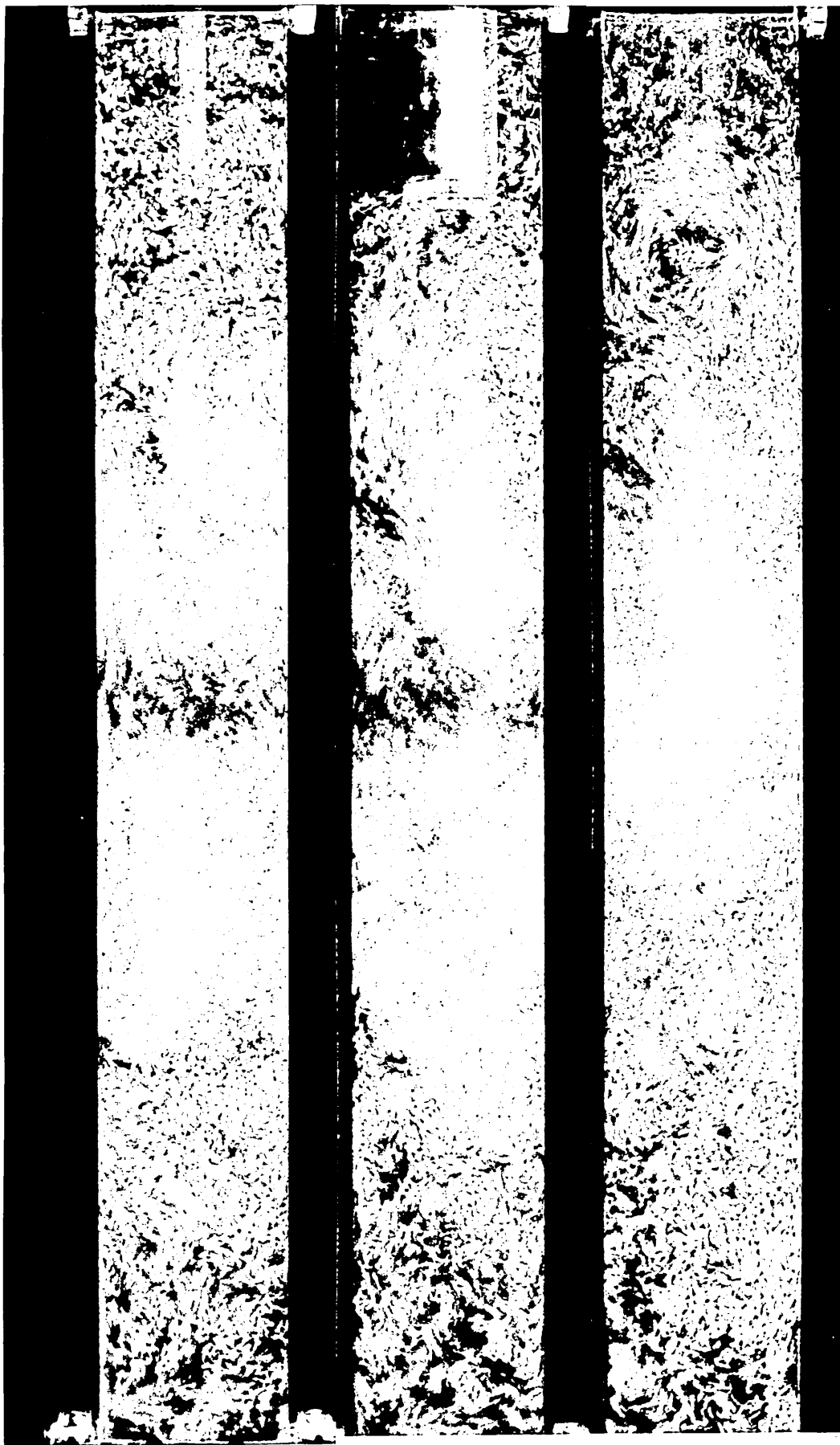
A - Nozzle 1; B - Nozzle 2; C - Nozzle 3.

Tracer: fine alumina flakes.

SEN submerged depth: 125 mm.

Casting speed: $1.33 \text{ m}\cdot\text{min}^{-1}$

(see facing page)



A

B

C

Plate 5.6 Fluid flow patterns developed on plane 3 when different SEN were used.

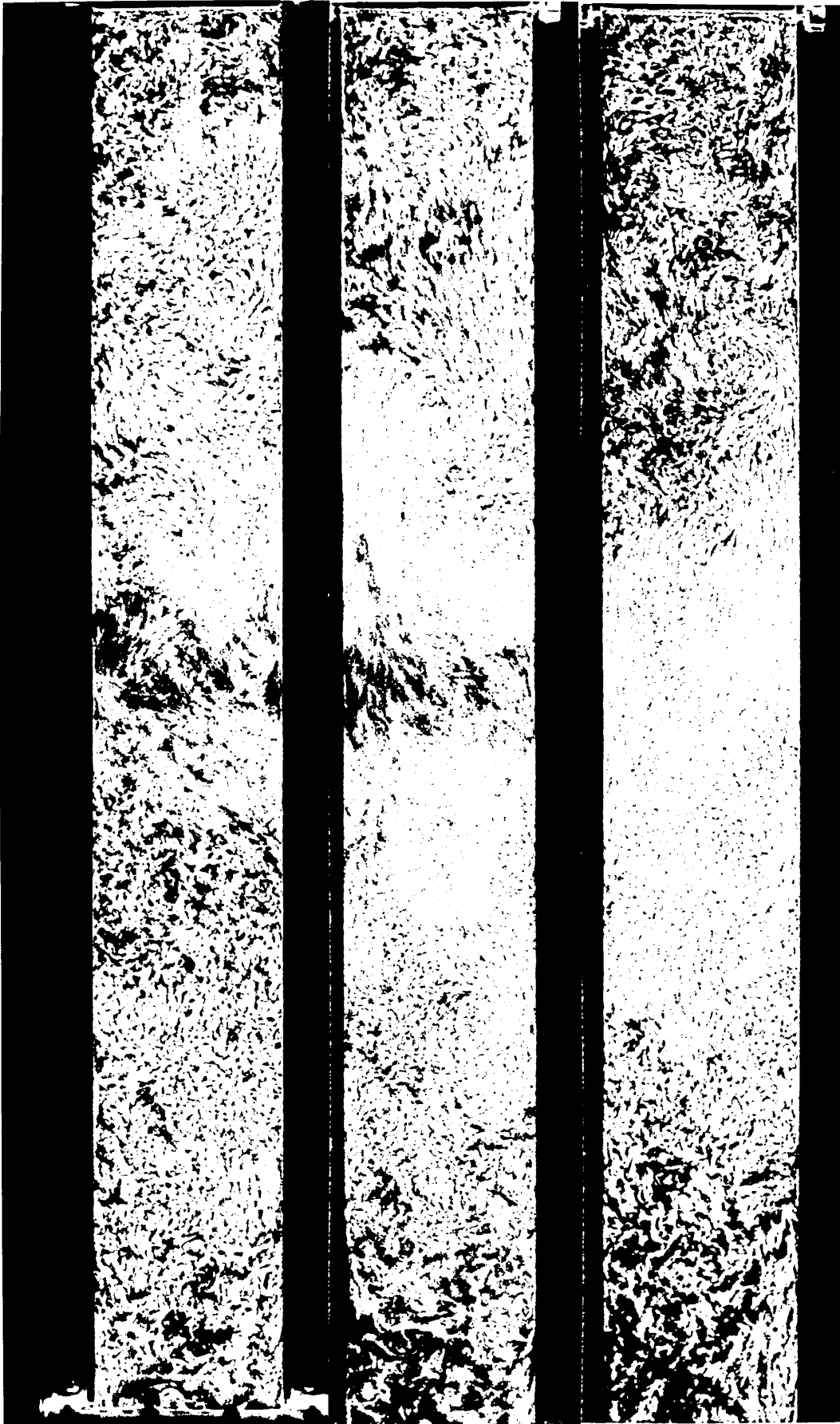
A - Nozzle 1; B - Nozzle 2; C - Nozzle 3.

Tracer: fine alumina flakes.

SEN submerged depth: 125 mm.

Casting speed: 1.33 m.min⁻¹

(see facing page)



A

B

C

Plate 5.7 Fluid flow patterns developed on central plane when different bifurcated SEN were used.

A - Nozzle 11 (25° downwards);

B - Nozzle 9 (15° downwards);

C - Nozzle 4 (0° horizontal);

D - Nozzle 5 (25° upwards).

Tracer: small air bubbles.

SEN submerged depth: 175 mm.

Casting speed: 0.55 m.min⁻¹

(see facing page)

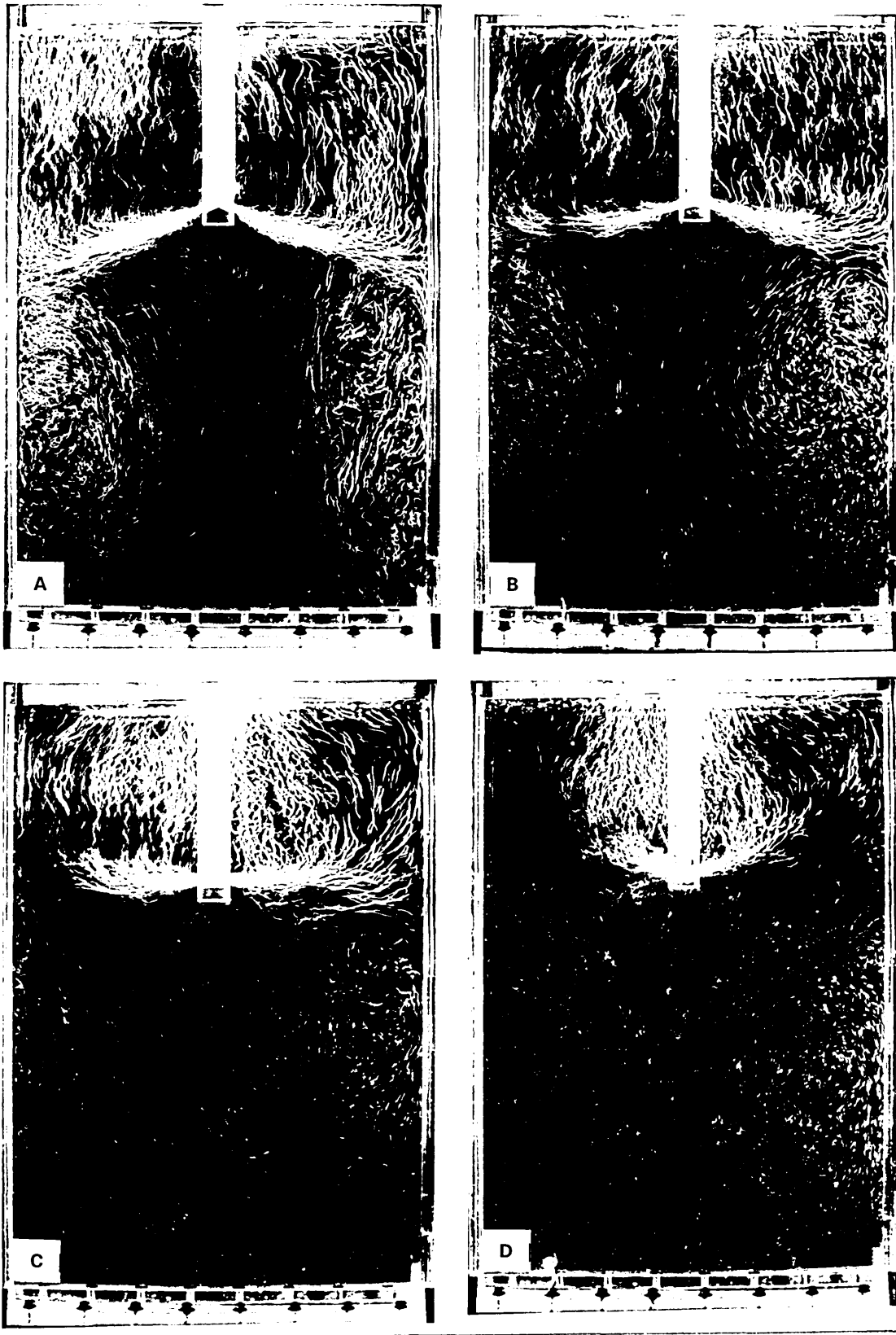


Plate 5.8 Fluid flow patterns developed on central plane when different bifurcated SEN were used.

A - Nozzle 11 (25° downwards);

B - Nozzle 9 (15° downwards);

C - Nozzle 4 (0° horizontal);

D - Nozzle 5 (25° upwards).

Tracer: small air bubbles.

SEN submerged depth: 150 mm.

Casting speed: 0.55 m.min⁻¹

(see facing page)

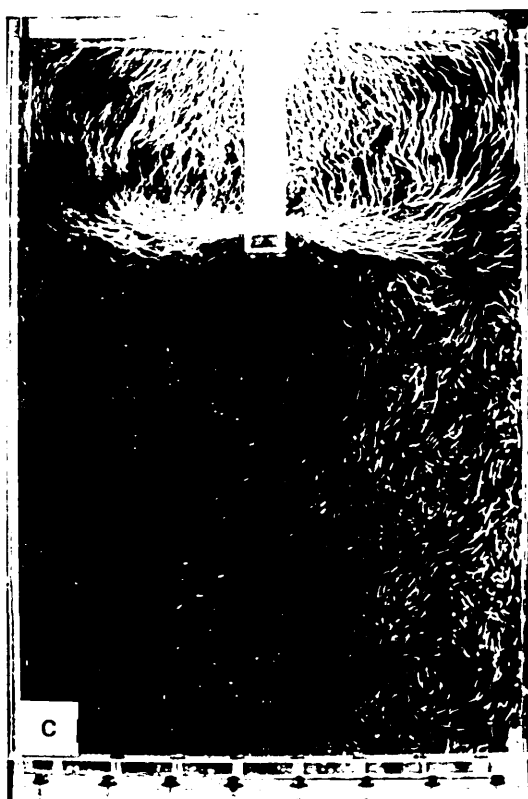
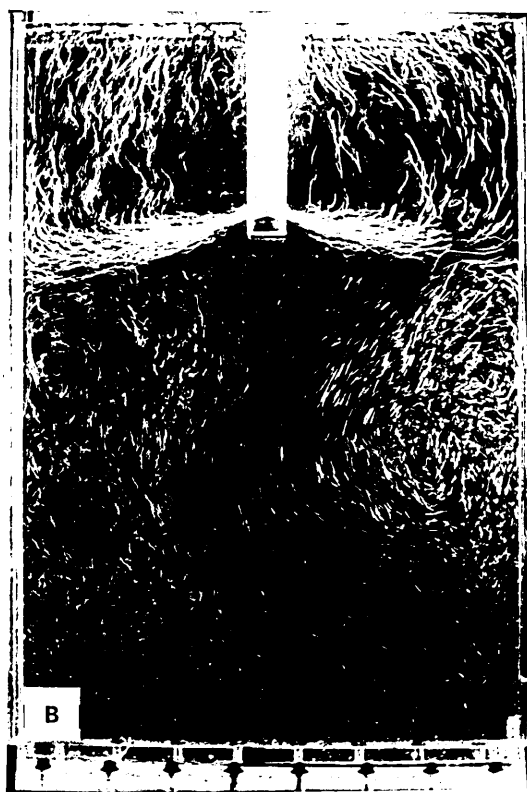
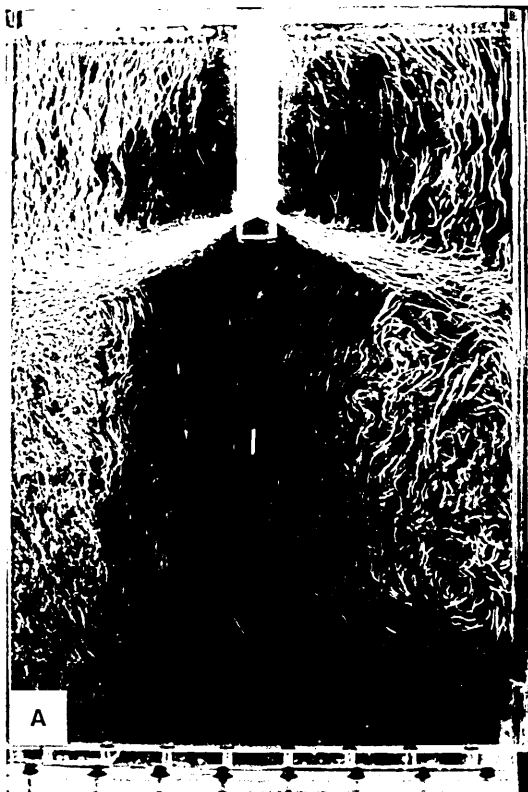


Plate 5.9 Fluid flow patterns developed on central plane when different bifurcated SEN were used.

A - Nozzle 11 (25° downwards);

B - Nozzle 9 (15° downwards);

C - Nozzle 4 (0° horizontal);

D - Nozzle 5 (25° upwards).

Tracer: small air bubbles.

SEN submerged depth: 125 mm.

Casting speed: 0.55 m.min⁻¹

(see facing page)

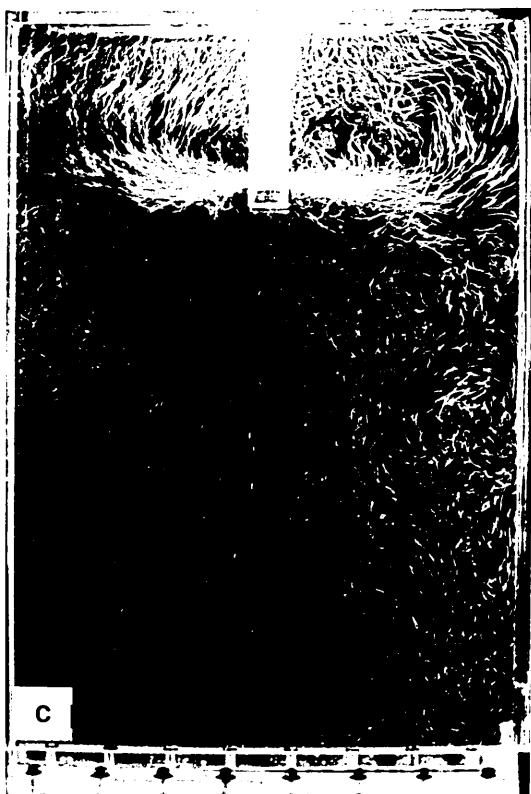
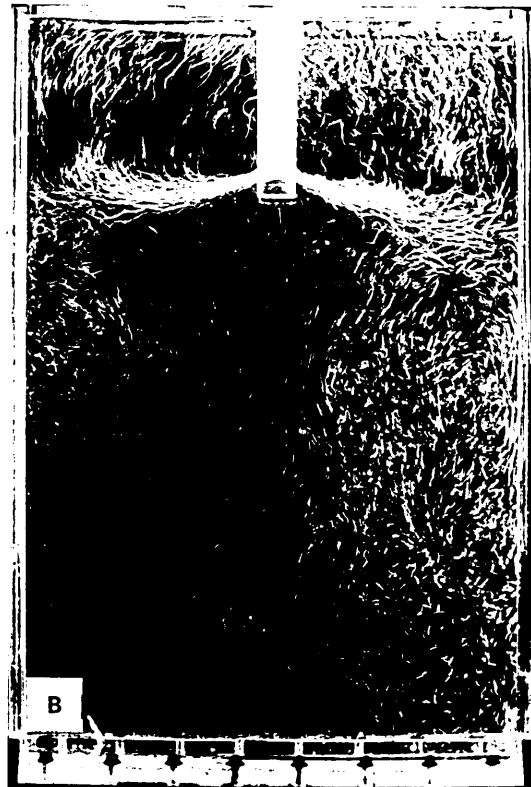
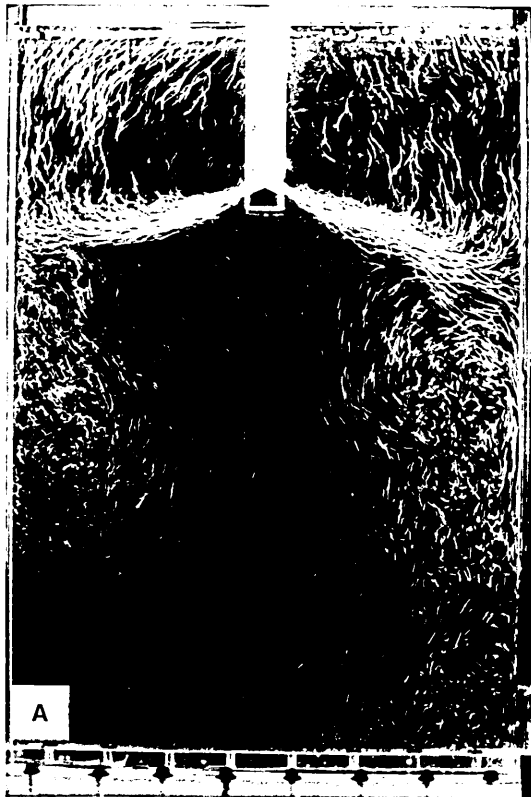


Plate 5.10 Fluid flow patterns developed on central plane when different bifurcated SEN were used.

A - Nozzle 11 (25° downwards);

B - Nozzle 9 (15° downwards);

C - Nozzle 4 (0° horizontal);

D - Nozzle 5 (25° upwards).

Tracer: small air bubbles.

SEN submerged depth: 100 mm.

Casting speed: 0.55 m.min⁻¹

(see facing page)

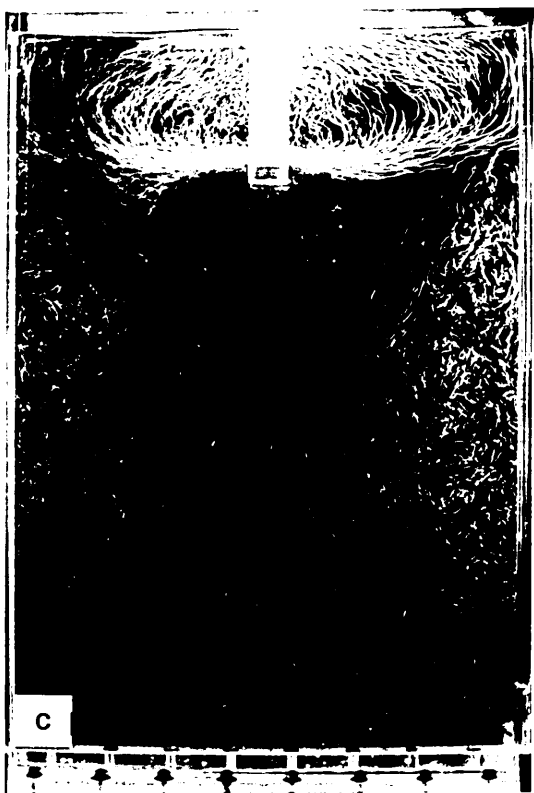
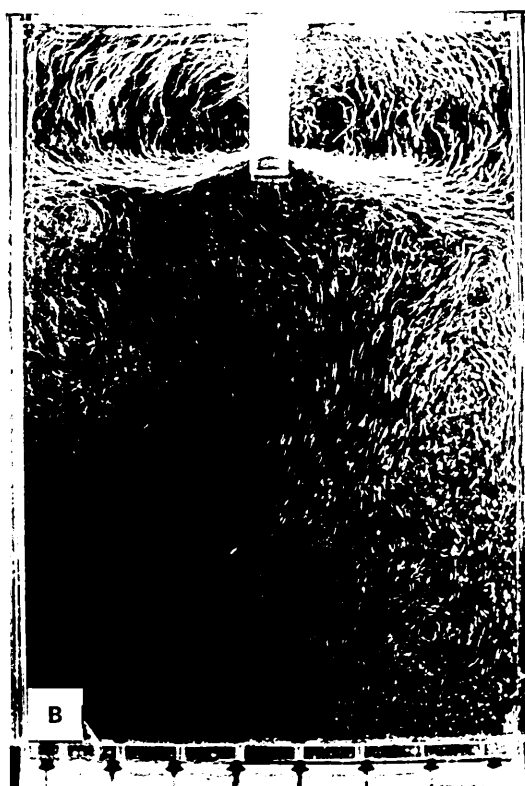


Plate 5.11 Fluid flow patterns developed on central plane when different bifurcated SEN were used.

A - Nozzle 11 (25° downwards);

B - Nozzle 9 (15° downwards);

C - Nozzle 4 (0° horizontal);

D - Nozzle 5 (25° upwards).

Tracer: small air bubbles.

SEN submerged depth: 75 mm.

Casting speed: 0.55 m.min⁻¹

(see facing page)

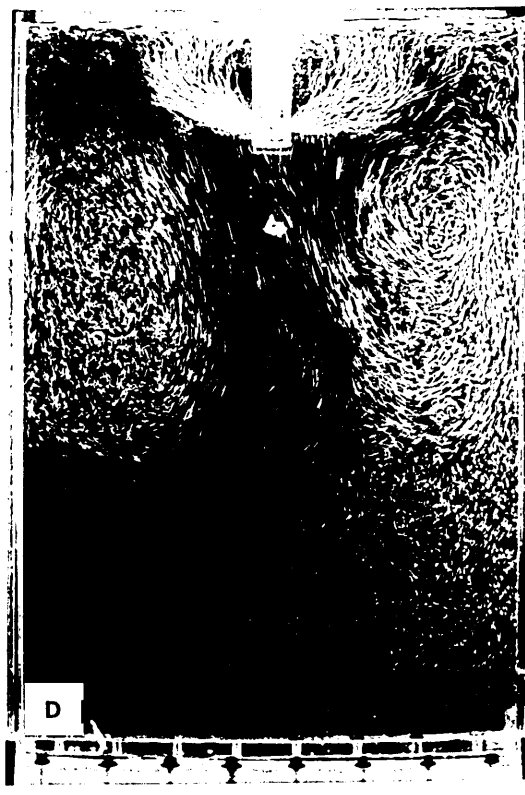
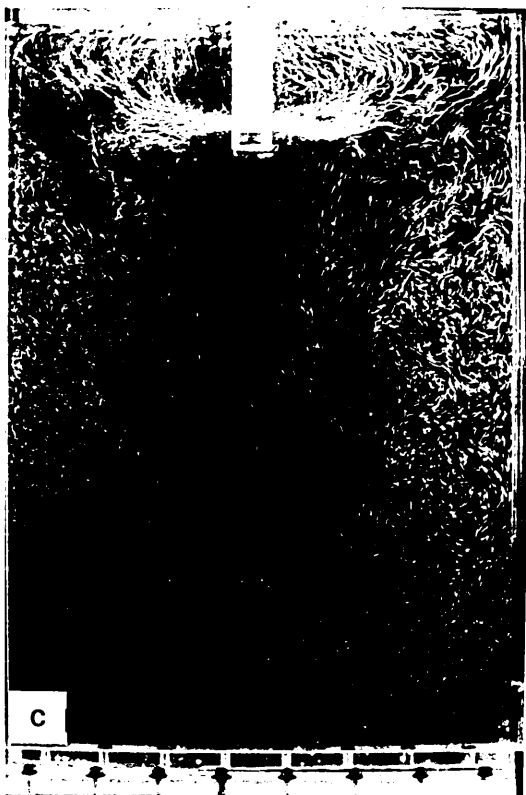
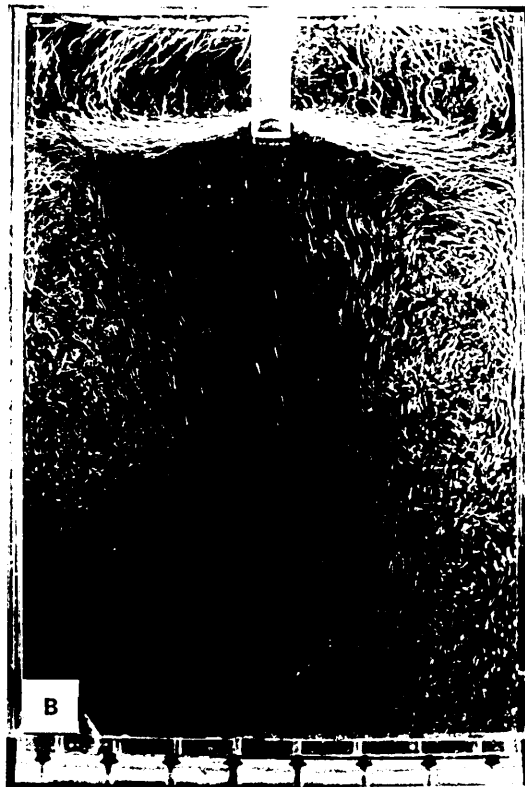
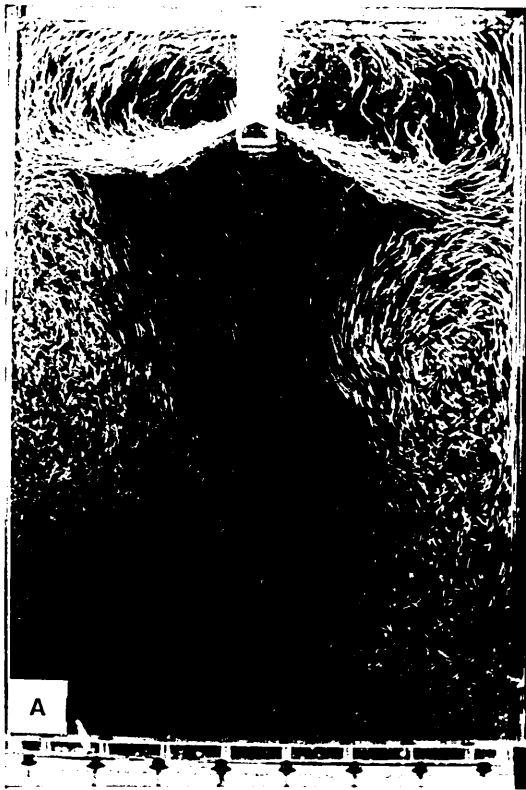


Plate 5.12 Fluid flow patterns developed on plane 1 using Nozzle 1
at different submerged depths.

SEN submerged depth (mm):

A - 150; B - 125; C - 100; D - 75; E - 50; F - 25.

Tracer: small air bubbles.

Casting speed: 1.33 m.min⁻¹.

(see facing page)

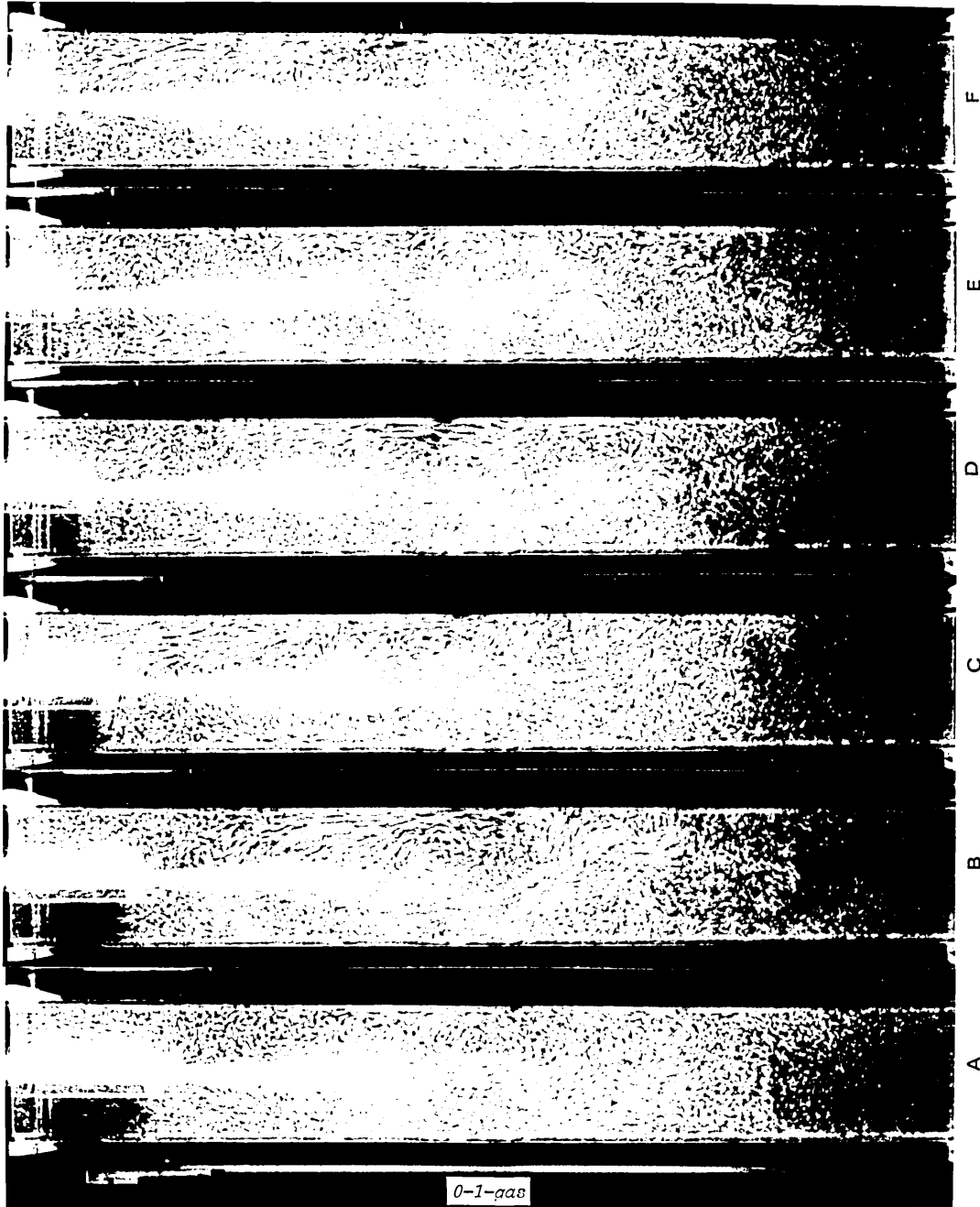


Plate 5.13 Fluid flow patterns developed on plane 2 using Nozzle 1
at different submerged depths.

SEN submerged depth (mm):

A - 150; B - 125; C - 100; D - 75; E - 50; F - 25.

Tracer: small air bubbles.

Casting speed: 1.33 m.min⁻¹.

(see facing page)

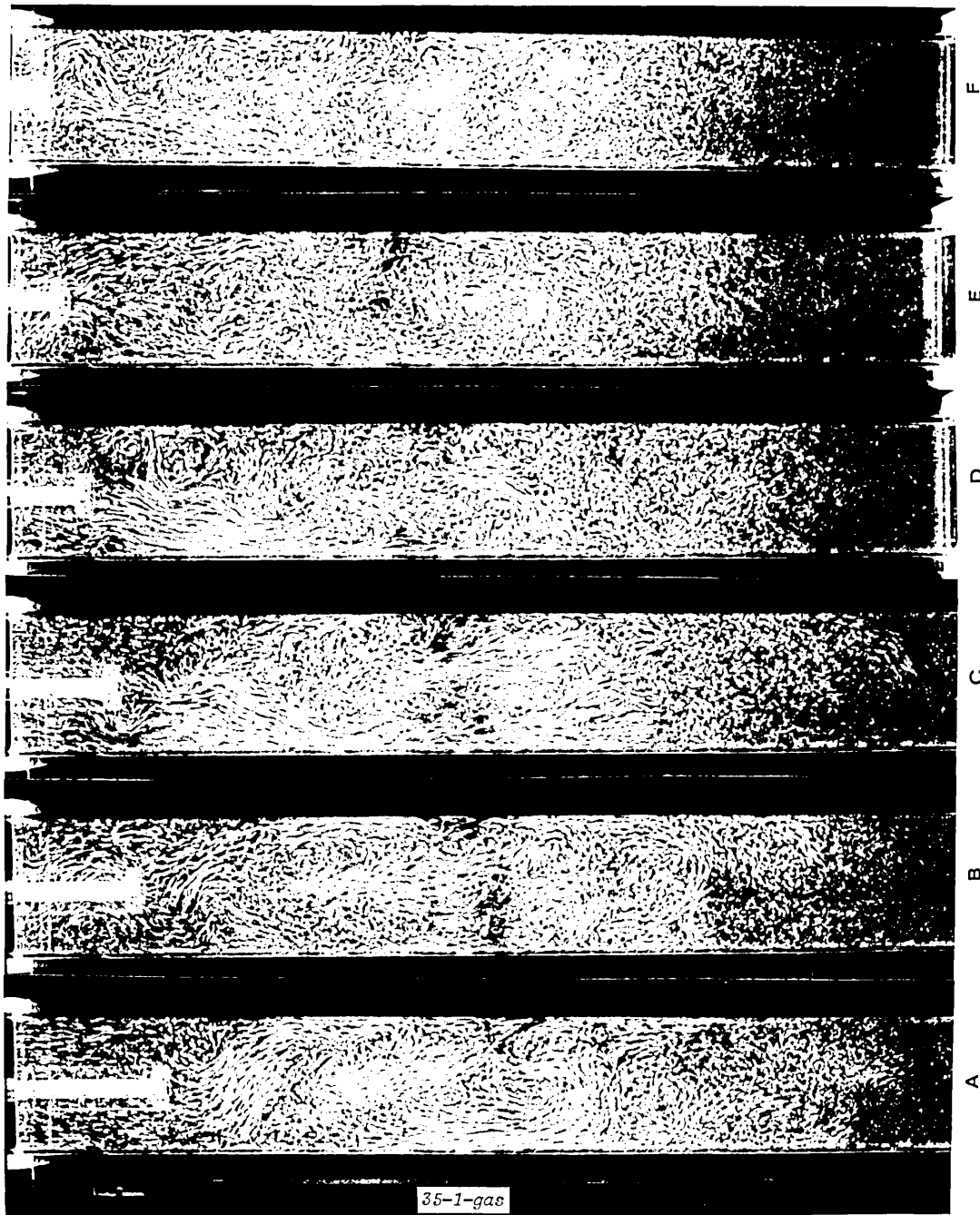


Plate 5.14 Fluid flow patterns developed on plane 3 using Nozzle 1
at different submerged depths.

SEN submerged depth (mm):

A - 150; B - 125; C - 100; D - 75; E - 50; F - 25.

Tracer: small air bubbles.

Casting speed: 1.33 m.min⁻¹.

(see facing page)

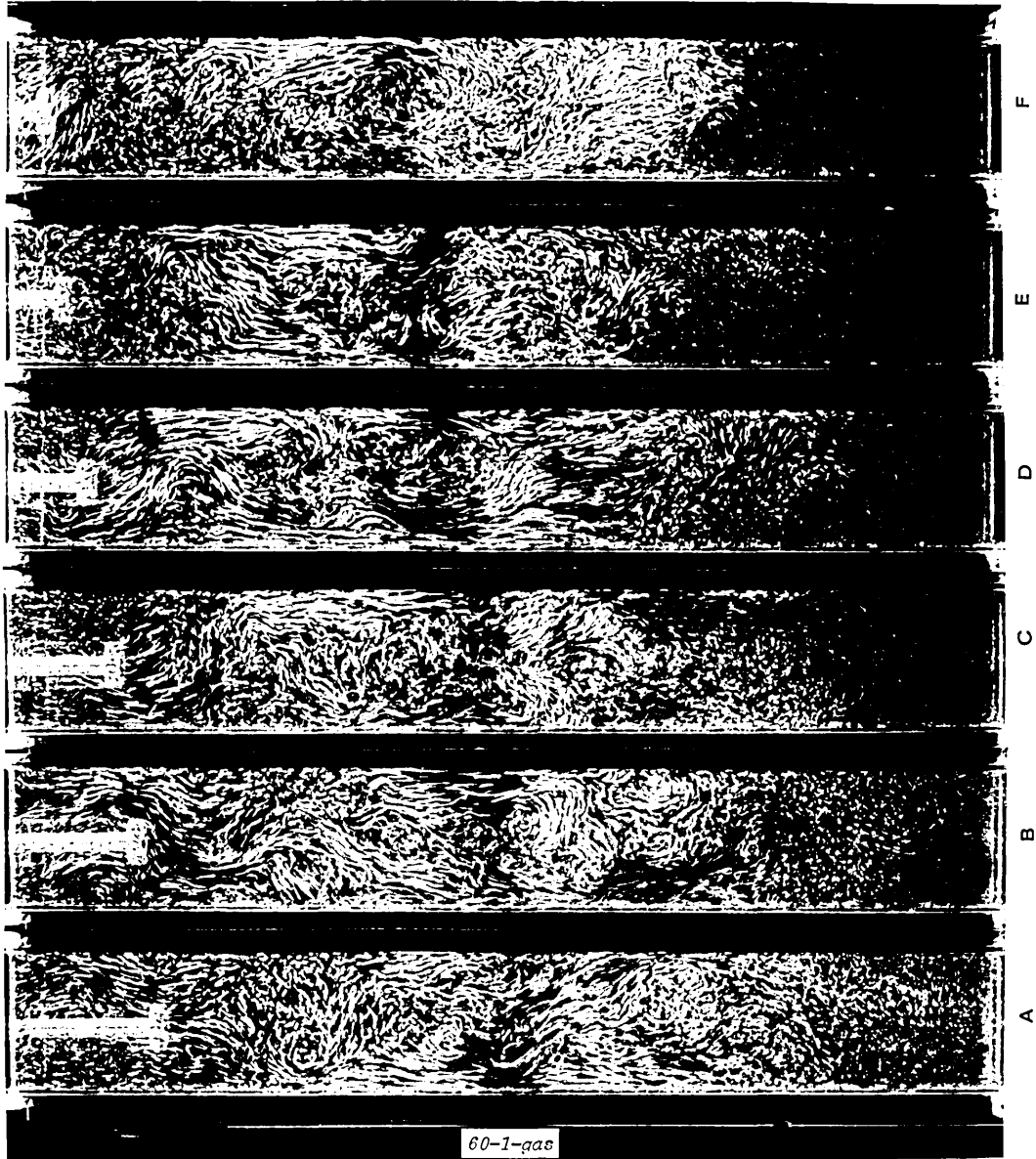


Plate 5.15 Fluid flow patterns developed on plane 1 using Nozzle 1
at different submerged depths.

SEN submerged depth (mm):

A - 150; B - 125; C - 100; D - 75; E - 50; F - 25.

Tracer: fine alumina flakes.

Casting speed: 1.33 m.min⁻¹.

(see facing page)

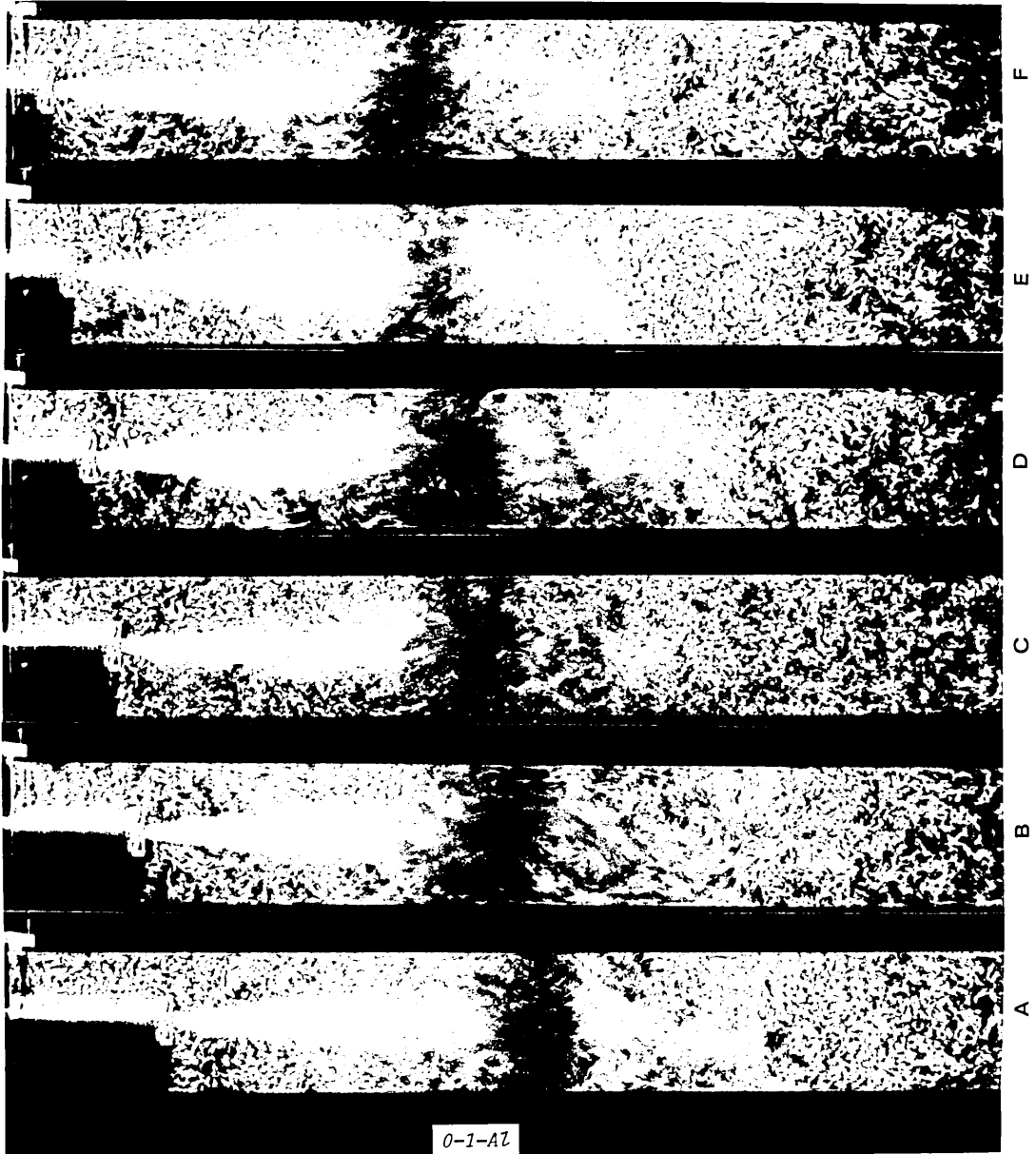


Plate 5.16 Fluid flow patterns developed on plane 2 using Nozzle 1
at different submerged depths.

SEN submerged depth (mm):

A - 150; B - 125; C - 100; D - 75; E - 50; F - 25.

Tracer: fine alumina flakes.

Casting speed: 1.33 m.min⁻¹.

(see facing page)

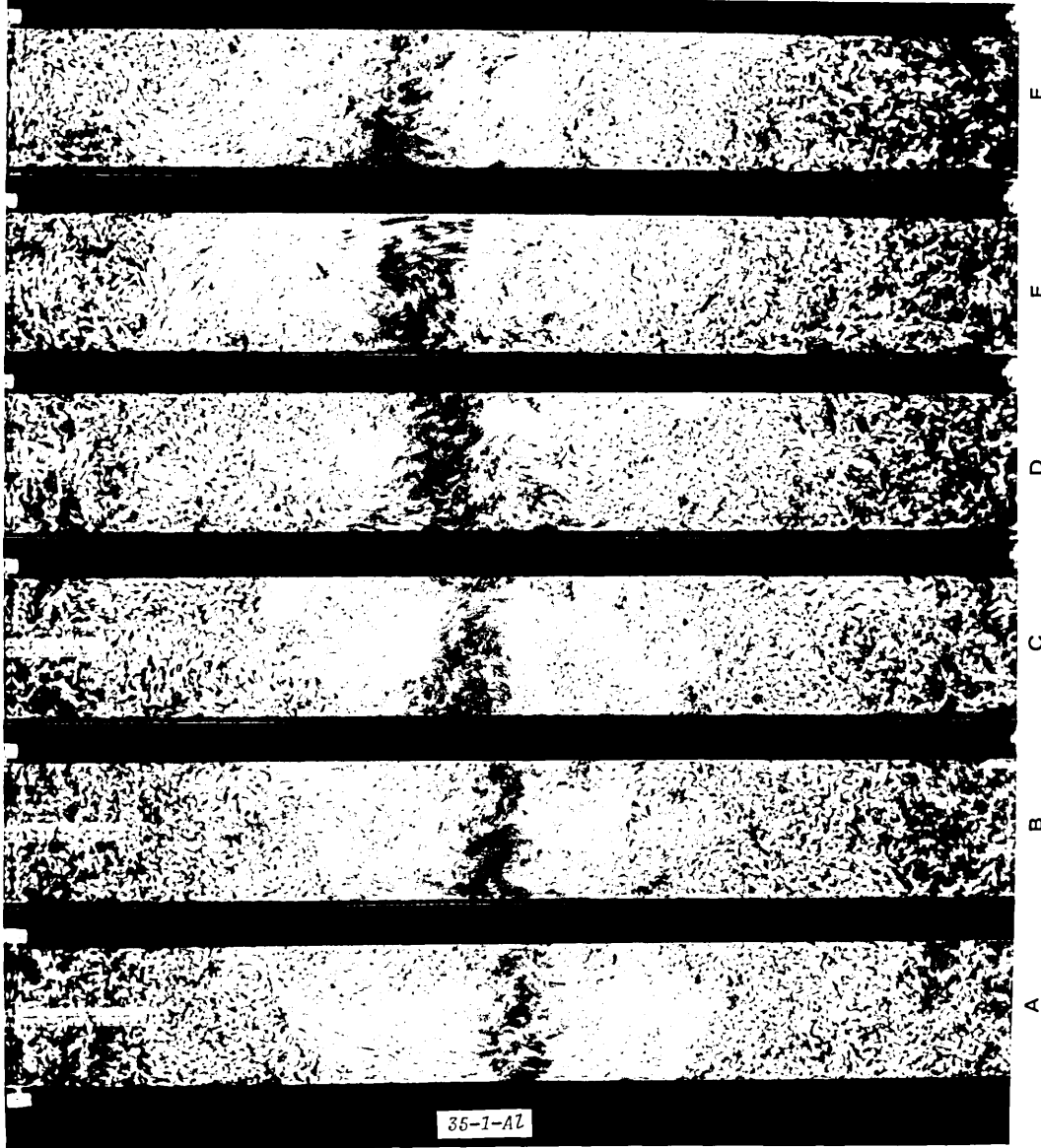


Plate 5.17 Fluid flow patterns developed on plane 3 using Nozzle 1
at different submerged depths.

SEN submerged depth (mm):

A - 150; B - 125; C - 100; D - 75; E - 50; F - 25.

Tracer: fine alumina flakes.

Casting speed: 1.33 m.min⁻¹.

(see facing page)

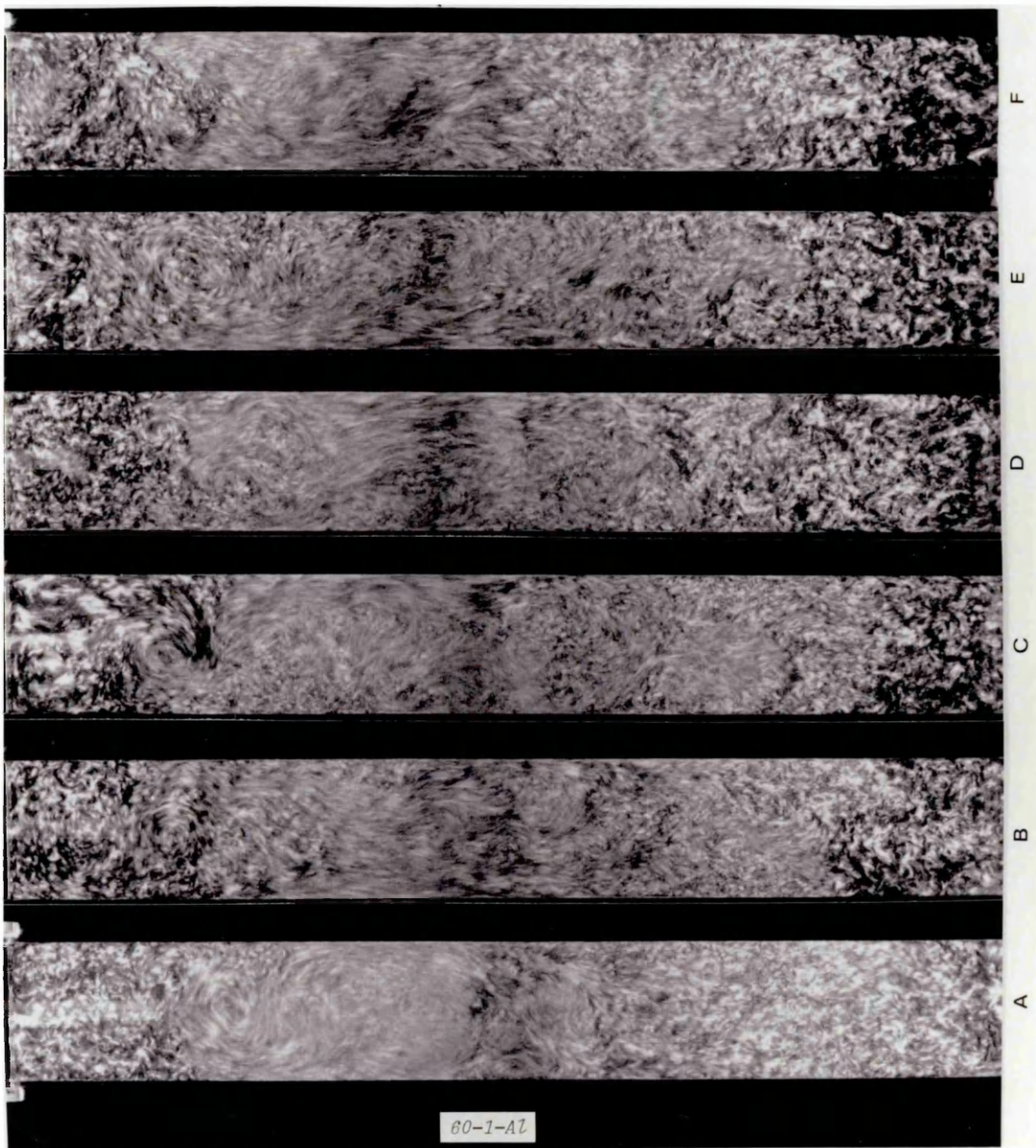


Plate 5.18 Fluid flow patterns developed on plane 1 using Nozzle 2
at different submerged depths.

SEN submerged depth (mm):

A - 150; B - 125; C - 100; D - 75; E - 50; F - 25.

Tracer: small air bubbles.

Casting speed: 1.33 m.min⁻¹.

(see facing page)

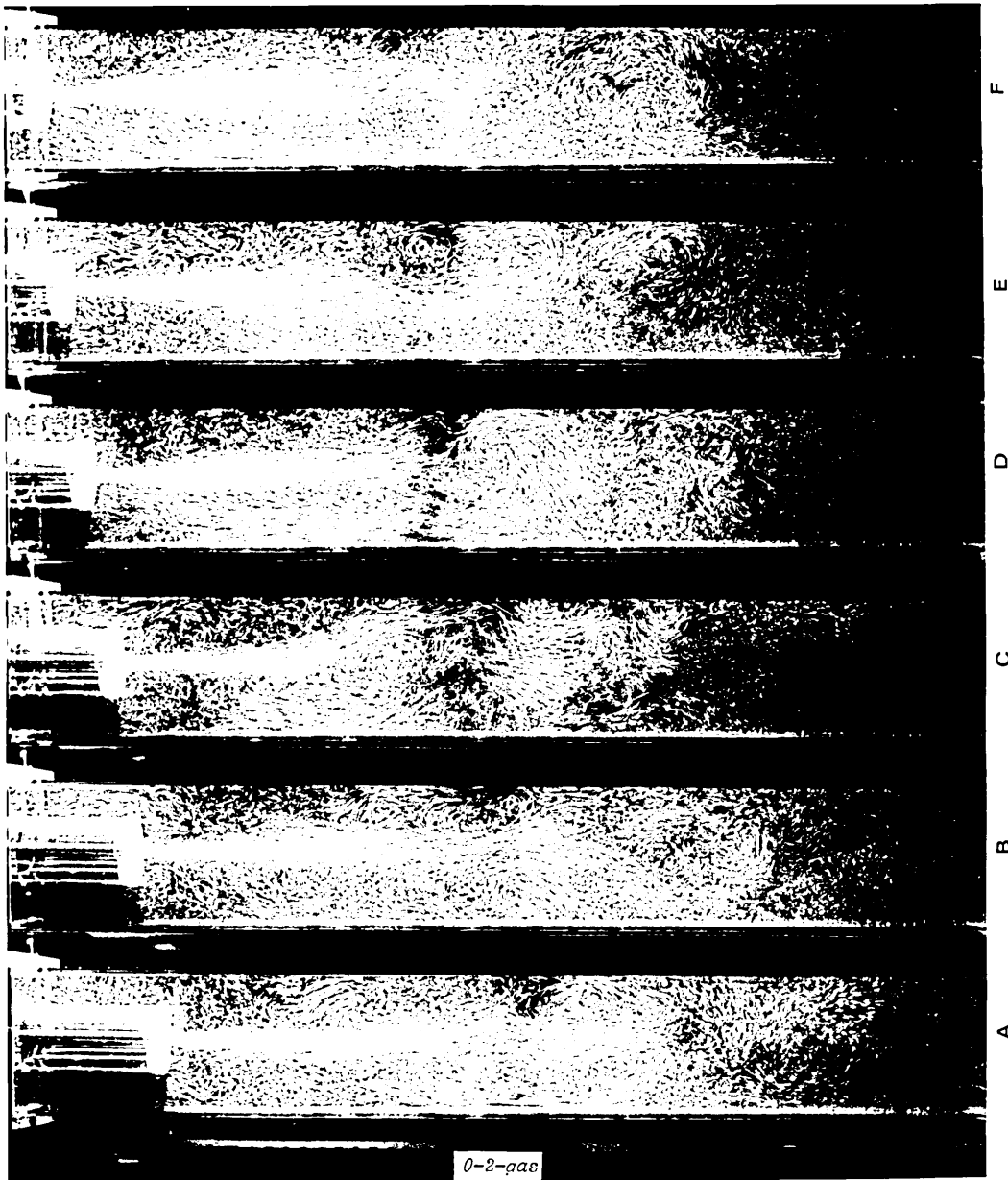


Plate 5.19 Fluid flow patterns developed on plane 2 using Nozzle 2
at different submerged depths.

SEN submerged depth (mm):

A - 150; B - 125; C - 100; D - 75; E - 50; F - 25.

Tracer: small air bubbles.

Casting speed: 1.33 m.min⁻¹.

(see facing page)

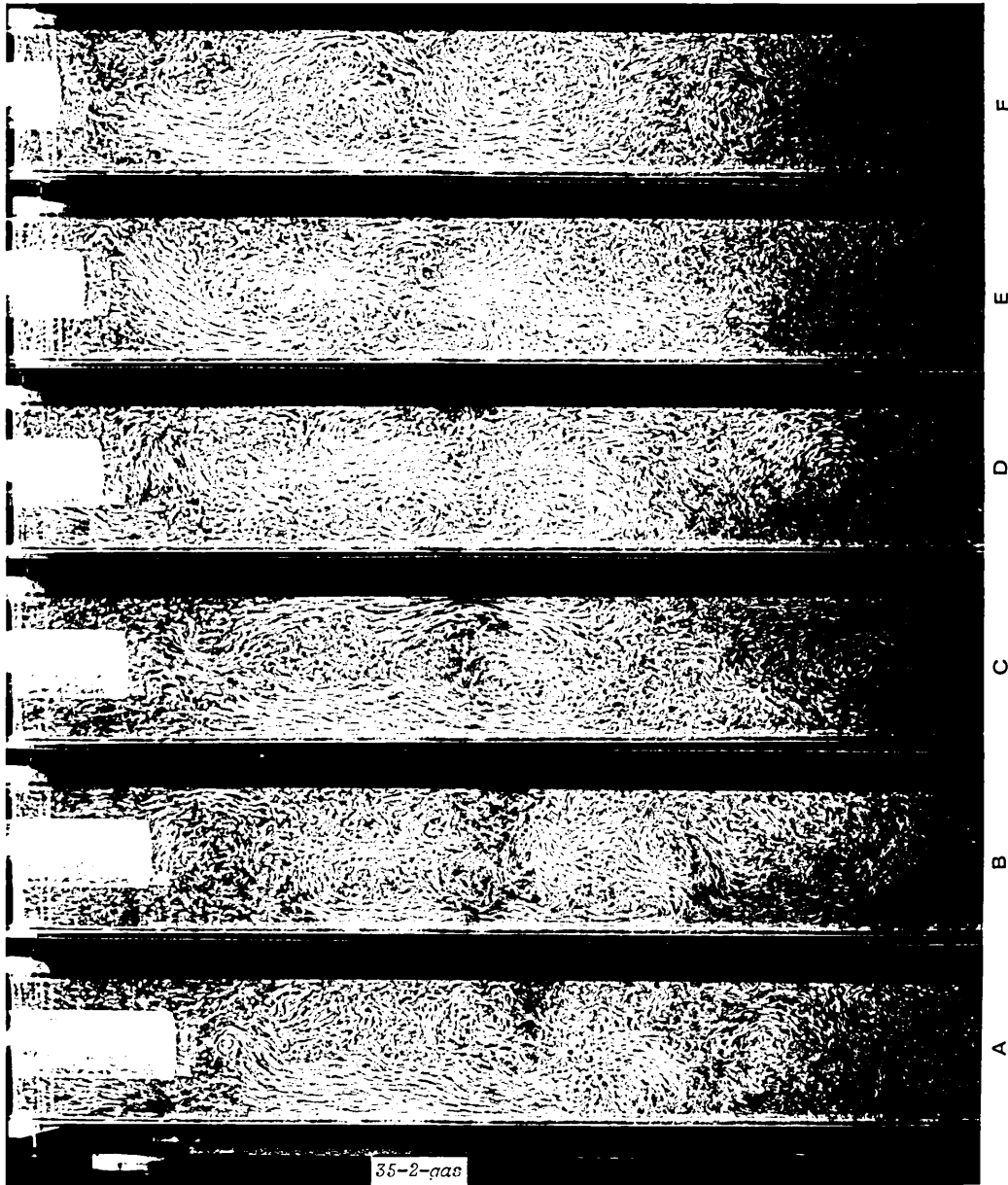


Plate 5.20

Fluid flow patterns developed on plane 3 using Nozzle 2
at different submerged depths.

SEN submerged depth (mm):

A - 150; B - 125; C - 100; D - 75; E - 50; F - 25.

Tracer: small air bubbles.

Casting speed: $1.33 \text{ m}\cdot\text{min}^{-1}$.

(see facing page)

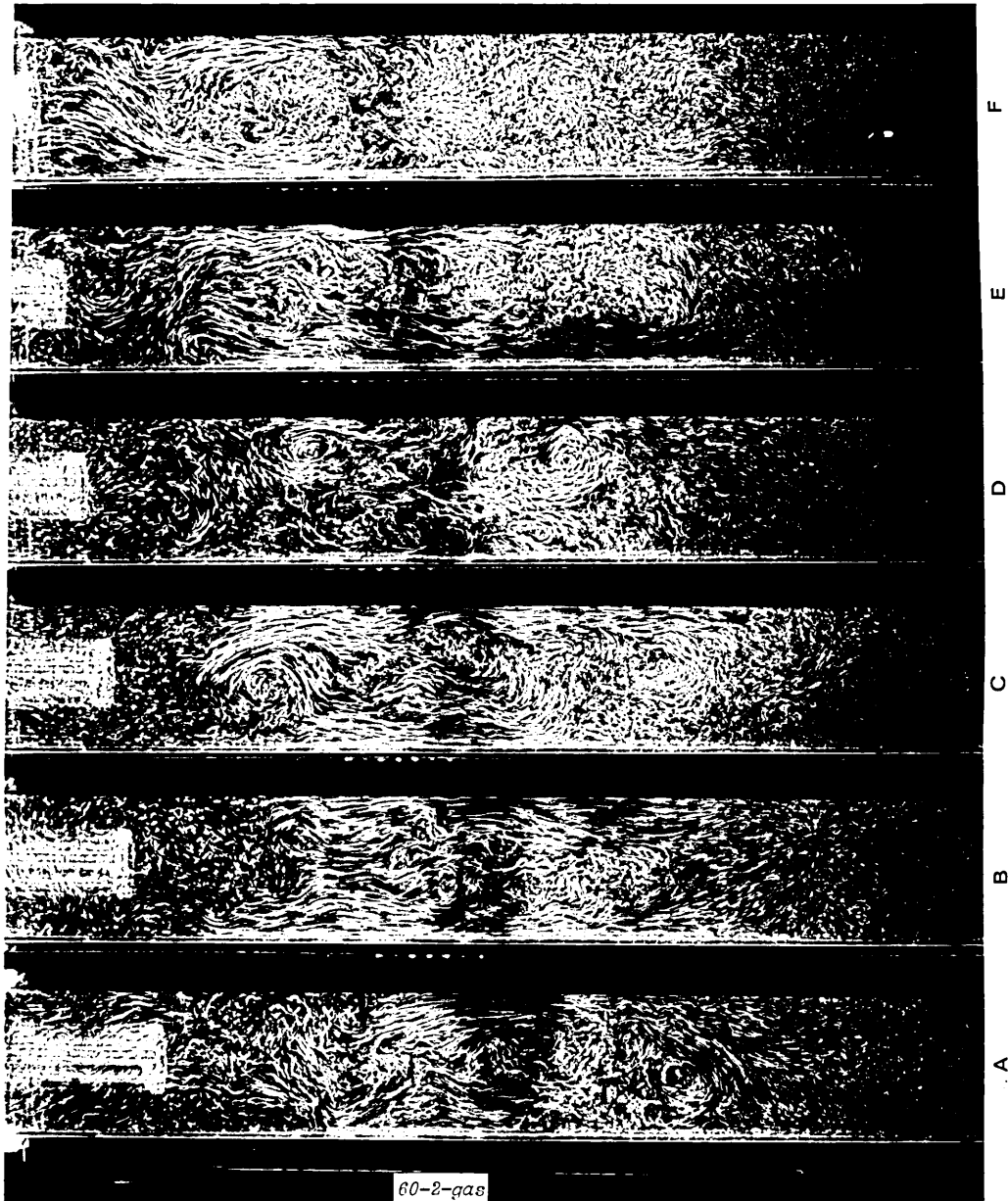


Plate 5.21 Fluid flow patterns developed on plane 1 using Nozzle 2
at different submerged depths.

SEN submerged depth (mm):

A - 150; B - 125; C - 100; D - 75; E - 50; F - 25.

Tracer: fine alumina flakes.

Casting speed: 1.33 m.min⁻¹.

(see facing page)



Plate 5.22 Fluid flow patterns developed on plane 2 using Nozzle 2
at different submerged depths.

SEN submerged depth (mm):

A - 150; B - 125; C - 100; D - 75; E - 50; F - 25.

Tracer: fine alumina flakes.

Casting speed: 1.33 m.min⁻¹.

(see facing page)



Plate 5.23 Fluid flow patterns developed on plane 3 using Nozzle 2
at different submerged depths.

SEN submerged depth (mm):

A - 150; B - 125; C - 100; D - 75; E - 50; F - 25.

Tracer: fine alumina flakes.

Casting speed: 1.33 m.min⁻¹.

(see facing page)

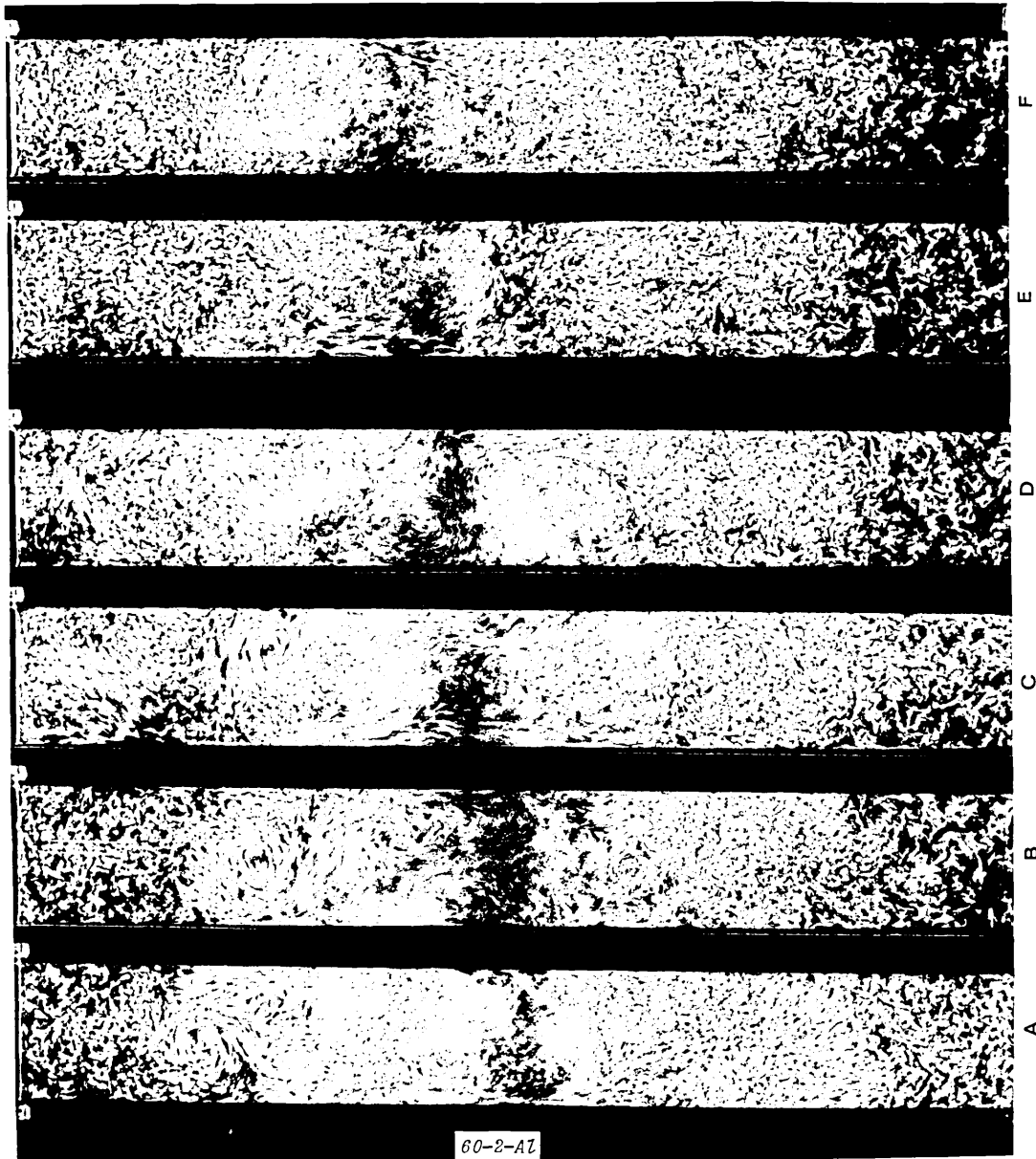


Plate 5.24 Fluid flow patterns developed on plane 1 using Nozzle 3
at different submerged depths.

SEN submerged depth (mm):

A - 150; B - 125; C - 100; D - 75; E - 50; F - 25.

Tracer: small air bubbles.

Casting speed: 1.33 m.min⁻¹.

(see facing page)

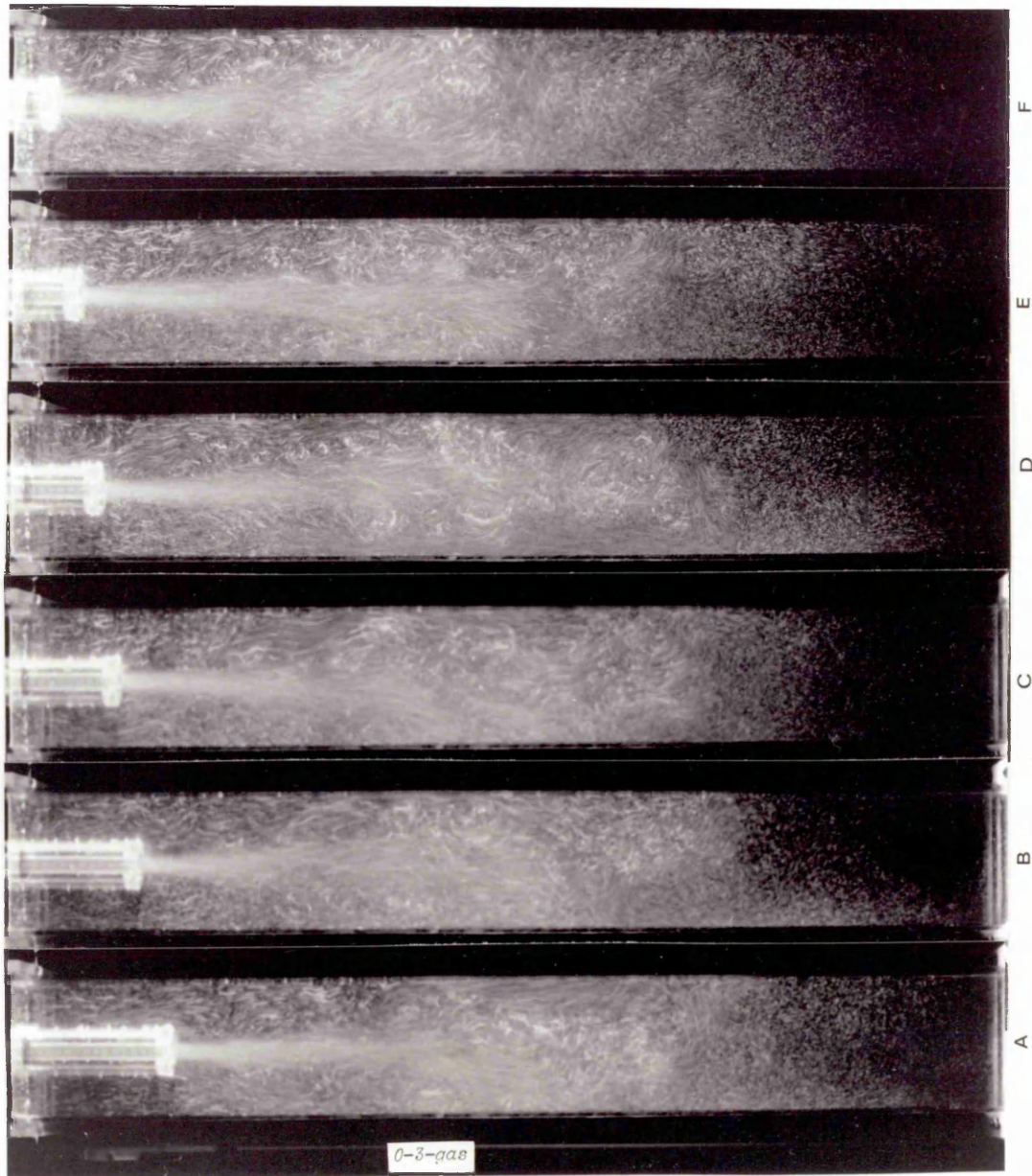


Plate 5.25 Fluid flow patterns developed on plane 2 using Nozzle 3
at different submerged depths.

SEN submerged depth (mm):

A - 150; B - 125; C - 100; D - 75; E - 50; F - 25.

Tracer: small air bubbles.

Casting speed: 1.33 m.min⁻¹.

(see facing page)

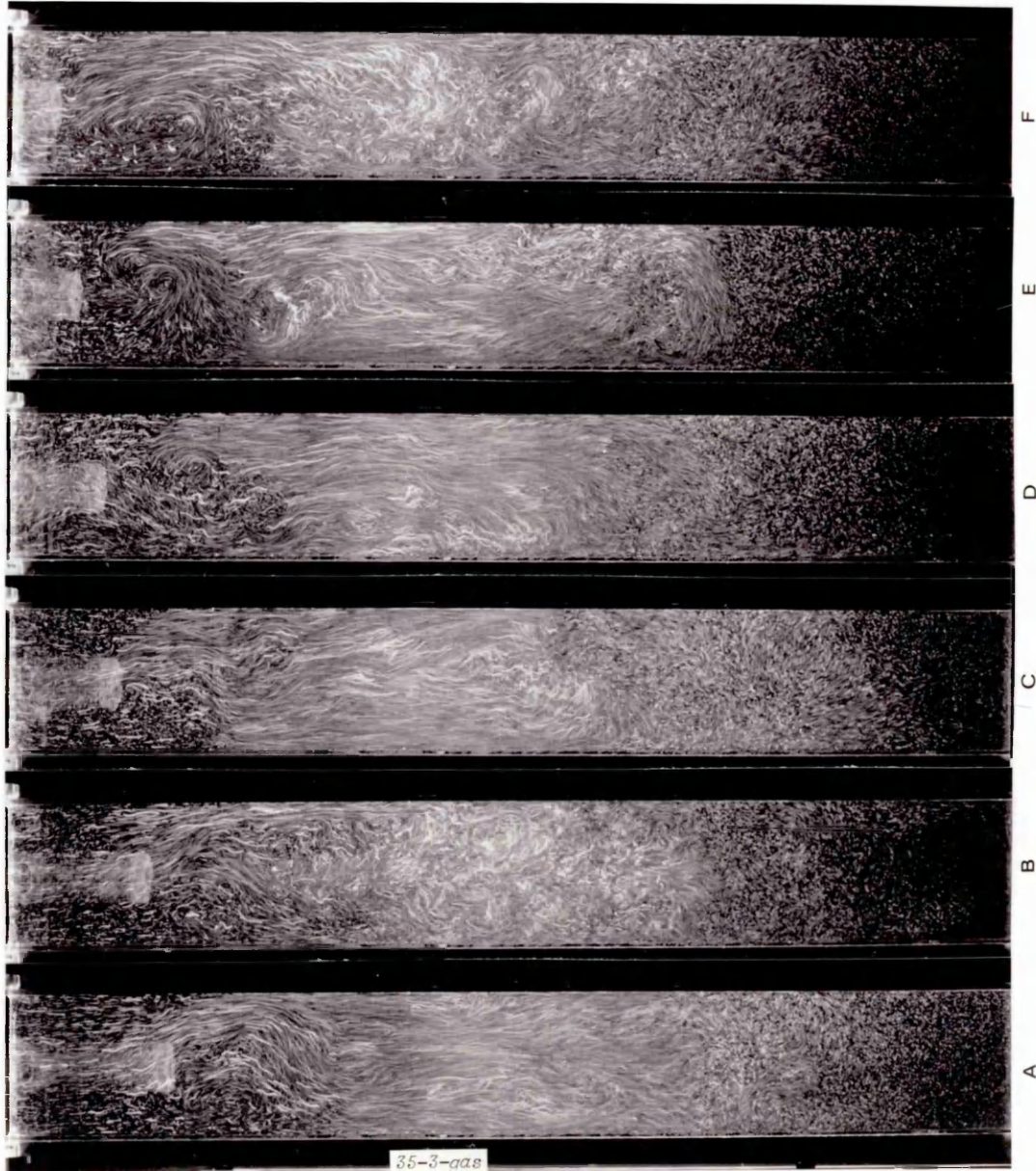


Plate 5.26 Fluid flow patterns developed on plane 3 using Nozzle 3
at different submerged depths.

SEN submerged depth (mm):

A - 150; B - 125; C - 100; D - 75; E - 50; F - 25.

Tracer: small air bubbles.

Casting speed: 1.33 m.min⁻¹.

(see facing page)

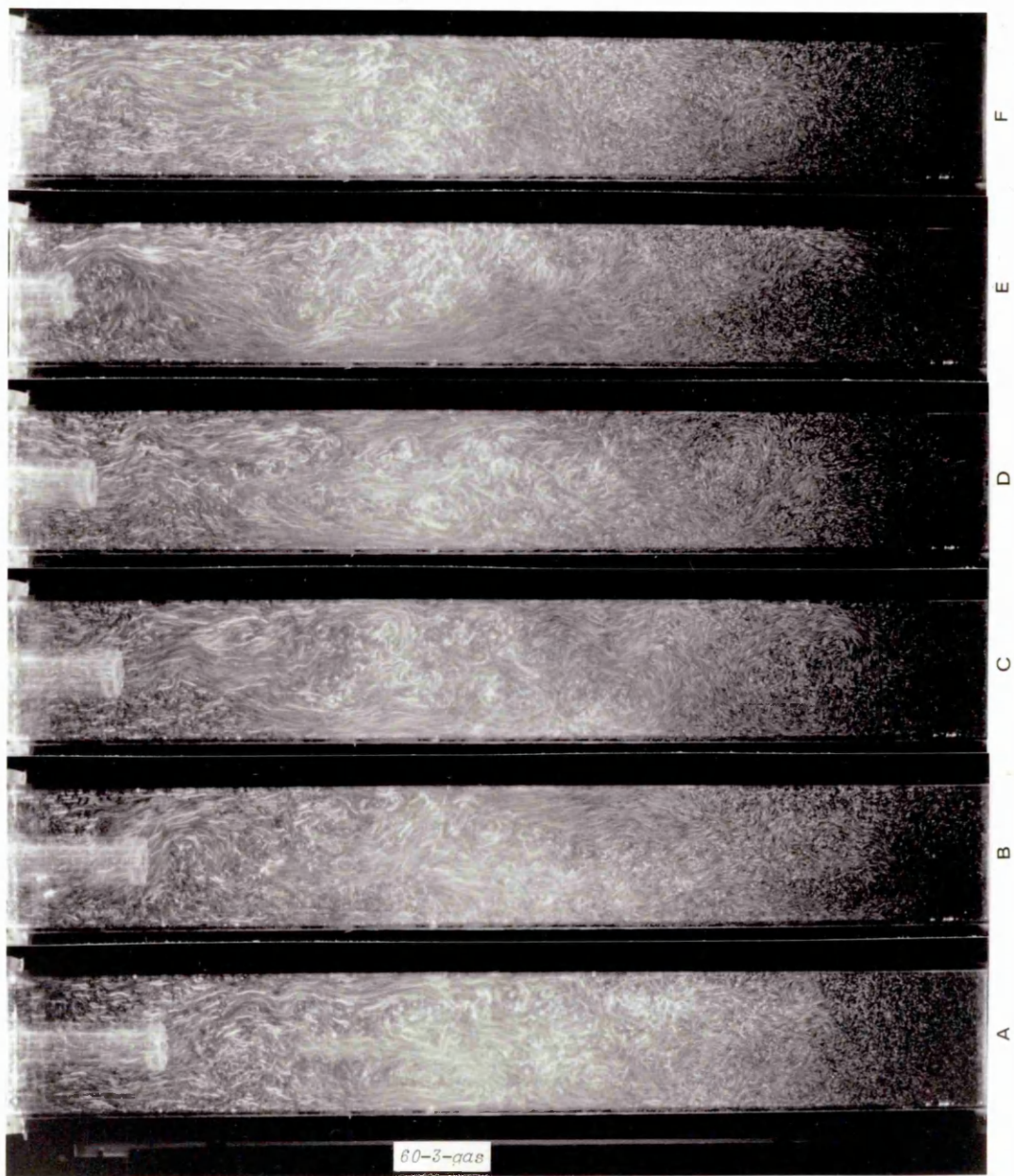


Plate 5.27 Fluid flow patterns developed on plane 1 using Nozzle 3
at different submerged depths.

SEN submerged depth (mm):

A - 150; B - 125; C - 100; D - 75; E - 50; F - 25.

Tracer: fine alumina flakes.

Casting speed: 1.33 m.min^{-1} .

(see facing page)



Plate 5.28 Fluid flow patterns developed on plane 2 using Nozzle 3
at different submerged depths.

SEN submerged depth (mm):

A - 150; B - 125; C - 100; D - 75; E - 50; F - 25.

Tracer: fine alumina flakes.

Casting speed: 1.33 m.min⁻¹.

(see facing page)

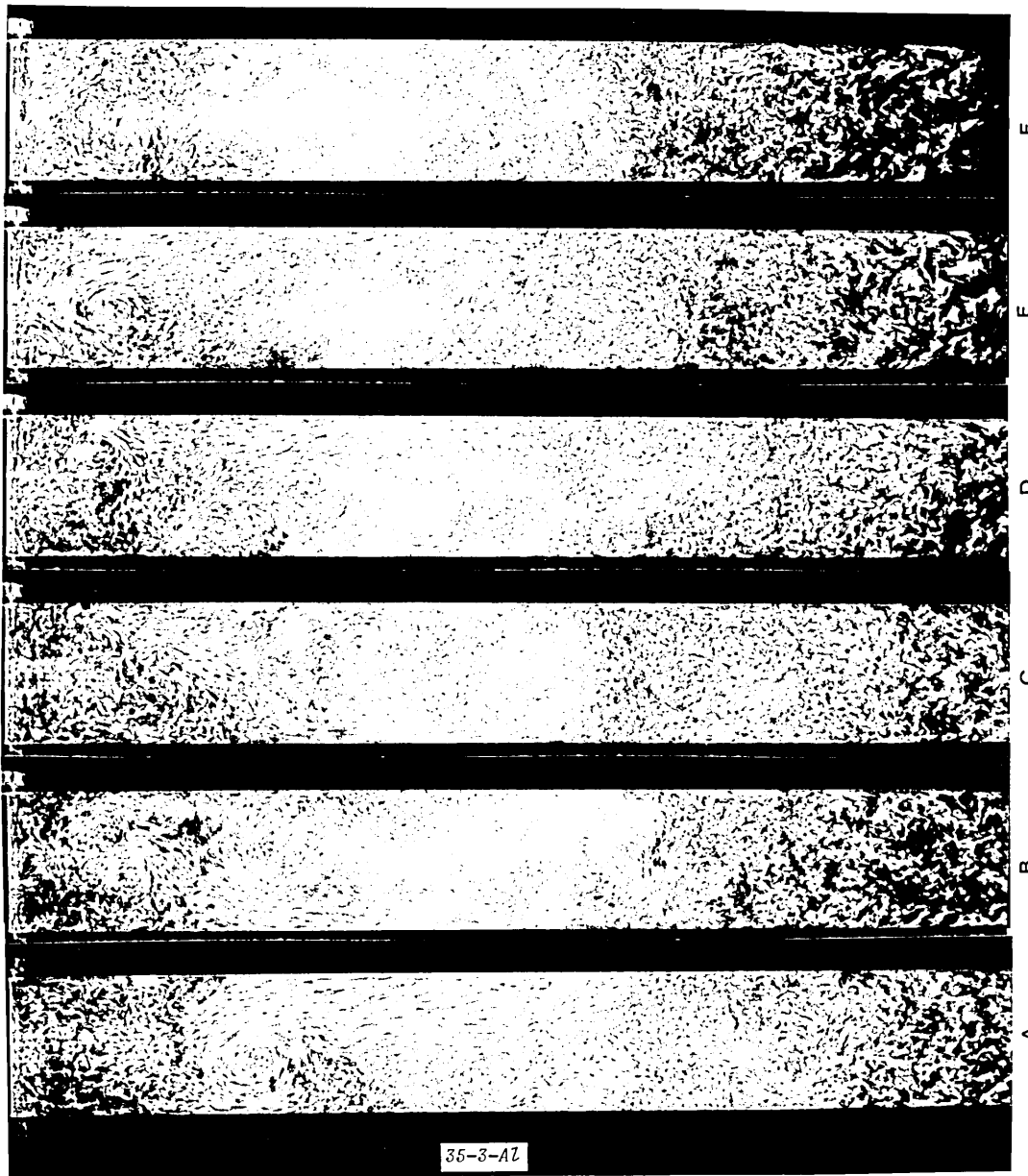


Plate 5.29 Fluid flow patterns developed on plane 3 using Nozzle 3 at different submerged depths.

SEN submerged depth (mm):

A - 150; B - 125; C - 100; D - 75; E - 50; F - 25.

Tracer: fine alumina flakes.

Casting speed: 1.33 m.min⁻¹.

(see facing page)

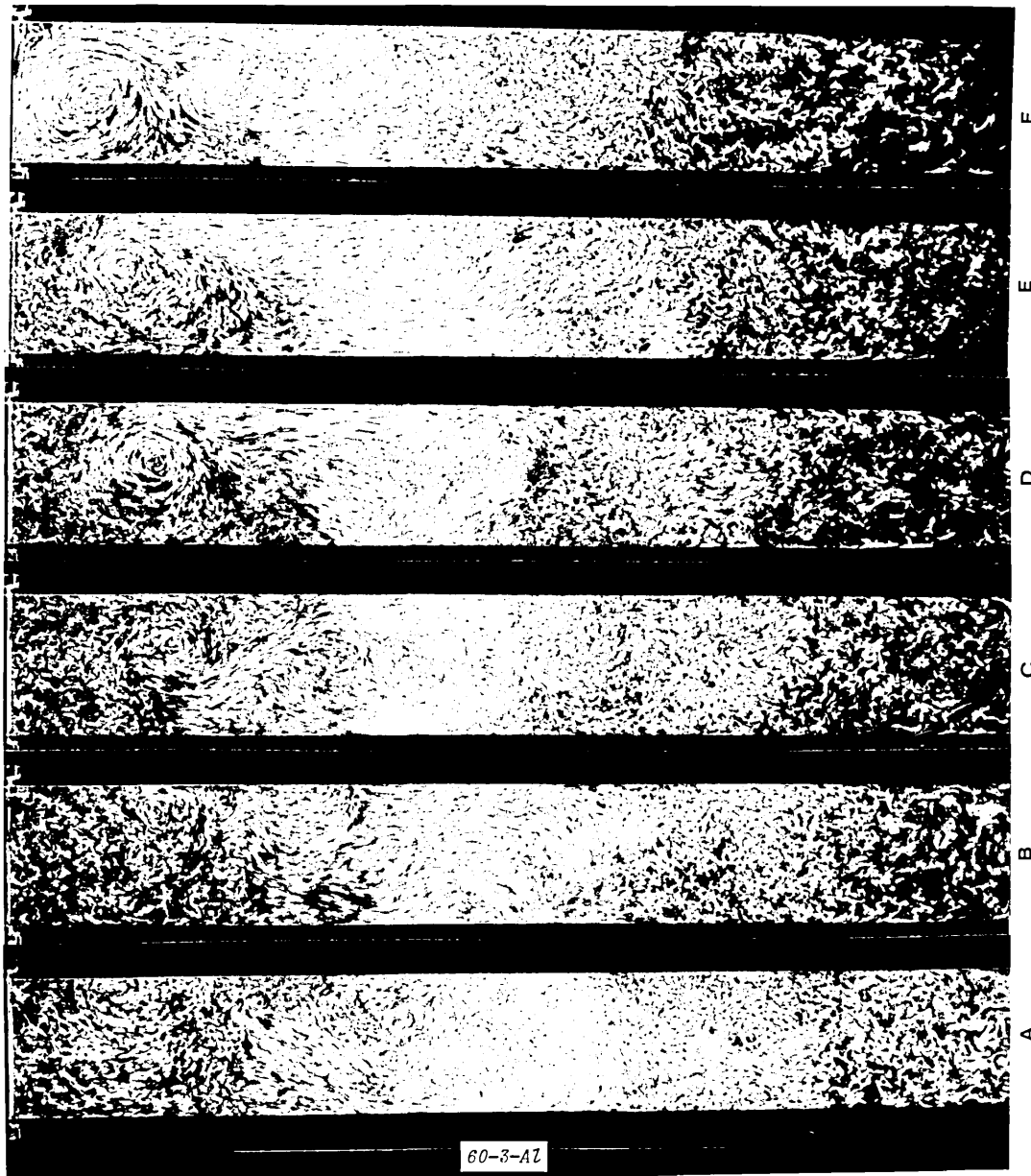


Plate 5.30 Fluid flow patterns developed on central plane using
Nozzle 4 at different submerged depths.

SEN submerged depth (mm):

A - 175; B - 150; C - 100; D - 75.

Nozzle: Nozzle 4 (0° horizontal).

Tracer: small air bubbles.

Casting speed: 0.55 m.min⁻¹.

(see facing page)

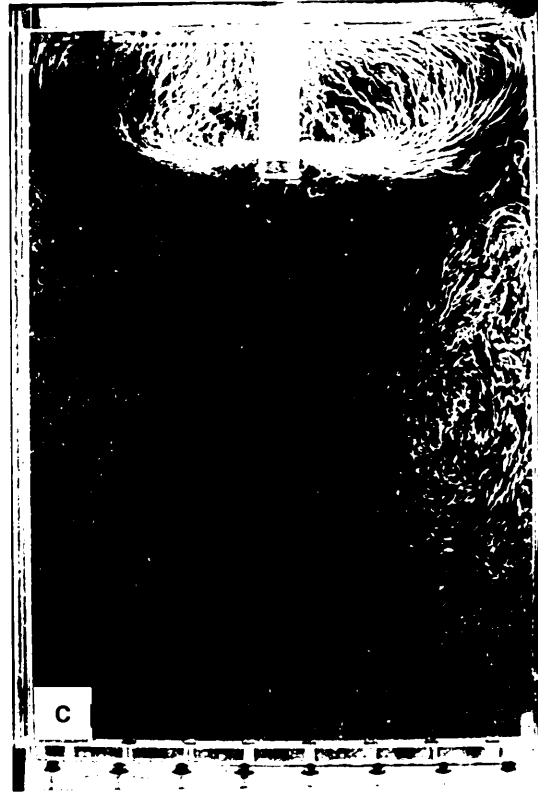
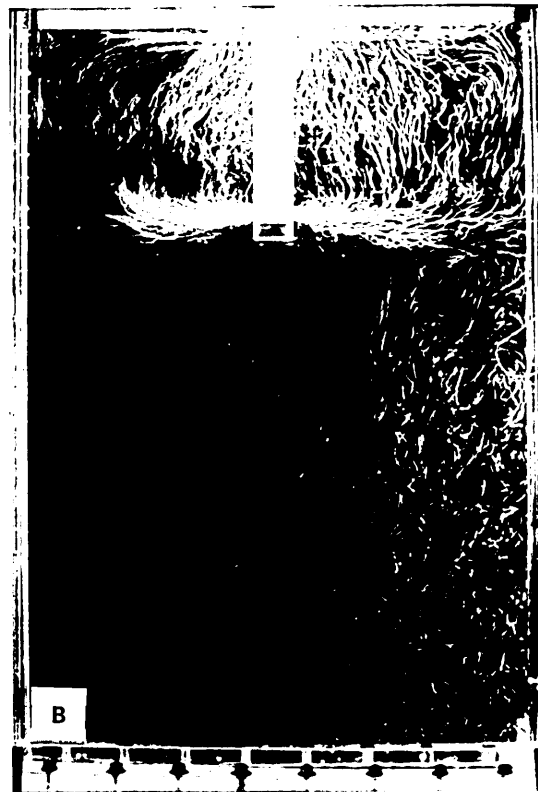
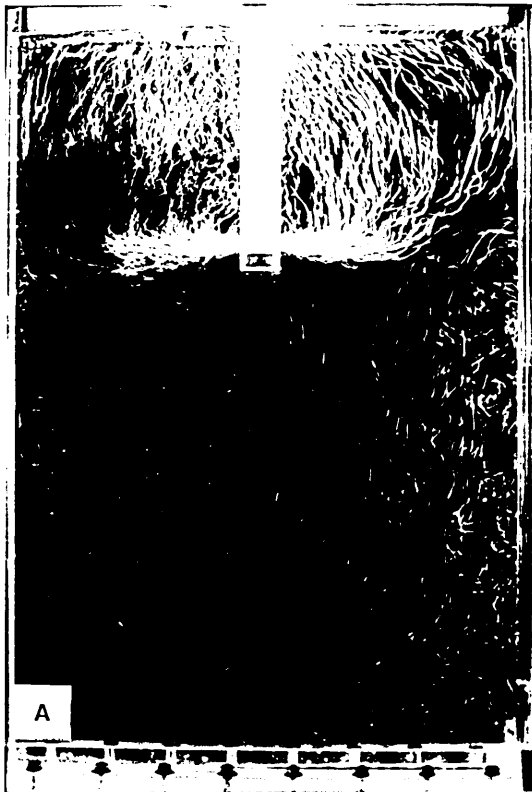


Plate 5.31 Fluid flow patterns developed on central plane using
Nozzle 5 at different submerged depths.

SEN submerged depth (mm):

A - 175; B - 150; C - 100; D - 75.

Nozzle: Nozzle 5 (25° upwards).

Tracer: small air bubbles.

Casting speed: 0.55 m.min⁻¹.

(see facing page)

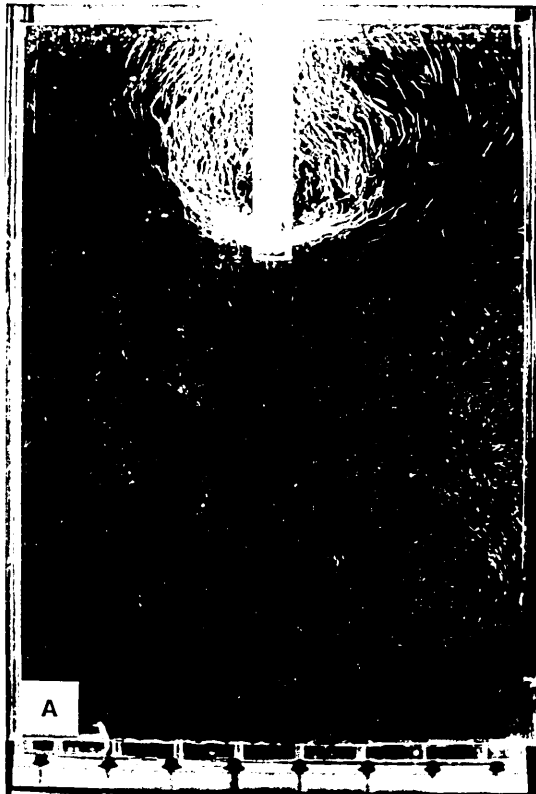


Plate 5.32 Fluid flow patterns developed on central plane using
Nozzle 9 at different submerged depths.

SEN submerged depth (mm):

A - 175; B - 150; C - 100; D - 75.

Nozzle: Nozzle 9 (15° downwards).

Tracer: small air bubbles.

Casting speed: 0.55 m.min⁻¹.

(see facing page)

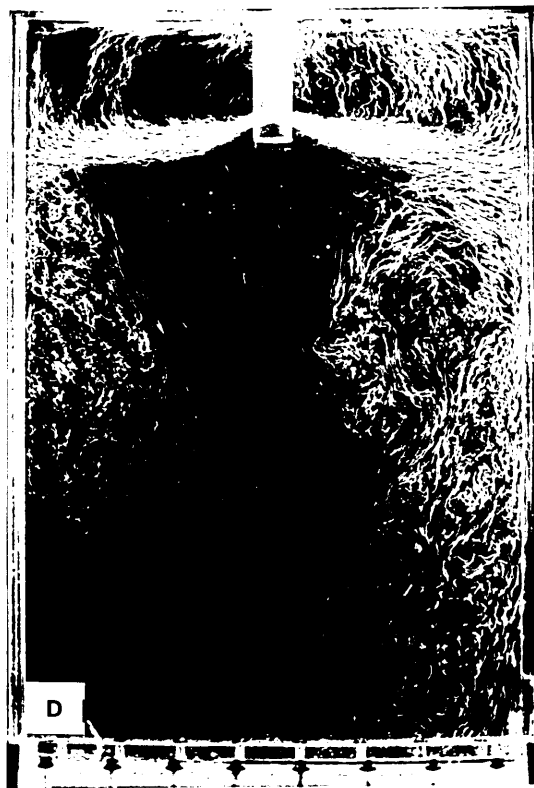
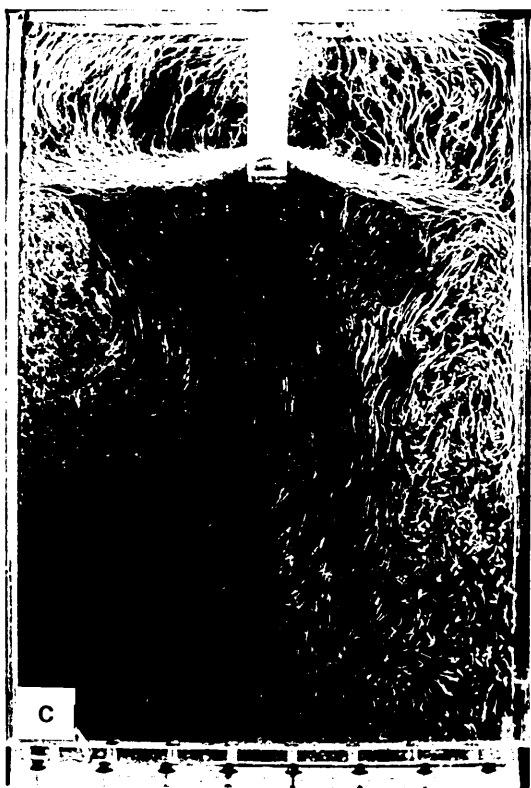
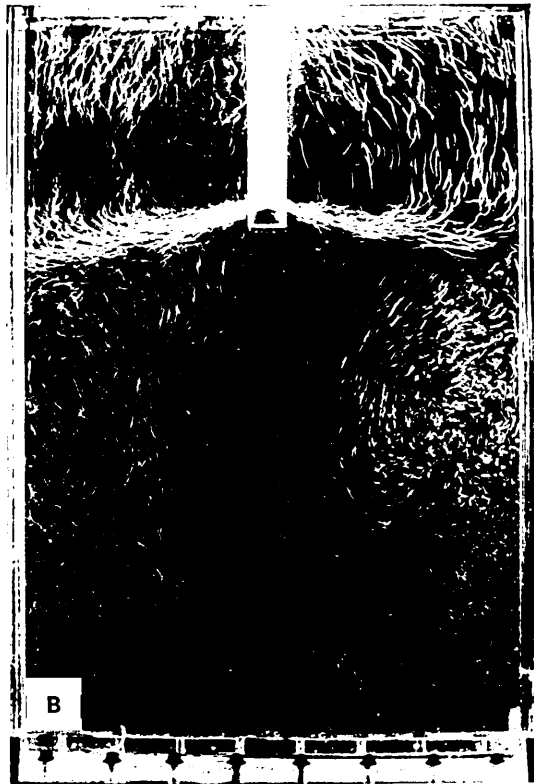
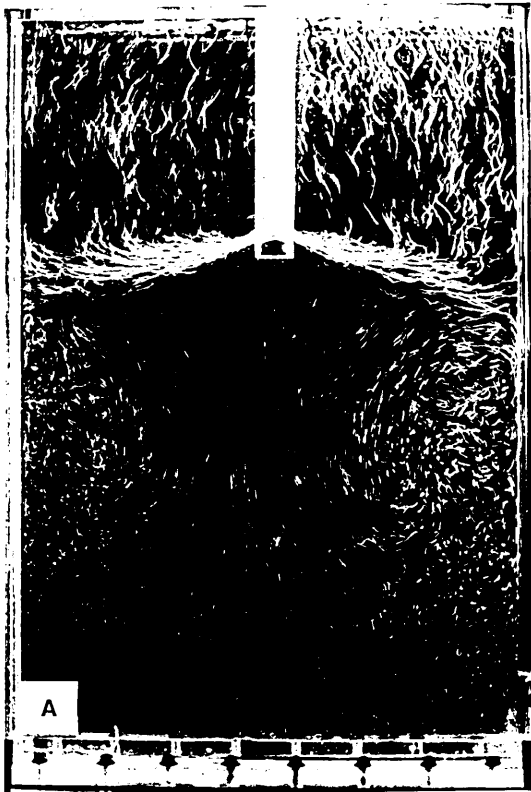


Plate 5.33 Fluid flow patterns developed on central plane using
Nozzle 11 at different submerged depths.

SEN submerged depth (mm):

A - 175; B - 150; C - 100; D - 75.

Nozzle: Nozzle 11 (25° downwards).

Tracer: small air bubbles.

Casting speed: 0.55 m.min⁻¹.

(see facing page)

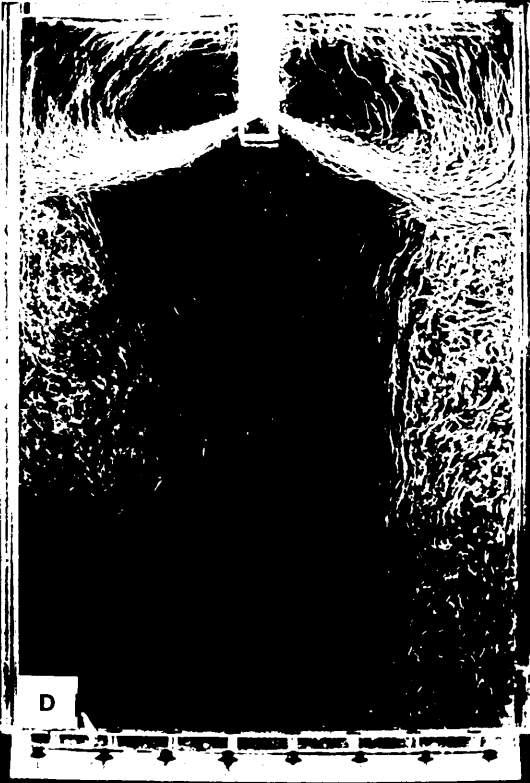
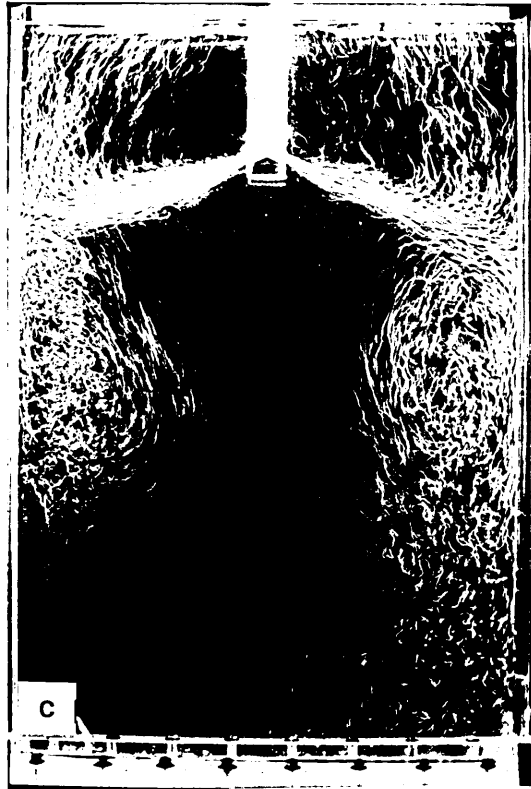
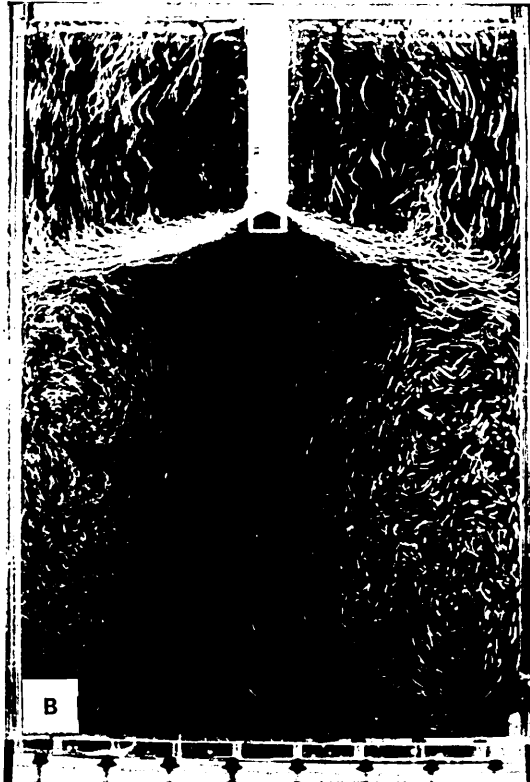
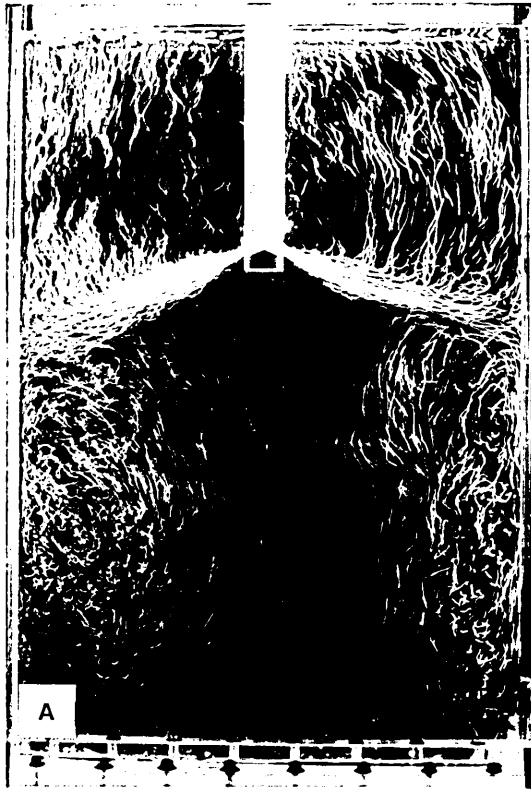


Plate 5.34 Fluid flow patterns developed on plane 1 using Nozzle 3
at different casting speeds.

Casting speed (m.min⁻¹):-

A - 2.00; B - 1.75; C - 1.50; D - 1.25; E - 1.00.

Tracer: fine alumina flakes.

SEN submerged depth: 125 mm.

(see facing page)

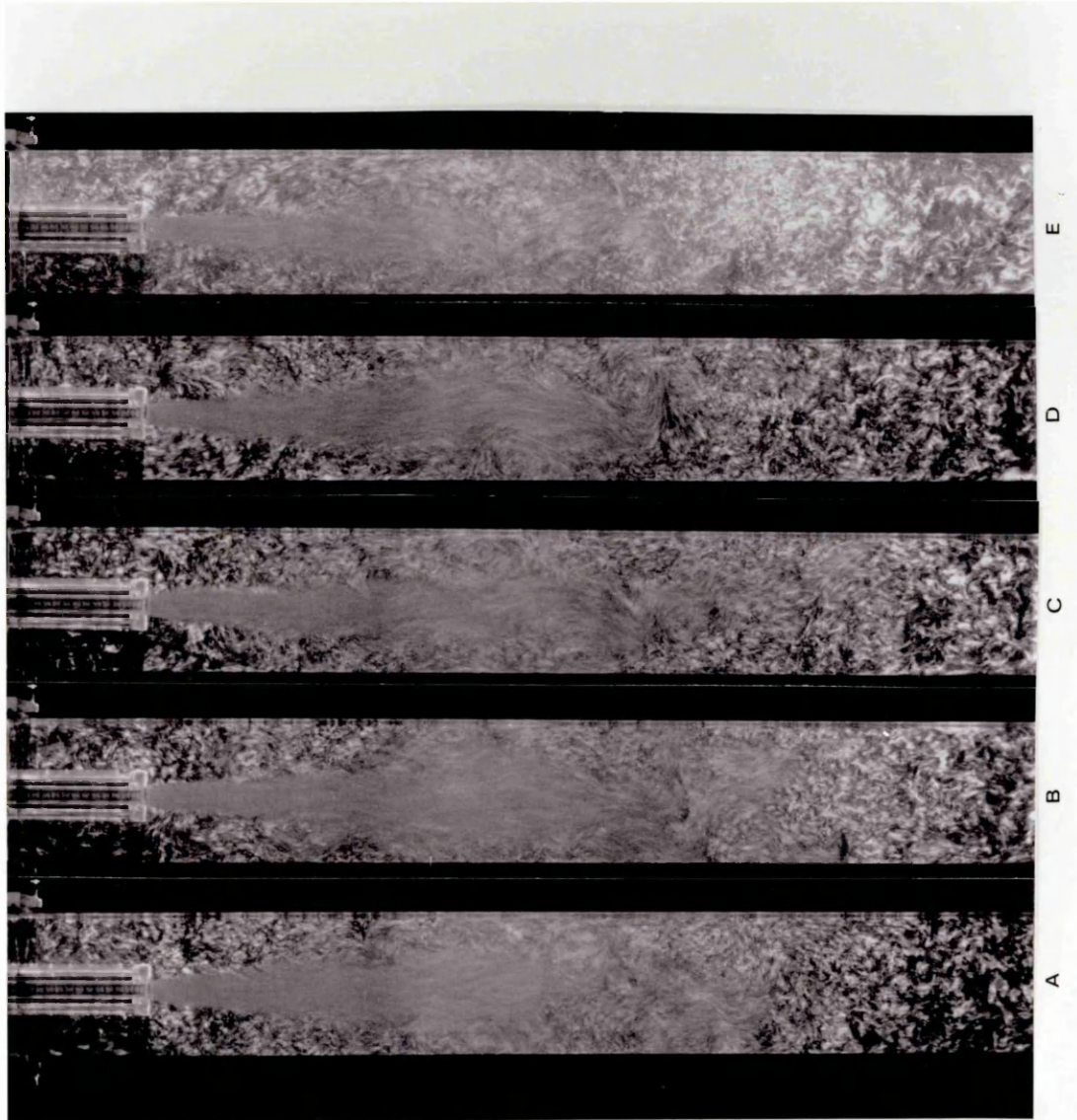
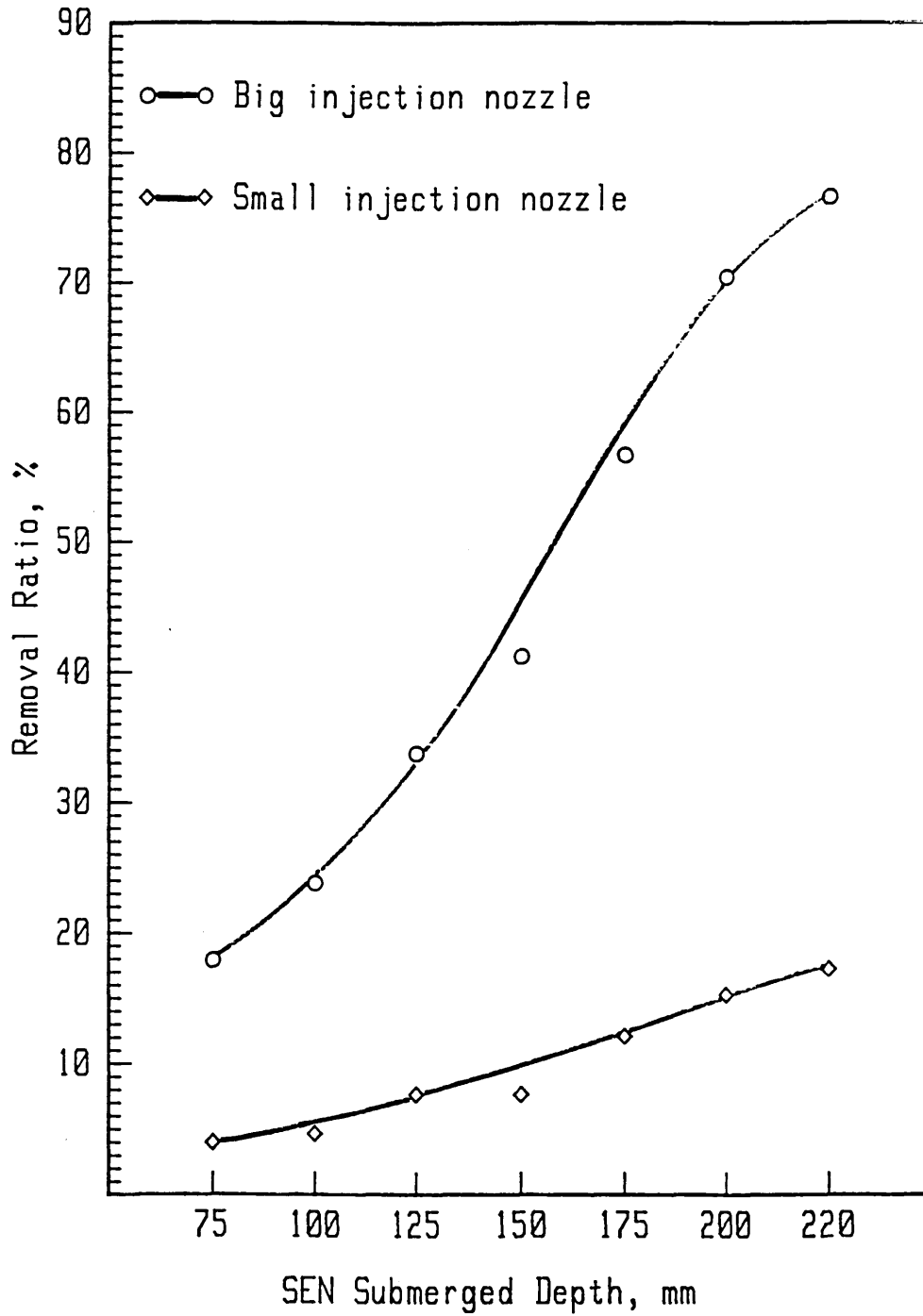


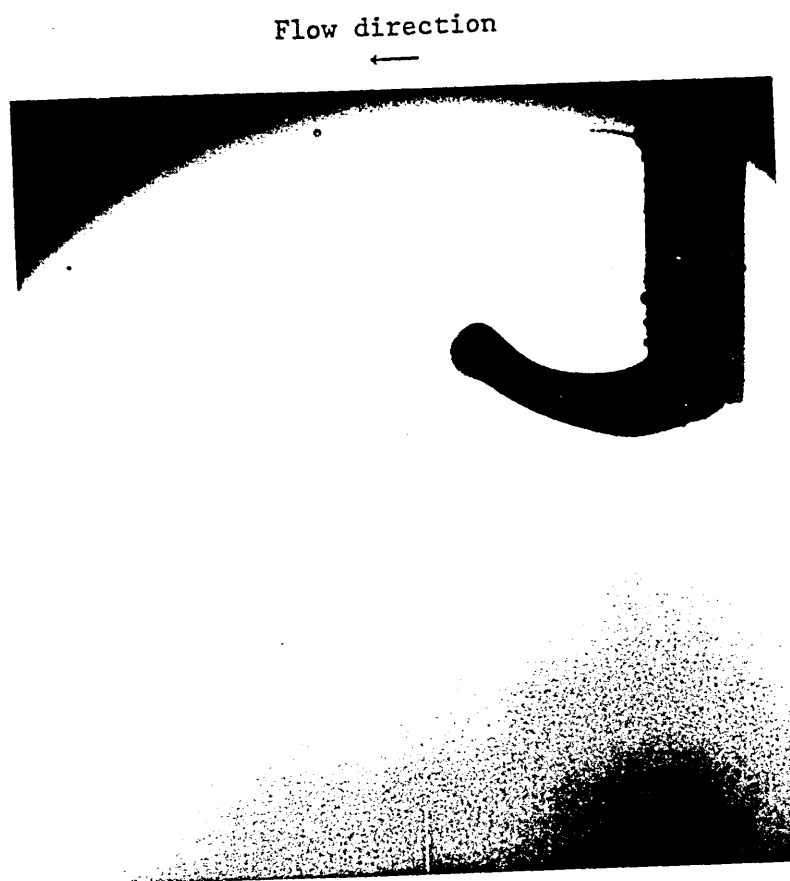
Figure 5.21



Effect of Injection Nozzle Size on the Inclusion
Removal Ratio in the Bloom Mould Model

SEN: Nozzle 4 (horizontal port angle)
Casting speed: 0.55 m/min

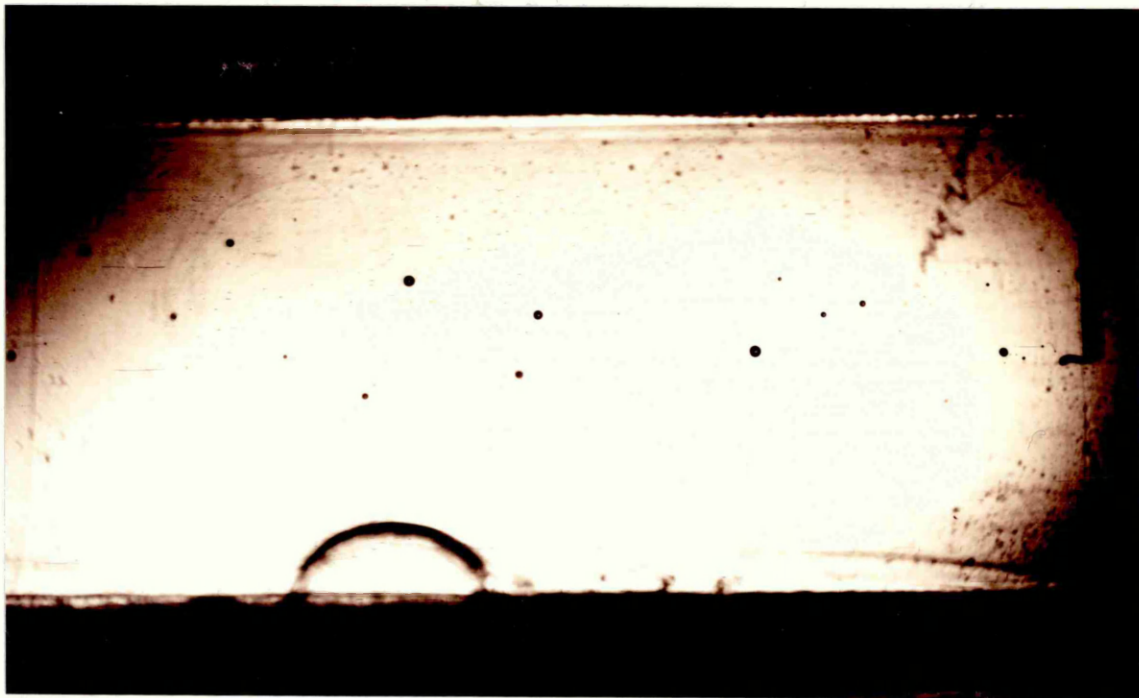
Plate 5.35



Close-up view of the tip area
when particles being generated.

Plate 5.36

Flow direction



General view of the tip area
when particles being generated.

6. DISCUSSION.

6.1. Accuracy and errors of the experimental method.

The aim of the present work has been to elucidate the behaviour of inclusions in the mould sump and the effects of the liquid fluid flow in the sump and operation parameters on inclusion removal into the slag layer on top of the meniscus. Before any conclusion can be drawn from the work carried out so far, it is necessary to assess the accuracy and errors of the experimental method.

For consideration of accuracy and errors the following terms will be used:-

Absolute errors:-

The absolute error of a variable C is defined as the result of its true value C minus its approximation c :-

$$\Delta = C - c \quad (6.1)$$

Generally speaking, the true value is not known, therefore Δ can not be worked out. But its magnitude can usually be estimated as follows:-

$$|\Delta| = |C - c| < \epsilon \quad (6.2)$$

where ϵ is usually termed as the limit of the absolute error of approximation.

So

$$C = c \pm \epsilon \quad (6.3)$$

or

$$c - \epsilon \leq C \leq c + \epsilon \quad (6.4)$$

Relative errors:-

The ratio of the absolute error to the true value of a approximation:-

$$\delta C = \frac{\Delta}{C} \quad (6.5)$$

is defined as the relative error of the approximation c .

Because the true value C is not known, in practice the approximation c is used instead of the true value C . So that:-

$$\delta C = \frac{\Delta}{c} \quad (6.6)$$

And the upper limit ψ of the absolute value of the relative error:-

$$|\delta C| = \left| \frac{\Delta}{c} \right| \leq \psi \quad (6.7)$$

is defined as the limit of the relative error of a approximation.

Propagation of errors:-

The propagation of the errors during arithmetic calculations can be treated using the differentiation method.

$$(i) \quad c = x \pm y$$

$$|dc| = |dx \pm dy| \leq |dx| + |dy| \quad (6.8)$$

i.e.

$$|\Delta c| \leq |\Delta x| + |\Delta y| \quad (6.9)$$

$$(ii) \quad c = xy$$

$$|dc| = |ydx + xdy| \leq |y||dx| + |x||dy| \quad (6.10)$$

or

$$|\delta c| \leq \left| \frac{dx}{x} \right| + \left| \frac{dy}{y} \right| = |\delta x| + |\delta y| \quad (6.11)$$

(iii) $c = x/y$

$$|dc| = \frac{|ydx - xdy|}{y^2} \leq \frac{|y||dx| + |x||dy|}{y^2} \quad (6.12)$$

or

$$|\delta c| \leq \left| \frac{dx}{x} \right| + \left| \frac{dy}{y} \right| = |\delta x| + |\delta y| \quad (6.13)$$

6.1.1. Flowrate measurement.

As mentioned earlier in section 3.1.9., the water flowrates through the model were given by a rotameter. The biggest margin of error of the rotameter was $\pm 2\%$ plus the reading error of ± 0.05 reading scale. The reading error was equivalent to, according to figure 3.11, ± 0.07 L.min⁻¹ of the water flowrate. Taking account of typical water flowrates of 26 L.min⁻¹ through the billet mould model and 15 L.min⁻¹ through the bloom mould model, the relative reading errors of flowrate measurement will be:-

on the billet mould model:- $\pm 0.3\%$;

on the bloom mould model :- $\pm 0.5\%$.

So, the error involved in the fluid flow measurement will be within $\pm 2.5\%$.

6.1.2. Calculation of casting speed from the flowrate measurement.

The casting speed used in the model was calculated by the following formula:-

$$V_c = \frac{Q_m}{A_m} \quad (6.14)$$

where V_c : casting speed;

Q_m : water flowrate through the model;

A_m : mould model cross-sectional area.

The mould cross-sectional area was obtained by measuring the mould thickness and width using a tape-measure. This area is less accurate than the other measurements because of the distortion of the perspex during the experiment. Although the thickness and width were measured to a precision of ± 0.5 mm a more realistic error is ± 3 mm. Therefore, the relative errors of mould cross-sectional area could be determined as:-

$$\begin{aligned} \text{for the billet mould:- } \delta(A_m) &= \delta(\text{thickness}) + \delta(\text{width}) \\ &= 3/140 + 3/140 \\ &\approx \pm 4\% \end{aligned}$$

$$\begin{aligned} \text{for the bloom mould:- } \delta(A_m) &= \delta(\text{thickness}) + \delta(\text{width}) \\ &= 3/425 + 3/65 \\ &\approx \pm 5\% \end{aligned}$$

So, according to equation (6.14), the relative error of the casting speed determination is:-

for the billet mould:-

$$\begin{aligned}\delta(Vc) &= \delta(Q_m) + \delta(A_m) \\ &\approx 2.5\% + 4\% = \pm 6.5\%\end{aligned}$$

for the bloom mould:-

$$\begin{aligned}\delta(Vc) &= \delta(Q_m) + \delta(A_m) \\ &\approx 2.5\% + 5\% = \pm 7.5\%\end{aligned}$$

6.1.3. Colorimetric measurement.

The instrument used for the colorimetric analysis claimed to give the wavelength accuracy of ± 1 nm and wavelength reproducibility of ± 0.5 nm, the photometric accuracy of $\pm 0.5\%$ and photometric reproducibility of $\pm 0.5\%$. The instrument has a self-test electronic device and it goes through self-test procedures whenever the instrument is turned on. So the error of the colorimetric measurement could be expected to be under $\pm 1\%$.

6.1.4. Coloured and colourless paraffin volume measurement.

The coloured paraffin volume was measured by a burette. The biggest margin of error of the burette used was ± 0.05 ml. For a typical injected amount of 10 ml, this will lead a relative error of coloured paraffin measurement of $\pm 0.5\%$. And for a injected amount of 5 ml, the relative error will be $\pm 1\%$.

The colourless paraffin was measured by a measure tube. Although the biggest margin of error of the measure tube was ± 1 ml, a more realistic error is ± 3 ml. For a typical amount of 150 ml, this error will give a relative error of $\pm 2\%$. For the volume of 50 ml as in the case of billet mould model, this will result a relative error of $\pm 6\%$.

6.1.5. Errors in inclusion removal ratio determination.

The inclusion removal ratios obtained from the experiments were calculated using equation (5.1) in Chapter 5. Therefore, the relative error could be expressed as:-

$$\delta(\eta_{inclusion}) = \delta(V_{in\ slag}) + \delta(V_{injected}) \quad (6.15)$$

And $V_{in\ slag}$ was obtained from Colorimetric measurement with the aid of calibration curve. The relative error can be determined from errors involved in colourless paraffin volume measurement, coloured paraffin volume measurement and Colorimetric measurement.

Therefore in billet mould:-

$$\delta(V_{in\ slag}) \approx 6\% + 0.5\% + 1\% = \pm 7.5\%$$

in bloom mould:-

$$\delta(V_{in\ slag}) \approx 2\% + 1\% + 1\% = \pm 4\%$$

Substituting into equation (6.15), we have:-

in billet mould:-

$$\delta(\eta_{inclusion}) \approx 7.5\% + 1\% = \pm 8.5\%$$

in bloom mould:-

$$\delta(\eta_{inclusion}) \approx 4\% + 1\% = \pm 5\%$$

6.2. Fluid flow patterns developed.

Unsurprisingly the fluid flow patterns revealed from the model investigation were similar to those described by Szekely and

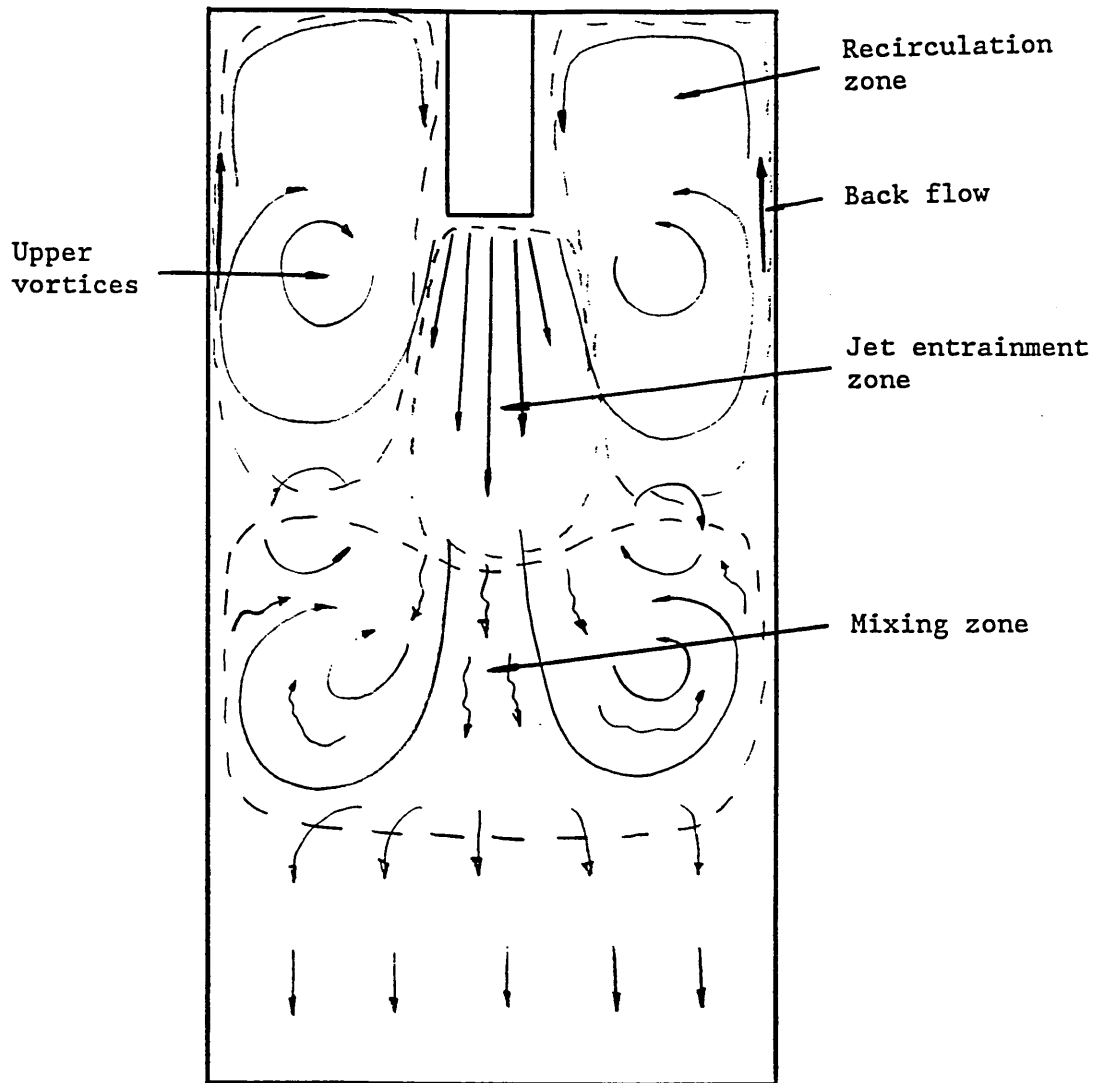
Yadaya^[28], figure 2.1. The jet from the nozzle was found to penetrate deeply into the pool and a recirculation pattern was developed. During its penetration, the jet entrains liquid fluid from the surroundings. This entrainment must, of course, be fed by back flows from both above and below the jet since it is only through the jet that liquid fluid flows into the sump. Thus a mixing zone exists below the jet in which the jet flow is evened out by the back flow to give a more or less uniform flow that flows into the rest of the strand. The recirculation patterns observed are also believed to be caused by the jet entrainment which pulls the back flow up towards the meniscus. Vortices were formed around the jet stream and the eyes of the vortices were not far from the bottom of the nozzle. Figure 6.1 shows schematically the fluid flow pattern developed inside the billet mould.

The fluid flow patterns obtained from the bloom mould model investigations also consist of three zones as described above although their configuration is different. These three zones are the jet entrainment zone, the recirculation zone and the mixing zone, as schematically shown in figure 6.2. Plate 6.1 shows the type of flow patterns that have been observed in the bloom mould model. The recirculatory flow into the meniscus region is much stronger with this type of flow pattern, therefore a higher inclusion removal ratio have been achieved in this case because it is the recirculatory flows which bring inclusion up to the meniscus region.

6.2.1. Effect of SEN geometry.

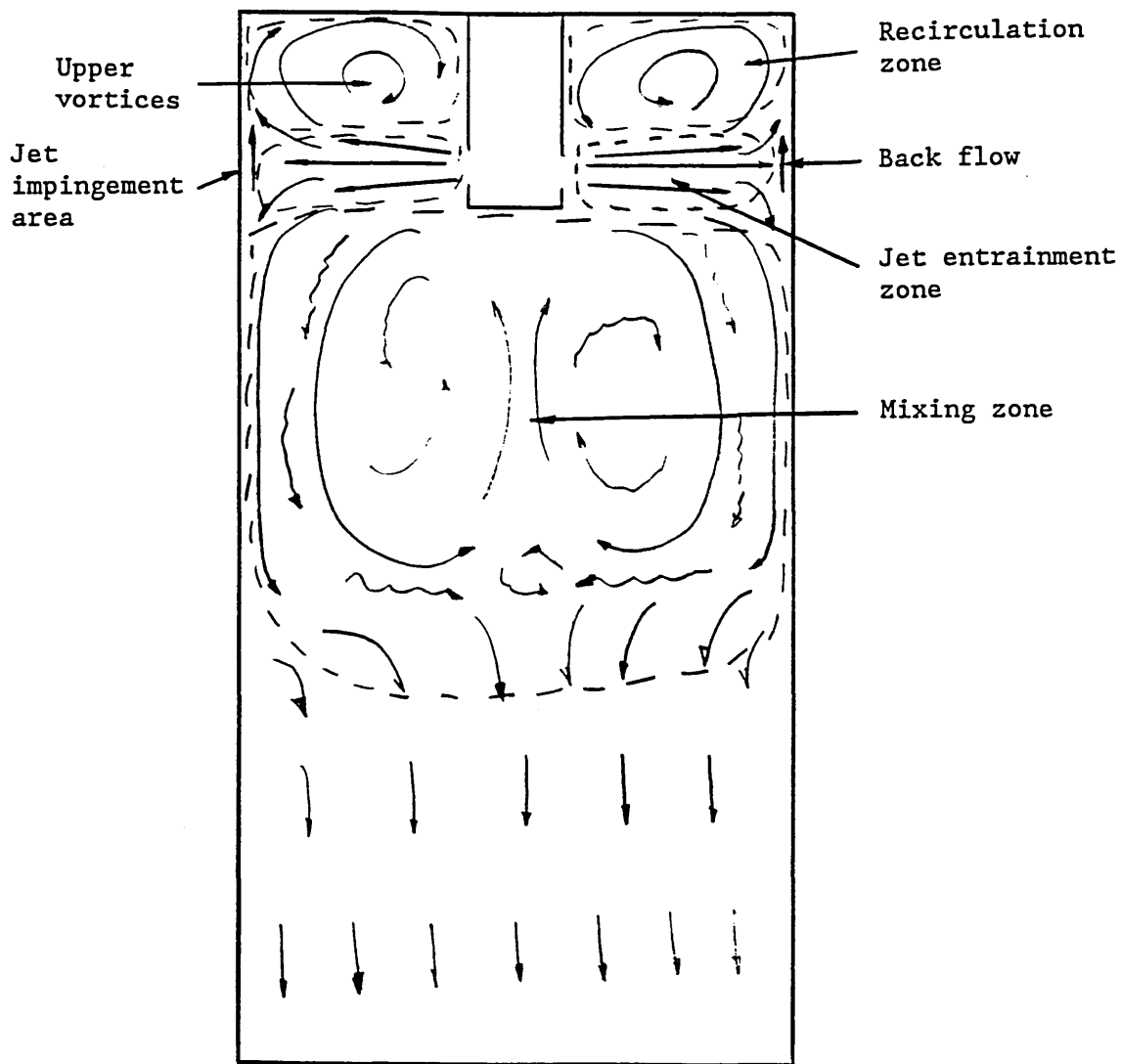
The outside diameter of the SEN mainly affects the fluid flow pattern

Figure 6.1



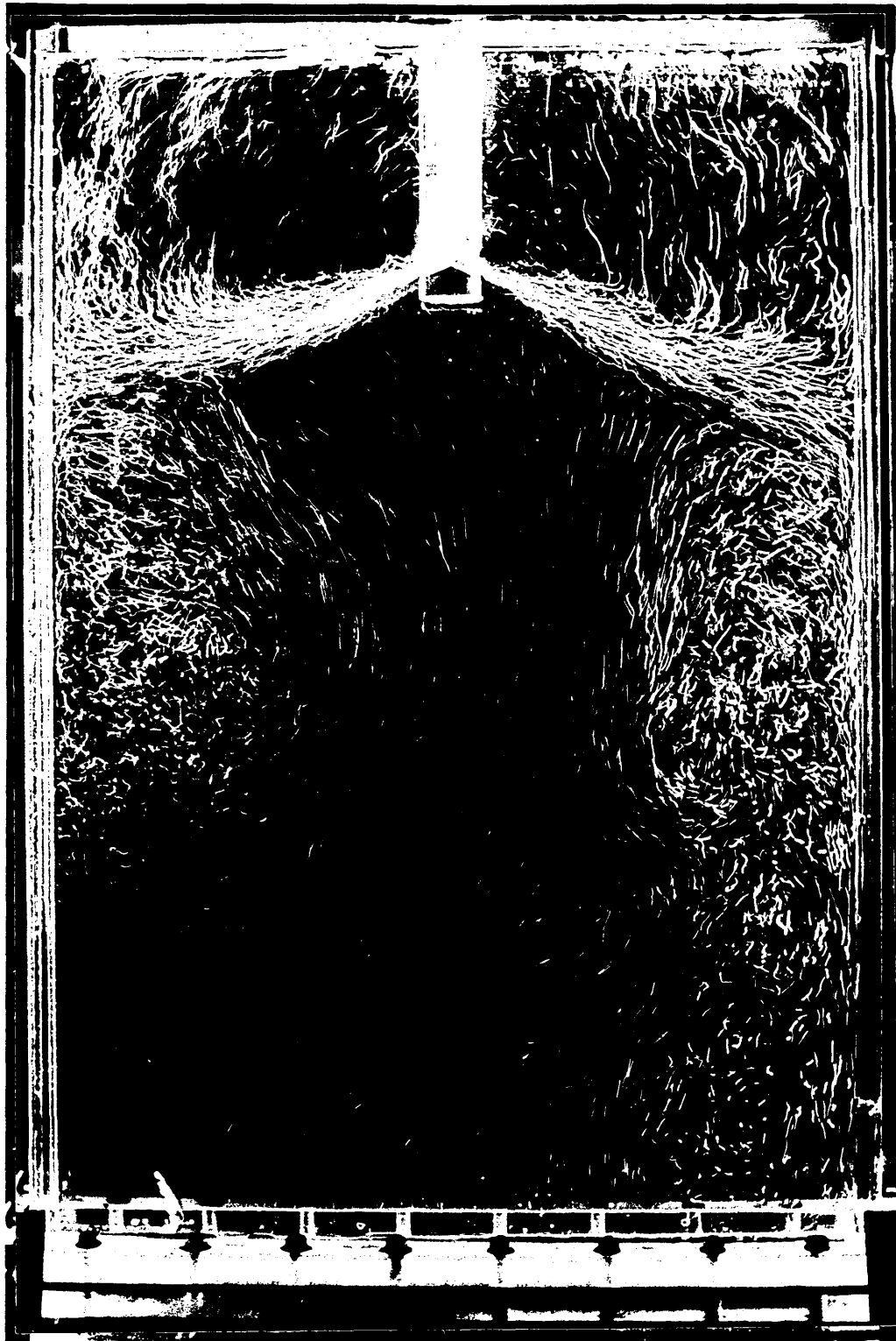
sketch of the fluid flow pattern developed in
the billet mould sump.

Figure 6.2



sketch of the fluid flow pattern developed in
the bloom mould sump.

Plate 6.1



Fluid flow pattern observed in the bloom mould model.

in the upper region of the mould. As the outside diameter of the SEN increases, the space, available for the fluid to recirculate in the recirculation zone, is restricted. As a result, the back flow towards the meniscus is weakened. Therefore, the fluid has a high rising velocity in the upper region near the meniscus when the nozzle with smaller outside diameter was used, plate 5.2 and 5.3.

The changes in the outside diameter of the SEN will not affect the characteristics of the mixing zone and the jet entrainment zone, which are governed by the exit velocity of the stream from the SEN. The exit velocity of the stream is affected, at a given casting speed, by the inside diameter of the nozzle mouth. At any given casting speed, the smaller the inside diameter, the higher the exit velocity, and hence, the more intensive the mixing zone and the jet entrainment zone.

The fluid flow patterns developed in the mould model are largely affected by the SEN port angle when bifurcated SENs were employed. First of all, the locations of the jet impingement area on narrow faces are different for different SENs. The location of the area shifts upwards as the SEN port angle moves towards an upward angle. Secondly, the characteristics of the back flow are quite different for different SENs. The velocity of the back flow increases as the SEN port angle changes towards an upward angle. Thirdly, the mixing characteristics of the fluid in the mixing zone are different for different SENs. The mixing is more intensive when employing a nozzle with downward angle than that with upward angle. And finally, the recirculation region is confined to a smaller area when employing a nozzle with upward angle than that with downward angle. As a

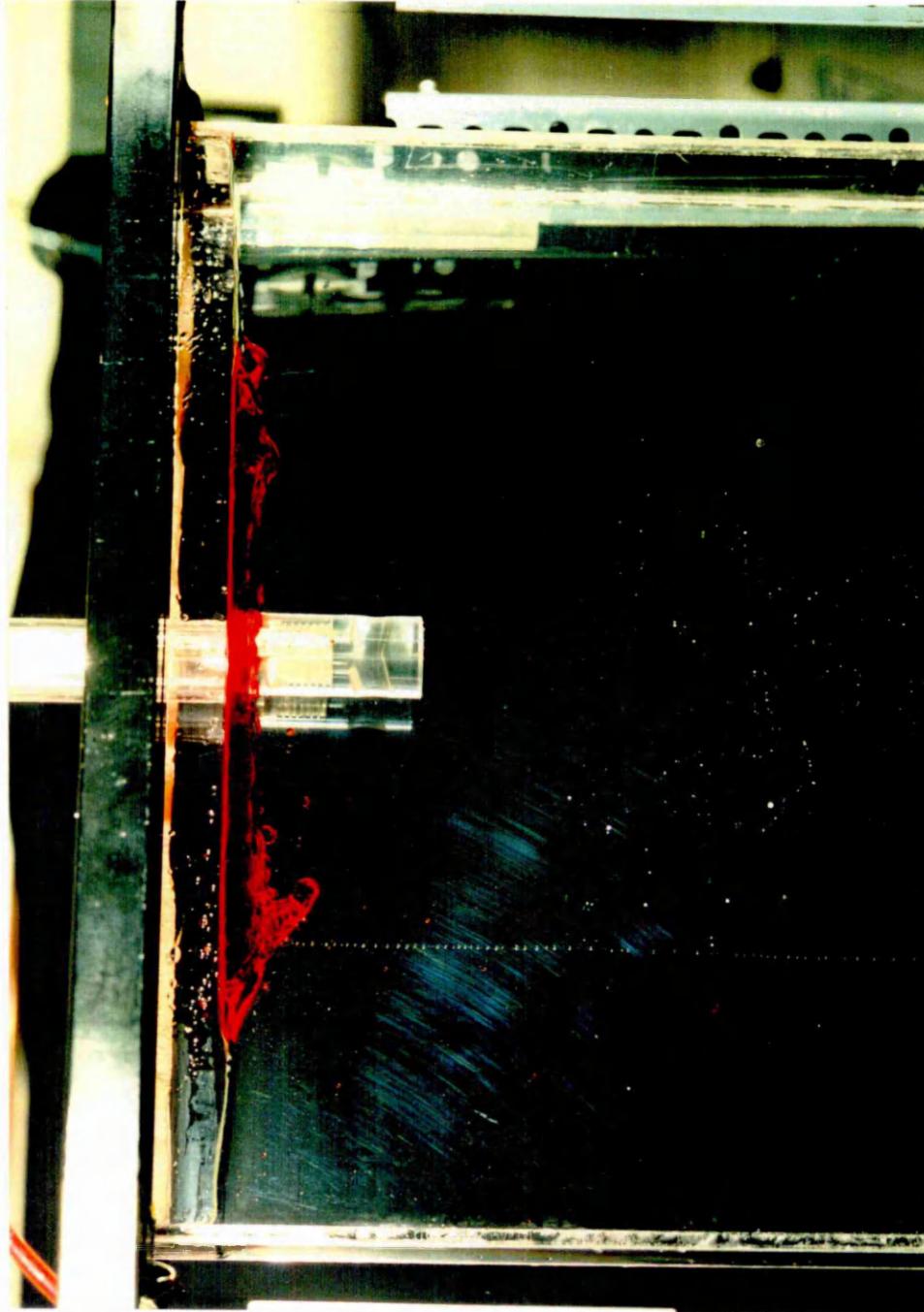
consequence, the 'slag' on top of the meniscus is pushed towards the SEN and this has left the meniscus uncovered unless SEN submergence depth is large enough to avoid the exposure of the meniscus.

6.2.2. Effect of SEN submerged depth.

Both the positions and the strengths of the recirculation zone in the mould are affected by the SEN submerged depth. As the SEN submerged depth increases, the location of the recirculation zone and the eyes of the upper vortices shifts downwards. This causes the recirculation zone to be enlarged and intensified, and hence the more fluid to be involved in the recirculation zone. Because the eyes of the upper vortices are away from the meniscus in this case, the fluid under the meniscus is very quiet and slowly moving cross the meniscus. Therefore, the back flow generated is of high velocity due to the large amount of the fluid involved in the recirculation zone. On the contrary, the eyes of the upper vortices are close to the meniscus when small SEN submerged depth is employed, causing the fluid to flow under the meniscus at high velocity. Although the locations of the jet entrainment zone and the mixing zone vary as the SEN submerged depth changes, their strengths will not be affected by the changes.

The location of the jet impingement area on the mould narrow face is also affected by the SEN submerged depth when bifurcated SENs are used. As the SEN submerged depth decreases, the impingement area moves towards the meniscus. The closer the jet impingement area is to the meniscus, the more intense is the fluid flow near the meniscus region. This intensity results in a high horizontal velocity of the

Plate 6.2



View of the meniscus when small SEN submerged depth was used.
(showing the "slag" on top of the meniscus being pushed towards the SEN and becoming entrapped)

fluid across the meniscus towards the SEN, see plate 5.30 to 5.33. The recirculation of the fluid is, consequently, confined in a small region and the 'slag' on top of the meniscus is pushed towards the SEN, resulting in the meniscus being partly denuded of slag, as shown in plate 6.2. The inclusion removal ratio is therefore less when the SEN submerged depth is small than when it is large. Plate 6.2 also shows that slag particles became entrapped when small SEN submerged depth are used. Employing too small an SEN submerged depth is therefore not good casting practice.

6.2.3. Effect of casting speed.

Casting speed has little effect on the fluid flow patterns in the upper portion of the mould, although an increase of casting speed will cause an increase in the intensity of the upper vortices. Because the eyes of the vortices remain in the same position, the characteristics of the recirculation zone are not affected by changes in the casting speed, provided that the SEN submerged depth is not too small. The sizes and the strengths of the jet entrainment zone and the mixing zone are, however, strongly affected by the casting speed. The higher the casting speed, the larger and stronger are the jet entrainment zone and the mixing zone.

6.3. Interpretation of experimental results.

One particular aspect of the experimental results was surprising. The clear trend shown in Figures 5.3 to 5.13 was for inclusion removal efficiency to increase with the depth to which the SEN was submerged. It is not immediately apparent from the theoretical

analysis why this should be so. Indeed intuition would suggest the opposite relationship. Discovering the reason for the trend was a major component in the interpretation of the experimental results.

A possible explanation for the trend was initially sought in the variation of Γ with submerged depth. The strategy adopted for the analysis of the experimental results was therefore planned in order to provide values of Γ . In the event, the influence of Γ was found to be minor but the interpretation strategy adopted proved to be very informative nevertheless and will therefore be described in some detail.

In order to determine values of Γ from the experimental results, equation (4.52) for η was rearranged as an equation for Γ , values of η being known from the experiments. The resulting equation, (4.69), is reproduced here, for convenience:-

$$\Gamma = \frac{-B \pm \sqrt{B^2 - 4AC}}{2A} \quad (4.69)$$

in which A, B and C are functions of the inclusion removal efficiency measured in the experiments, the enhancement factor e, and the parameters a , β , ζ and ν . The evaluation of these latter parameters is described in the next section which shows that the ν is strongly dependent on the mean inclusion diameter in the region just below the meniscus, but the accurate estimates can be made of the other parameters. The parameter 'e' depends on the effective turbulent diffusivity in the region immediately below the meniscus, which is unknown. The region is not highly turbulent so that e is unlikely to be far from 1. This value is assumed in the analysis at this stage,

but this assumption is examined further in section 6.4.

Equation (4.69) provides two roots for Γ . However, that the root evaluated using the negative sign is always negative. Since a negative interchange flux has no physical meaning, this root has been neglected, the positive sign being taken as providing the valid root.

6.3.1. Determination of the values of a , β , ζ , and v .

a) Determination of the value of a .

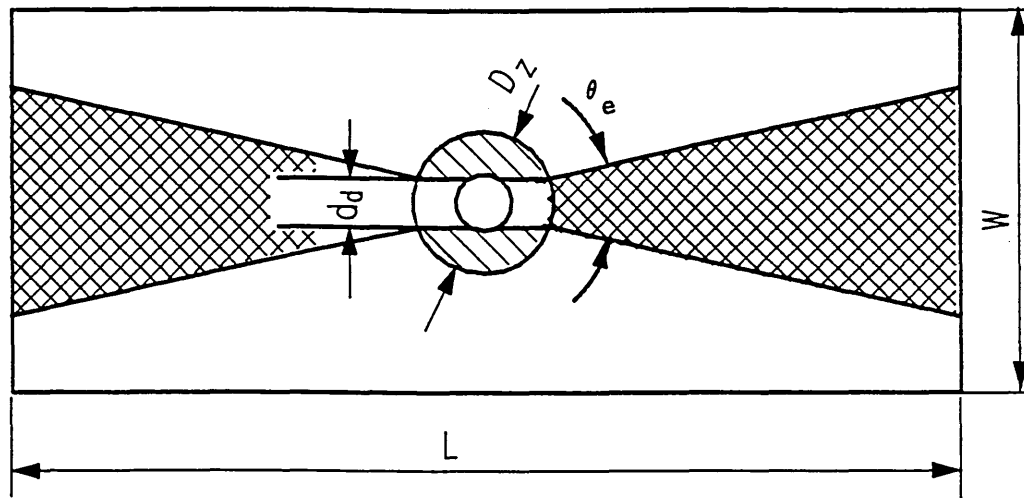
As defined in equation (4.35), a is the area of the jet region projected onto the horizontal plane as a fraction of the mould cross sectional area. The area of contact between the jet entrainment zone and the recirculation zone projected onto a horizontal plane, A_J , can be calculated using the information about jet penetration depth and jet expanded angle. From the jet theory^[99] and the experimental results obtained in the present work, the jet expanded angle θ_e is taken as 14° , as shown in figures 6.3 and 6.4.

Figure 6.3 shows schematically the area of contact between the jet entrainment zone and the recirculation zone projected onto the horizontal plane, together with the mould dimensions for the case of the model bloom mould. According to the diagram, the projected area A_J can be expressed as:-

$$A_J = 2(L/2 - D_Z/2) \left[(L/2 - D_Z/2) \tan(\theta_e/2) + d_d/2 \right] \quad (6.16)$$

The cross section area of the mould can be obtained using the following formula:-

Figure 6.3



Jet projected area in the bloom mould.

$$A_B = L.W \quad (6.17)$$

Therefore, the fractional jet projected area in the bloom mould model can be expressed as:-

$$a = \frac{A_J}{A_B} = \frac{2(L/2 - D_Z/2)}{L.W} \left[(L/2 - D_Z/2) \tan(\theta_e/2) + d_d/2 \right] \quad (6.18)$$

For the bloom mould model employed here, we have the following dimensions:-

$$L = 425 \text{ mm}, W = 65 \text{ mm}, D_Z = 32 \text{ mm}, d_d = 13 \text{ mm and } \theta_e = 14^\circ.$$

Thus, according to equation (6.18), the fractional jet projected area a for the bloom mould model is 0.44.

Figure 6.4 shows schematically the area of contact between the jet entrainment zone and the recirculation zone projected onto a horizontal plane together with the mould dimensions and jet penetration depth for the case of the model billet caster mould. The jet projected area is:-

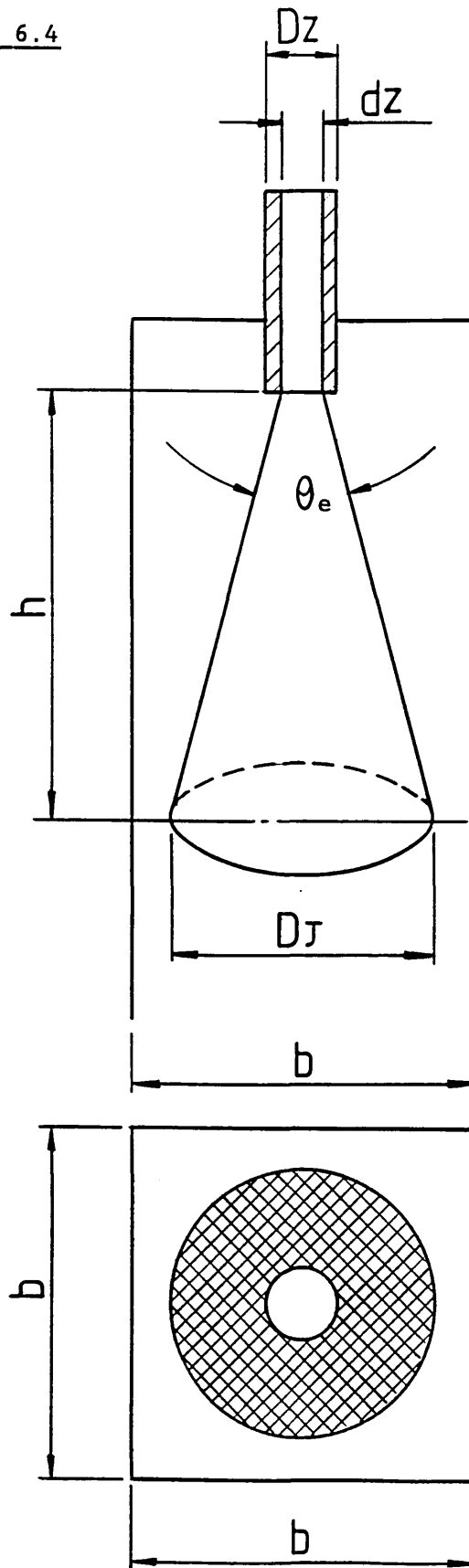
$$A_J = \frac{\pi(D_J^2 - D_Z^2)}{4} \quad (6.19)$$

where D_J is the maximum jet diameter which is expressed as:-

$$D_J = d_Z + 2h \cdot \tan(\theta_e/2) \quad (6.20)$$

and h is the distance from the nozzle mouth to the point where jet diameter reaches maximum, as shown in figure 6.4 h is about 3/4 of the jet penetration depth.

Figure 6.4



Jet projected area in the billet mould.

Substituting equation (6.20) into equation (6.19), we have:-

$$A_J = \frac{\pi((d_Z + 2h.\tan(\theta_e/2))^2 - D_Z^2)}{4} \quad (6.21)$$

The mould cross section area for billet mould model is:-

$$A_B = b^2 \quad (6.22)$$

Therefore, the fractional jet projected area for billet mould model can be written as:-

$$a = \frac{A_J}{A_B} = \frac{\pi((d_Z + 2h.\tan(\theta_e/2))^2 - D_Z^2)}{4b^2} \quad (6.23)$$

Substituting the following values for the billet mould model into equation (6.23):-

$$b = 140 \text{ mm}, d_Z = 15 \text{ mm}, h = 450 \text{ mm}, \theta_e = 14^\circ,$$

and

$$D_Z = 50 \text{ mm for Nozzle 1 and Nozzle 3,}$$

$$D_Z = 70 \text{ mm for Nozzle 2,}$$

we obtained the values of a for the billet mould model. The fractional jet projected area for the billet mould model when employing Nozzle 1 and Nozzle 3 is 0.53 and a for Nozzle 2 is 0.43.

b) Determination of the value of β .

As mentioned in chapter 4, β is ratio of Γ_{JM} to Γ_{JR} . According to the definition of Γ_{xx} in equation (4.32), β could be further expressed as the ratio of \dot{M}_{JM} to \dot{M}_{JR} , i.e.:-

$$\beta = \frac{\dot{M}_{JM}}{\dot{M}_{JR}} \quad (6.24)$$

where \dot{M}_{JM} is the liquid metal interchange mass flux between the jet entrainment zone and the mixing zone.

\dot{M}_{JR} is the liquid metal interchange mass flux between the jet entrainment zone and the recirculation zone.

Therefore, according to the characteristics of the fluid flow fields revealed from the bloom and the billet mould experiments, β can be taken as 1 for the bloom mould model with horizontal outlet bifurcated nozzle because the jet from the nozzle entrains more or less equally from both sides, and β for the billet mould model can be as high as 10 because there is little entrainment from the recirculation zone occurred.

c) Determination of the value of ζ .

As defined in section 4.2.3, ζ is the geometric factor which describes the obscuration of the upper surface of the meniscus due to the insertion of the nozzle and the denuding of the liquid surface when vigorous liquid flows in the recirculation zone swept the liquid slag away from the walls of the mould. ζ is always less than 1. The factor consists of two parts, the first part, due to the obscuration of the nozzle is easy to estimate, but the second part, due to the denudation is not so straight forward. The denudation of the meniscus is affected by the nozzle submersion depth and the casting

speed. The smaller the nozzle submersion depth and the higher the casting speed, the smaller the value of ζ is. Therefore, in the following discussion, we will use values of ζ listed in table 6.1 for the bloom mould model and values listed in table 6.2 for the billet mould model, which are estimated from the experimental observations.

d) Determination of the value of v

As defined in equation (4.34), v is the dimensionless Stokes rise velocity, which is rewritten as follows:-

$$v = \frac{V_{St}}{V_c} \quad (6.25)$$

So at a certain casting speed and in a certain medium, v varies only with the inclusion particle diameter D_p . Thus, we can assume that:-

$$v = \gamma \cdot D_p^2 \quad (6.26)$$

$$\text{where : } \gamma = \frac{(\rho - \rho_p)g}{18 \mu V_c} \quad (6.27)$$

ρ : density of the medium;

ρ_p : density of the inclusion particle;

g : gravitational acceleration;

μ : viscosity of liquid medium;

V_c : casting speed.

Now let us calculate the values of γ for the bloom mould model and the billet mould model respectively. The following are the

TABLE 6.1. Values of ζ for the bloom mould model.

SEN Submerged Depth (mm)	ζ
220	0.95
200	0.90
175	0.80
150	0.70
125	0.60
100	0.50
75	0.40

TABLE 6.2. Values of ζ for the billet mould model.

SEN Submerged Depth (mm)	ζ for Nozzle 1 & 3	ζ for Nozzle 2
175	0.85	0.75
150	0.80	0.70
125	0.75	0.65
100	0.70	0.60
75	0.65	0.55
50	0.60	0.50

properties of water and paraffin:-

$$\text{density of water} \quad \rho = 1.0 \text{ g.cm}^{-3}$$

$$\text{density of paraffin} \quad \rho_p = 0.8 \text{ g.cm}^{-3}$$

$$\text{gravitational acceleration} \quad g = 981 \text{ cm.s}^{-2}$$

$$\text{viscosity of water} \quad \mu = 0.01 \text{ g.cm}^{-1}\text{s}^{-1}$$

In the bloom mould model, the casting speed employed was 0.55 m.min⁻¹. Substituting this casting speed together with the above listed properties into equation (6.27), we obtained the value of γ for the bloom mould model as:-

$$\gamma = 11.89 \text{ mm}^{-2} \quad (6.28)$$

In the billet mould model, the casting speed employed was 1.33 m.min⁻¹. Similarly, this gives γ a value of 4.92 mm⁻².

That is:-

$$\gamma = 4.92 \text{ mm}^{-2} \quad (6.29)$$

Therefore, according to equation (6.26), (6.28) and (6.29), we have the following expressions of v for the bloom mould model and billet mould model respectively:-

For the bloom mould model we have:-

$$v = 11.89 (D_p/\text{mm})^2 \quad (6.30)$$

For the billet mould model we have:-

$$v = 4.92 (D_p/\text{mm})^2 \quad (6.31)$$

6.3.2. Analysis of the results for Γ .

The previous section shows that equation (4.69) cannot be used to determine values of Γ from the experimentally determined removal efficiencies unless the average diameter of the inclusions in the region immediately below the liquid meniscus is known. Since this diameter is not known, two experiments were carried out for each set of fluid flow conditions. In one experiment, inclusions were produced at nozzles made from large hypodermic tubing, small diameter hypodermic tubing being used in the other experiments. The symbols D_p and d_p are used to represent, respectively, the average inclusion diameter in each case.

It was originally assumed that the ratio d_p/D_p would be the same as the ratio of the internal diameters of the capillary tubes, that is 0.635. This being the case, the two measurements of η for the two sizes of inclusions would allow both the value of D_p and Γ to be determined. A graphic method was planned based on the interpretation of equation (4.69) for both the large diameter experiments and the small diameter experiments.

For the results of the experiment with the large diameter inclusions, equation (4.69) can be represented as:-

$$\Gamma = f_L(D_p) \quad (6.32a)$$

where f_L is the function that results when A, B and C are calculated using the inclusion removal efficiency measured in the experiments with the large nozzles. Similarly, the equation for the small diameter inclusions can be represented as:-

$$\Gamma = f_S(d_p) \quad (6.32b)$$

where f_S is the function that results when the inclusion removal efficiency measured in the small nozzle experiments is used. It was thought that equation (6.32b) could be represented as:-

$$\Gamma = f_S(R.D_p) \quad (6.32c)$$

so that a graph of the two functions against D_p would yield the values of Γ and D_p from the point where the two function curves intersected.

In the event, it was found that the two curves did not intersect when the value of R was taken as 0.635. It was therefore necessary to re-examine the way in which the results were interpreted.

6.3.3. Analysis of the results for D_p and R .

Since single values of Γ could not be found that were compatible both with the inclusion removal efficiencies measured in any one pair of experiments and with a value of R of 0.635, the results were re-examined with a view to determining values of D_p and R . It might be thought that, since the value of Γ was unknown, such determinations could not be carried with very great accuracy. As will be shown, however, the value of Γ has a relatively minor influence so that highly accurate estimates of D_p and R can be made from a fairly coarse estimate of the value of Γ .

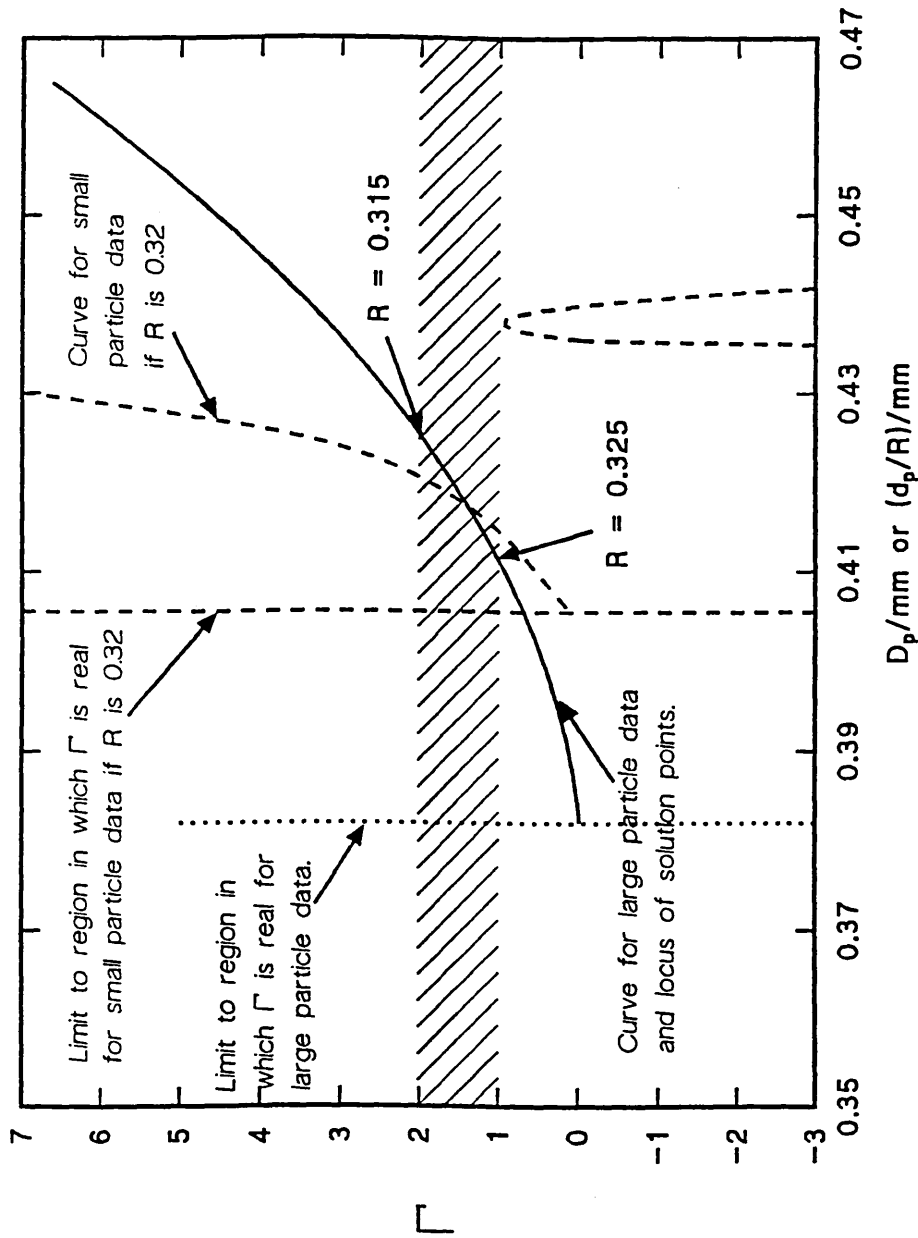
This latter estimate is explained in appendix 1 where it is shown that Γ would be expected to vary between 1 and 2 for the bloom

caster. Thus it is possible to plot the functions shown by equations (6.32a) and (6.32c) for the results of the bloom caster with different values of R , and to examine solutions that give values of Γ that lie between 1 and 2.

Figure 6.5 shows one such plot. The equation function for the large inclusion results, (6.32a), is plotted as the full curve. The shaded region between $\Gamma = 1$ and $\Gamma = 2$ shows the region in which solutions are to be expected. The dashed curve is the plot of equation (6.32c) for the small inclusions with the value of R being taken as 0.32. The point of intersection of this dashed curve with the full curve gives a solution for D_p equal to 0.418 mm. Varying the value of R moves the position of the dashed curve, thus moving the solution point along the full curve and varying the value of D_p for which a solution can be found. However, since solutions are limited to points of intersection in the shaded region, D_p can only vary between 0.415 mm and 0.425 mm. The values of R that correspond to these two limiting values of D_p are 0.325 and 0.315, respectively. It is apparent, then, that a coarse estimate of Γ allows estimates to be made for both R and D_p that are accurate to better than 5%.

Figure 6.5 provides more information about the solution regime, showing areas in which equations (6.32a) and (6.32b) give imaginary values of Γ . It also shows that the equation for the small inclusion results pass through infinity and then produces values of Γ that are always less than 1, and negative for most values of D_p . The curve for the large inclusion results can show similar behaviour at larger values of D_p so that the two curves can intersect again. However, this intersection always corresponds to a negative value of Γ and so

Figure 6.5



Determination of D_p and R for an SEN penetration depth of 220 mm. Γ values calculated from Experiments 200 (large D_p) and 210 (small d_p) plotted for $R = 0.32$ showing variation with assumed values of D_p as well as solution point where curves intersect. Valid solutions exist for Γ values between 1 and 2, i.e. for $0.315 \leq R \leq 0.325$ and $0.415 \leq D_p/\text{mm} \leq 0.425$.

has no physical meaning.

The solution technique outlined above is essentially a trial and error technique in which several different curves are plotted from the small inclusion results, each with a different trial value of R . Carrying out this procedure graphically for all the experimental results that had been obtained would have been prohibitively laborious. A computer programme was therefore written in Turbo Basic to evaluate functions (6.32a) and (6.32c) with different values of R , and find those values that gave Γ values between 1 and 2 for the same value of D_p . The programme then displayed on the screen the range of D_p , Γ and d_p values within which the solution had been found so that a visual check could be made of the accuracy of the resulting values of D_p and R .

The programme is listed in Appendix 2 and Table 6.3 is the screen print of a typical output screen, actually for the results plotted in figure 6.5. The values tabulated under 'm' are the values of Γ , and it can be seen that the two roots for Γ are tabulated throughout - as a check that the root derived using the negative sign in equation (4.69) is always negative.

The results determined as described above for the experimental results at different submerged depth, as reported in section 5.2.6, are listed in table 6.4. The relationship between the SEN submerged depth and R is shown in figure 6.6. The changes of the average equivalent particle diameter in the meniscus region with the SEN submerged depth are given in figure 6.7. These results show that average inclusion diameters are greatly affected by the SEN submerged

TABLE 6.3. Example of screen output.

The solution for M can be found in the following table.
 i.e. The value of the large diameter is 0.418 mm and M = 1.505
 Diff = 0.026

Parametric values for this set of calculations:-

beta	gamma	a	eta(large)	eta(small)	R	p	CRT
1.00	11.89	0.44	0.76	0.18	0.320	0.95	0.15
For large nozzle							
Dp	m (+ sign)	m (- sign)	Dp	m (+ sign)	m (- sign)	For small nozzle	
0.411	1.122E+00	-0.833E+00	0.132	0.616E+00	-6.266E-02		
0.412	1.176E+00	-0.841E+00	0.132	0.713E+00	-7.073E-02		
0.413	1.230E+00	-0.848E+00	0.132	0.816E+00	-7.764E-02		
0.414	1.285E+00	-0.855E+00	0.132	0.928E+00	-8.367E-02		
0.415	1.342E+00	-0.862E+00	0.133	1.050E+00	-8.901E-02		
0.416	1.399E+00	-0.869E+00	0.133	1.183E+00	-9.381E-02		
0.417	1.458E+00	-0.876E+00	0.133	1.329E+00	-9.816E-02		
0.418	1.518E+00	-0.883E+00	0.134	1.492E+00	-0.102E+00		
0.419	1.579E+00	-0.889E+00	0.134	1.674E+00	-0.106E+00		
0.420	1.641E+00	-0.896E+00	0.134	1.878E+00	-0.109E+00		
0.421	1.704E+00	-0.903E+00	0.135	2.110E+00	-0.112E+00		
0.422	1.769E+00	-0.909E+00	0.135	2.375E+00	-0.115E+00		
0.423	1.835E+00	-0.915E+00	0.135	2.683E+00	-0.118E+00		
0.424	1.903E+00	-0.922E+00	0.136	3.042E+00	-0.121E+00		

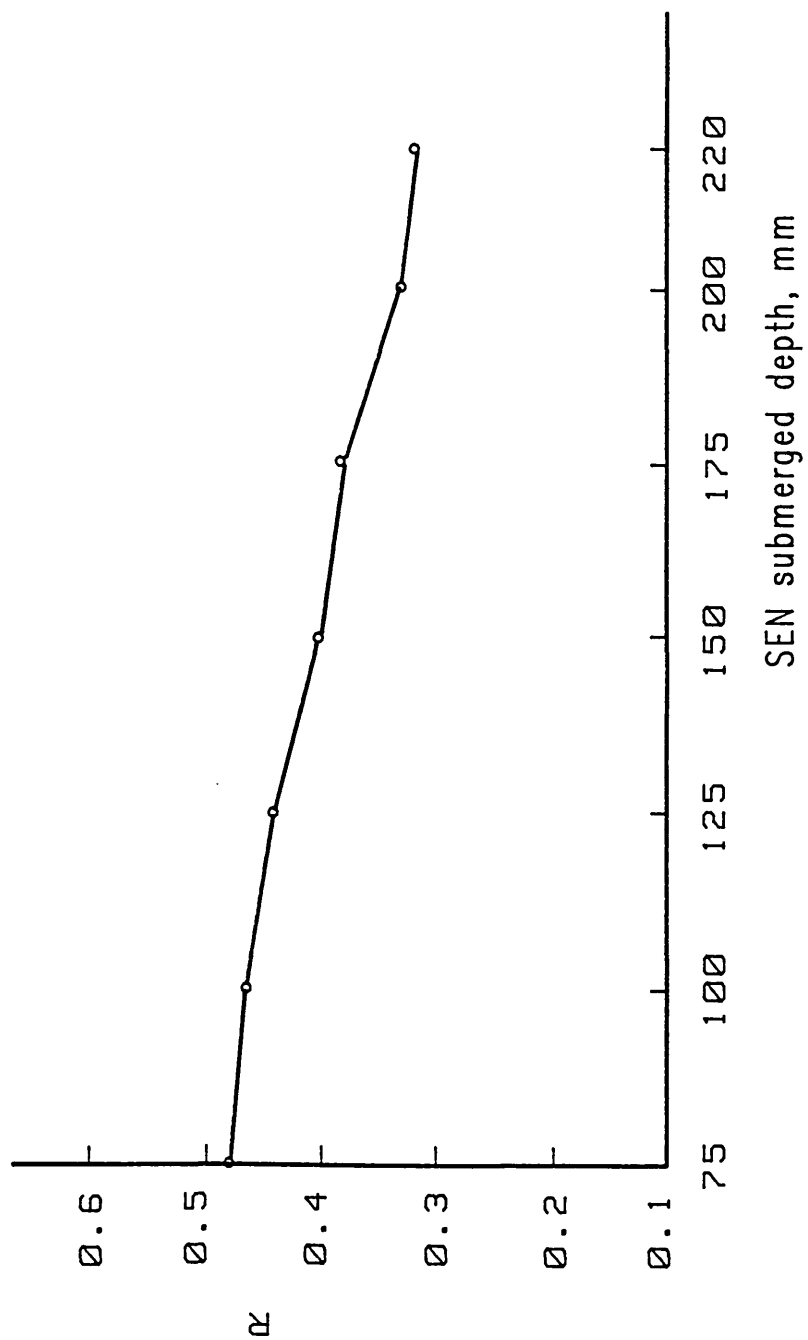
***** THE END OF THIS SET OF CALCULATIONS *****
 Do you wish to carry out some more calculations?

TABLE 6.4. The values of R.

SEN Submerged Depth (mm)	η_{big}	η_{small}	ζ	R	D_p (μm)	d_p (μm)	Γ
220	0.76	0.18	0.95	0.32	418	134	1.505
200	0.70	0.15	0.90	0.33	374	123	1.431
175	0.56	0.12	0.80	0.38	303	115	1.481
150	0.41	0.08	0.70	0.40	247	99	1.468
125	0.33	0.07	0.60	0.44	225	99	1.471
100	0.23	0.05	0.50	0.465	195	91	1.380
75	0.18	0.04	0.40	0.48	188	90	1.559

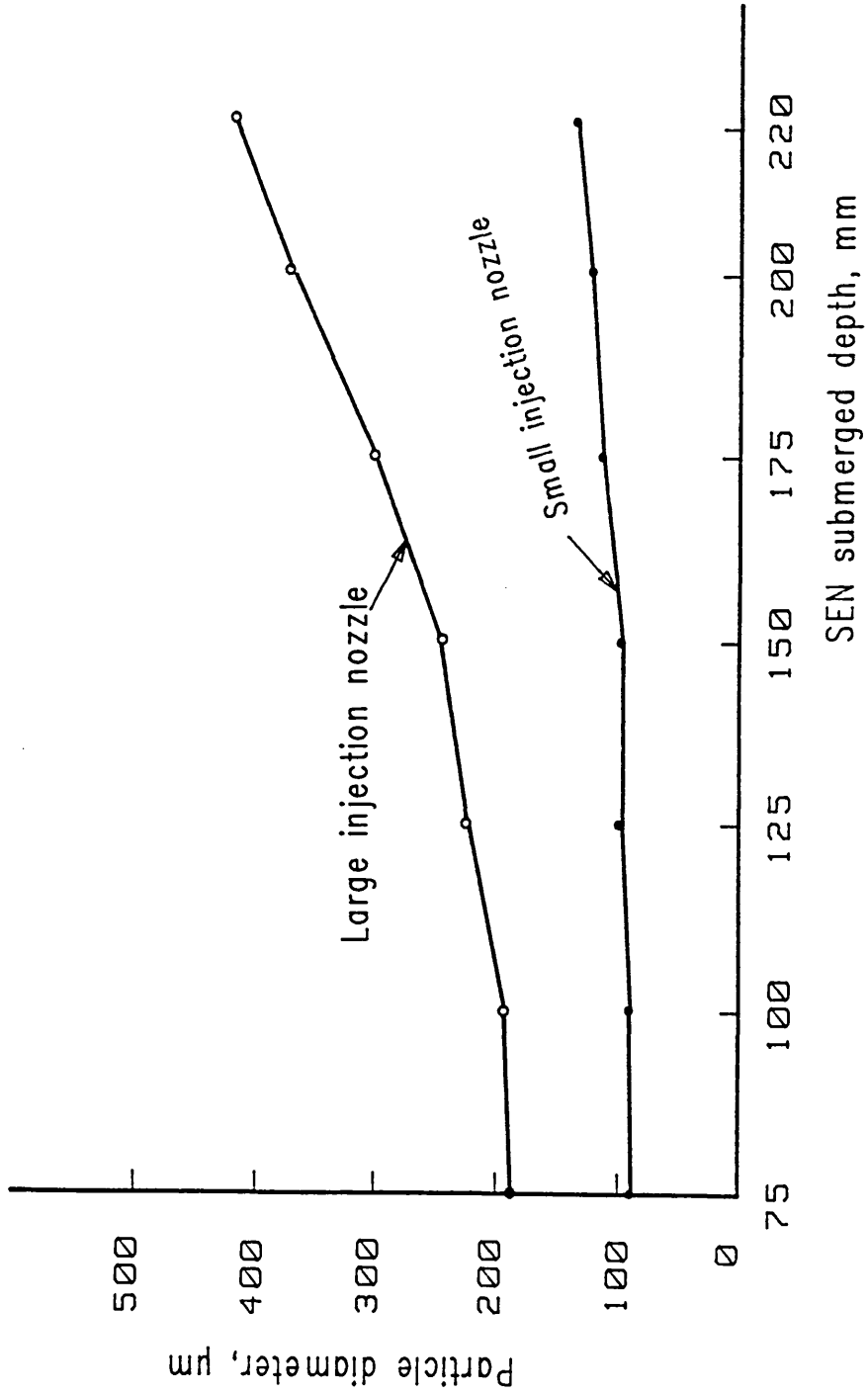
$\beta = 1$; $a = 0.44$; $\gamma = 11.89$.

Figure 6.6



The Values of R and SEN Submerged Depth

Figure 6.7



The Particle Diameter and SEN Submerged Depth

depth. It is thus the increase of the average particle diameter with the increase of the SEN submerged depth, resulting in a rapid increase in the Stokes' rise velocity, that causes the efficiency of inclusion removal in the sump to be increased as the SEN is lowered into the sump.

6.3.4. Sensitivity to changes in the mixing parameter values.

Let us now use the above information to explore inclusion removal sensitivity to changes in values of the mixing parameter. For the purpose of exploration, we may suppose that:-

for the bloom mould model:-

$$\Gamma_{JR} = \Gamma_{JM} = \Gamma$$

$$\zeta = 0.9, \quad e = 1 \quad \text{and} \quad a = 0.44.$$

Substituting (4.47) into (4.52), gives:-

$$\eta = \frac{1}{1 + \frac{(1 + \Gamma/\alpha^*)}{(\Gamma + \nu) + \frac{(\Gamma + 0.44\nu)\nu}{(1 + \Gamma)}}} \quad (6.33)$$

From the above assumption and equation (4.60) and (6.30), we have:-

$$\nu = 11.89 \frac{D_p^2}{p} \quad (6.34)$$

$$\alpha^* = e\zeta\nu = 10.701 \frac{D_p^2}{p} \quad (6.35)$$

Substituting into equation (6.33), we obtain:-

$$\eta = \frac{1}{1 + \frac{(1 + \Gamma/10.701 D_p^{-2})}{(\Gamma + 11.89 D_p^2) + \frac{11.89(\Gamma + 5.2316 D_p^2) D_p^2}{(1 + \Gamma)}}$$

(6.36)

For the comparison reason, the curves in figure 6.8 have been calculated for four different Γ values, namely Γ equals 1.5, 2.5, 5.0 and 10. It can be clearly seen from the figure that the inclusion removal efficiency is rather insensitive to changes in the values of Γ , which explains why the value of Γ can be chosen fairly approximately without to much lack of precision. For instance, the values of Γ derived in appendix 1 could be used for the corresponding cases of bloom and billet mould, i.e.:-

For the bloom mould model:-

$$\Gamma_{JR} = \Gamma_{JM} = 1.45 \quad (6.37)$$

For the billet mould model:-

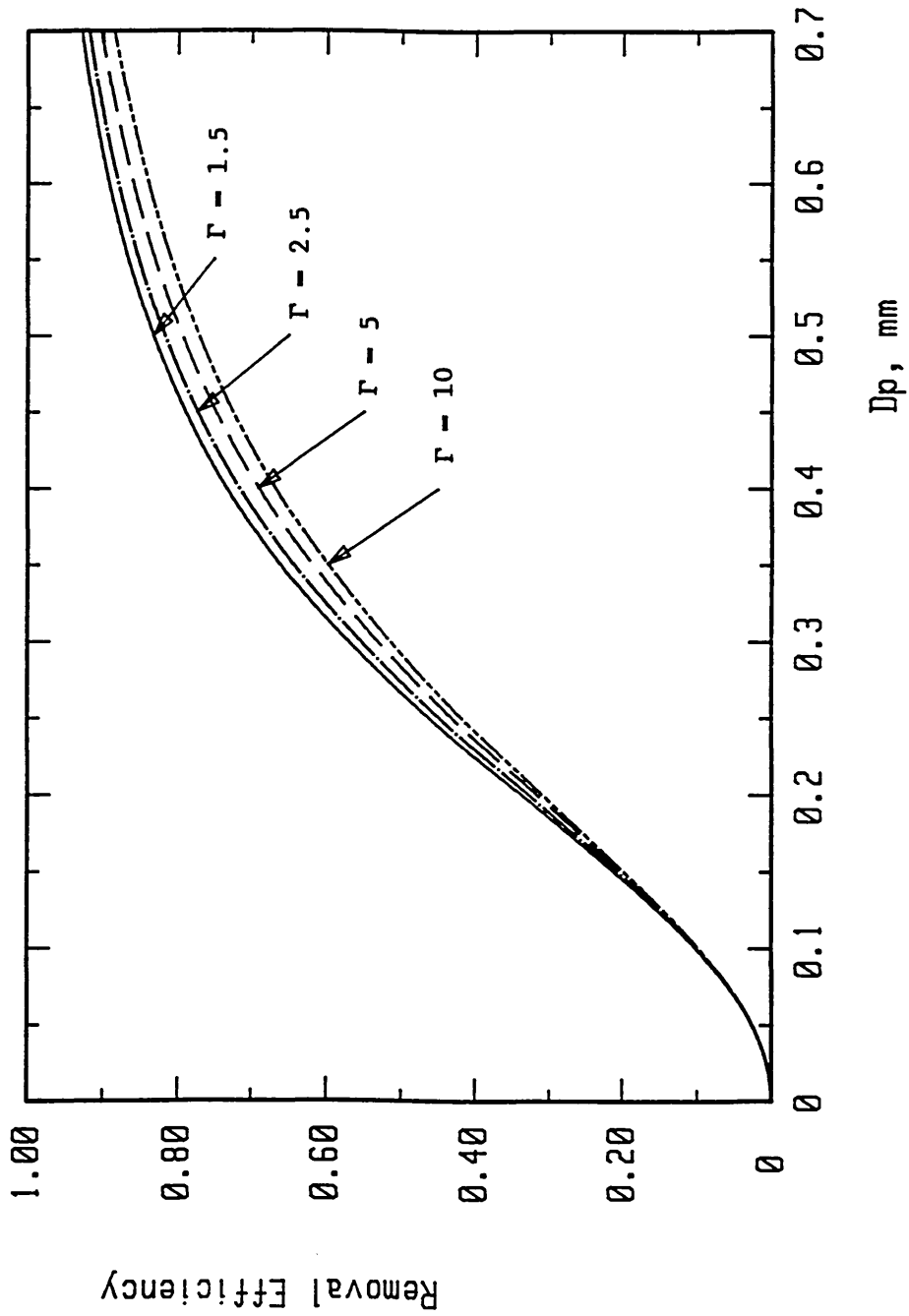
$$\begin{aligned} \Gamma_{JR} &= 1.10 \\ \Gamma_{JM} &= 11.0 \end{aligned} \quad (6.38)$$

6.3.5. Sensitivity to changes in the value of β .

Let us now use the information about jet entrainment fluxes presented in appendix 1 to explore inclusion removal sensitivity to changes in the value of β .

As derived in section A1.6 in appendix 1, the dimensionless interchange mass fluxes between the jet entrainment zone and

Figure 6.8



Inclusion removal efficiency in the bloom mould model
 ($\beta = 1$; $\zeta = 0.9$; $a = 0.44$)

surrounding zones can be expressed as follows:-

$$\Gamma_{JR} = \frac{\Gamma_{entrain}}{1 + \beta} \quad (6.39)$$

and

$$\Gamma_{JM} = \frac{\beta \Gamma_{entrain}}{1 + \beta} \quad (6.40)$$

where $\Gamma_{entrain}$ is the dimensionless jet entrainment flux, which has an average value of 3.0, and this value will be used in this section. For the reason of clarity, Γ_{en} will be used to represent $\Gamma_{entrain}$ in the following discussions.

For the purpose of exploration, similarly as the previous section, we may suppose that:-

$$\zeta = 0.9, \quad e = 1 \text{ and } a = 0.44.$$

Thus equations (6.34) and (6.35) are also valid.

Substituting equation (4.47) into equation (4.52) and rearranging it, gives:-

$$\eta = \frac{1}{1 + \frac{(1 + \Gamma_{JR}/\alpha^*)}{(\Gamma_{JR} + \nu) + \frac{(\Gamma_{JR} + 0.44\nu)\nu}{(1 + \Gamma_{JM})}}$$

Substituting equations (6.37), (6.38), (6.39) and (6.40) into the above equation, we have:-

$$\eta = \frac{1}{1 + \frac{(1 + \Gamma_{en}/(1+\beta)/10.701 D_p^{-2})}{\Gamma_{en}/(1+\beta) + 11.89 D_p^2 + \frac{11.89(\Gamma_{en}/(1+\beta) + 5.2316 D_p^2) D_p^2}{(1 + \beta\Gamma_{en}/(1+\beta))}}$$

(6.41)

For the comparison reason, the curves in figure 6.9 have been calculated for five different β values, namely β equals 1, 2, 0.5, 4 and 0.25. It is clearly shown in the figure that the inclusion removal efficiency is slightly affected by the changes in the value of β . Decreasing β from 1, which corresponds to employing an SEN with an upward port angle, causes inclusion removal efficiency to increase slightly, and on the contrary, increasing β from 1, corresponding to the case of employing an SEN with a downward port angle, slightly reduces inclusion removal efficiency.

6.3.6. Sensitivity to changes in the value of the inclusion mass transfer coefficient.

Now let us explore inclusion removal sensitivity to changes in the value of the inclusion mass transfer coefficient. For the purpose of exploration we may assume that:-

for the bloom mould model:-

$$a = 0.44$$

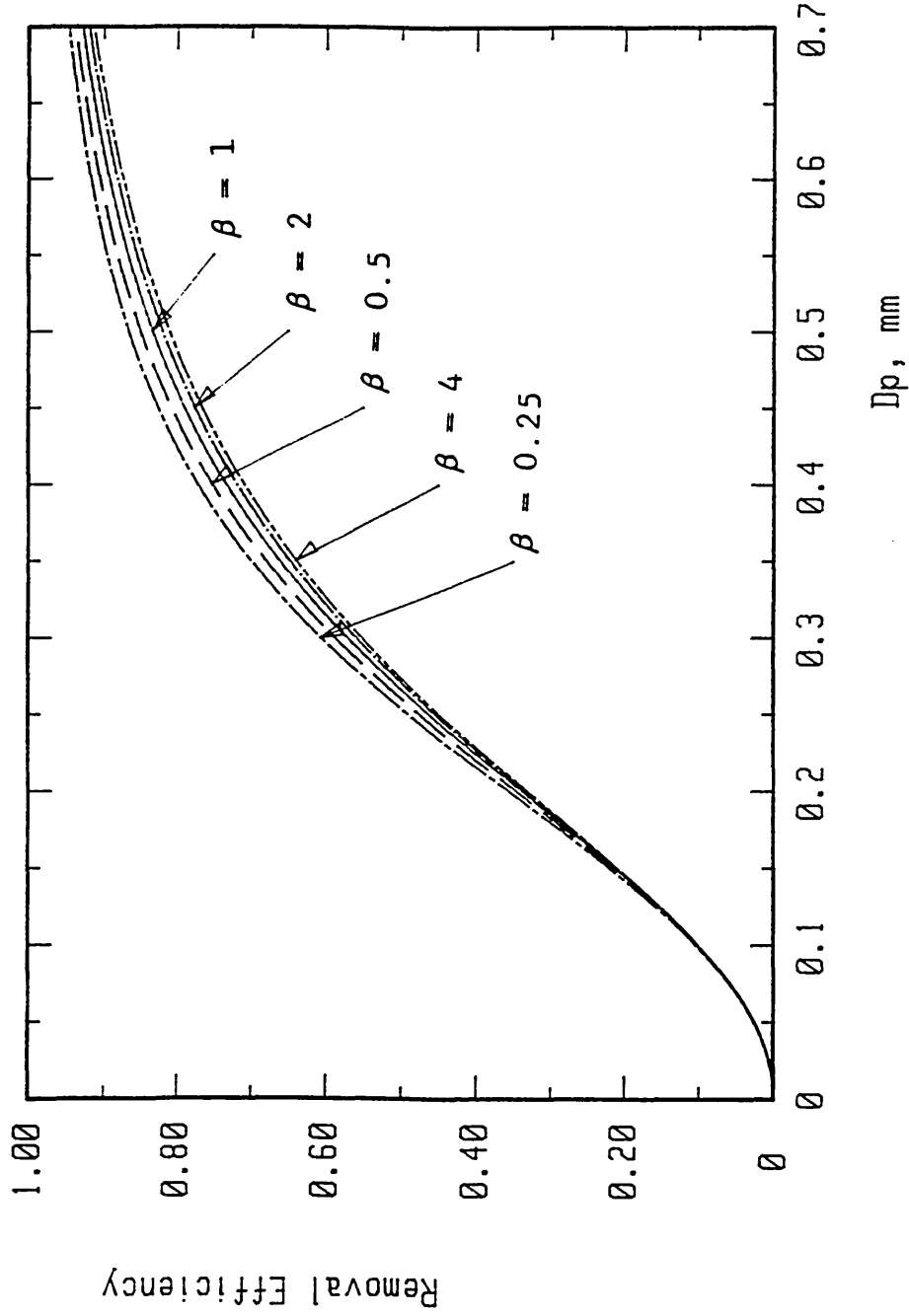
$$\zeta = 0.9$$

$$v = 11.89 D_p^2$$

and

$$\Gamma_{JR} = \Gamma_{JM} = \Gamma = 1.45$$

Figure 6.9



Inclusion removal efficiency in the bloom mould model

($\zeta = 0.9$; $a = 0.44$; $\Gamma_{\text{entrain}} = 3.0$)

Substituting equation (4.47) into (4.52), gives:-

$$\eta = \frac{1}{1 + \frac{(1 + \Gamma/\alpha^*)}{(\Gamma + \nu) + \frac{(\Gamma + 0.44\nu)\nu}{(1 + \Gamma)}}$$

or

$$\eta = \frac{1}{1 + \frac{(1 + \Gamma/\alpha^*)}{(\Gamma + 11.89 \frac{D^2}{P}) + \frac{11.89(\Gamma + 5.2316 \frac{D^2}{P}) \frac{D^2}{P}}{(1 + \Gamma)}}$$

(6.42)

where α^* , according to equation (4.60), could be expressed in term of ν , i.e. $\alpha^* = e\zeta\nu$.

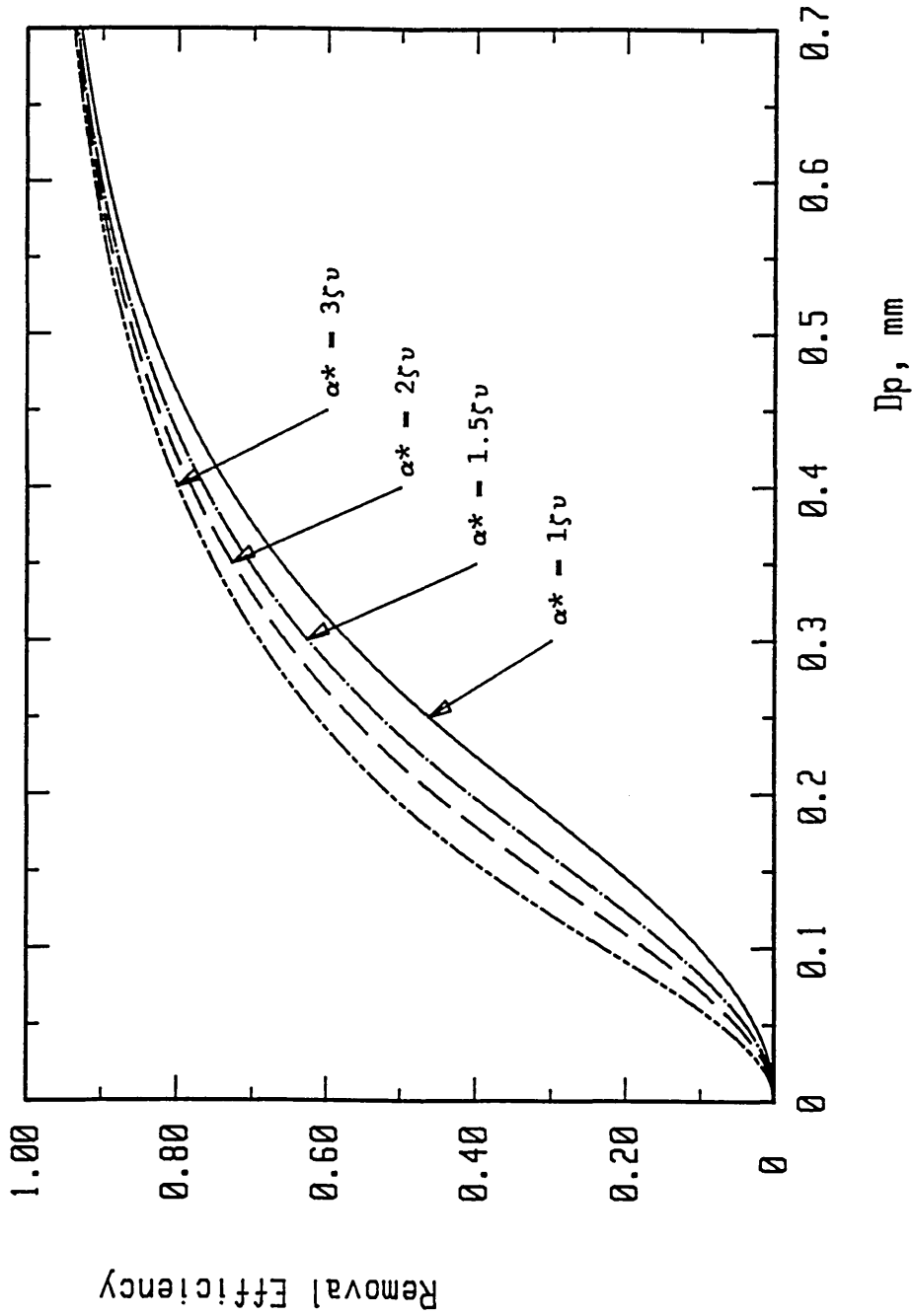
The effect of changes in the value of α^* is shown in figure 6.10.

The curves in the figure have been calculated by using equation (6.42) with the values of α^* equal to $\zeta\nu$, $1.5\zeta\nu$, $2\zeta\nu$ and $3\zeta\nu$, i.e. enhancement factor "e" equals 1, 1.5, 2 and 3 respectively.

It can be seen from the figure that the changes of the value of α^* affect more on inclusion removal efficiency when the inclusion particles are small in size than when they are large. This is because when the inclusion sizes are large, the removal process is dominated by Stokes rise, hence turbulent diffusion plays a very minor role in this kind of situation.

These curves also suggest that the interpretation of the experimental

Figure 6.10



Inclusion removal efficiency in the bloom mould model
 ($\Gamma_{JR} = \Gamma_{JM} = 1.45$; $\zeta = 0.9$; $a = 0.44$)

results could be affected, especially for the inclusions from the small nozzle, if the enhancement factor 'e' was as high as 1.5. However, as will be seen from section 6.4, table 6.6, the value of 'e' can be shown to be no more than 1.10 so that there is virtually no effect.

6.3.7. Effects of the operation practice on inclusion removal.

6.3.7.1. Effect of SEN geometry.

Three nozzles were employed in studying of the effect of nozzle geometry on inclusion removal in the billet mould sump. The experiments were conducted with different SEN submerged depth for each nozzle, the results being shown in figure 5.14. As expected, inclusion removal ratio was higher when the small outside diameter nozzle, Nozzle 1, was used. There are two reasons for this. In the first place, the small nozzle corresponds to higher values of a and ζ and, in the second, the small nozzle gives rise to flow pattern in the upper region that are more favourable to the inclusion agglomeration process. Figure 5.14 shows that inclusion removal ratios with Nozzle 1 are nearly twice those with Nozzle 2 under otherwise identical conditions. The effect of increases of the values of a and ζ with Nozzle 1, only increases inclusion removal ratio by 11%. Thus the increase in the inclusion removal ratio shown in figure 5.14 is mainly due to the modified fluid flow patterns produced by the small nozzle. Section 6.2.1 referred to the observation that the rising velocities in the recirculation zone were higher when using Nozzle 1 than when using Nozzle 2. It is these higher rising velocities that promote the exchange of fluid between

the jet region and the recirculation region, and hence affect the inclusion removal in the sump.

Nozzle 1 and Nozzle 3 have the same outside diameter, but the inside diameter of Nozzle 3 is greater than that of Nozzle 1. Thus, at the same casting speed, the exit velocity of the stream from Nozzle 3 is less than that from Nozzle 1, and hence the exit momentum from Nozzle 3 is less than that from Nozzle 1. Other factors being equal, this will cause less movement of the fluid when using Nozzle 3. So the values of the inclusion agglomeration rate for Nozzle 3 were less than that for Nozzle 1, and therefore inclusion removal ratios for Nozzle 3 should be less than those for Nozzle 1. Figure 5.14 shows that this was the relationship found experimentally.

6.3.7.2. Effect of SEN submerged depth.

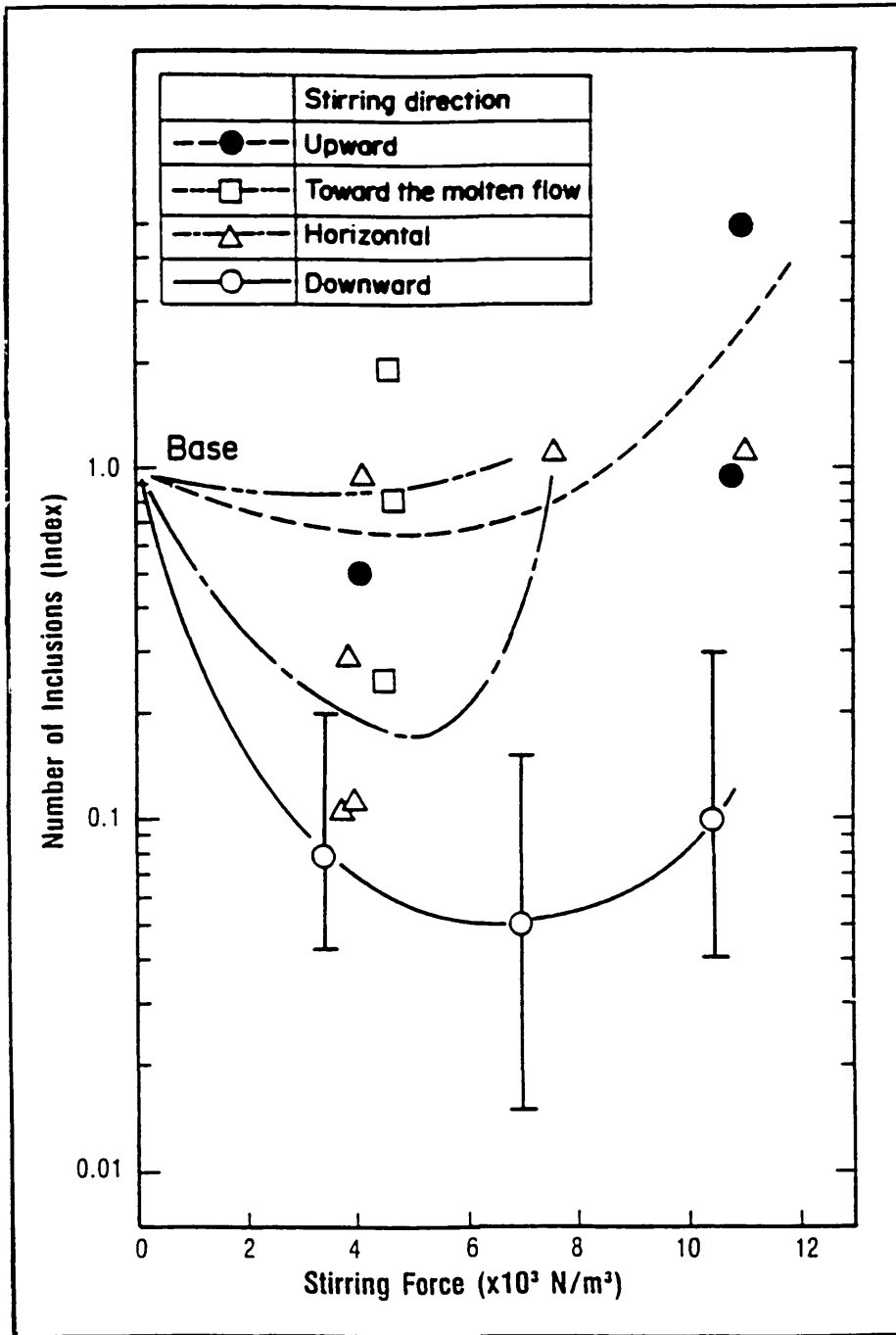
The effects of the SEN submerged depth on inclusion removal are very similar for all the nozzles used, Nozzle 1 to 11, see figure 5.3 to 5.13. Just as expected from the fluid flow analysis, the inclusion removal ratios increase with increase in the SEN submerged depth. This is because the increasing rising velocities with the increase of the SEN submerged depth helped to promote the exchange of the fluid between jet region and recirculation region and also the inclusion agglomeration. But as the SEN submerged depth exceeds a certain limit, some where between 150 mm and 175 mm in the billet mould model, inclusion removal ratio is not further improved, figures 5.3 and 5.4. This is because that the increase in the jet penetration depth is not proportional to the increase in the SEN submerged depth and because the fluid flow patterns in the upper

recirculation zone are less and less affected by the vortices in the jet region as they were further and further away from the meniscus. Further increase in the penetration depth causes the inclusions from the entry stream to be carried more deeply into the sump. The inclusion removal ratio therefore tends to decrease as the SEN submerged depth further increased. This tendency, however, is not so marked for Nozzle 3 as it is for Nozzles 1 and 2. Even when the SEN submerged depth for Nozzle 3 is 175 mm, inclusion removal ratio shows no sign of decreasing, as shown in figure 5.5. This is because the lower momentum of the stream from Nozzle 3 allows it to penetrate less strongly into the sump at any given casting speed and SEN submerged depth. However, if the SEN submerged depth of Nozzle 3 had been further increased, inclusion removal ratio would eventually start to decrease.

In the case of Nozzles 4 to 11 in the bloom mould model, the inclusion removal ratio has been shown to increase as the SEN submerged depth increases even when the depth had reached 175 mm. In fact, as shown in figure 5.21, inclusion removal ratio shows no sign of decreasing for the SEN submerged depth up to 220 mm when employing Nozzle 4.

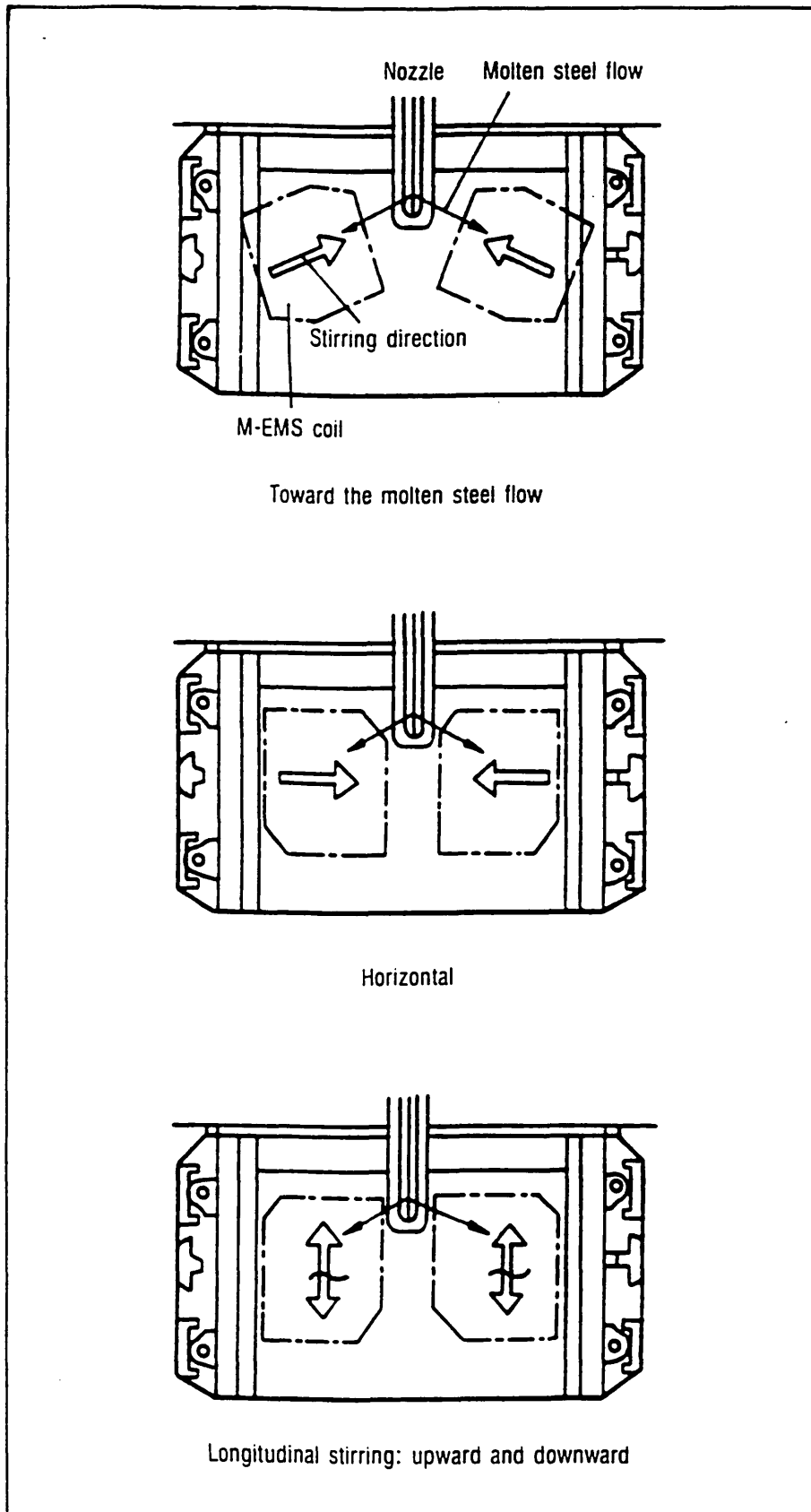
Recently, Hoshikawa et al. [100] have reported comparable results in their paper on the effects of longitudinal stirring, with a linear motor in-mould electromagnetic stirrer (M-EMS). Their results are shown in figure 6.11, a schematic view of M-EMS stirring directions being shown in figure 6.12. Figure 6.11 shows that stirring inclined upward towards the SEN had no positive effect on inclusion removal,

Figure 6.11



Relationship between stirring force and the number of inclusions for each stirring direction^[100].

Figure 6.12



Schematic view of M-EMS stirring directions [100].

and may even decrease inclusion removal ratio. Horizontal stirring towards the SEN exhibited a wide variation of effects, both beneficial and detrimental. Downward stirring, in contrast, showed consistent and positive effects on inclusion removal.

6.3.7.3. Effect of SEN port angle.

The experimental results, figure 5.15, showed that the use of an SEN with large upward port angle, at deep SEN submerged depth, is beneficial to inclusion removal. As the SEN submerged depth is reduced, however, the use of this type of nozzle turns to become detrimental.

There are a number of reasons for the effect of SEN port angle on inclusion removal efficiency. First, changing the port angle from zero in either direction increases the length over which the jet can entrain fluid, and therefore results in larger values of Γ_{entrain} and of Γ . This also increases the time that the inclusions can agglomerate in the turbulent region of the jet, resulting in larger inclusions in the meniscus region, and therefore higher values of Stokes rise velocity. Second, employing upward SEN port angles decreases the value of β as well as increasing Γ_{JR} which, as figure 6.9 shows, results in a small increase in inclusion removal efficiency. This also increases the flow intensity and hence the turbulence at the meniscus, hence increasing the value of the enhancement factor "e".

The results given in figure 5.15 show that inclusion removal efficiency is increased as the port angle changes in either direction

from zero, but that the improvement is more marked when the port angle is positive upward. These findings are in keeping with the points discussed above except for the situation at very shallow SEN submerged depths. Here employing the upward port angle results in a stronger flow at the meniscus - sufficiently strong to sweep the slag towards the SEN and resulting in an obscuration factor ζ that is significantly less than 1.

Therefore, it is anticipated that, as the SEN submerged depth decreases, the best inclusion removal ratio should be achieved by using a SEN with a port angle shifted towards a small upward angle and further towards a downward angle. And this is the case shown by the experimentally measured results, see figure 5.15. At SEN submerged depth of 175 mm, the best inclusion removal ratio was achieved by using Nozzle 5 (25° upward). However, when the SEN submerged depth reduced to 75 mm, the best inclusion removal ratio was achieved by employing Nozzle 4 (0°). When using nozzles with large downward port angle, inclusion removal ratio will not be affected very much by the SEN submerged depth unless the depth is very small, for example, less than 100 mm. Generally speaking, employing a nozzle with the port angle other than 0° will give a good inclusion removal result unless the SEN submerged depth is very small (<100 mm).

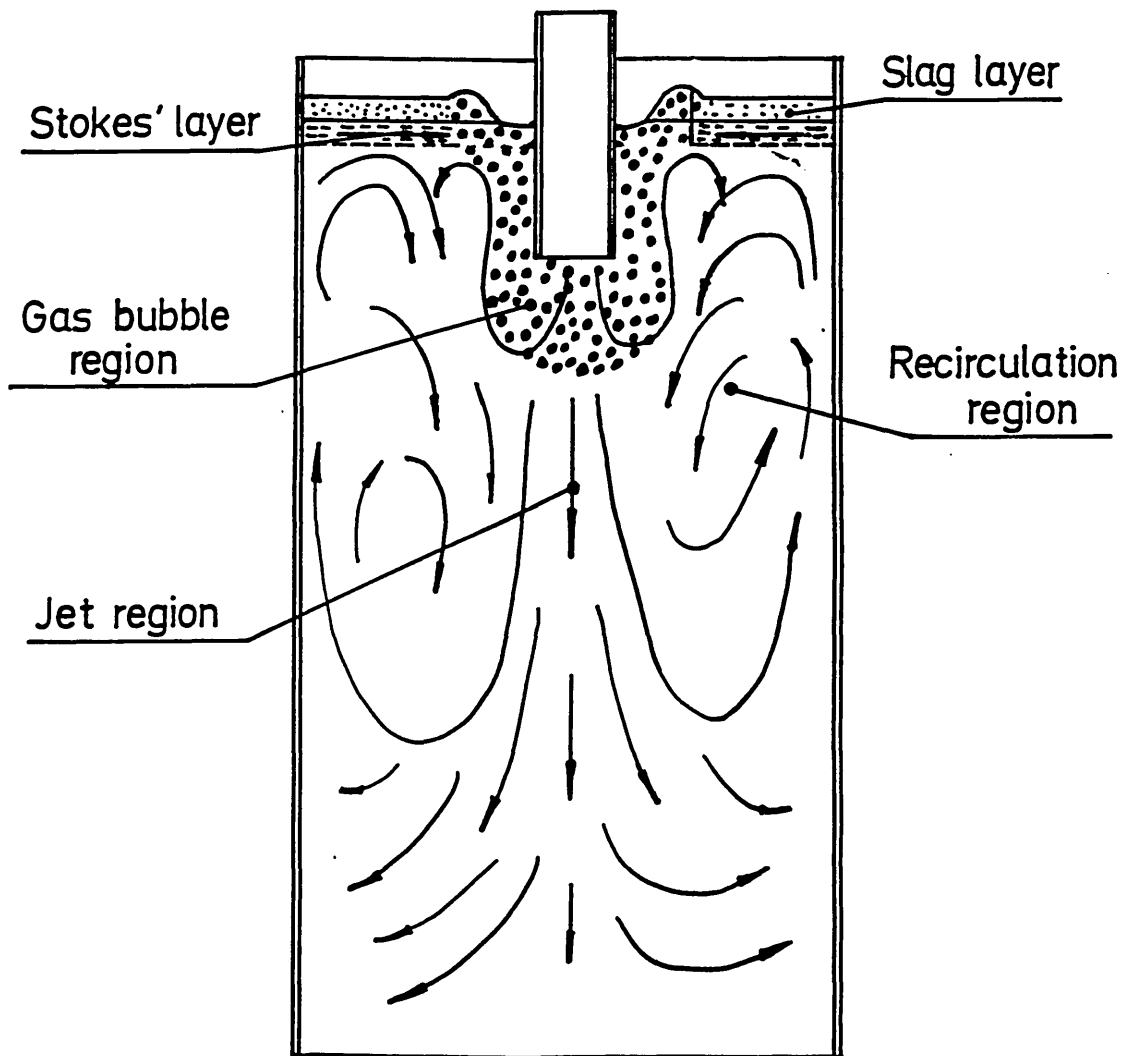
6.3.7.4. Effect of gas bubbling.

Although argon gas introduced into the tundish nozzle stream offers protection from nozzle blockage, figure 5.16 shows that it is not beneficial to inclusion removal in the billet sump. This is because

the presence of argon gas in the tundish nozzle reduces the values of a and ζ , as well as interchange mass flux between the jet region and the recirculation region. These effects are illustrated in figure 6.13. Experiments on the bloom mould model showed that the introduction of argon gas into the SEN stream had no or a little positive effects on inclusion removal, see figure 5.17 to 5.19.

The reduction in inclusion removal efficiency is because of the reversed flow near to the nozzle. The gas bubbles leaving the nozzle created an upward flow close to the SEN, which was against the downward flow induced by the flow in the recirculation zone. Thus the area of the surface in contact with the recirculating flow bringing inclusion from the jet entrainment zone to the surface is reduced. This reverse circulation produced by the gas bubbles does, of course, bring inclusions to the surface but these have come from the jet region close to the nozzle. Inclusions from this region will be smaller in size, having been less exposed to the agglomeration processes in the jet. These smaller inclusions will give a lower mass transfer coefficient over the portion of the surface exposed to the bubble driven reverse circulation.

Therefore, if the introduction of argon gas was sought to be employed with the intention to promote inclusion removal, the SEN employed should be one with downward port angle with small amount of argon injection at a deep SEN submerged depth.

Figure 6.13

Schematic view of the flow pattern developed in the mould
with gas bubbling.

6.3.7.5. Effect of casting speed.

As can be expected from the fluid flow pattern analyses, increasing the casting speed causes inclusion removal ratio to decrease. This is mainly due to the decrease that occurs in the values of v and α^* . However, the inclusion agglomeration rate increases with casting speed, and this effect reduces the overall influence that casting speed has on inclusion removal. Figure 5.20 shows that when the casting speed for the billet caster increases from 1.00 m.min^{-1} to 2.00 m.min^{-1} , for example, the removal ratio decreases from 6.5% to 5.0%. There would be little to be gained, therefore, if an optimum casting speed were sought with the intention of maximising the inclusion removal rate.

6.4. Estimation of the values of the diffusion mass transfer coefficients from the experimentally measured inclusion removal ratios.

As a result of the theoretical development, Chapter 4, the inclusion removal ratio has been derived as expressed in equation (4.52), which will be rewritten here:-

$$\eta = \frac{1}{1 + (1 + \Gamma_{JM})(1 + \Gamma_{JR}/\alpha^*)/\Phi} \quad (4.52)$$

$$\text{where } \Phi = (1 + \Gamma_{JM})(\Gamma_{JR} + v) + (\Gamma_{JR} + av)v$$

The subscript '*inclusion*' has been omitted in equation (4.52) mainly for the reason of clarity.

Therefore, the effective dimensionless inclusion mass transfer coefficient α^* could be expressed as:-

$$\alpha^* = \frac{(1 + \Gamma_{JM})\Gamma_{JR}}{(1/\eta - 1)\Phi - (1 + \Gamma_{JM})} \quad (6.43)$$

Now let us use the experimental results listed in table 5.18 to find out the values of α^* for the bloom mould model.

The values of Γ_{JR} and Γ_{JM} can be chosen as follows according to the foregoing discussions:-

$$\Gamma_{JR} = \Gamma_{JM} = 1.45$$

The values of v can be calculated according to equation (6.30), which is rewritten here:-

$$v = 11.89 (D_p/\text{mm})^2$$

where the values of D_p could be obtained from table 6.4 for different SEN submerged depth.

The value of a has already been determined in section 6.3.1 with a value of 0.44 for the present case.

All the calculated results are listed in table 6.5 for different SEN submerged depth.

Now let us make our estimation one step further. In the following discussion we will try to estimate the value of turbulent diffusivity D_T from the α^* values obtained above, table 6.5.

From equation (4.33) we obtain α as:-

TABLE 6.5. The values of α^* estimated from the experimentally measured inclusion removal ratios.

SEN Submerged Depth (mm)	η	D_p (μm)	v	Φ	α^*
220	0.76	418	2.07747	13.5536	1.94116
200	0.70	374	1.66313	11.2557	1.49649
175	0.56	303	1.09161	8.33408	0.86684
150	0.41	247	0.72540	6.61308	0.50273
125	0.33	225	0.60193	6.05945	0.36057
100	0.23	192	0.43831	5.34645	0.22995
75	0.18	188	0.42024	5.26914	0.16482

$$\Gamma_{JR} - \Gamma_{JM} = 1.45; a = 0.44; v = 11.89 D_p^2.$$

$$\alpha = \frac{\alpha^* V_c}{\zeta} \quad (6.44)$$

where V_c is casting speed, $V_c = 0.55 \text{ m.min}^{-1}$, the value of ζ could be found in table 6.1 with a value of 0.95 for an SEN submerged depth of 220 mm.

From equations (4.26) and (4.59) we have:-

$$\alpha = V_{St} (1 + 2/\tau_e^*) = e \cdot V_{St} \quad (6.45)$$

where $V_{St} = v \cdot V_c = 0.107 (D_p/\text{mm})^2 \text{ (m.s}^{-1}\text{)}$

where D_p is the inclusion particle diameter.

Thus

$$e = \frac{\alpha}{V_{St}} \quad (6.46)$$

where e is the enhancement factor.

Therefore,

$$\tau_e^* = \frac{2}{(e - 1)} \quad (6.47)$$

And according to equation (4.13),

$$\tau_e^* = \frac{(V_{St})^2 \tau_e}{D_T} \quad (6.48)$$

So the turbulent diffusivity D_T could be expressed as:-

$$D_T = \frac{(V_{St})^2 \tau_e}{\tau_e^*} \quad (6.49)$$

where τ_e is the total time for which a fluid packet is exposed to the liquid meniscus, its value has been estimated in section 4.1.5 as 0.32 for the present case.

The calculated results are listed in table 6.6 for the bloom mould model. It can be seen that the result obtained for D_T is the same order as that proposed in section 4.1.5, and that the enhancement factor "e" has a value of 1.083.

6.5. Role of inclusion agglomeration in the sump flow patterns.

As discovered in the foregoing sections, inclusion agglomeration in the sump fluid flow field play an important role in inclusion removal in the sump. The deeper the SEN submerged depth, the bigger the average inclusion diameter in the meniscus region, as shown in figure 6.7. The flow pattern from either injection nozzle to the exit nozzles of the SEN is the same irrespective of the SEN submerged depth so the average diameter of the inclusion particles as they enter the sump is independent of the submerged SEN depth. The difference in the inclusion average diameters in the meniscus region is thus solely due to the phenomenon of inclusion agglomeration. The inclusion agglomeration process will be discussed in the next section, but, here we notice, from figure 6.7, that the average diameter of inclusions generated by the large injection nozzle always increases more rapidly than that of inclusions from small injection

TABLE 6.6. The value of D_T estimated.

Inclusion Removal Ratio η	:	0.76
Inclusion Diameter D_p , (μm)	:	418
Dimensionless Effective Inclusion Mass Transfer Coefficient α^*	:	1.94116
Meniscus Obscuration Factor ζ	:	0.95
Effective Inclusion Mass Transfer Coefficient α , ($\text{m}\cdot\text{s}^{-1}$)	:	0.02043
Inclusion Relative Rising Velocity V_{St} , ($\text{m}\cdot\text{s}^{-1}$)	:	0.01887
Enhancement Factor e	:	1.083
Dimensionless exposure Time τ_e^*	:	24.1444
Turbulent diffusivity D_T , ($\text{m}^2\cdot\text{s}^{-1}$)	:	4.7e-06

nozzle.

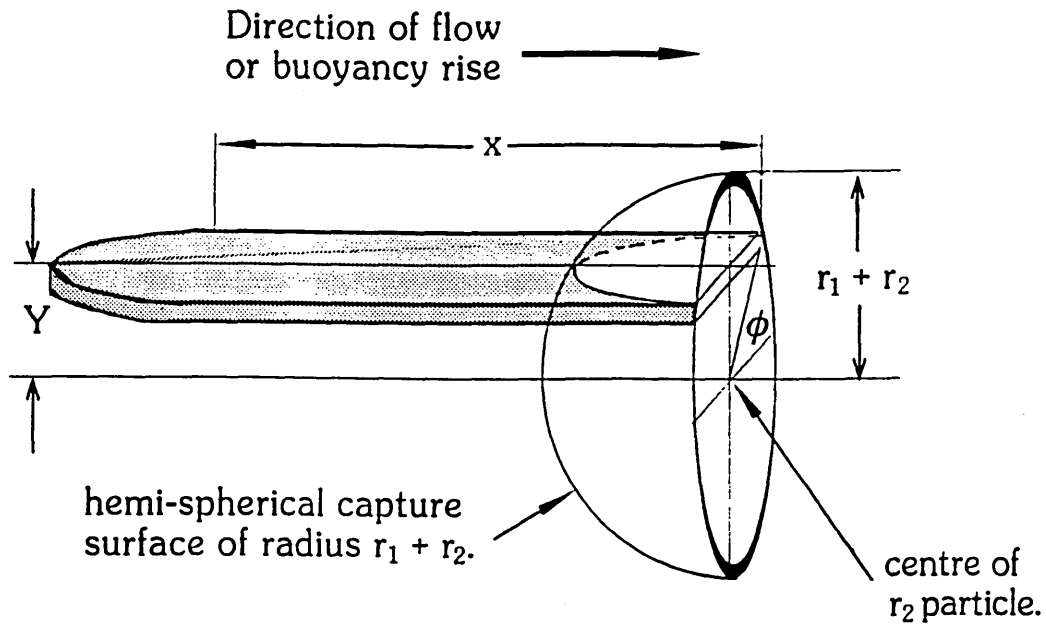
Thus, as shown in figure 6.6, the deduced values of R are all less than the ratio, 0.635, of the diameters of the orifices where the inclusion particles were generated. The fact that large inclusion particles agglomerate more rapidly than smaller inclusion particles is compatible with mechanisms discussed in the next section.

6.6. Prediction of inclusion agglomeration rates due to turbulent shear and gravity field flow.

Inclusion particles in the continuous casting mould sump may be brought into proximity with each other or may collide due to several processes:- Stokes rise, turbulent eddy diffusion, Brownian motion and local fluid flow gradients (turbulent shear). Turbulent eddy diffusion, however, only becomes important if the turbulent accelerations are of the same magnitude as gravity acceleration. This is usually not so^[104] in the case of liquids. For the inclusion particle size considered in this work, the Brownian motion is not very important either. Thus Stokes rise and local fluid flow gradients (turbulent shear) are the only processes to be considered.

Let us now consider pairs of particles of radii r_1 and r_2 within unit volume of the flow field. The number densities of these particles are n_1 and n_2 respectively. An r_1 particle collides with an r_2 particle if its centre arrives onto a spherical surface of radius $(r_1 + r_2)$ around the r_2 particle - see figure 6.14. Depending on the collision mechanism in operation, a unitary collision volume will

Figure 6.14 Generic slice of the unitary collision volume



Collision mechanism	x (length of slice)	remark
Buoyancy rise	$2\Delta\rho g(r_1^2 - r_2^2)/(9\mu_s)$	independent of Y
Velocity gradient	$(\partial U/\partial y)Y$	linear function of Y with a similar volume in front of r_2 particle, but below 'equator'.

Slice at height ' Y ' of the $r_1 + r_2$ unitary collision volume behind a particle of radius r_2 . All the particles of radius r_1 with centres inside the unitary collision volume at the start of a unit time interval will collide with the r_2 particle during that time interval.

about this spherical capture surface such that all the r_1 particles whose centres lie within this volume at the start of a unit time interval will collide with the r_2 particle before the end of that interval. (The actual size of this unitary collision volume is proportional to the magnitude of the time interval chosen, so that its dimensions are those of volume per unit time.)

Representing this volume as Ψ , we can see that the rate at which r_1 particles collide with the single r_2 particle is $n_1\Psi$. Since there are n_2 of r_2 particles in unit volume of the flow field, the rate of r_1/r_2 collisions per unit volume of the flow field is $n_1n_2\Psi$. As discussed in the next two sections, it is the shape, size and the position of the unitary volume, Ψ , that depends on the collision mechanism, so that it is through Ψ that the collision mechanism controls the rate of collisions.

A generic slice of the unitary collision volume is shown in figure 6.14 at a height Y above the 'equator' of the r_2 particle. The next two sections show that all the r_1 particles with centres in this slice travel at the same speed relative to the r_2 particle. Thus the length of the generic slice is the same across its surface and its shape is that of a rectangle with a semi-circular indent in contact with the capture surface and an identically shaped semi-circular protuberance at the other end. The area of the slice is thus equal to its common length times its width - that is, it is equal to the area of the rectangle. It is the length of this rectangle and its variation with the height Y that depend upon the collision mechanism.

Agglomeration due to Stokes rise:-

Figure 6.15 shows particles of two different sizes rising under the action of buoyancy forces and Stokes drag. According to equation (4.1) the velocity difference between particles is:-

$$\Delta u = C_{St} |r_1^2 - r_2^2| \quad (6.50)$$

where

$$C_{St} = \frac{2(\rho_s - \rho_p)g}{9\mu_s} \quad (6.51)$$

It is known from equation (6.50) that the velocity difference is independent of locations of the particles. Thus all the generic slice are of the same length and the unitary collision volume is a circular cylinder with a height of Δu . Thus the collision rate \dot{N}_{St} due to Stokes rise collision is:-

$$\begin{aligned} \dot{N}_{St} &= n_1 n_2 C_{St} |r_1^2 - r_2^2| \pi (r_1 + r_2)^2 \\ &= \pi n_1 n_2 C_{St} |r_1 - r_2| (r_1 + r_2)^3 \end{aligned} \quad (6.52)$$

Obviously, when $r_1 = r_2$, the collision rate $\dot{N}_{St} = 0$. Therefore Stokes rise will not cause particle collisions between particles of equal size.

Agglomeration due to velocity gradient:-

Consider a velocity gradient $\partial u / \partial y$, represented by U_Δ , existing over a finite distance δ in the fluid flow direction, with two particles of radii r_1 and r_2 moving with the fluid a distance Y apart normal to the fluid flow direction - see figure 6.16. The velocity difference

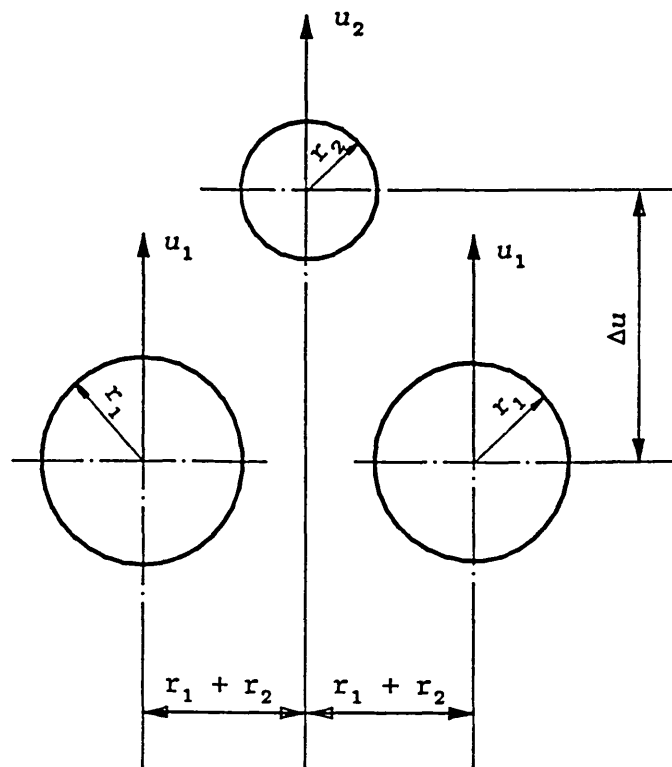
Figure 6.15

Diagram of particles rising under Stokes Law.

Figure 6.16

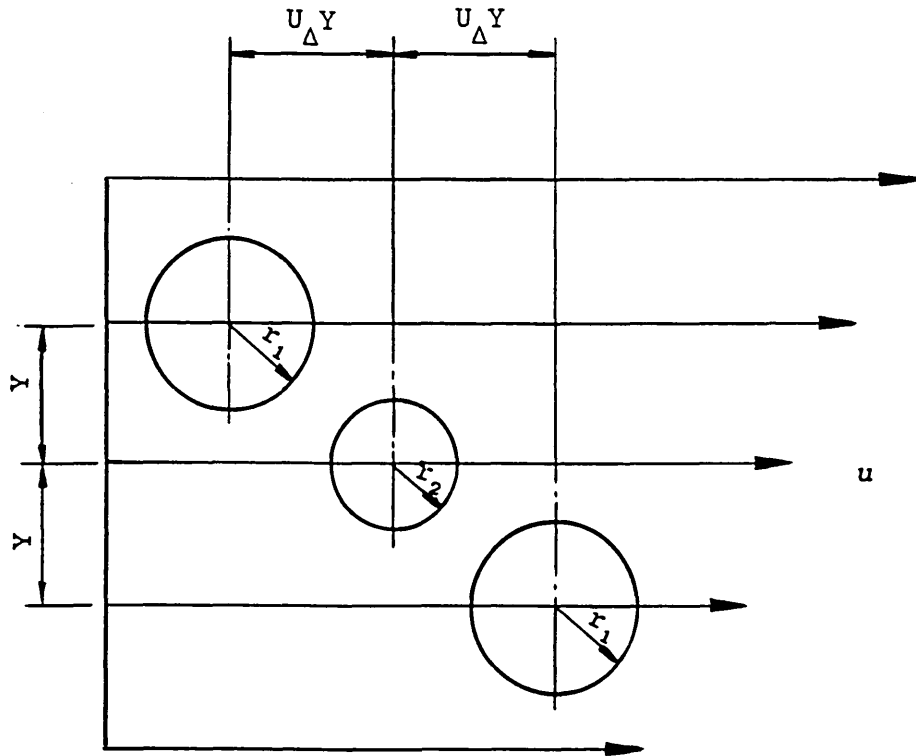


Diagram of particles moving with fluid
in a velocity gradient field

between the two particles, their relative velocity, is $U_{\Delta} Y$. The faster moving particle will catch up the slower particle if the distance between their centres measured along the flow direction is not greater than $U_{\Delta} Y$. This therefore is the length of the generic slice of the unitary collision volume.

Thus the length of the unitary collision volume behind the r_2 particle varies linearly with height. As we have seen, the cross sectional area of each generic slice is equal to that of a rectangle, so that the unitary collision volume behind the r_2 particle has the same volume as the diagonally cut half cylinder shown in figure 6.17. Reference back to figure 6.14, shows that:-

$$\text{width of the generic slice} = 2(r_1 + r_2)\cos\phi$$

$$\text{thickness of generic slice} = (r_1 + r_2)\partial\phi\cos\phi$$

$$\text{length of generic slice} = U_{\Delta}(r_1 + r_2)\sin\phi$$

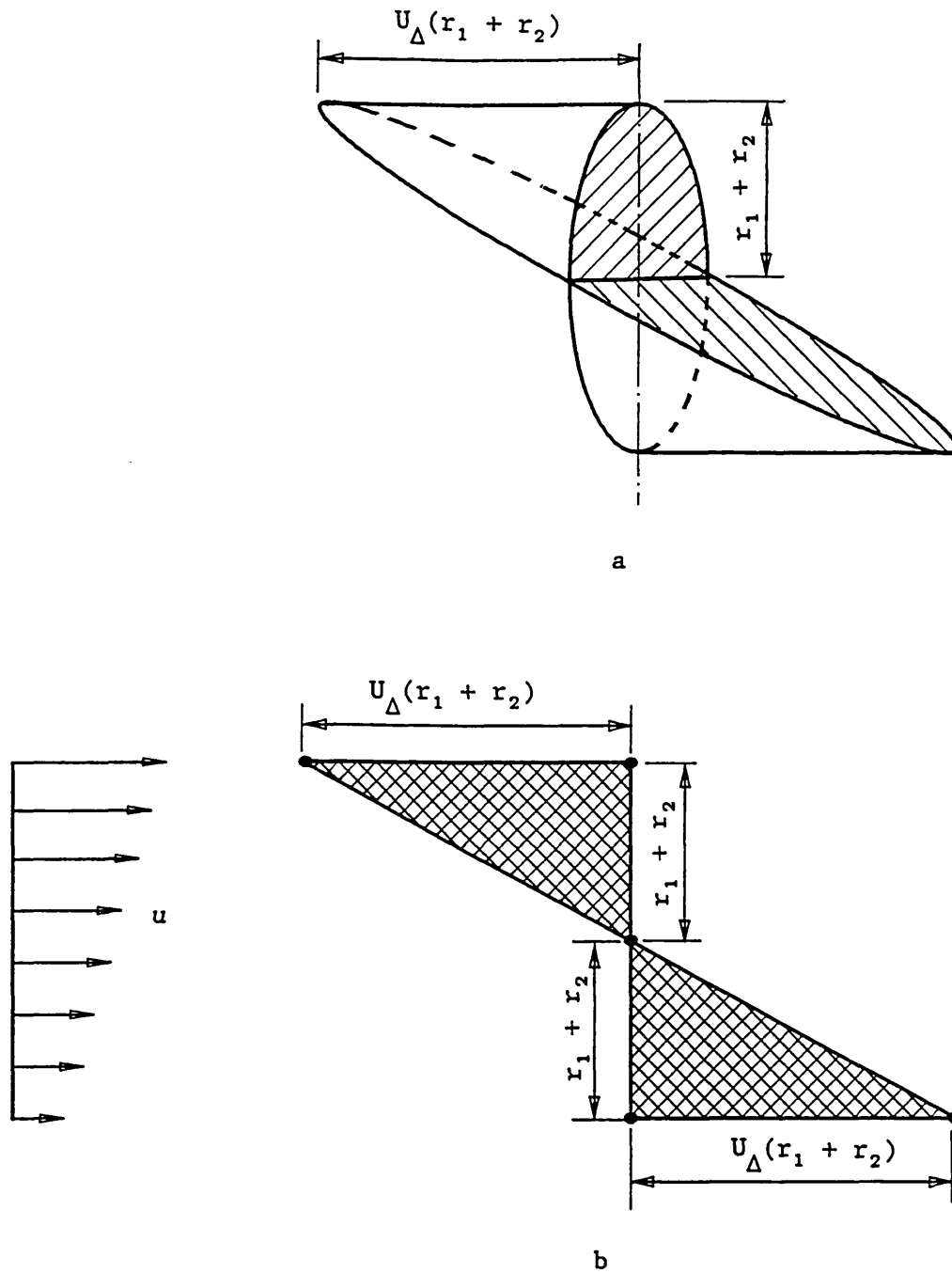
Thus the volume of the generic slice is $2U_{\Delta}(r_1 + r_2)^3\cos^2\phi.\sin\phi\partial\phi$ and the total size of the unitary collision volume behind the r_2 particle is:-

$$\int_0^{\pi/2} 2U_{\Delta}(r_1 + r_2)^3\cos^2\phi.\sin\phi\partial\phi = (2/3)U_{\Delta}(r_1 + r_2)^3$$

Since the r_2 particle is moving faster in the shear flow than the r_1 particles 'below' it, a similar section of the unitary collision volume exists in front of the r_2 particle, but below its 'equator'. Thus the total unitary collision volume for the gradient collision mechanism is:-

$$\Psi = (4/3)U_{\Delta}(r_1 + r_2)^3 \quad (6.53)$$

Figure 6.17



Collision volume involved in the gradient collision.

a: Collision volume (two truncated half cylinder);

b: Collision volume projected area.

and we can write:-

$$\dot{N}_{grad} = (4/3)U_{\Delta}n_1n_2(r_1 + r_2)^3 \quad (6.54)$$

Saffman and Turner^[105] obtained a similar expression for the case of three-dimensional turbulent flow, which are used by Linder^[106] to study the collisions of small particles in a turbulent metallic melt during deoxidation of steel. The velocity gradient in the turbulent metallic melt within a small eddy could be expressed as:-^[114]

$$|U_{\Delta}| = \left[\frac{\epsilon}{15\nu} \right]^{\frac{1}{2}} \quad (6.55)$$

where ϵ : energy dissipation in turbulence, the values of ϵ for the nozzle outlet could be obtained from the computer simulation of Thomas, Mika and Najjar^[98];

ν : kinematic viscosity of the fluid.

Therefore, equation (6.54) could be written in the following form for the turbulent fluid flow inside the mould sump:-

$$\dot{N}_{grad} = \frac{4}{3} n_1n_2(r_1 + r_2)^3 \left[\frac{\epsilon}{15\nu} \right]^{\frac{1}{2}} \quad (6.56)$$

Agglomeration due to simultaneous Stokes rise and velocity gradient:-

When the particle relative velocities due to Stokes rise and due to velocity gradient are of the same order of magnitude, there might be

a mutual interaction effect of the two actions in such a manner that the collision rate is not just the sum of the collision rates due to the two actions considered separately. In this case, generally speaking, the inclusion particle collision rate \dot{N} has a value of:-

$$\dot{N}_{St} \text{ (or } \dot{N}_{grad}) \leq \dot{N} < \dot{N}_{St} + \dot{N}_{grad} \quad (6.57)$$

So the particle collision rate under this condition could be considered according each of the two actions. If the relative velocity of the two particles due to Stokes rise is much bigger than that due to velocity gradient, the contribution from the latter could be neglected. Hence $\dot{N} = \dot{N}_{St}$. But as mentioned earlier, the Stokes rise will not give the collisions between particles of equal diameter. Therefore in such a case, $\dot{N} = \dot{N}_{grad}$.

Thus we can see why deep submersion of the SEN increase the efficiency of inclusion removal in the sump. The initial jet entrainment region where the inlet streams enter the sump is a region of high shear rates. Thus gradient collisions will occur in this region and will rapidly widen the distribution of inclusion sizes. Once this widening has occurred, the Stokes rise mechanism becomes effective and is able to take over from the turbulent shear mechanism. As the liquid flows out of the immediate jet entrainment zone and the shear rates drop, the agglomeration mechanism changes from shear agglomeration to Stokes rise agglomeration.

When the jet entrainment region is at an appreciable depth within the flow field, considerable time is available for the Stokes agglomeration mechanism to occur as the flow moves up against the

solidification front. Equations (6.52) and (6.54) show that the rate of agglomeration is proportional to the third power of the sum of the radii of the agglomerating particles, so the Stokes agglomeration mechanism occurs with greater and greater effectiveness as the liquid in the sump moves up towards the meniscus region.

Shallow submersion of the SEN does not allow time for Stokes agglomeration to take place so that the mean inclusion size in the region below the meniscus and, therefore, the inclusion mass transfer coefficient, are both small. As a consequence, the inclusion removal efficiency is low. Increasing the SEN submerged depth allows more and more time for Stokes agglomeration to occur leading to a larger average inclusion size in the meniscus region. This larger size gives higher mass transfer coefficients and thus higher removal efficiencies.

Particle collision efficiencies.

As observed by many researchers^[106-111], when two particles are brought to proximity of each other, a collision may be not always resulted. Figure 6.18^[106] shows what happens when a large particle approaches a small one. At first, it would appear that a collision will take place if the distance between the smaller particle and the centre axis of the larger particle is smaller than the sum of the radii, but as the two particles come closer, the smaller one will be pressed aside by the flow around the larger one. Only particles coming from a distance less than the sum of the two radii will collide.

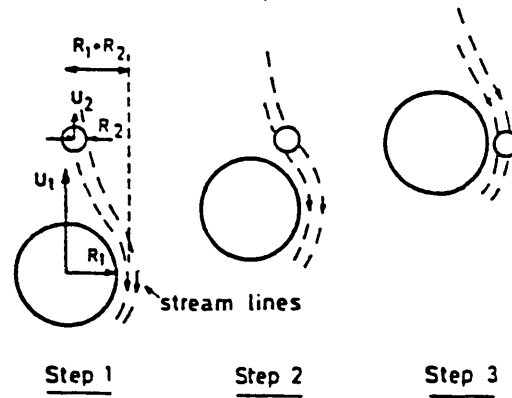
Figure 6.18

Illustration of the approach of
a larger particle to a smaller one. [106]

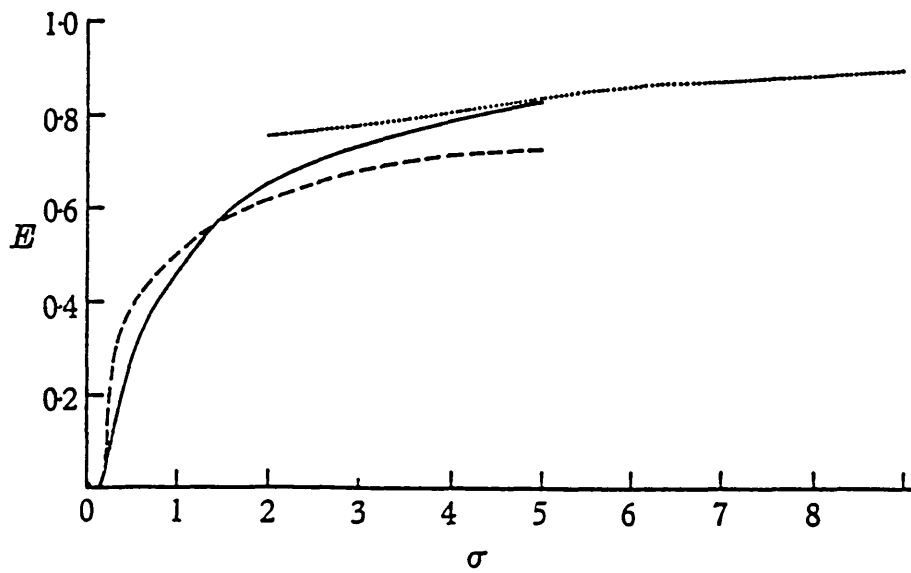
The efficiencies for particle collision have been studied by several authors [111-112]. Figure 6.19 gives some of their predicted results, as the collision efficiency E as a function of σ , where σ is the Stokes number, the velocity ratio of the two particles

$$\sigma = \frac{2}{9} \frac{u_1 r_1}{\nu} \left[\frac{\rho_p}{\rho_s} \right] \left[\frac{r_2}{r_1} \right] \quad (6.58)$$

$$\omega = \left[\frac{r_2}{r_1} \right]^2 \quad (6.59)$$

The average velocity along the narrow faces in the mould sump can be taken as $0.2 \text{ m}\cdot\text{sec}^{-1}$, this number having been obtained from water modelling results of Wang [113]. For the case of $\omega = 0.4$ and $r_1 = 150 \mu\text{m}$, we obtain the values of σ as 3.5 and 1.5 for the water-paraffin

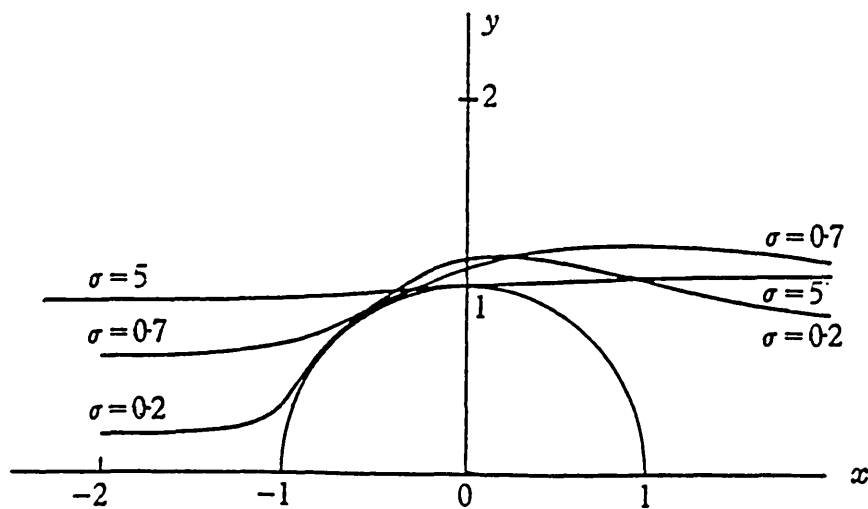
Figure 6.19



Collision efficiency E as a function of σ .

- , Michael and Norey^[111];
- - - , Langmuir and Blodgett^[112];
- , analytical result for large σ ^[111].

Figure 6.20



Grazing particle trajectories for values of $\sigma = 0.2, 0.7, 5.0$.^[111]

model system and steel-inclusion system respectively. Therefore, according to figure 6.19, the collision efficiencies of two systems are 75% and 60% respectively. Hence the collision process takes place in the mould sump efficiently. Figure 6.20^[111] shows the grazing particle trajectories for different values of σ . It is shown that only 95% of particles coming from the target area actually collide even when σ is as high as 5.

6.7. Prediction of $\eta_{inclusion}$ for steel casting system (prototype)

The values of $\eta_{inclusion}$ for the steel casting system (prototype) can be predicted by applying the present theory with the following parameter values of bloom and billet casters and the properties of liquid steel and inclusion particles:-

1) Mould section sizes:-

bloom caster : 425 mm x 305 mm;

billet caster : 140 mm x 140 mm.

2) Submerged entry nozzles:-

bloom caster : 0° bifurcated nozzle, nozzle outside
diameter of 90 mm, port diameter of 30 mm;

billet caster : vertical outlet nozzle with nozzle outside
diameter of 50 mm and inside diameter of
15 mm.

3) inclusion particle density $\approx 3 \text{ g.cm}^{-3}$.

4) liquid steel density $\approx 7 \text{ g.cm}^{-3}$.

5) dynamic viscosity of the liquid steel $\approx 7 \times 10^{-2} \text{ g.cm}^{-1}\text{s}^{-1}$.

6) dimensionless liquid metal flux between zone:-

bloom caster : $\Gamma_{JR} = \Gamma_{JM} = 1.5$;

billet caster : $\Gamma_{JR} = 1.10$; $\Gamma_{JM} = 11.0$.

7) fractional jet projected area 'a' :-

according to equation (6.18) and (6.23) and the data given above the values of a are:-

a = 0.1 for bloom caster and

a = 0.5 for billet caster respectively.

8) turbulent diffusivity:-

bloom caster : $D_T = 1 \times 10^{-6} \text{ m}^2 \cdot \text{s}^{-1}$;

billet caster : $D_T = 1 \times 10^{-7} \text{ m}^2 \cdot \text{s}^{-1}$.

9) total exposure time of the liquid packet at the steel meniscus:-

bloom caster : $\tau_e = 0.32$ seconds;

billet caster : $\tau_e = 1.50$ seconds.

The calculations were done by using equation (4.52) and (4.47) for different sizes of inclusion particles. According to the data given above and equation (4.33), (4.34), (4.1), (4.19) and (4.13), two undetermined variables in equation (4.47) and (4.52) can be expressed as functions of inclusion particle diameter D_p and casting speed V_c as follows:-

1) bloom caster:-

$$v = 18.6858 \frac{D_p^2}{V_c} \quad (6.60)$$

$$\alpha^* = \frac{0.6\zeta}{V_c} (31.143D_p^2) \left[1 + (2/\tau_e^*) \text{erf}(\frac{1}{2}/\tau_e^*) \right] \quad (6.61)$$

where $\tau_e^* = 31036 D_p^4$

2) billet caster:-

v is the same as that for bloom caster, equation (6.60).

$$\alpha^* = \frac{0.6\zeta}{V_c} (31.143D_p^2) \left[1 + (2/\tau_e^*) \operatorname{erf}(\frac{1}{2}\sqrt{\tau_e^*}) \right] \quad (6.62)$$

$$\text{where } \tau_e^* = 1454829 D_p^4$$

where, in the above equations,

D_p : inclusion particle diameter in mm;

V_c : machine casting speed in $\text{m}\cdot\text{min}^{-1}$;

ζ : obscuration factor of the upper surface of the meniscus, which is affected by the SEN submerged depth and the gas injection practice. Different values as proposed in table 6.1 and 6.2 will be used in the prediction.

The results for different sizes of inclusions at different casting speeds in the bloom caster are given in table 6.7 and shown in figure 6.21. The same results for the billet caster are given in table 6.8 and shown in figure 6.22. The effects of ζ on inclusion removal are shown in figure 6.23 and 6.24 for the bloom caster at a casting speed of 0.55 m/min and for the billet caster at a casting speed of 1 m/min respectively.

It can be concluded from the results obtained here that the removal of inclusions of size smaller than 40 μm (final size) in the sump is impracticable for nozzles of this type in steel continuous casters. However, as shown by Duncombe, Jiang and Preshaw^[115] recently, the

inclusions of size smaller than 45 μm will be uniformly distributed across the thickness direction of the cast products, and will therefore be less harmful to product quality.

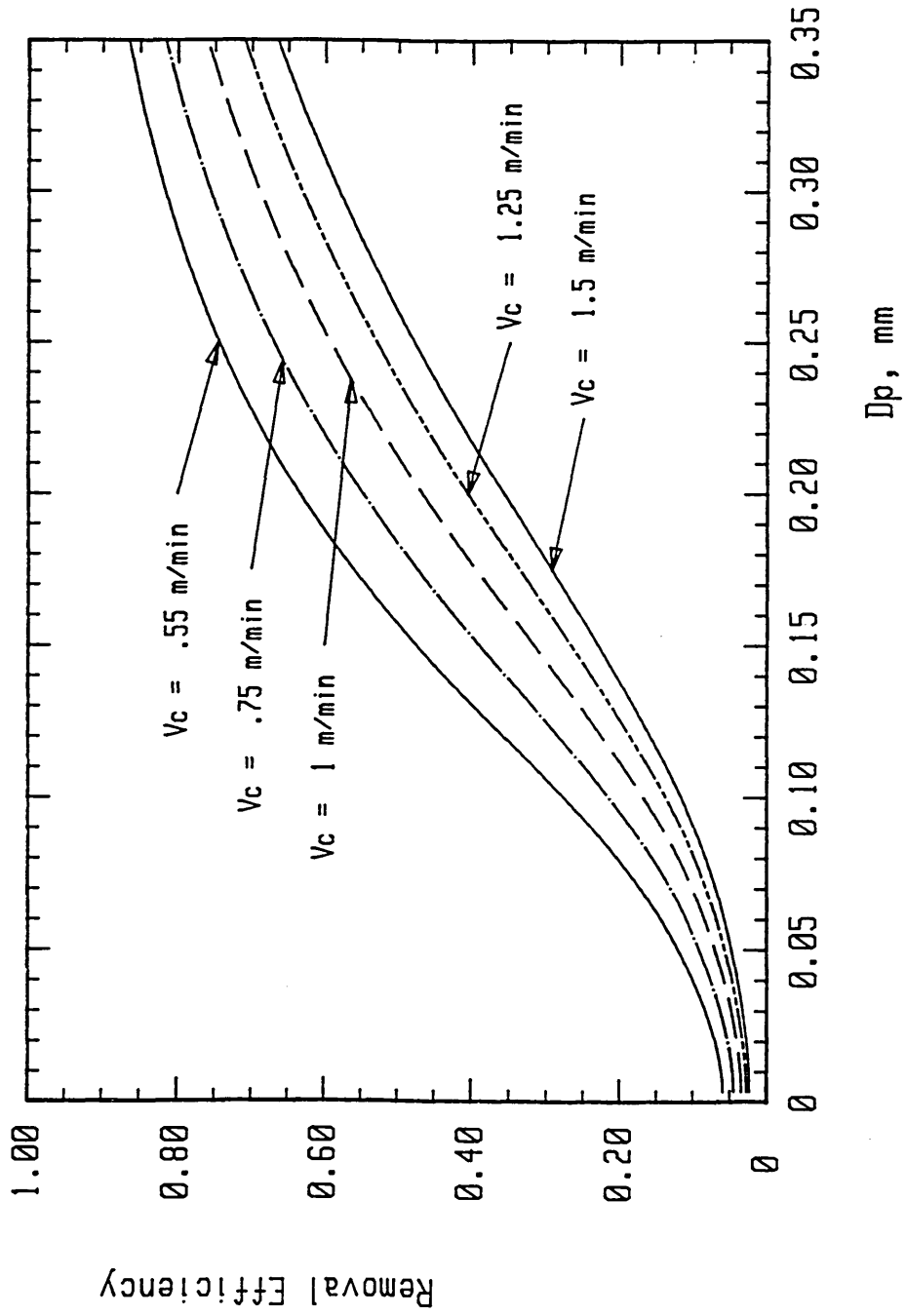
TABLE 6.7. Predictions on the inclusion removal ratios $\eta_{inclusion}$ for bloom steel casting system (prototype).

Casting speed m.min ⁻¹	Diameters of particles, D_p , (μm)										
	20	40	60	80	100	120	140	160	180	200	
0.55	7.00	10.00	14.39	20.25	27.62	35.69	43.67	51.08	57.71	63.47	
0.75	5.28	7.56	10.93	15.51	21.47	28.30	35.40	42.36	48.90	54.87	
1.00	4.04	5.80	8.40	11.98	16.77	22.42	28.53	34.76	40.87	46.69	
1.25	3.27	4.70	6.82	9.76	13.74	18.54	23.84	29.40	35.01	40.50	
1.50	2.74	3.95	5.74	8.23	11.64	15.79	20.46	25.44	30.57	35.70	

Mould section size 425 mm x 305 mm.

$\xi = 0.95$

Figure 6.21



Inclusion removal efficiency in the bloom caster

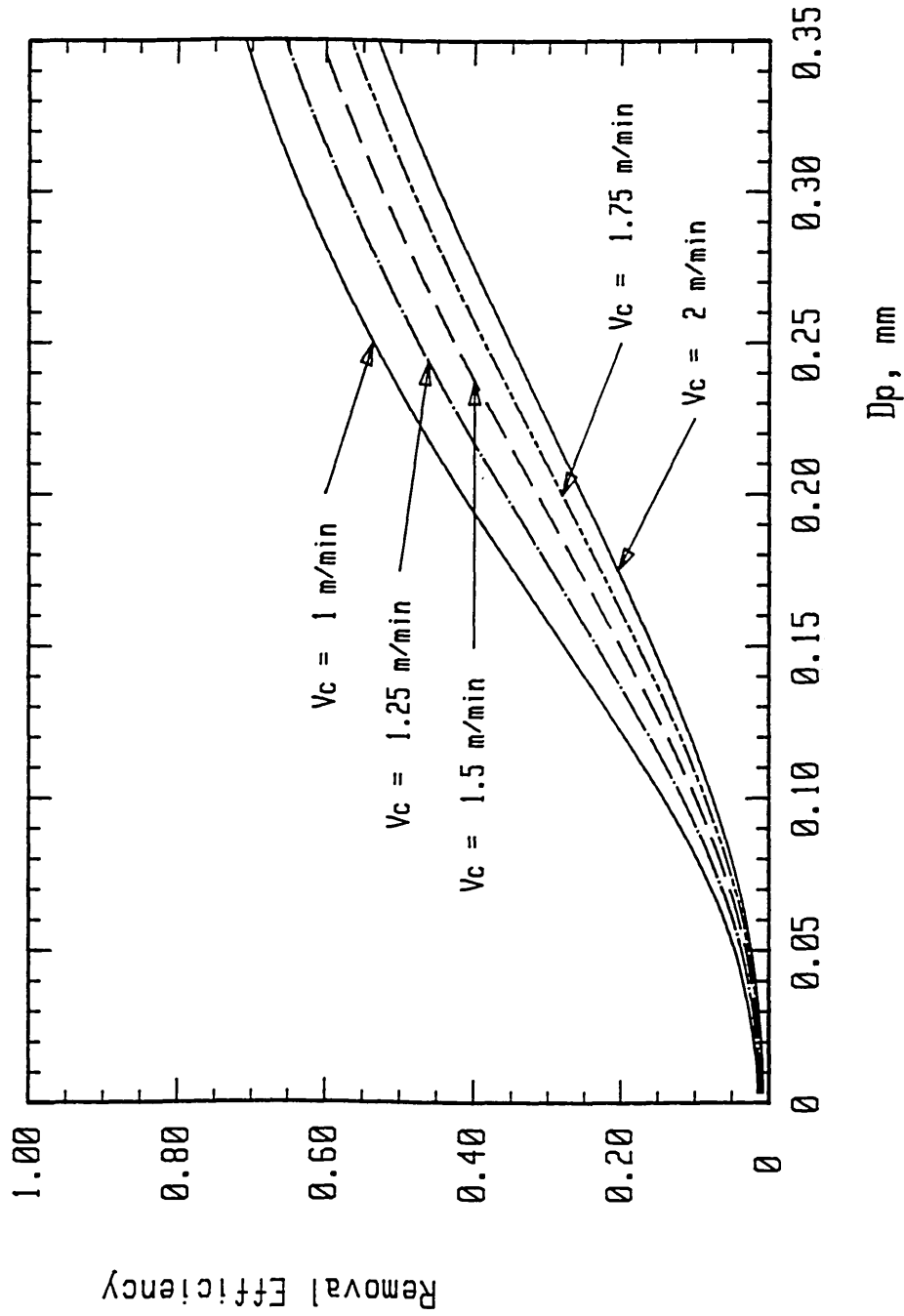
TABLE 6.8. Predictions on the inclusion removal ratios $\eta_{inclusion}$ for billet steel casting system (prototype).

Casting speed m.min ⁻¹	Diameters of particles, D_p , (μm)									
	20	40	60	80	100	120	140	160	180	200
1.00	2.03	3.53	6.00	9.69	14.29	19.47	24.98	30.61	36.17	41.53
1.25	1.63	2.48	4.85	7.88	11.70	16.09	20.86	25.83	30.87	35.85
1.50	1.37	2.38	4.07	6.64	9.91	13.71	17.89	22.34	26.91	31.52
1.75	1.17	2.05	3.50	5.73	8.59	11.94	15.67	19.67	23.84	28.10
2.00	1.03	1.80	3.08	5.04	7.58	10.57	13.93	17.56	21.39	25.34

Mould section size 140 mm x 140 mm.

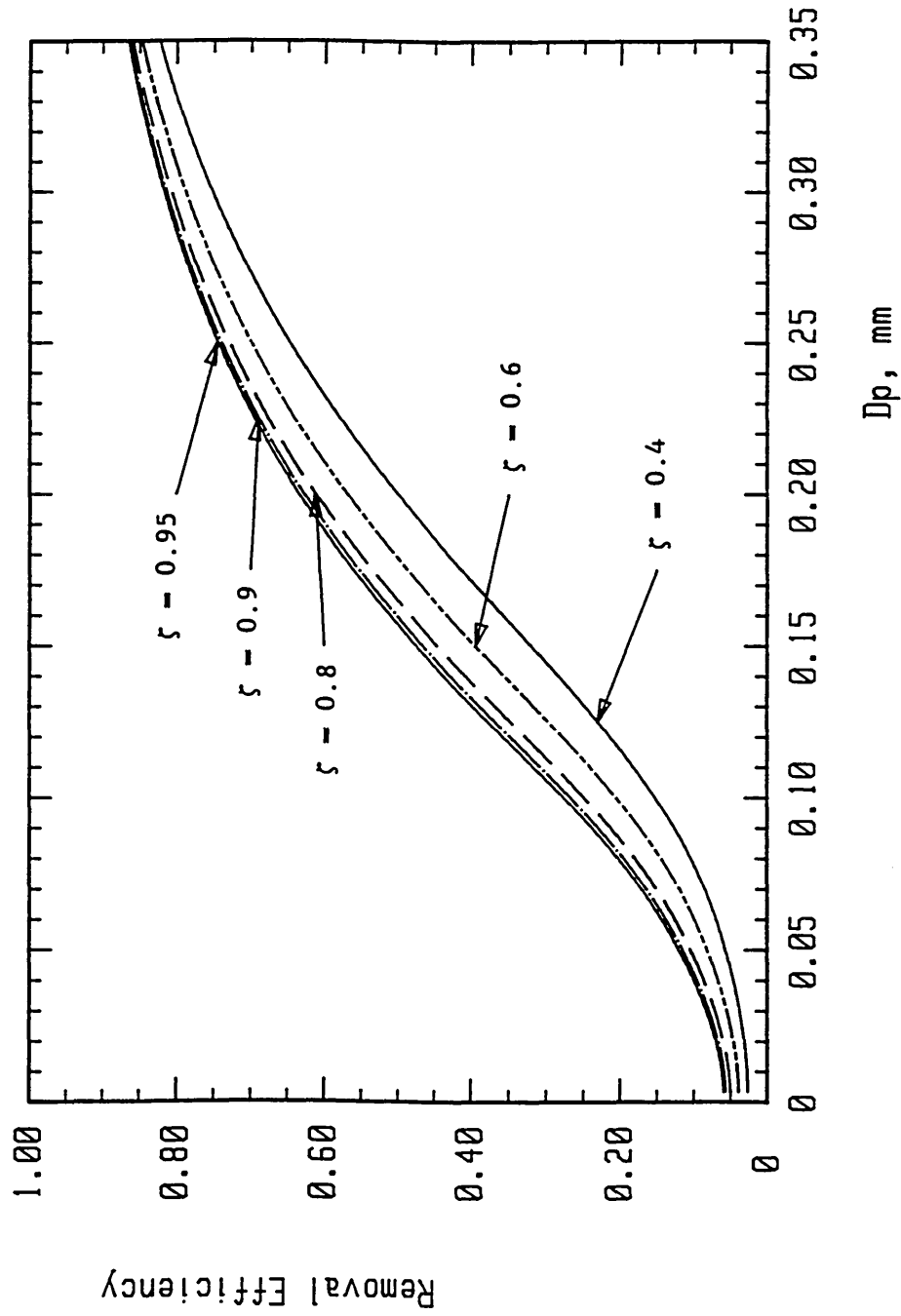
$\zeta = 0.85$

Figure 6.22



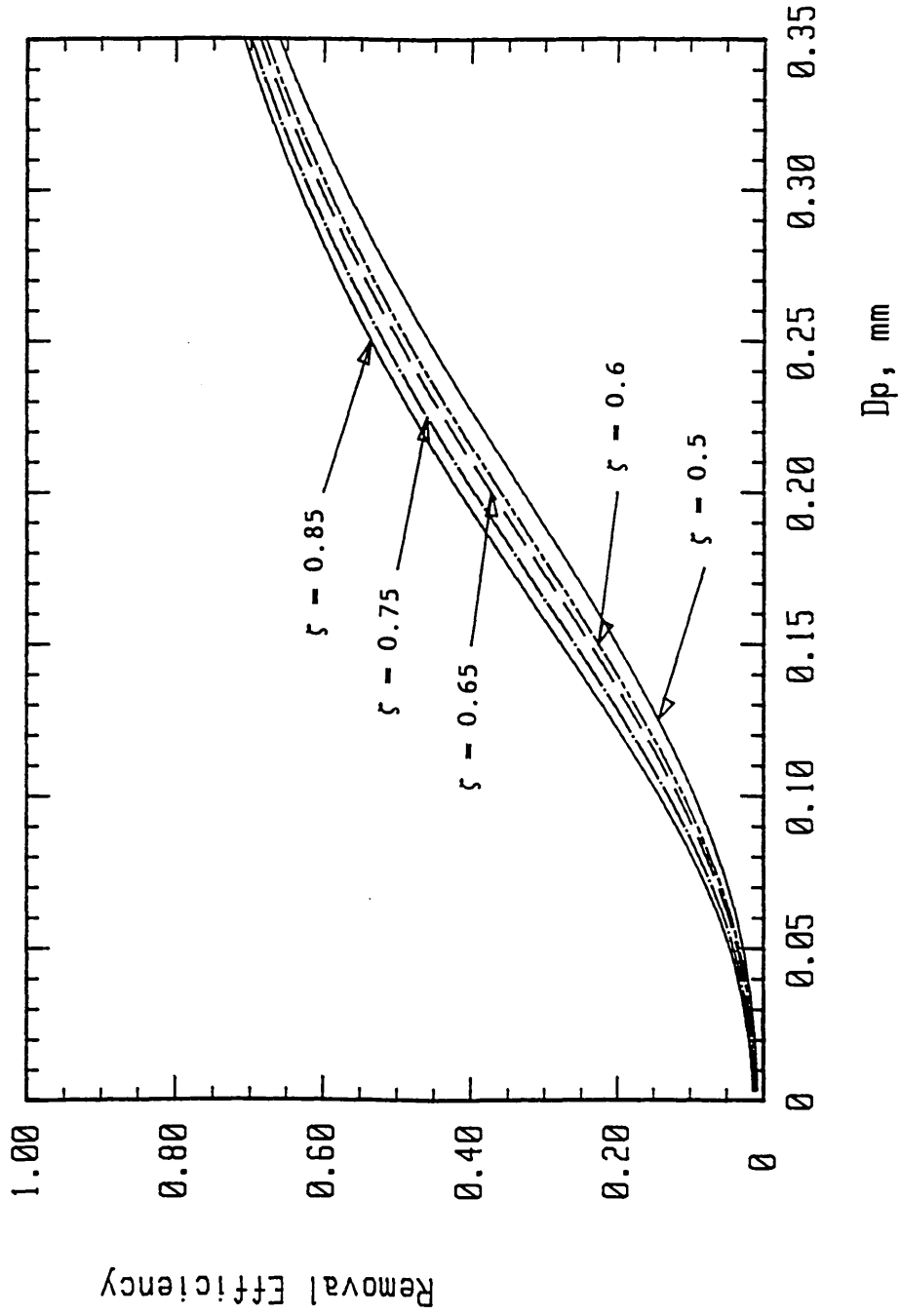
Inclusion removal efficiency in the billet caster

Figure 6.23



Inclusion removal efficiency in the bloom caster

Figure 6.24



Inclusion removal efficiency in the billet caster

7. CONCLUSIONS.

A theoretical model has been formulated which relates the inclusion removal in the sump to the fluid flow there. The inclusion removal ratio in the sump for a given continuous casting machine can be predicted using this theoretical model. The model, using the properties of liquid steel and practicable casting speeds, demonstrates that the removal of inclusions of sizes less than 40 μm from the sump of billet caster is less than 5% using an SEN that directs the steel stream downwards.

The inclusion agglomeration or collision plays a very important role in the mould sump in the removal of inclusions. By using a bifurcated nozzle and a deep SEN submerged depth, the inclusion size can be doubled or even tripled from its size at the entry ports of an SEN.

An experimental method has been devised to simulate the behaviour of inclusions in the sump during continuous casting. The use of a colourless paraffin layer on the top of the water in the model mould together with the injection of fine droplets of coloured paraffin into the nozzle entry stream gives a good simulation.

The use of fine aluminium flakes or small air bubbles together with a plane light source has been found to be useful in studying the fluid flow patterns developed in the three-dimensional continuous casting sump model. Using this method, the fluid flow patterns developed within the model mould have been viewed and recorded photographically on different planes. These photographs of the fluid flow patterns help to explain the results for the removal of inclusions.

The fluid flow patterns developed when small outside diameter nozzles with deep SEN submerged depth is employed are beneficial to the removal of inclusions.

Reducing the nozzle outside diameter increases the inclusion removal ratio. When the nozzle is submerged deep enough, over 175 mm, the SEN port angle has a little effect on inclusion removal in the mould sump.

Increasing the SEN submerged depth promotes inclusion agglomeration, and therefore increases the inclusion removal ratio. But when the SEN submerged depth exceeds a certain limit, the inclusion removal ratio in the billet mould tends to decrease. The optimum SEN submerged depth for the separation of inclusions in the sump is 125 — 150 mm for the present billet mould. In contrast, the inclusion removal ratio in the bloom mould showed no signs of decreasing even when the SEN submerged depth had reached 220 mm.

Reducing the casting speed increases the inclusion removal ratio in the sump, but the influence of the casting speed on the inclusion removal in the sump is not very strong. Control strategies for the control of casting speed can be left to satisfy other constrains on the casting process.

Although argon gas introduced into the tundish nozzle stream offers protection from nozzle blockage, it will not be beneficial to the removal of inclusion in the sump unless the injection rate is very low and an SEN with large downward port angle is employed.

8. FURTHER WORK.

- a) Experiments should be further carried out on the determination of the agglomeration of inclusion particles in relation to the SEN and mould geometries and SEN submerged depth.
- b) A study should be undertaken to elucidate the inclusion size distribution after agglomeration.
- c) The theoretical model should be refined by incorporating an appropriate inclusion size distribution function obtained from experiments described in a) and b).
- d) The experiments on the water model should be continued by including a simulation of the solidification front in the mould, to investigate the effect of the solidifying shells on inclusion removal. Inserting layers of gauze in the position of the solidification front provide a good initial basis for further investigation.
- e) Plant trials should be undertaken to compare the effect of SEN submerged depth on the inclusion removal efficiency in the mould sump.
- f) A comparative analysis of the behaviour of different type of inclusions in the sump under different fluid flow conditions can be undertaken by employing the theoretical model developed in the present thesis with the property data of inclusions available in the literature.

9. REFERENCES

1. Jaffrey, D., Dover, I., and Hamilton, L., Metals Forum, vol.7 (1984), no.2, 67 - 78.
2. Relander, K., Lounamaa, K., and Lindholm, T., Ironmaking and Steelmaking, 1979, no.5, 245 - 250.
3. Hibbins, S., Bansal, H., Fryia, C., Heaslip, L., and Swartz, L., 24th Annual Conference of Metallurgists; Vancouver, British Columbia, Canada; 18 - 21 Aug. 1985; The Metallurgical Society of CIM; pp. 88 - 123.
4. Tia, M. C., Chou, C. L., and Chen, C. H., 4th International Conference Continuous Casting; Preprints, vol.1; Brussels, Belgium; 17 - 19 May 1988; pp. 259 - 270.
5. Astrov, E. I., Klipov, A. D., and Polushkin, N. A., Stal, in English, vol.10 (1966), no.10, 796 - 797.
6. Suzuki, I., Suzuki, Y., and Kosuge, T., Nippon Steel Technical Report, no. 13, June 1979, p. 24.
7. Takeda, M., Komano, T., Yanai, T. and Hino, T., Nippon Steel Technical Report, no. 13, June 1979, p. 36.
8. Nakatani, M., Adachi, T., Kimiya, S., and Kimura, K., Sumitomo Steel Report, 1984, p. 416.
9. Wychaert, A., Ironmaking and Steelmaking, 1977, no.6, 340 - 349.
10. Offerman, C., Scand. J. Metallurgy, vol.10 (1981), 25 - 28.
11. Mills, N. T., and Barnhardt, L. F., J. Metals, 1971, no.11, 37 - 43.
12. Hashio, M., et al., 2nd Process Technology Conf., vol.2, Chicago, 1981, pp. 65 - 73.
13. Sobolewski, S., and Hurtuk, D. J., 2nd Process Technology

- Conf., vol.2, Chicago, 1981, pp. 160 - 165.
14. Wei, T. X., and Carlsson, G., Scand. J. Metallurgy, vol.12 (1982), 121 - 128.
 15. Nemoto, H., and Kawawa, T., J. Metals, vol.21 (1969), Aug., 62 - 67.
 16. Robertson, A. D., and Sheridan, A. T., J. Iron Steel Inst., vol.208 (1970), 625 - 632.
 17. McPherson, N. A., The Shrouding of Steel Flow for Casting and Teeming, Iron and Steel Society, Pennsylvania, USA, 1986, pp. 31 -43.
 18. Feretti, A., Podrini, M., and Schino, G. D., The Shrouding of Steel Flow for Casting and Teeming, Iron and Steel Society, Pennsylvania, USA, 1986, pp.45 - 53.
 19. Moton, S. K., and Weinberg, F., J. Iron Steel Inst., vol.211 (1973), 13 - 23.
 20. Brimacombe, J. K., and Weinberg, F., J. Iron Steel Inst., vol.211 (1973), 23 - 32.
 21. Lait, J. E., Brimacombe, J. K., and Weinberg, F., Ironmaking Steelmaking, vol.(1974), 35 -
 22. Lait, J. E., Brimacombe, J. K., and Weinberg, F., Ironmaking Steelmaking, vol.(1974), 90 -
 23. Raju, K. R., Tool and Alloy Steels — Annual, December 1985, pp. 397 - 403.
 24. Themlis, N. J., et al., Trans. of the Metallurg. Soc. of AIME, vol.6 (1966), 821 - 828.
 25. Levenspiel, O., "Chemical Reaction Engineering", John Wiley and Sons, New York, (1962).

26. Easton, R., and Meyer, S. W., Iron Steel Eng., vol.145 (1965), p.139.
27. Williams, F., and Neumann, F., Concast News, vol.7 (1968), no.2, 5 - 6.
28. Szekely, J., and Yadoya, R. T., Metallurg. Transactions, vol.3 (1972), 2673 - 2680.
29. Hsiao, T. C., Lehner, T., and Kjellberg, B., Scand. J. Metallurgy, vol.9 (1980), 105 - 110.
30. Robertson, T., Moore, P., and Hawkins, R. J., Ironmaking Steelmaking, vol.13 (1986), no.4, 195 - 203.
31. Szekely, J., "Fluid flow Phenomenon in Metals Processing", Academic Press, (1969).
32. Johnstone, R. E., and Thring, M. W., "Pilot Plants, Models and Scale-up Methods in Chemical Engineering", McGraw Hill, (1957).
33. GuKman, A. A., "Introduction to the Theory of Similarity", Academic Press, (1965).
34. Heaslip, L. J., McLean, A., and Sommerville, I. D., "Continuous Casting. vol.1, Chemical and Physical Interactions During Transfer Operations.", Iron and Steel Institute/AIME, (1983).
35. Skvortov, A. A., and Akiemenko, A. D., Izvest. VUZ-Chem. Met., 1958, no.3, p.21 Henry Bruther Trans. no. 5945.
36. Astrov, E. I., Klipov, A. D., and Polushkin, N. A., Stal, in English, vol.10 (1966), no.10, 885-888.
37. Akiemenko, A. D., Izvest. VUZ-Chem. Met., 1963, no.6, p. 179, Henry Bruther Trans. no. 6821.
38. Habu, Y. et al., Transactions ISIJ, vol.15 (1975), 246 - 251.
39. Krainer, H., and Tarmann, B., Extrait de la Revue Universelle

- des Mines, Liege, 1958.
40. Arnoult, J., Kohn, A., and Plumesi, J. P., Rev. Met., 1969, p.585.
 41. Afanaseva, K. I., and Iventsov, T. P., Stal, vol.18 (1958), no.7, p.599.
 42. Nemoto, H., The 12th Nishiyama Technical Lecture, ISIJ, May 1971.
 43. Teman, R., "Navier-Stokes Equations and Nonlinear Functional Analysis", Society for Industrial and Applied Mathematics, (1983).
 44. Savage, J., and Pritchard, W. H., J. Iron Steel Inst., vol.179 (1954), 269-
 45. Adenis, J. O., Coats, K. H., and Ragone, D. V., J. Inst. Metals, vol.91 (1963), 395-430.
 46. Hills, A. W. D., J. Iron Steel Inst., vol.203 (1965), 18-26.
 47. Donaldson, J. W., and Hess, M., Electric Furnace Proc., 1966, p.78.
 48. Mizikar, E., Trans. TMS-AIME, vol.239 (1967), 1747-1753.
 49. Fahidy, T. Z., J. Iron Steel Inst., vol.207 (1969), 1373-
 50. Szekely, J. and Stanek, V., Met. Trans., vol.(1970), 119-126.
 51. Levin, V. B., High Temperature, vol.2 (1964), 531-
 52. Bradshaw, P., Ferris, D. H., and Atwell, N. P., J. Fluid Mech., vol.38 (1967), 593-
 53. Spalding, D. B., J. Fluid Mech., vol.27 (1967), 97-
 54. Wolfshtein, M., Int. J. Heat Mass Transfer, vol.12 (1969), 301-
 55. Spalding, D. B., Chemi. Eng. Sci., vol.26 (1971), 95-
 56. Gosman, A. D. et al., "Heat and Mass Transfer in Recirculating

- Flows", Academic Press, London, (1969).
57. Szekely, J., and Yadoya, R. T., Met. Trans., vol.4 (1973), 1379-1388.
 58. Szekely, J., and Asai, S., Met. Trans., vol.5 (1974), 463-467.
 59. Szekely, J., Asai, S., and Chang, C. W., Proc. Internat. Iron and Steel Conf., Dusseldorf, 1974, Preprints, vol.3, 5.2.2.1. 1-18.
 60. Nakanishi, K., Szekely, J., and Chang, C. W., Ironmaking and Steelmaking (Quarterly), 1975, No.2, 115-124.
 61. Asai, S., and Szekely, J., Ironmaking and Steelmaking (Quarterly), 1975, No.3, 205-213.
 62. Tanaka, S., Lye, M., Salcudean, M., and Guthrie, R. I. L., 24th Annual Conference of Metallurgists; Vancouver, British Columbia, Canada; 18 - 21 Aug. 1985; The Metallurgical Society of CIM; pp.142-161.
 63. Debroy, T., and Sychterz, J. A., Met. Trans. B, vol.16B (1985), 497-504.
 64. He, Y., and Sahai, Y., Steelmaking Proceedings, vol.69, Washington, D.C., USA, 6-9 April, 1986, Iron and Steel Society, 745-754.
 65. Szekely, J., and El-Kaddah, N., Steelmaking Proceedings, vol.69, Washington, D.C., USA, 6-9 April, 1986, Iron and Steel Society, 761-776.
 66. Ilegbusi, O. J., and Szekely, J., Mathematical Modelling of Materials Processing Operations, Palm Springs, California, USA, 29 Nov. - 2 Dec. 1987, The Metallurgical Society/AIME, 409-429.
 67. Yadoya, R. T., Ph.D. Thesis, State University of New York at

- Buffalo, 1972.
68. Launder, B. E., and Spalding, D. B., "Mathematical Models of Turbulence", Academic press, New York, 1972.
 69. Jones, W. P., and Launder, B. E., Int. J. Heat Mass Transfer, vol.15 (1972), 269-289.
 70. Peyret, R., and Taylor, T. D., "Computational Methods for Fluid Flow", Springer-verlag, New York, (1983).
 71. Peaceman, D. W., and Rachford, H. H., J. Soc. Indus. Appl. math., vol.3 (1955), 28-41.
 72. Douglas, J., and Gunn, J. E., Numer. Math., vol.6 (1964), 428-453.
 73. Mitchell, A. R., "Computational Methods in Partial Differential Equations", Wiley, New York, (1969).
 74. Strang, G., SIAM J. Numerical Analysis, vol.5 (1968), 506-517.
 75. Gourlay, A. R., and Morris, J. L., J. Comput. Phys., vol.5 (1970), 229-243.
 76. Lindemuth, J., and Killeen, J., J. Comput. Phys., vol.13 (1973), 181-208.
 77. Briley, W. R., and McDonald, H., J. Comput. Phys., vol.22 (1977), 372-397.
 78. Briley, W. R., and McDonald, H., J. Comput. Phys., vol.34 (1980), 54-73.
 79. Diserens, M., et al., Scand. J. Metallurgy, vol.10 (1981), 19-23.
 80. Miyashita, Y., et al., The 2nd Japan-USSR Joint Symposium on Physical Chemistry of Metallurgical processes, pp. 101-102. Spec. Rep. No.10, The Iron and Steel Institute of Japan, Tokyo, (1969).
 81. Sano, N., Shiomi, S., and Matsushita, Y., Transactions ISIJ,

- vol.7 (1967), 244-253.
82. Kawawa, T., and Ohkubo, M., Transactions ISIJ, vol.8 (1968),
203-219.
83. Torssell, K., Jernkont. Ann. vol.151 (1967), 890-949.
84. Levich, V. G., "physico-chemical Hydrodynamics", Prentice-Hall,
Englewood Cliffs, N.J., (1962).
85. Landau, L. D., and Lifschitz, E. M., "Fluid Mechanics", Pergamon
Press, London, (1966).
86. Batchelor, G. K., "The Theory of Homogeneous Turbulence",
University Press, Cambridge, (1970).
87. Davies, J. T., "Turbulence Phenomena", Academic Press, New York,
(1972).
88. Kemeny, F. L., et al., 2nd Process Technology Conf., vol.2,
Chicago, 1981, pp.232-245.
89. Sahai, Y., and Ahuja, R., Steelmaking Proceedings, vol.69,
Washington, D.C., USA, 6-9 April, 1986, Iron and Steel Society,
677-688.
90. Nakajima, H., et al., Steelmaking Proceedings, vol.69,
Washington, D.C., USA, 6-9 April, 1986, Iron and Steel Society,
705-716.
91. Martinez, E., et al., Transactions ISIJ, vol.26 (1986), 724-731.
92. Hsu, K. C., and Chou, C. L., China Steel Tech. Rep.,
30 Oct. 1987, (1), 26-30.
93. Nakajima, K., and Kawasaki, M., Tetsu-to-Hagane, vol.73 (1987),
852-859.
94. Nakajima, K., and Kawasaki, M., Tetsu-to-Hagane, vol.73 (1987),
860-867.

95. Ilegbusi, O. J., and Szekely, J., *Steel Res.*, vol.59 (1988), 399-405.
96. Engh, T. A., and Lindskog, N., *Scand. J. Metallurgy*, Vol.4 (1975) 49-58.
97. Carslaw, H. S., and Jaeger, J. C., "Conduction of Heat in Solids", Oxford University Press, (1959), p388.
98. Thomas, B. G., Mika, L. J., and Najjar, F. M., *Met. Trans. B*, vol.21b (1990), 387-400.
99. Abramovich, G. N., "The Theory of Turbulent Jets", The M.I.T. Press, Massachusetts, (1963).
100. Hoshikawa, I., et al., *Iron & Steel Maker*, April 1991, 45-52.
101. Forstall, W., and Shapiro, A. H., *J. Appl. Mech.*, Vol.17 (1950), No.4, p399.
102. Abramovich, G. N., "The Theory of Turbulent Jets", The M.I.T. Press, Massachusetts, (1963), pp12-13.
103. Abramovich, G. N., "The Theory of Turbulent Jets", The M.I.T. Press, Massachusetts, (1963), p199, p196.
104. Levich, V. G., *Physicochemical Hydrodynamics*, Prentice Hall, New York, 1962
105. Saffman, P. G., and Turner, J. S., *J. Fluid Mech.* Vol.1 (1956), 16-30.
106. Linder, S., *Scand. J. Metallurgy*, Vol. 3 (1974), 137-150.
107. Hoching, L. M., *Quart. J. Royal Meterol. Soc.*, Vol.85 (1959), 44-50.
108. Manley, R. St. J., and Mason, S. G., *J. Colloidal Sci.*, Vol. 7 (1952), 354-369.
109. Manley, R. St. J., and Mason, S. G., *Can. J. Chemistry*, Vol. 33

- (1955), 763-773.
110. Telford, J. W., Thorndike, N. S., and Bowen, E. G.,
Quart. J. R. Met. Soc., Vol. 81 (1955), 241-250.
111. Michael, D. H., and Norey, P. W., J. Fluid Mech., Vol. 37
(1969), 565-575.
112. Langmuir, I. and Blodgett, K., J. Meteorol. Vol. 5 (1948),
175-186.
113. Wang, Y. H., Steelmaking Conference Proceedings, Vol. 73 (1990),
473-480.
114. Hinze, H., Turbulence, McGraw-hill, New York, 1959.
115. Duncombe, J. T., Jiang, G. S. and Preshaw, D. A., 1st European
Conference on Continuous Casting, Florence, Italy, Sept. 23-25,
1991, 2.459-2.468.

ESTIMATION OF THE VALUES OF THE MIXING PARAMETERS BASED ON JET
ENTRAINMENT THEORY.

A1.1. Velocity profile in a round submerged jet.

The mixing parameters of the SEN stream mixing with the surrounding fluid in the mould sump can be estimated by using the theory of a submerged free jet. The submerged free jet is the type of turbulent jet spreading through a medium at rest.

Figure A1.1 shows a diagram of a submerged free jet together with the velocity variation along the radius direction at several locations.

Figure A1.2^[101] shows a universal profile of the dimensionless velocity at any cross section of the jet. The dimensionless velocity is expressed as a function of r/r_c :-

$$\frac{u}{u_m} = f\left(\frac{r}{r_c}\right) \quad (A1.1)$$

where u : local velocity;

u_m : axial velocity (velocity on the jet axis);

r : distance from the jet axis;

r_c : distance between the jet axis and the point at which the velocity is equal to half of the axial velocity;
i.e. $0.5u_m$.

According to figure A1.2, we know that:-

Figure A1.1

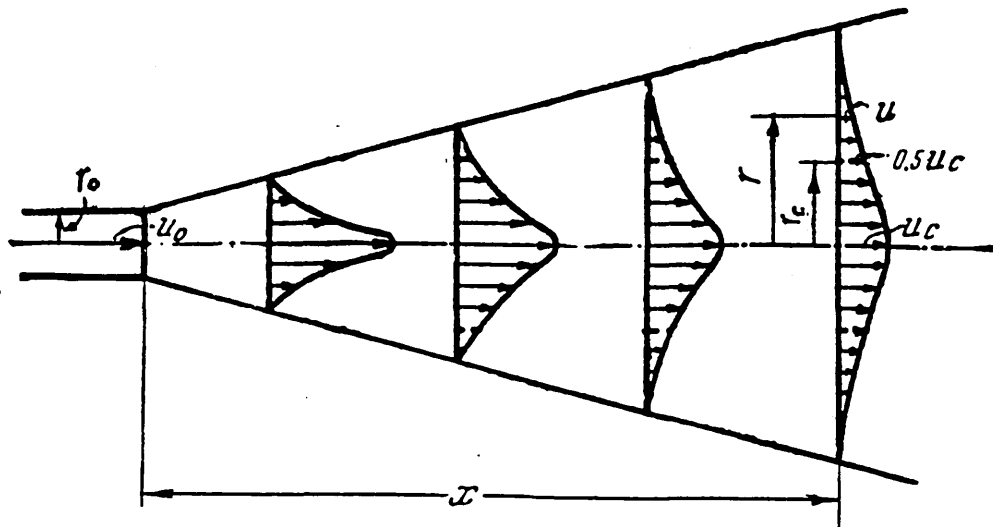
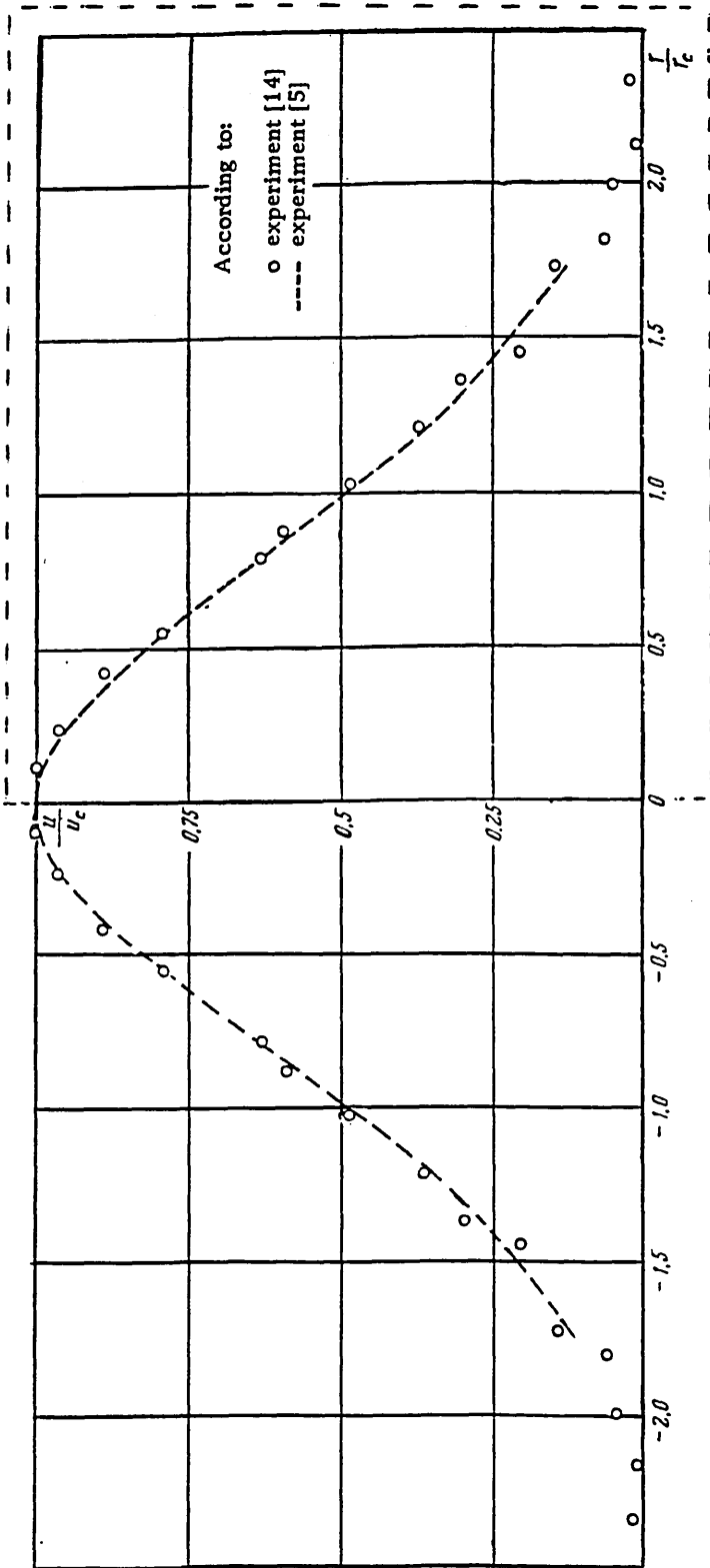


Diagram of a submerged free jet.

Figure A1.2



Dimensionless velocity profile in the main region of axially symmetric submerged jet. The figure inside the dotted rectangle is taken from Abramovich [99] and has been extended by the present author to illustrate the discussion.

$$f\left(\frac{r}{r_c}\right) = f\left(-\frac{r}{r_c}\right) \quad (\text{A1.2})$$

$$f(0) = 1 \quad (\text{A1.3})$$

$$f(1) = 0.5 \quad (\text{A1.4})$$

and

$$f(0.5) \approx 0.84 \quad (\text{A1.5})$$

Therefore the function describing the velocity profile in a given cross section of the jet can be expressed as:

$$\frac{u}{u_m} = e^{-a\xi^2} \quad (\text{A1.6})$$

where a : constant, $a = 0.693$

$$\xi = \frac{r}{r_c} \quad (\text{A1.7})$$

A1.2. Velocity variation along the axis of a round submerged jet.

As shown by numerous experiment, the pressure in the jet is virtually invariable and equal to the pressure in the surrounding space. On account of this the total momentum flow of the fluid mass in the jet should be the same in all the cross section of the jet:-

$$\int_0^m u dm = \text{Const.} \quad (\text{A1.8})$$

where dm : mass flow through an element of the cross section of the jet;

m : total mass flow through cross section of jet;

u : velocity at the centre of the element.

or in another form:-

$$\int_0^F \rho u^2 dF = \text{Const.} \quad (\text{A1.9})$$

where dF : area of the element;

ρ : density of the fluid in the jet;

F : total jet cross section area.

For a round jet:-

$$dF = 2\pi r dr \quad (\text{A1.10})$$

where r : distance from the jet axis.

Substituting into equation (A1.9), we obtain the constant total momentum for the round jet as:-

$$u_m^2 x^2 \int_0^\infty \left[\frac{u}{u_m} \right]^2 \frac{r}{x} \frac{dr}{x} = \text{Const.} \quad (\text{A1.11})$$

in which u_m is the axial velocity of the given sections, x is the

distance between the given section and the jet pole.

According to jet theory^[102]

$$r_c = b.x \quad (A1.12)$$

where b is a constant.

Therefore, from equation (A1.6), (A1.7) and (A1.12), it is concluded that the dimensionless velocity (u/u_m) at a selected point is a function of only the dimensionless coordinate (r/x), i.e.:-

$$\frac{u}{u_m} = f(r/x) \quad (A1.13)$$

Hence,

$$\int_0^\infty \left[\frac{u}{u_m} \right]^2 \frac{r}{x} \frac{dr}{x} = \text{Const.} \quad (A1.14)$$

As a result of the equation (A1.11) the velocity in the centre of a given section of a round submerged jet is inversely proportional to the distance from the pole:-

$$u_m = \frac{\text{const.}}{x}$$

One of the most commonly used expression^[103] for the part of jet in the main region is:-

$$\frac{u_m}{u_o} = 12.4 \left(\frac{r_o}{x} \right) \quad (A1.15)$$

where r_o is the nozzle radius.

A1.3. Momentum conservation.

As mentioned in the previous section, the total momentum flow of the fluid mass is the same in all the cross sections of the jet:-

$$\int_0^F \rho u^2 dF = \text{Const.} \quad (\text{A1.16})$$

Total momentum flow through a jet at a distance x from the jet pole may be expressed as:-

$$\begin{aligned} m_x &= \int_0^\infty \rho u^2 2\pi r dr \\ &= 2\pi \rho u_m^2 \frac{r_c^2}{c} \int_0^\infty \left[\frac{u}{u_m} \right]^2 \frac{r}{r_c} \frac{dr}{r_c} \end{aligned}$$

Let $\frac{r}{r_c} = \xi$, therefore:-

$$\begin{aligned} d\xi^2 &= 2\xi d\xi \\ &= 2 \frac{r}{r_c} \frac{dr}{r_c} \end{aligned}$$

So

$$m_x = \pi \rho u^2 r_c^2 \int_0^{\infty} e^{-2a\xi^2} d(\xi^2)$$

And
$$\int_0^{\infty} e^{-2a\xi^2} d(\xi^2) = \frac{1}{2a} .$$

So that

$$m_x = \pi \rho u^2 r_c^2 \frac{1}{2a} \quad (\text{A1.17})$$

The total momentum flow of the fluid mass at the jet mouth is:-

$$m_o = \rho u_o^2 \pi r_o^2 \quad (\text{A1.18})$$

Hence:-

$$\pi \rho u^2 r_c^2 \frac{1}{2a} = \rho u_o^2 \pi r_o^2 \quad (\text{A1.19})$$

or

$$\left[\frac{u_m}{u_o} \right]^2 = 2a \left[\frac{r_o}{r_c} \right]^2 \quad (\text{A1.20})$$

Substituting equation (A1.12) into equation (A1.20), we have:-

$$\left[\frac{u_m}{u_o} \right]^2 = \frac{2a}{b^2} \left[\frac{r_o}{x} \right]^2 \quad (\text{A1.21})$$

or in the other form:-

$$\frac{u_m}{u_o} = \frac{\sqrt{2a}}{b} \left(\frac{r_o}{x} \right) \quad (\text{A1.22})$$

From equation (A1.15) we know that:-

$$\frac{\sqrt{2a}}{b} = 12.4 \quad (\text{A1.23})$$

Therefore

$$b = \frac{\sqrt{2a}}{12.4} = \frac{\sqrt{2 \times 0.693}}{12.4} = 0.09494 \quad (\text{A1.24})$$

A1.4. Jet entrainment.

As mentioned in section A1.2, there is virtually no pressure variation in the jet, and the present experiments were carried out at a constant temperature. We can therefore assume that no thermal expansion or contraction occurs within the fluid. The amount of the fluid liquid entrained into the jet can therefore be worked out by determining the difference between the volume flow through a given cross section of jet and its initial volume flow.

Volume flow through a given section of jet:-

$$\begin{aligned}\dot{V}_x &= \int_0^F u dF \\ &= \int_0^\infty 2\pi r u dr \\ &= u_m r_c^2 \int_0^\infty 2\pi \frac{r}{r_c} \frac{u}{u_m} \frac{dr}{r_c}\end{aligned}$$

Let $\frac{r}{r_c} = \xi,$

so $d(\xi^2) = 2\xi d\xi = 2 \frac{r}{r_c} \frac{dr}{r_c} .$

Therefore,

$$\dot{V}_x = u_m r_c^2 \pi \int_0^\infty e^{-a\xi^2} d(\xi^2) \quad (\text{A1.25})$$

Because

$$\int_0^\infty e^{-a\xi^2} d(\xi^2) = \frac{1}{a}$$

the volume flow through a given cross section is:-

$$\dot{V}_x = u_m r_c^2 \pi \frac{1}{a} \quad (\text{A1.26})$$

The initial volume flow from the jet:-

$$\dot{V}_J = u_o \pi r_o^2 \quad (\text{A1.27})$$

Therefore the jet entrainment volume flow is:-

$$\begin{aligned} \dot{V}_{entrain} &= \dot{V}_x - \dot{V}_J \\ &= u_o \pi r_o^2 \left[\frac{u_m}{u_o} \left[\frac{r_c}{r_o} \right]^2 \frac{1}{a} - 1 \right] \end{aligned} \quad (\text{A1.28})$$

A1.5. Jet entrainment flux

The dimensionless jet entrainment mass flux from its surrounding zone could be expressed by:-

$$\Gamma_{entrain} = \frac{\rho \dot{V}_{entrain}}{\rho \dot{V}_J} = \frac{\dot{V}_x - \dot{V}_J}{\dot{V}_J} \quad (\text{A1.29})$$

Substituting equation (A1.27) and (A1.28) into equation (A1.29), we have:-

$$\Gamma_{entrain} = \frac{u_m}{u_o} \frac{r_c^2}{r_o^2} \frac{1}{a} - 1 \quad (\text{A1.30})$$

According to equation (A1.12), (A1.15) and (A1.24), we can rewrite equation (A1.30) as:-

$$\Gamma_{entrain} = 0.161 \left(\frac{x}{r_o} \right) - 1 \quad (A1.31)$$

In the case of bloom mould experiment employing SEN with horizontal outlets, $r_o = 6.5$ mm and $x = 130 \rightarrow 200$ mm. Therefore the $\Gamma_{entrain}$ for this situation is:-

$$\Gamma_{entrain} \approx 2 \rightarrow 4$$

A1.6. The values of Γ_{JR} and Γ_{JM} .

Assuming that the total dimensionless interchange mass fluxes between the jet entrainment zone and its surrounding zones are in the same order as the jet entrainment flux, the values of Γ_{JR} and Γ_{JM} could be estimated as follows.

The assumption leads to the following expression:-

$$\Gamma_{JR} + \Gamma_{JM} = \Gamma_{entrain} \quad (A1.32)$$

and according to equation (6.23), we have:-

$$\Gamma_{JR} + \beta \Gamma_{JR} = \Gamma_{entrain}$$

or

$$\Gamma_{JR} = \frac{\Gamma_{entrain}}{1 + \beta} \quad (A1.33)$$

In the bloom mould model:-

The experiments revealed that the jet from the bifurcated nozzle penetrated a distance equal to 20 to 30 times of the nozzle radius, i.e. $x/r_o = 20 \rightarrow 30$. Therefore, according to equation (A1.31),

$$\Gamma_{\text{entrain}} = 2.22 \rightarrow 3.83$$

The value of β can be taken as 1 in the case of employing bifurcated nozzles. Therefore, Γ_{JR} for the bloom mould model is about 1.11 to 1.92, i.e.

$$\Gamma_{\text{JR}} = 1.11 \rightarrow 1.92 \quad (\text{A1.34})$$

and

$$\Gamma_{\text{JM}} = \beta \Gamma_{\text{JR}} = 1.11 \rightarrow 1.92 \quad (\text{A1.35})$$

In the billet mould model:-

The experiments revealed that the jet from vertical outlet nozzles in the billet mould model penetrated a distance of 600 mm to 675 mm. Comparing with the nozzle radius of 7.5 mm, this distance is equal to 80 to 90 times of the nozzle radius, i.e. $x/r_o = 80 \rightarrow 90$. Therefore, from equation (A1.31), we have:-

$$\Gamma_{\text{entrain}} = 11.88 \rightarrow 13.49$$

Because of the characteristics of the fluid flow field revealed from the billet mould model, the interchange mass flux between the jet entrainment zone and the mixing zone is much higher than that between

the jet entrainment zone and recirculation zone, giving a possible value of β of 10. Therefore, Γ_{JR} for the billet mould model is about 1.08 to 1.23, i.e.

$$\Gamma_{JR} = 1.08 \rightarrow 1.23 \quad (A1.36)$$

and

$$\Gamma_{JM} = \beta \Gamma_{JR} = 10.8 \rightarrow 12.3. \quad (A1.37)$$

PROGRAMME LIST

```

'Programme to explore the values produced by the equation for mixing
'in the liquid sump during continuous casting
,
'The equation being explored is the equation (4.65) in Chapter 4.
,
DEFINT J,K,F,I
DEFDBL E,D,V,A,B,C,M
DIM E(2), DP(100), V(100,2), A(100,2), B(100,2), C(100,2), SIG$(100,2),_
    , M(100,2,2), DETV(100,2), DET(2), FF(100)
CLS
PRINT "This programme finds the values of capital gamma, represented"
PRINT "by m in this programme, from the equation:-"
?
?"A*m^2 + B*m + C = 0 where:-
?"
?"A = p*beta*v*(eta - 1) + eta*beta
?"B = p*v*(eta - 1)*(1 + v*(beta + 1)) + eta*(beta*p*v + 1)
?"C = p*v*(v*(1+a*v)*(eta-1) + eta)
?"
?"where: beta = mJM/mJR; m = mJR; a = A(J)/A(B)
?"v = v(STOKE)/v(CAST) = gamma(Dp/mm)^2 ; alpha = p*v(STOKE)
?"eta = fraction of inclusions removed
?"p represents zeta in the mixing equation"
?
?"Values of m are calculated for 100 specified values of the diameter"
?"of droplets from the larger nozzle and for 100 values of the"
?"corresponding droplet diameter from the smaller nozzle - ie R times"
?"the value from the larger nozzle"
?"
F = 100 : I = 1 : B = 1 : G = 11.89 : A = 0.44
E(1) = 0.76 : E(2) = 0.18
R = 0.32 : p = 0.95: CRT = 0.15: LF =1.5
PRINT "The current first value of the larger diameter is ";
PRINT USING "#.### mm";F/1000
CALL signal
INPUT "Enter a new value or press return ";QFE
IF QFE = 0 THEN F = F ELSE F = INT( (QFE + 0.00045) * 1000)
FFV = F
?
PRINT "The current last value of the larger diameter is ";
PRINT USING "#.### mm";LF
CALL signal
INPUT "Enter a new value or press return "; LFE
IF LFE = 0 THEN LF = LF ELSE LF = LFE
again:
?
PRINT "The preset parametric values for the calculations are:-"
PRINT " beta gamma a eta(large) eta(small) R p CRT"
? USING " #.## #.# #.# #.# #.# #.###";_
B,G,A,E(1),E(2),R;

```

```

? USING "  #.## #.## ";_
P,CRT
?
?"You may change them if you wish by entering a letter at the next "
?"prompt. Please enter the relevant letter at the prompt, "
?"or press return."
?
?"b for beta, g for gamma, a for the jet subtended area ratio, "
?"e for eta with the larger nozzle, s for eta with the smaller "
?"nozzle, f for the first value in the range of larger particle "
?"diameters for which calculations are done, or i for the increment "
?"[NB both in mm], p for the ratio of alpha/v(STOKES), r for the ratio"
?"of the diameters, L for the last value in the range of larger "
?"particle diameters for which calculations are done, and C for CRT."
,
values:
CALL signal
?
INPUT "- Enter the first letter of your choice or just press return ",_
CHOICE$
CHOICE$ = UCASE$(CHOICE$)
SELECT CASE CHOICE$
CASE "F"
  PRINT "The current first value of the larger diameter is ";
  PRINT USING "#.### mm";F/1000
  CALL signal
  INPUT "Enter a new value or press return "; QFE
  IF QFE = 0 THEN F = F ELSE F = INT( (QFE + 0.00045) * 1000 )
  FFV = F
CASE "L"
  PRINT "The current last value of the larger diameter is ";
  PRINT USING "#.### mm";LF
  CALL signal
  INPUT "Enter a new value or press return "; LFE
  IF LFE = 0 THEN LF = LF ELSE LF = LFE
CASE "I"
  PRINT "The current increment in the values of the larger";
  PRINT "diameter is ";
  PRINT USING "#.### mm";I/1000
  CALL signal
  INPUT "Enter a new value or press return "; QIE
  IF QIE = 0 THEN I = I ELSE I = INT( (QIE + 0.00045) * 1000 )
CASE "R"
  PRINT "The current value of the diameter ratio is ";
  PRINT USING "#.### mm";R
  CALL signal
  INPUT "Enter a new value or press return "; RE
  IF RE = 0 THEN R = R ELSE R = RE
CASE "B"
  PRINT "The current value of beta is ";
  PRINT USING "#.## ";B
  CALL signal
  INPUT "Enter a new value or press return "; BE
  IF BE = 0 THEN B = B ELSE B = BE
CASE "G"

```

```

PRINT "The current value of gamma is ";
PRINT USING "##.# ";G
CALL signal
INPUT "Enter a new value or press return "; GE
IF GE = 0 THEN G = G ELSE G = GE
CASE "A"
PRINT "The current value of the fractional jet area, 'a' is ";
PRINT USING "#.## ";A
CALL signal
INPUT "Enter a new value or press return "; AE
IF AE = 0 THEN A = A ELSE A = AE
CASE "E"
PRINT "The current value of removal efficiency for the";
PRINT "larger nozzle is ";
PRINT USING "#.## ";E(1)
CALL signal
INPUT "Enter a new value or press return "; EE
IF EE = 0 THEN E(1) = E(1) ELSE E(1) = EE
CASE "S"
PRINT "The current value of removal efficiency for the";
PRINT "smaller nozzle is ";
PRINT USING "#.## "; E(2)
CALL signal
INPUT "Enter a new value or press return "; EE
IF EE = 0 THEN E(2) = E(2) ELSE E(2) = EE
CASE "P"
PRINT "The current value of the alpha/v(STOKE) ratio is ";
PRINT USING "#.## ";P
CALL signal
INPUT "Enter a new value or press return "; PE
IF PE = 0 THEN P = P ELSE P = PE
CASE "C"
PRINT "The current value of the CRT is ";
PRINT USING "#.## ";CRT
CALL signal
INPUT "Enter a new value or press return "; CE
IF CE = 0 THEN CRT = CRT ELSE CRT = CE
END SELECT
'
?"
PRINT "The present parametric values for the calculations are:-"
? " beta gamma a eta(large) eta(small) R p CRT"
? USING " #.## #.## #.## #.## #.## #.## #.##";_
B,G,A,E(1),E(2),R;
? USING " #.## #.##";_
P,CRT
?
CALL signal
INPUT "Do you wish to change any more values? Y/N ", MORE$
MORE$ = UCASE$(LEFT$(MORE$,1))
IF MORE$ = "Y" THEN GOTO values
CALL signal
?
INPUT "Do you wish to use auto-choosing procedure? ", Auto$
Auto$ = UCASE$(LEFT$(Auto$,1))

```

```

IF Auto$ = "Y" THEN Auto% = 1 ELSE Auto% = 0
twomore:
F = F - I
FOR J = 1 TO 100
  F = F + I: FF(J) = F
  DP(J) = F/1000 : V(J,1) = G*DP(J)^2 : V(J,2) = G*(R*DP(J))^2
  FOR K = 1 TO 2
    A(J,K) = P*B*V(J,K)*(E(K) - 1) + E(K)*B
    B(J,K) = P*V(J,K)*(E(K) - 1)*(1+V(J,K)*(B+1))_
    + E(K)*(B*P*V(J,K)+1)
    C(J,K) = P*V(J,K)*(V(J,K)*(1+A*V(J,K))*(E(K) - 1) + E(K))
    DET(K) = B(J,K)^2 - 4*A(J,K)*C(J,K) : DETV(J,K) = DET(K)
    IF DET(K) < 0 THEN
      SIG$(J,K) = "Imaginary"
      GOTO cont1
    ELSE
      SIG$(J,K) = ""
      END IF
    M(J,K,1) = 0.5*( - B(J,K) + SQR(DET(K)))/A(J,K)
    M(J,K,2) = 0.5*( - B(J,K) - SQR(DET(K)))/A(J,K)
  cont1:
NEXT K
NEXT J
'
IF Auto% = 0 THEN
  JST = 1: JSTE = -17
  GOTO morepr
ELSE
  JSTE = -13
'
FOR J=1 TO 100
  IF DP(J) >= LF THEN GOTO big
  IF SGN(M(J,1,1)) + SGN(M(J,2,1)) = -2 AND SGN (M(J+1,1,1)) + _
  SGN(M(J+1,2,1)) <> 2 THEN GOTO oncemore
  IF SIG$(J,1)="Imaginary" OR SIG$(J,2)="Imaginary" THEN
    GOTO oncemore
  ELSEIF M(J,1,1)<=0 OR M(J,2,1)<=0 THEN
    IF J = 100 THEN GOTO oncemore

    IF M(J,2,1) <= 0 THEN
      IF M(J+1,2,1) < 0 THEN GOTO oncemore
      IF M(J+1,2,1) < M(J,1,1) THEN
        GOTO maybe0
      ELSE
        IF M(J+1,1,1) > 0 THEN
          IF M(J+1,1,1) < M(J+1,2,1) THEN MM = 0.5*(M(J,1,1)_
          + M(J+1,1,1)) ELSE MM = 0.5*(M(J,1,1) + M(J+1,2,1))
          GOTO maybe
        ELSE
          GOTO maybe0
        END IF
      END IF
    ELSE
      IF M(J+1,1,1) < 0 THEN GOTO oncemore
      IF M(J+1,1,1) < M(J,2,1) THEN

```

```

GOTO maybe0
ELSE
IF M(J+1,2,1) > 0 THEN
  IF M(J+1,1,1) < M(J+1,2,1) THEN MM = 0.5*(M(J,2,1)
    + M(J+1,1,1)) ELSE MM = 0.5*(M(J,2,1) + M(J+1,2,1))
  GOTO maybe
  ELSE
    GOTO maybe0
  END IF
END IF
END IF

ELSE
IF SGN(M(J + 1,1,1)) = -1 OR SGN(M(J + 1,2,1)) = -1 THEN
IF SGN(M(J + 1,2,1)) = -1 AND SGN(M(J+1,1,1)) = 1 THEN
  MM = 0.5*(M(J,1,1) + M(J+1,1,1))
  GOTO maybe
ELSEIF SGN(M(J + 1,1,1)) = -1 AND SGN(M(J+1,2,1)) = 1 THEN
  MM = 0.5*(M(J,2,1) + M(J+1,2,1))
  GOTO maybe
  ELSE
    GOTO maybe0
  END IF
maybe0:
  cls
  ?"There may be a solution in the following table. ";
  ?"Please check yourself"
  ?"The current values are as follows:"
  ?
  GOTO maybe1
maybe:
  cls
  JSTE = 12
  ?"There may be a solution in the following table. Please check."
  ? "i.e. the value of the large diameter is ";
  ?USING"### mm and M = ###.###"; DP(J),MM
  ?"The current values are as follows:"
  ?
maybe1:
  IF J>7 THEN JST = J - 7 ELSE JST = 1
  F = FF(J + 1)
  GOTO morepr
  ELSEIF ABS(M(J,1,1) - M(J,2,1))/M(J,1,1) <= CRT THEN
  IF ABS(M(J,1,1) - M(J,2,1)) > ABS(M(J+1,1,1) - M(J+1,2,1))_
  THEN GOTO oncemore
  cls
  IF J > 7 THEN JST = J - 7 ELSE JST = 1
  ?"The solution for M can be found in the following table."
  ?"i.e. The value of the large diameter is ";
  PRINT USING "### mm"; DP(J);
  ?USING" and M =###.###"; 0.5*(M(J,2,1)+M(J,1,1))
  ?" ";
  ?USING"Diff = ### " ; ABS(M(J,1,1) - M(J,2,1))
  F = FF(J+2)
  GOTO morepr

```

```

ELSE
  IF M(J,1,1)>10^10 OR M(J,2,1)>10^10 THEN
    cls
    ?"There is no suitable solution. The M values are too big."
    ?"The current values are as follows:"
    ?
    IF J > 7 THEN JST = J - 7 ELSE JST = 1
    F = FF(J + 1)
    GOTO morepr
  END IF
END IF
END IF
oncemore:
NEXT J
IF F/1000 < LF THEN GOTO twomore
,
big:
cls
?"No suitable solution for the particles of diameter ";
?USING"#.### mm to #.### mm"; FFV/1000,LF
?"The current values are:"
?
IF J > 7 THEN JST = J - 7 ELSE JST = 1
F = 100
END IF
,
morepr:
  morepr1:
  PRINT "Parametric values for this set of calculations:-
  PRINT " beta gamma a eta(large) eta(small) R p CRT"
  PRINT USING " #.## #.# #.# #.# #.## ";_
  B,G,A,E(1),E(2);
  PRINT USING " #.### #.# #.##";_
  R,P,CRT
  ?" For large nozzle For small nozzle
  ?"Dp m (+ sign) m(- sign) Dp m (+ sign) m(- sign)"
  FOR J = JST TO JST + JSTE
    IF SIG$(J,1) = "" THEN
      PRINT USING "#.### #.# #.# #.# #.# #.##";_
      DP(J),M(J,1,1),M(J,1,2);
    ELSE
      PRINT USING "#.### "; DP(J);
      PRINT "DETERMINANT = ";
      PRINT USING "#.# #.# #.# #.# #.# #.##"; DETV(J,1);
    END IF
    IF SIG$(J,2) = "" THEN
      DSM = R*DP(J)
      PRINT USING "#.### #.# #.# #.# #.# #.##";_
      DSM,M(J,2,1),M(J,2,2)
    ELSE
      PRINT USING "#.### "; DSM;
      PRINT "DETERMINANT = ";
      PRINT USING "#.# #.# #.# #.# #.# #.##"; DETV(J,2)
    END IF
  IF J = 100 THEN GOTO setval

```

```

NEXT J
'
IF Auto% = 0 THEN
INPUT "Enter 'M' if you wish to see more values ",M$
IF UCASE$(LEFT$(M$,1)) = "M" THEN JST = J : GOTO morepr1
?
CALL signal:
?"***** YOU DO NOT WANT TO SEE MORE VALUES *****"
?"**** BUT IF YOU WISH, YOU CAN CARRY OUT SOME MORE CALCULATIONS ****"
GOTO wish
END IF
setval:
CALL signal
?"***** THE END OF THIS SET OF CALCULATION *****"
wish:
CALL signal : SOUND 600,3
INPUT "Do you wish to carry out some more calculations? ",m$
IF UCASE$(LEFT$(M$,1)) <> "Y" THEN END
?
?"Do you wish to start at the present value of the larger diameter"
PRINT USING "which is #.### mm"; F/1000;
CALL signal
INPUT CHN$
IF UCASE$(LEFT$(CHN$,1)) = "Y" THEN
?
PRINT "OK - but how about the last value of the large diameter?"
GOTO last
END IF
CALL signal
INPUT "Please enter the start value that you require then ", QFE
IF QFE = 0 THEN F = F ELSE F = INT((QFE + 0.00045)*1000)
'
last:
FFV = F
?
?"Do you wish to end at the present value of the larger diameter "
PRINT USING "which is #.### mm"; LF;
CALL signal
INPUT CHN$
IF UCASE$(LEFT$(CHN$,1)) = "Y" THEN
?
PRINT "OK - but you have the choice of changing any other";
PRINT " parametric values anyway"
GOTO again
END IF
CALL signal
?
INPUT "Please enter the end value that you require then ", LFE
IF LFE = 0 THEN LF = LF ELSE LF = LFE
GOTO again
'
SUB signal
SOUND 600,1
END SUB
END

```